

VOLUME 81

FEBRUARY 24, 1977

NUMBER 4

JPCHAX

---

THE JOURNAL OF  
PHYSICAL  
CHEMISTRY

---



PUBLISHED BIWEEKLY BY THE AMERICAN CHEMICAL SOCIETY

# THE JOURNAL OF PHYSICAL CHEMISTRY

**BRYCE CRAWFORD, Jr., Editor**  
**STEPHEN PRAGER, Associate Editor**  
**ROBERT W. CARR, Jr., C. ALDEN MEAD, Assistant Editors**

**EDITORIAL BOARD:** C. A. ANGELL (1973-1977), F. C. ANSON (1974-1978), V. A. BLOOMFIELD (1974-1978), J. R. BOLTON (1976-1980), L. M. DORFMAN (1974-1978), W. FALCONER (1977-1978), H. L. FRIEDMAN (1975-1979), H. L. FRISCH (1976-1980), W. A. GODDARD (1976-1980), E. J. HART (1975-1979), W. J. KAUZMANN (1974-1978), R. L. KAY (1977-1981), D. W. McCLURE (1974-1978), K. MYSELS (1977-1981), R. M. NOYES (1973-1977), R. G. PARR (1977-1979), W. B. PERSON (1976-1980), J. C. POLANYI (1976-1980), S. A. RICE (1976-1980), F. S. ROWLAND (1973-1977), R. L. SCOTT (1973-1977), W. A. STEELE (1976-1980), J. B. STOTHERS (1974-1978), F. A. VAN-CATLEDGE (1977-1981), B. WEINSTOCK (1977)

Published by the  
**AMERICAN CHEMICAL SOCIETY**  
**BOOKS AND JOURNALS DIVISION**

D. H. Michael Bowen, Director  
 Marjorie Laflin, Assistant to the Director

Editorial Department: Charles R. Bertsch,  
 Head; Marianne C. Brogan, Associate  
 Head; Celia B. McFarland, Joseph E.  
 Yurvati, Assistant Editors

Magazine and Production Department:  
 Bacil Guiley, Head

Research and Development Department:  
 Seldon W. Terran, Head

Advertising Office: Centcom, Ltd., 50 W.  
 State St., Westport, Conn. 06880.

© Copyright, 1977, by the American  
 Chemical Society. No part of this publication  
 may be reproduced in any form without  
 permission in writing from the American  
 Chemical Society.

Published biweekly by the American  
 Chemical Society at 20th and Northampton  
 Sts., Easton, Pennsylvania 18042. Second  
 class postage paid at Washington, D.C. and  
 at additional mailing offices.

## Editorial Information

**Instructions for authors** are printed in  
 the first issue of each volume. Please conform  
 to these instructions when submitting manu-  
 scripts.

**Manuscripts for publication** should be  
 submitted to *The Journal of Physical  
 Chemistry*, Department of Chemistry, Uni-  
 versity of Minnesota, Minneapolis, Minn.  
 55455. Correspondence regarding **accepted  
 papers and proofs** should be directed to the

Editorial Department at the ACS Easton  
 address.

**Page charges** of \$60.00 per page are as-  
 sessed for papers published in this journal.  
 Ability to pay does not affect acceptance or  
 scheduling of papers.

**Bulk reprints or photocopies** of indi-  
 vidual articles are available. For information  
 write to Business Operations, Books and  
 Journals Division at the ACS Washington  
 address.

Requests for **permission to reprint**  
 should be directed to Permissions, Books and  
 Journals Division at the ACS Washington  
 address. The American Chemical Society and  
 its Editors assume no responsibility for the  
 statements and opinions advanced by con-  
 tributors.

## Subscription and Business Information

1977 Subscription rates—including surface  
 postage

	U.S.	PUAS	Canada, Foreign
Member	\$24.00	\$33.00	\$34.00
Nonmember	96.00	105.00	106.00
Supplementary material	15.00	19.00	20.00

**Air mail and air freight** rates are avail-  
 able from Membership & Subscription Ser-  
 vices, at the ACS Columbus address.

**New and renewal subscriptions** should  
 be sent with payment to the Office of the  
 Controller at the ACS Washington address.

**Changes of address** must include both old  
 and new addresses with ZIP code and a recent  
 mailing label. Send all address changes to the  
 ACS Columbus address. Please allow six  
 weeks for change to become effective. **Claims  
 for missing numbers** will not be allowed if  
 loss was due to failure of notice of change of  
 address to be received in the time specified:

if claim is dated (a) North America—more  
 than 90 days beyond issue date, (b) all other  
 foreign—more than 1 year beyond issue date;  
 or if the reason given is "missing from files".  
 Hard copy claims are handled at the ACS  
 Columbus address.

**Microfiche subscriptions** are available  
 at the same rates but are mailed first class to  
 U.S. subscribers, air mail to the rest of the  
 world. Direct all inquiries to Special Issues  
 Sales, at the ACS Washington address or call  
 (202) 872-4554. **Single issues** in hard copy  
 and/or microfiche are available from Special  
 Issues Sales at the ACS Washington address.  
 Current year \$4.75. Back issue rates available  
 from Special Issues Sales. **Back volumes** are  
 available in hard copy and/or microform.  
 Write to Special Issues Sales at the ACS  
 Washington address for further information.  
**Microfilm** editions of ACS periodical pub-  
 lications are available from volume 1 to the  
 present. For further information, contact  
 Special Issues Sales at the ACS Washington  
 address. **Supplementary material** men-  
 tioned in the journal appears in the microfilm  
 edition. Single copies may be ordered directly  
 from Business Operations, Books and Jour-  
 nals Division, at the ACS Washington ad-  
 dress.

	U.S.	PUAS, Canada	Other Foreign
Microfiche	\$2.50	\$3.00	\$3.50
Photocopy			
1-7 pages	4.00	5.50	7.00
8-20 pages	5.00	6.50	8.00

Orders over 20 pages are available only on  
 microfiche, 4 × 6 in., 24X, negative, silver  
 halide. Orders must state photocopy or mi-  
 crofiche if both are available. Full bibli-  
 ographic citation including names of all au-  
 thors and prepayment are required. Prices  
 are subject to change.

American Chemical Society  
 1155 16th Street, N.W.  
 Washington, D.C. 20036  
 (202) 872-4600

Member & Subscription Services  
 American Chemical Society  
 P.O. Box 3337  
 Columbus, Ohio 43210  
 (614) 421-7230

Editorial Department  
 American Chemical Society  
 20th and Northampton Sts.  
 Easton, Pennsylvania 18042  
 (215) 258-9111

Volume 81, Number 4 February 24, 1977

JPCHAx 81(4) 281-372 (1977)

ISSN 0022-3654

Ion-Molecule Reactions in SiH <sub>4</sub> -CF <sub>4</sub> Mixtures . . . . .	<b>J. R. Krause and F. W. Lampe*</b>	281
The Temperature Dependences of the Ultraviolet Absorption Cross Sections of CCl <sub>2</sub> F <sub>2</sub> and CCl <sub>3</sub> F, and Their Stratospheric Significance . . . . .	<b>C. C. Chou, W. S. Smith, H. Vera Ruiz, K. Moe, G. Crescentini, M. J. Molina, and F. S. Rowland*</b>	286
Flash Photolysis Resonance Fluorescence Investigation of the Temperature Dependencies of the Reactions of Cl( <sup>2</sup> P) Atoms with CH <sub>4</sub> , CH <sub>3</sub> Cl, CH <sub>3</sub> F, CH <sub>3</sub> F <sup>†</sup> , and C <sub>2</sub> H <sub>6</sub> . . . . .	<b>Ronald G. Manning and Michael J. Kurylo*</b>	291 ■
Kinetics and Mechanism of the Gas Phase Reaction of OH Radicals with Aromatic Hydrocarbons Over the Temperature Range 296-473 K . . . . .	<b>R. A. Perry, R. Atkinson,* and J. N. Pitts, Jr.</b>	296 ■
Radiolysis of Adenine in Dilute Neutral Aqueous Solution . . . . .	<b>George Gorin,* C. Lehman, C. A. Mannan, L. M. Raff, and S. E. Scheppele</b>	304
A Chromatographic Investigation of Ternary Nonelectrolyte Systems . . . . .	<b>Jon F. Parcher* and Theodore N. Westlake</b>	307
Predictive Scheme for Thermochemical Properties of Polycyclic Aromatic Hydrocarbons . . . . .	<b>S. E. Stein, D. M. Golden,* and S. W. Benson</b>	314
Phase Relationships and Thermodynamic Properties of Transition Metal Borides. 1. The Molybdenum-Boron System and Elemental Boron . . . . .	<b>Edmund Storms* and Barbara Mueller</b>	318
Internal Pressures and Solubility Parameters for Carbon Disulfide, Benzene, and Cyclohexane . . . . .	<b>J. A. R. Renuncio, G. J. F. Breedveld,* and J. M. Prausnitz</b>	324 ■
Coadsorption of <i>n</i> -Alkyl Alcohols and Hydrogen Sulfide at the Aqueous Solution Interface . . . . .	<b>Graeme G. Strathdee* and Russell M. Given</b>	327
Chemical and Spectroscopic Properties of Copper Containing Zeolites . . . . .	<b>J. Texter, D. H. Strome, R. G. Herman, and K. Klier*</b>	333
Spectroscopic Characterization of the Pheophytin a Dication . . . . .	<b>Walter Oettmeier, Thomas R. Janson, Marion C. Thurnauer, Lester L. Shipman, and Joseph J. Katz*</b>	339
Vibrational Spectra and Force Constants of Heptasulfur Imide . . . . .	<b>Ralf Steudel</b>	343
A Detailed Study of <i>N,N,N',N'</i> -Tetramethyl- <i>p</i> -phenylenediamine Luminescence in Organic Glasses. Evidence for a Protonation Reaction . . . . .	<b>J. Blais and M. Gauthier*</b>	349
Electron Spin Resonance of Radicals in $\gamma$ -Irradiated Mono- and Polycyclic Olefins. 4. Electronic Structure and Electron Spin Resonance Properties of a Norbornenyl Fused Cyclopentadienyl Radical . . . . .	<b>A. Faucitano,* A. Buttafava, F. Faucitano Martinotti, S. Cesca, and R. Fantechi</b>	354
An Electron Spin Resonance Study of the Benzene Anion Radical. A Model of Its Ion Pair with Alkali Metal Ions . . . . .	<b>M. T. Jones* and T. C. Kuechler</b>	360
Substituted Benzylidenemalononitrile Anion Radicals . . . . .	<b>Arthur McB. Block, Rosario Concepción, and Gerald R. Stevenson*</b>	367

■ Supplementary and/or miniprint material for this paper is available separately (consult the masthead page for ordering information); it will also appear following the paper in the microfilm edition of this journal.

\* In papers with more than one author, the asterisk indicates the name of the author to whom inquiries about the paper should be addressed.

#### AUTHOR INDEX

- |                          |                      |                         |                       |
|--------------------------|----------------------|-------------------------|-----------------------|
| Atkinson, R., 296        | Gauthier, M., 349    | Lehman, C., 304         | Rowland, F. S., 286   |
| Benson, S. W., 314       | Given, R. M., 327    | Mannan, C. A., 304      | Scheppele, S. E., 304 |
| Blais, J., 349           | Golden, D. M., 314   | Manning, R. G., 291     | Shipman, L. L., 339   |
| Block, A. McB., 367      | Gorin, G., 304       | Martinotti, F. F., 354  | Smith, W. S., 286     |
| Breedveld, G. J. F., 324 | Herman, R. G., 333   | Moe, K., 286            | Stein, S. E., 314     |
| Burkhart, R. D., 370     | Janson, T. R., 339   | Molina, M. J., 286      | Steudel, R., 343      |
| Buttafava, A., 354       | Jones, M. T., 360    | Mueller, B., 318        | Stevenson, G. R., 367 |
| Cesca, S., 354           | Katz, J. J., 339     | Oettmeier, W., 339      | Storms, E., 318       |
| Chou, C. C., 286         | Klier, K., 333       | Parcher, J. F., 307     | Strathdee, G. G., 327 |
| Concepción, R., 367      | Krause, J. R., 281   | Perry, R. A., 296       | Strome, D. H., 333    |
| Crescentini, G., 286     | Kuechler, T. C., 360 | Pitts, J. N., Jr., 296  | Texter, J., 333       |
| Fantechi, R., 354        | Kurylo, M. J., 291   | Prausnitz, J. M., 324   | Thurnauer, M. C., 339 |
| Faucitano, A., 354       | Lampe, F. W., 281    | Raff, L. M., 304        | Vera Ruiz, H., 286    |
|                          |                      | Renuncio, J. A. R., 324 | Westlake, T. N., 307  |

#### ANNOUNCEMENT

On the last two pages of this issue you will find reproduced the table of contents of the January 1977 issue of the *Journal of Chemical and Engineering Data*.





# THE JOURNAL OF PHYSICAL CHEMISTRY

Registered in U. S. Patent Office © Copyright, 1977, by the American Chemical Society

VOLUME 81, NUMBER 4 FEBRUARY 24, 1977

## Ion-Molecule Reactions in $\text{SiH}_4\text{-CF}_4$ Mixtures<sup>1</sup>

J. R. Krause and F. W. Lampe\*

Davey Laboratory, Department of Chemistry, The Pennsylvania State University, University Park, Pennsylvania 16802  
(Received October 4, 1976)

Publication costs assisted by The Pennsylvania State University

The reactions of  $\text{Si}^+$ ,  $\text{SiH}^+$ ,  $\text{SiH}_2^+$ , and  $\text{SiH}_3^+$  with  $\text{CF}_4$  and the reactions of  $\text{F}^+$ ,  $\text{CF}^+$ ,  $\text{CF}_2^+$ , and  $\text{CF}_3^+$  with  $\text{SiH}_4$  have been investigated by tandem mass spectrometry. In related experiments the reactions of  $\text{SiH}_3^+$  with  $\text{CF}_3\text{H}$  have been studied also. Reaction cross sections have been determined over the range of 1–4 eV in the laboratory system and phenomenological rate constants for a reactant-ion energy of 1 eV are reported. The major reaction of positive ions containing fluorine with  $\text{SiH}_4$  is  $\text{H}^-$  abstraction and the major reaction of positive silicon ions with  $\text{CF}_4$  is  $\text{F}^-$  abstraction. Also observed in the reactive encounters of  $\text{CF}_3^+$  and  $\text{CF}_2^+$  with  $\text{SiH}_4$  are products in which extensive redistribution of F and H between carbon and silicon centers has occurred. These redistribution reactions, which involve the breaking and reforming of up to six bonds, must occur within a single collision complex. A mechanism for this redistribution, in the case of the reaction of  $\text{CF}_3^+$  with  $\text{SiH}_4$ , is proposed in which the collision complex is held together by alternating hydrogen and fluorine bridges.

### Introduction

Hydrogen is generally bonded to silicon more weakly than to carbon<sup>2-9</sup> while the reverse appears to be true for corresponding bonds of fluorine to silicon and carbon.<sup>10,11</sup> Accordingly, mixtures of silanes and fluorocarbons should be very reactive systems with a strong thermodynamic tendency for the fluorine and hydrogen atoms to exchange their binding partners. As part of a general program concerned with the effects of ionizing radiation on volatile silicon compounds, we have had occasion to study ion-molecule reactions characteristic of  $\text{SiH}_4\text{-CF}_4$  mixtures and thereby to examine the ionic pathways of such an exchange. This paper is a report of our findings.

### Experimental Section

The tandem mass spectrometer used in these studies has been previously described.<sup>12</sup> Basically, the instrument consists of two quadrupole mass filters separated by a collision chamber and ion lenses mounted in an "in-line" configuration. Mass-selected reactant ions having kinetic energy variable down to about 1 eV are injected into the collision chamber containing the neutral reactant molecule at 0.001 Torr and the product ions are drawn out of the

chamber and mass analyzed by the second filter. Retarding field measurements indicate that the energy spread of the reactant ion beam entering the collision chamber is about 1 eV.

General operation of the instrument was checked by examining the energy dependence of the cross section for the formation of  $\text{ArD}^+$  in  $\text{Ar}^+\text{-D}_2$  collisions over the range 1–10 eV (laboratory energy). The dependence of the cross section on the kinetic energy of  $\text{Ar}^+$  was found to be in satisfactory agreement with that found by Teloy and Gerlich<sup>13</sup> over the given energy range.

Relative reaction cross sections, computed from the intensities of reactant ions and product ions and collision chamber pressure, were determined for reactant-ion energies in the range of 1–4 eV (lab). Conversion of the relative cross sections to absolute cross sections was made by comparison, at 1 eV (lab), with relative cross sections for reactions 1–3, the cross sections or rate constants of

$$\text{CD}_4^+ + \text{CD}_4 \rightarrow \text{CD}_5^+ + \text{CD}_3 \quad (1)$$
$$\text{CH}_3^+ + \text{SiH}_4 \rightarrow \text{SiH}_3^+ + \text{CH}_4 \quad (2)$$
$$\text{CF}_2^+ + \text{CF}_4 \rightarrow \text{CF}_3^+ + \text{CF}_3 \quad (3)$$

which have previously been reported.<sup>14-17</sup> The agreement

TABLE I: Reactions of Silicon-Containing Ions<sup>a</sup> with CF<sub>4</sub><sup>b</sup>

Reactant ion (m/e)	Major reactant ion	Cross section in Å <sup>2</sup> for formation of product ion having m/e:					
		47	48	49	50	51	69
28	<sup>28</sup> Si <sup>+</sup> (100%)	3.9					0.36
29	<sup>28</sup> SiH <sup>+</sup> (96%)	0.43	0.06				0.53
30	<sup>28</sup> SiH <sub>2</sub> <sup>+</sup> (98%)	0.14	0.09	1.1	0.17	0.03	4.4
31	<sup>28</sup> SiH <sub>3</sub> <sup>+</sup> (94%)			0.68		0.40	7.2

<sup>a</sup> Reactant-ion energy of 1.0 eV (laboratory). <sup>b</sup> Collision-chamber pressure of 1.0 × 10<sup>-3</sup> Torr.

from the three calibration reactions was within ±10%.

Both monosilane and tetrafluoromethane were purchased from the Matheson Co. The gases were subjected to several freeze-pump-thaw cycles before use and mass spectrometric analysis revealed no impurities.

## Results

We have investigated the reactions of all singly charged fluorine-containing ions in the primary mass spectrum of CF<sub>4</sub> with SiH<sub>4</sub> and of all the primary ions derived from SiH<sub>4</sub> with CF<sub>4</sub>. Reaction cross sections at 1 eV reactant-ion energy (lab) are shown in Tables I and II and these cross sections refer to the <sup>28</sup>Si isotope.

With the exception of the reaction (m/e 29)<sup>+</sup> + CF<sub>4</sub> → (m/e 48)<sup>+</sup> in Table I, all corrections for the naturally occurring <sup>29</sup>Si (4.7%) and <sup>30</sup>Si (3.1%) isotopes were less than 7%.

In Tables I and II the reactant ion, the reactant molecule, and the product ion are clearly identified for each ion-molecule reaction. Complete reaction identification requires also knowledge of the electrically neutral products. Thermochemical considerations aid in making a choice between various stoichiometrically possible sets of neutral products, particularly if one knows if the reaction forming the given ion is exothermic or endothermic. As described previously,<sup>18,19</sup> the shapes of the reaction cross section vs. energy curves have been used to differentiate between exothermic and endothermic reactions. The cross sections of endothermic reactions generally rise, with increasing reactant-ion energy, from zero at the energy threshold to a broad maximum several electron volts above the threshold. The cross sections of exothermic reactions usually decrease for all values of increasing ion energy, although exceptions to this can arise when symmetry and spin properties of the molecular orbitals of reactants and products prevent the reaction from occurring on the lowest potential energy surfaces.<sup>20,21</sup>

The predominance of CF<sub>3</sub><sup>+</sup> (m/e 69) as a product ion in Table I indicates that the major process involved when silicon-containing ions attack CF<sub>4</sub> is F<sup>-</sup> transfer. Similarly, the predominance of SiH<sub>3</sub><sup>+</sup> (m/e 31) and SiD<sub>3</sub><sup>+</sup> (m/e 34) in Table II shows that H<sup>-</sup> transfer is the principal reaction that takes place when fluorocarbon ions attack SiH<sub>4</sub>. The

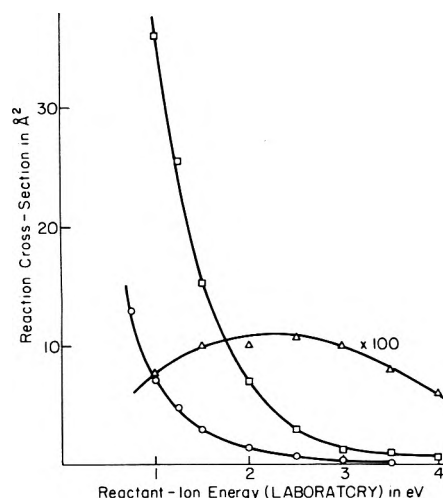


Figure 1. Kinetic energy dependence of reaction cross sections: (O) SiH<sub>3</sub><sup>+</sup> + CF<sub>4</sub> → CF<sub>3</sub><sup>+</sup> + SiH<sub>2</sub>F; (□) CF<sub>3</sub><sup>+</sup> + SiH<sub>4</sub> → SiH<sub>3</sub><sup>+</sup> + CF<sub>3</sub>H; (Δ) SiH<sub>3</sub><sup>+</sup> + CF<sub>4</sub> → (m/e 50)<sup>+</sup> (see text).

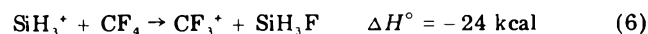
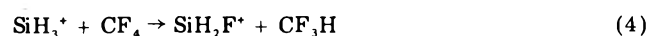
tendency of CF<sub>4</sub> toward F<sup>-</sup> transfer to attacking positive ions and of SiH<sub>4</sub> toward H<sup>-</sup> transfer to attacking positive ions has been reported previously.<sup>17,19</sup> The energy dependences of the cross sections of these major F<sup>-</sup> and H<sup>-</sup> transfer reactions are shown in Figure 1.

## Discussion

In this section we discuss the characteristics of the individual elementary reactions that take place when the various reactant pairs are brought together.

(a) SiH<sub>3</sub><sup>+</sup> + CF<sub>4</sub>. As shown in Table I the reaction of SiH<sub>3</sub><sup>+</sup> ions of 1 eV kinetic energy (laboratory) with CF<sub>4</sub> yields product ions having m/e values of 49, 51, and 69, of which the latter predominates by an order of magnitude. These ions are clearly SiH<sub>2</sub>F<sup>+</sup>, CF<sub>2</sub>H<sup>+</sup>, and CF<sub>3</sub><sup>+</sup>, respectively.

On the basis of the dependence of cross section on reactant-ion energy it is concluded that the processes forming m/e 49, 51, and 69 are exothermic. If we write the neutral products of each reaction as those that yield the largest exothermicity, the reactions forming these ions are as shown in (4)–(6). The standard enthalpy changes



of (5) and (6) have been calculated from published thermochemical data,<sup>5,10,23–25</sup> and, in agreement with our conclusion from the energy dependence of the reaction cross sections, these reactions are seen to be exothermic. The standard enthalpy of formation of SiH<sub>2</sub>F<sup>+</sup> is not known but, on the basis of our observation that (4) is exothermic, we may assign the upper limit: ΔH<sub>f</sub><sup>o</sup>(SiH<sub>2</sub>F<sup>+</sup>) ≤ 183 kcal/mol.

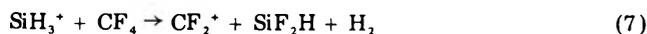
At higher collision energies m/e 50 is observed as a product of the collisions of m/e 31 from SiH<sub>4</sub> with CF<sub>4</sub>.

TABLE II: Reactions of Fluorine-Containing Ions<sup>a</sup> with SiH<sub>4</sub><sup>b</sup>

Reactant ion	Target molecule	Cross section in Å <sup>2</sup> for formation of product ion having m/e:											
		15	28	29	30	31	32	33	34	47	49	51	80
F <sup>+</sup>	SiH <sub>4</sub>		0.5	1.0	0.5	0.9				0.7			
CF <sup>+</sup>	SiD <sub>4</sub>						2		15	1.3		0.18	
CF <sub>2</sub> <sup>+</sup>	SiH <sub>4</sub>	0.38				33				13 <sup>c</sup>		10 <sup>c</sup>	0.08
CF <sub>3</sub> <sup>+</sup>	SiH <sub>4</sub>	0.67				37		1.0		0.1	1.7	10	

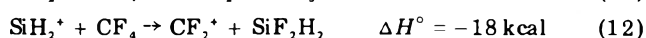
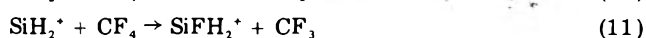
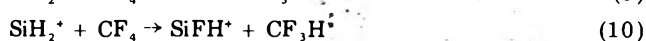
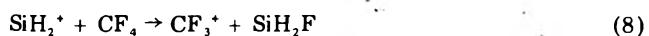
<sup>a</sup> Reactant-ion energy of 1.0 eV (laboratory) unless otherwise indicated. <sup>b</sup> Collision-chamber pressure of 1.0 × 10<sup>-3</sup> Torr unless otherwise indicated. <sup>c</sup> Estimated from data at 4 eV (laboratory) for CF<sub>3</sub><sup>+</sup> + SiD<sub>4</sub> system.

As shown in Figure 1, the dependence of cross section on energy indicates the reaction to be endothermic. The intensity of  $m/e$  50 at 1 eV seen in Figure 1 is due to the ions  $^{29}\text{SiH}_2\text{F}^+$  and  $\text{CF}_2^+$  that are formed by the exothermic reactions of  $^{29}\text{SiH}_2^+$  (6% of the  $m/e$  31 beam) with  $\text{CF}_4$ . Since parent molecular ions are not found in the mass spectrum of  $\text{SiH}_3\text{Cl}$ ,<sup>22</sup> it is not likely that the endothermic product of  $m/e$  50 is  $\text{SiH}_3\text{F}^+$  and, on the basis of this admittedly weak analogy, we conclude that  $\text{CF}_2^+$  is the endothermic product observed. Assuming that the most energetically stable neutral products are formed the reaction would be as in (7).



The standard enthalpy of formation of  $\text{SiF}_2\text{H}$  is not known but estimation of it from bond energy data<sup>11</sup> indicates that reaction 7 is endothermic by 63 kcal/mol.

(b)  $\text{SiH}_2^+ + \text{CF}_4$ . The predominant product of this reaction pair is also  $\text{CF}_3^+$ , as may be seen in Table I, and, in addition, smaller amounts of  $\text{SiF}^+$  ( $m/e$  47),  $\text{SiFH}^+$  ( $m/e$  48),  $\text{SiFH}_2^+$  ( $m/e$  49),  $\text{CF}_2^+$ , and  $\text{CF}_2\text{H}^+$  are produced. With the exception of  $\text{CF}_2\text{H}^+$  all product ions appear to be formed in exothermic reactions and, again writing the neutral products as those most feasible on energetic grounds, the reactions involved are those shown in (8)–(12).



On the basis of our observation that (8), (10), and (11) are exothermic, we may derive the following upper limits to standard enthalpies of formation:  $\Delta H_f^\circ(\text{SiH}_2\text{F}) \leq -38$  kcal/mol;  $\Delta H_f^\circ(\text{SiFH}^+) \leq 226$  kcal/mol; and  $\Delta H_f^\circ(\text{SiFH}_2^+) \leq 175$  kcal/mol. In view of the very low intensities of  $\text{CF}_2\text{H}^+$ , it was not possible to obtain reliable measurements of the cross section as a function of energy. No dramatic increases in its intensity were noted at higher ion energies so the reaction forming it is probably exothermic.

(c)  $\text{SiH}^+ + \text{CF}_4$ . Three product ions are observed as a result of collisions of  $\text{SiH}^+$  with  $\text{CF}_4$ , namely,  $\text{SiF}^+$ ,  $\text{SiFH}^+$ , and  $\text{CF}_3^+$ .  $\text{SiFH}^+$  is formed only in very small amounts, and there is reason to doubt that it is formed at all since ~80% of the intensity observed at  $m/e$  48 (before isotope correction) is due to the isotope  $^{29}\text{SiF}^+$ . The cross sections of all ionic products decrease with increasing ion energy over the entire range studied, so it is concluded that all reactions are exothermic and may be written as shown in (13)–(15). As in the reactions of  $\text{SiH}_3^+$  and  $\text{SiH}_2^+$  with



$\text{CF}_4$ , F<sup>-</sup> transfer to the attacking Si-containing ion, (13), is the most probable reaction of  $\text{SiH}^+$  and  $\text{CF}_4$  but the absolute cross section for the latter pair is lower by about an order of magnitude.

The exothermic nature of (14), calculated from thermochemical data, agrees with the conclusion drawn from the cross section energy dependence. The indicated exothermicity of (13) then leads to the upper limit of  $\Delta H_f^\circ(\text{SiHF}) < -55$  kcal/mol. This value implies that the bond dissociation energy  $D(\text{FSi-H})$  is greater than 109 kcal/mol and this is surely too high. It seems likely, therefore, that (13) is actually endothermic for ground-

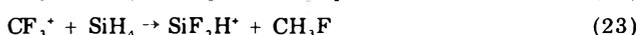
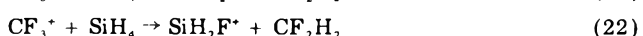
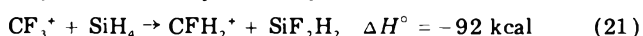
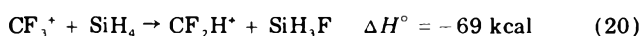
state reactants and the apparent exothermicity is due to the presence of internal excitation energy in the  $\text{SiH}^+$  reactant ions. This is not surprising in view of the fact that  $\text{SiH}^+$  is produced from  $\text{SiH}_4$  by electron impact and the involvement of excess energy in this process has been previously noted.<sup>5</sup> Such effects of internal energy, which have been noted before in ion-molecule reaction studies,<sup>27,28</sup> are usually accompanied by small reaction cross sections and this is consistent with the data in Table I. Little can be said about the energetic characteristics of (15) since for this reactant pair the product ion observed at  $m/e$  48 is predominantly  $^{29}\text{SiF}^+$ .

(d)  $\text{Si}^+ + \text{CF}_4$ . Only two products result from the collision of 1-eV  $\text{Si}^+$  ions with  $\text{CF}_4$ , namely,  $\text{SiF}^+$ , the product of F-atom transfer, and  $\text{CF}_3^+$ , the product of F<sup>-</sup>-ion transfer. The dependence of cross section on energy suggests that both reactions are exothermic processes and may be written as shown in (16) and (17). Standard



enthalpies of formation<sup>10,24,26</sup> indicate that (16) is exothermic for ground-state reactants, as suggested by our cross-section energy dependence, but that (17) is endothermic. The exothermic dependence of the cross section for (17) on ion energy must therefore pertain to excited  $\text{Si}^+(^4\text{P})$  ions which have an energy of 5.5 eV in excess of the ground-state  $\text{Si}^+(^2\text{P})$  ions.<sup>29</sup> The relative magnitudes of the cross sections for (16) and (17) in Table I are consistent with (17) being restricted energetically to  $\text{Si}^+(^4\text{P})$  ions while (16) may be undergone by  $\text{Si}^+(^2\text{P})$  and  $\text{Si}^+(^4\text{P})$  ions. Previous studies of the  $\text{Si}^+(\text{D}_2, \text{D}) \text{SiD}^+$  reaction,<sup>30</sup> in which the technique<sup>31</sup> of collisional attenuation of the ion beam was used, indicate that about 38% of the  $\text{Si}^+$  ion beam is  $\text{Si}^+(^4\text{P})$ .

(e)  $\text{CF}_3^+ + \text{SiH}_4$ . As may be seen in Table II, the collisions of 1-eV  $\text{CF}_3^+$  ions with  $\text{SiH}_4$  result in the formation of product ions having  $m/e$  values of 15, 31, 33, 49, and 51 of which 31 is by far the most abundant. Observation of the mass shifts that result when  $\text{SiH}_4$  is replaced by  $\text{SiD}_4$  enable us to make the following assignments:  $\text{CH}_3^+$  ( $m/e$  15),  $\text{SiH}_3^+$  ( $m/e$  31),  $\text{CFH}_2^+$  ( $m/e$  33),  $\text{SiH}_2\text{F}^+$  ( $m/e$  49), and  $\text{CF}_2\text{H}^+$  ( $m/e$  51). In addition, but not shown in Table II, a small amount of  $\text{SiF}_2\text{H}^+$  was also detected. Again writing the most energetically stable set of neutral products for each reaction (with the exception of (21)), we arrive at the elementary reactions shown in (18)–(23). The enthalpy changes shown in (18)–(21) were



calculated from available thermochemical data.<sup>5,10,24,25</sup> The assumption of exothermicity and the assumed neutral products in (22) and (23) lead to the following upper limits:  $\Delta H_f^\circ(\text{SiH}_2\text{F}^+) < 214$  kcal/mol and  $\Delta H_f^\circ(\text{SiF}_2\text{H}^+) < 174$  kcal/mol.

The major reaction of  $\text{CF}_3^+$  with  $\text{SiH}_4$ , namely (19), is clearly that of H<sup>-</sup> abstraction and, since this reaction is only 34 kcal exothermic, the neutral product must be as written. On the basis of our experience with the kinetics of H<sup>-</sup> abstraction from silanes,<sup>32,33</sup> it is most probable that (19) occurs mainly by a direct mechanism,

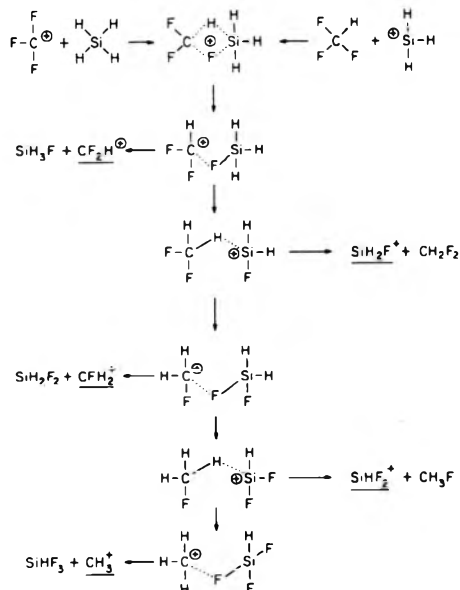


Figure 2. Proposed reaction mechanism for the redistribution of F and H in  $\text{CF}_3^+-\text{SiH}_4$  and  $\text{SiH}_3^+-\text{CF}_3\text{H}$  collisions.

as opposed to a long-lived intermediate complex.<sup>34</sup>

The nature of the other products of this reaction is most interesting because of the extensive redistribution of fluorine and hydrogen that occurs between the carbon and silicon centers. Keeping in mind the fact that at the pressures used all products must result from a *single collision* of  $\text{CF}_3^+$  and  $\text{SiH}_4$ , the formation of  $\text{CH}_2\text{F}^+$ ,  $\text{SiF}_2\text{H}^+$ , and  $\text{CH}_3^+$  is quite remarkable. For example, to form  $\text{CH}_3^+$  a collision complex must be formed that holds together long enough for six bonds to be broken and six bonds to be formed. In view of the tendency of positive carbon centers to abstract  $\text{H}^-$  ions from silanes<sup>19,35-37</sup> (cf. reaction 19) and the tendency of positive silicon centers to abstract  $\text{F}^-$  from  $\text{CF}_4$  (cf. reactions 6 and 8), we propose a mechanism (shown in Figure 2) for this extensive redistribution of F and H that involves a long-lived complex held together by  $\text{F}^-$  and  $\text{H}^-$  bridges. As the  $\text{CF}_3^+$  ion approaches  $\text{SiH}_4$ , a hydride bridge forms between carbon and silicon and the center of positive charge moves toward silicon. As silicon becomes positive the fluoride bridge begins to form, eventually replacing the hydride bridge, as the positive charge becomes associated with silicon. At some intermediate stage the complex passes through the double-bridged structure, only the first of which is shown in Figure 2. This "flip-flop" mechanism continues driving the system toward the final products,  $\text{CH}_3^+$  and  $\text{SiHF}_3$  (or  $\text{SiF}_2 + \text{HF}$ ), with random unimolecular dissociation of the intermediate yielding the other observed products, as shown in Figure 2.

The mechanism receives support from the fact that we observe the same set of H and F redistribution products to be formed in collisions of  $\text{SiH}_3^+$  and  $\text{CF}_3\text{H}$ , a system which produces the same collision complex as the  $\text{CF}_3^+-\text{SiH}_4$  system. Entrance into the proposed mechanistic sequence by the reactants  $\text{SiH}_3^+$  and  $\text{CF}_3\text{H}$  is shown in the upper right of Figure 2. It is of interest to note that the extensive redistribution products  $\text{CH}_3^+$ ,  $\text{CFH}_2^+$ , etc. are definitely not formed in  $\text{SiH}_3^+-\text{CF}_4$  collisions. We do not understand this fact in a mechanistic sense but it does indicate the uniqueness of the intermediate complex that contains three F atoms and four H atoms.

The dependence of the relative yields of the various reaction products on collision energy is complex and we do not understand the fine details. However, since  $\text{CH}_3^+$  is the end dissociation product of a complex that yields

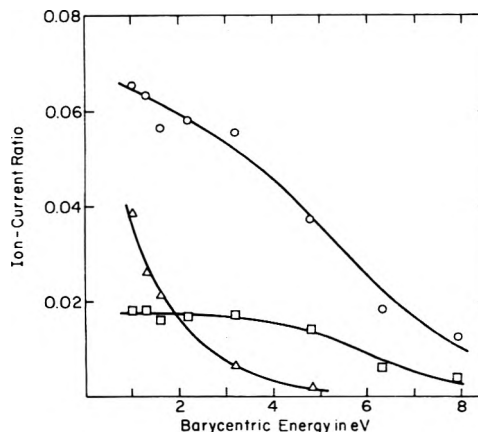


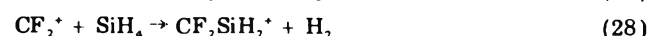
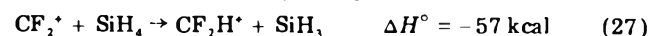
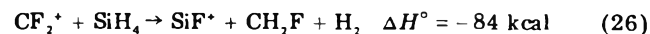
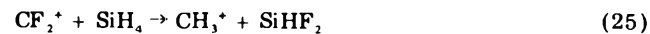
Figure 3. Relative yields of redistribution products as a function of collision energy: (O)  $i(\text{CH}_3^+)/i(\text{CF}_2\text{H}^+)$ ; (□)  $i(\text{CH}_3^+)/i(\text{SiH}_3^+)$ ; (Δ)  $i(\text{CH}_3^+)/i(\text{SiH}_2\text{F}^+)$ .

other products of lesser redistribution, the yields of  $\text{CH}_3^+$  relative to the other dissociation products should decrease with decreasing average lifetime of the complex (i.e., with increasing barycentric energy of the reactants.) As shown in Figure 3 the yields of  $\text{CH}_3^+$  relative to  $\text{CF}_2\text{H}^+$ ,  $\text{SiH}_2\text{F}^+$ , and  $\text{SiH}_3^+$  increase with increasing energy, in accord with expectations from the mechanism of Figure 2.

As noted earlier, the predominant mode of formation of  $\text{SiH}_3^+$  is probably via a direct mechanism, i.e., not involving the complex. It was not possible to examine quantitatively the yields of  $\text{CFH}_2^+$  and  $\text{SiHF}_2^+$  because of interference from the much more intense  $\text{SiH}_3^+$  and  $\text{CF}_3^+$  beams.

Whatever mechanism is proposed it must involve a collision complex that accounts for all the products observed and that holds together long enough for all the F atoms on  $\text{CF}_3^+$  or  $\text{CF}_3\text{H}$  to be replaced by H atoms. We think the mechanism proposed in Figure 2 is a very plausible one because it does meet these requirements and, at the same time, incorporates the known tendencies of  $\equiv\text{C}^+$  to abstract  $\text{H}^-$  from silanes and  $\equiv\text{Si}^+$  to abstract  $\text{F}^-$  from  $\text{CF}_4$ , as well as utilize the known bridging properties of hydrogen and fluorine in inorganic and organosilicon compounds.<sup>38,39</sup>

(f)  $\text{CF}_2^+ + \text{SiH}_4$ . The reaction of  $\text{CF}_2^+$  with  $\text{SiH}_4$  yields predominantly  $\text{SiH}_3^+$  ( $m/e$  31) but significant amounts of  $\text{CH}_3^+$  ( $m/e$  15),  $\text{SiF}^+$  ( $m/e$  47),  $\text{CF}_2\text{H}^+$  ( $m/e$  51), and  $\text{CF}_2\text{SiH}_2^+$  ( $m/e$  80) are also formed, as may be seen in Table II. All reactions appear to be exothermic processes which, if we write to yield the maximum exothermicity, must be as shown in (24)–(28). In these equations the

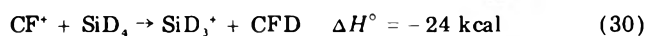
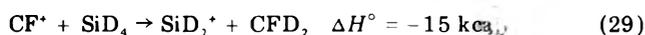


indicated standard enthalpy changes are those calculated from available thermochemical data.<sup>5,24-26</sup> The fact that (25) and (28) are exothermic allow us to assign the following limits:  $\Delta H_f^\circ(\text{SiHF}_2) < -15 \text{ kcal/mol}$ ;  $\Delta H_f^\circ(\text{CF}_2\text{SiH}_2^+) < 245 \text{ kcal/mol}$ .

The formation of  $\text{CH}_3^+$  by (25) shows that extensive redistribution of F and H between carbon and silicon centers occurs also in single collisions of  $\text{CF}_2^+$  and  $\text{SiH}_4$ . This reaction must then occur via a collision complex that holds together long enough for the breaking of five bonds and forming of five new bonds. We suppose the mech-

anism to be similar to that shown in Figure 2 for CF<sub>3</sub><sup>+</sup>-SiH<sub>4</sub> collisions; however, the bonding in the CF<sub>2</sub><sup>+</sup>-SiH<sub>4</sub> complex is probably more complicated, due to the presence of at least one unpaired electron on CF<sub>2</sub><sup>+</sup> and the availability of low-lying 3d orbitals on Si. The observed formation of CF<sub>2</sub>SiH<sub>2</sub><sup>+</sup> via (28) is consistent with some type of C-Si bonding in the complex.

(g) CF<sup>+</sup> + SiD<sub>4</sub>. These reactions were studied using SiD<sub>4</sub>, since the reactant ion CF<sup>+</sup> has the same (*m/e*) as the expected H<sup>-</sup>-transfer product SiH<sub>3</sub><sup>+</sup>. As shown in Table II, the products of this reaction are SiD<sub>2</sub><sup>+</sup> (*m/e* 32), SiD<sub>3</sub><sup>+</sup> (*m/e* 34), SiF<sup>+</sup> (*m/e* 47), and SiFD<sub>2</sub><sup>+</sup> (*m/e* 51), with the predominant product being, as expected that of D<sup>-</sup> transfer. The dependence of cross section on the kinetic energy of CF<sup>+</sup> indicates that SiD<sub>3</sub><sup>+</sup>, SiF<sup>+</sup>, and SiFD<sub>2</sub><sup>+</sup> are formed in exothermic processes. Due to mass interference from the CF<sup>+</sup> reactant ion (*m/e* 31) it was not feasible to examine the energy dependence of the cross section for SiD<sub>2</sub><sup>+</sup> (*m/e* 32) formation but the magnitude at 1.0 eV (laboratory) suggests that the reaction is exothermic. The indicated reactions and the standard enthalpy changes (calculated where sufficient data exist) are shown in (29)-(32). Obviously it is possible for the neutral products



of (31) to be CD<sub>3</sub> + D or CD<sub>2</sub> + D<sub>2</sub> but the neutral products of (29) and (30) must be as written. The fact that (32) is exothermic yields the limit:  $\Delta H_f^\circ(\text{SiFD}_2^+) \leq 190 \text{ kcal/mol}$ .

Small yields of C<sup>+</sup>, CH<sup>+</sup>, and CH<sub>2</sub><sup>+</sup> are observed in addition to very small amounts of CH<sub>3</sub><sup>+</sup>. Energetic considerations indicate that such products as the former must be due to the presence of considerable amounts of internally excited CF<sup>+</sup> ions in the reactant beam.

(h) F<sup>+</sup> + SiH<sub>4</sub>. F<sup>+</sup> ions react with SiH<sub>4</sub> to form Si<sup>+</sup>, SiH<sup>+</sup>, SiH<sub>2</sub><sup>+</sup>, SiH<sub>3</sub><sup>+</sup>, and SiF<sup>+</sup>. The cross sections for formation of SiH<sup>+</sup> and SiF<sup>+</sup> have been examined as a function of energy and they show very little dependence on kinetic energy of F<sup>+</sup>. The nature of the reactant and products, however, leaves little doubt that the reactions are exothermic. Based on the established dominant role of H<sup>-</sup> abstract from SiH<sub>4</sub> by positive ions, we suggest that the formation of Si<sup>+</sup>, SiH<sup>+</sup>, SiH<sub>2</sub><sup>+</sup>, and SiH<sub>3</sub><sup>+</sup> occurs by the very exothermic hydride transfer followed by dissociation of energy-rich SiH<sub>3</sub><sup>+</sup> ions. SiF<sup>+</sup> is assumed to be formed by (37).



(i) *Total Cross Sections and Phenomenological Rate Constants.* Phenomenological rate constants, determined from the cross sections at 1 eV (laboratory), for the total reaction of the various ions with CF<sub>4</sub> and SiH<sub>4</sub> (SiD<sub>4</sub>) are shown in Table III. Also shown in Table III are the theoretical rate constants for orbiting encounters according to the Langevin theory.<sup>40</sup> All observed rate constants are considerably below the Langevin value except for the rate constant for reaction of CF<sub>2</sub><sup>+</sup> with SiH<sub>4</sub> which approaches the theoretical value.

(j) *Thermochemistry.* For a number of reactions observed in this study enthalpy changes could not be cal-

TABLE III: Total Reaction Cross Sections and Phenomenological Rate Constants<sup>a</sup>

Reactants	$\sigma_{\text{Total}}$ , Å <sup>2</sup>	$10^{10}k$ , cm <sup>3</sup> /s	$10^{10}k_{\text{Langevin}}$ , cm <sup>3</sup> /s
Si <sup>+</sup> + CF <sub>4</sub>	4.3	1.1	8.6
SiH <sup>+</sup> + CF <sub>4</sub>	1.0	0.3	8.5
SiH <sub>2</sub> <sup>+</sup> + CF <sub>4</sub>	5.9	1.5	8.4
SiH <sub>3</sub> <sup>+</sup> + CF <sub>4</sub>	8.7	2.2	8.3
F <sup>+</sup> + SiH <sub>4</sub>	3.6	1.1	15.8
CF <sup>+</sup> + SiD <sub>4</sub>	19	4.7	13.4
CF <sub>2</sub> <sup>+</sup> + SiH <sub>4</sub>	57	11	12.4
CF <sub>3</sub> <sup>+</sup> + SiH <sub>4</sub>	39	6.5	11.7

<sup>a</sup> At 1-eV reactant ion energy (lab).

TABLE IV: Upper Limits of Standard Enthalpies of Formation

Species	Upper limit to $\Delta H_f^\circ$ , kcal/mol	Reaction
SiH <sub>2</sub> F	-38	8
SiHF <sub>2</sub>	-15	25
SiHF <sup>+</sup>	226	10
SiH <sub>2</sub> F <sup>+</sup>	175	11
CF <sub>2</sub> SiH <sub>2</sub> <sup>+</sup>	245	28

culated because of the lack of some standard enthalpies of formation. In such cases it was possible to assign limits to standard enthalpies of formation of some of the ions and neutral species involved. The upper limits so derived and the pertinent reaction number are collected in Table IV. All values are consistent with estimates from thermochemical bond energies.<sup>11</sup>

*Acknowledgment.* This work was supported by the U.S. Energy Research and Development Administration under Contract No. ER(11-1)-3416. We also wish to thank the Education Committee of the Gulf Oil Corporation for a grant that assisted in the construction of the tandem mass spectrometer.

## References and Notes

- (1) U.S. Energy Research and Development Administration Document No. COO-3416-24.
- (2) P. Potzinger, A. Ritter, and J. Krause, *Z. Naturforsch. A*, **30**, 347 (1975).
- (3) W. C. Steele, L. D. Nichols, and F. G. A. Stone, *J. Am. Chem. Soc.*, **84**, 4441 (1962).
- (4) W. C. Steele and F. G. A. Stone, *J. Am. Chem. Soc.*, **84**, 3599 (1962).
- (5) P. Potzinger and F. W. Lampe, *J. Phys. Chem.*, **73**, 3912 (1969).
- (6) P. Potzinger and F. W. Lampe, *J. Phys. Chem.*, **74**, 719 (1970).
- (7) I. M. T. Davidson and I. L. Stephenson, *J. Chem. Soc. (London) A*, 282 (1968).
- (8) I. M. T. Davidson and A. B. Howard, *J. Chem. Soc., Faraday Trans. 1*, **71**, 69 (1975).
- (9) A. Hosaka and F. S. Rowland, *J. Phys. Chem.*, **77**, 705 (1973).
- (10) D. D. Wagman, W. H. Evans, V. B. Parker, I. Halow, S. M. Bailey, and R. H. Schumm, *Natl. Bur. Stand. (U.S.), Tech. Note*, No. 270-3 (1968).
- (11) T. L. Cottrell, "The Strengths of Chemical Bonds," 2nd ed. Butterworths, London, 1958.
- (12) T. Y. Yu, T. M. H. Cheng, V. Kempler, and F. W. Lampe, *J. Phys. Chem.*, **76**, 3321 (1972).
- (13) E. Teloj and D. Gerlich, *Chem. Phys.*, **4**, 417 (1974).
- (14) S. K. Gupta, E. G. Jones, A. G. Harrison, and J. J. Myher, *Can. J. Chem.*, **45**, 3107 (1967).
- (15) T. M. H. Cheng, T. Y. Yu, and F. W. Lampe, *J. Phys. Chem.*, **77**, 2587 (1973).
- (16) N. H. McAskill, *Aust. J. Chem.*, **23**, 893 (1970).
- (17) R. J. Blint, T. B. McMahon, and J. L. Beauchamp, *J. Am. Chem. Soc.*, **96**, 1269 (1974).
- (18) T. M. H. Cheng and F. W. Lampe, *Chem. Phys. Lett.*, **19**, 532 (1973).
- (19) T. M. H. Cheng, T. Y. Yu, and F. W. Lampe, *J. Phys. Chem.*, **77**, 2587 (1973).
- (20) J. J. Kaufman and W. S. Koski, *J. Chem. Phys.*, **50**, 1942 (1969).
- (21) A. Pipano and J. J. Kaufman, *J. Chem. Phys.*, **56**, 5258 (1972).
- (22) P. Potzinger, private communication.

- (23) T. A. Walter, C. Lifshitz, W. A. Chupka, and J. Berkowitz, *J. Chem. Phys.*, **51**, 3531 (1963).
- (24) J. L. Franklin, J. G. Dillard, H. M. Rosenstock, J. T. Herron, K. Draxl, and F. H. Field, *Natl. Stand. Ref. Data Ser., Natl. Bur. Stand.*, **No. 26** (June 1969).
- (25) J. B. Pedley and B. S. Iseard, "CATCH Tables for Silicon Compounds," University of Sussex, 1972.
- (26) J. W. C. Johns and R. F. Barrow, *Proc. Phys. Soc. (London)*, **71**, 476 (1958).
- (27) T. M. H. Cheng and F. W. Lampe, *J. Phys. Chem.*, **77**, 2841 (1973).
- (28) R. J. Cotter and W. S. Koski, *J. Chem. Phys.*, **59**, 784 (1973).
- (29) C. E. Moore, *Natl. Bur. Stand. (U.S.), Circ.*, **No. 467** (1949).
- (30) W. N. Allen, T. M. H. Cheng, and F. W. Lampe, *J. Chem. Phys.*, submitted for publication.
- (31) B. R. Turner, J. A. Rutherford, and D. M. J. Compton, *J. Chem. Phys.*, **48**, 1602 (1968).
- (32) T. M. Mayer and F. W. Lampe, *J. Phys. Chem.*, **78**, 2195 (1974).
- (33) T. M. Mayer and F. W. Lampe, *J. Phys. Chem.*, **78**, 2429 (1974).
- (34) R. Wolfgang, *Acc. Chem. Res.*, **3**, 48 (1970).
- (35) G. W. Stewart, J. M. S. Henis, and P. P. Gaspar, *J. Chem. Phys.*, **57**, 1990 (1972).
- (36) T. M. Mayer and F. W. Lampe, *J. Phys. Chem.*, **78**, 2433 (1974).
- (37) J. R. Krause and P. Potzinger, *Int. J. Mass Spectrom. Ion Phys.*, **18**, 303 (1975).
- (38) B. L. Shaw, "Inorganic Hydrides," Pergamon Press, New York, N.Y., 1967.
- (39) R. J. P. Corriu and M. Henner, *J. Organometal. Chem.*, **74**, 1 (1974).
- (40) G. Gioumousis and D. P. Stevenson, *J. Chem. Phys.*, **29**, 294 (1958).

## The Temperature Dependences of the Ultraviolet Absorption Cross Sections of $\text{CCl}_2\text{F}_2$ and $\text{CCl}_3\text{F}$ , and Their Stratospheric Significance

C. C. Chou, W. S. Smith, H. Vera Rulz, K. Moe, G. Crescentini, M. J. Molina,<sup>†</sup> and F. S. Rowland\*

Department of Chemistry, University of California, Irvine, California 92717 (Received July 26, 1976)

Publication costs assisted by the U.S. Energy Research and Development Administration

The photochemical absorption cross sections of  $\text{CCl}_2\text{F}_2$  and  $\text{CCl}_3\text{F}$  have been measured between 1900 and 2200 Å for stratospheric temperatures in the range from 212 to 257 K. The cross sections are monotonically lower with lower temperatures, with larger decreases for the longer wavelengths. The calculated photodissociation coefficients at each stratospheric altitude are correspondingly lower than previously estimated. The atmospheric residence times for  $\text{CCl}_2\text{F}_2$  are 8–17% longer than estimated from room temperature absorption cross sections. The changes are much smaller for  $\text{CCl}_3\text{F}$ , corresponding to about 3–6% increases in residence times.

### Introduction

The primary known terrestrial process for the destruction of the widely used chlorofluoromethanes  $\text{CCl}_2\text{F}_2$  and  $\text{CCl}_3\text{F}$  is through stratospheric photolysis by solar ultraviolet radiation, as in (1) and (2).<sup>1,2</sup> The release of



Cl atoms at stratospheric altitudes initiates the  $\text{ClO}_x$ -chain removal of O and  $\text{O}_3$  by reactions 3 and 4, providing



substantial environmental importance to the details of reactions 1 and 2.<sup>1-3</sup> In previous estimates of the altitudes for photodissociation and of the average atmospheric residence times for these molecules, the calculations have been based upon the absorption cross sections measured at about 296 K, even though actual stratospheric temperatures range as low as 210 K.<sup>2</sup> Measurements by Rebbert and Ausloos of these absorption cross sections at 2139 Å over a range of temperatures have shown that absorption can be appreciably less at lower temperatures,<sup>4</sup> introducing some error into the earlier estimates. However, the temperature effect is observed to be largest near the threshold for absorption (about 2200 Å for  $\text{CCl}_2\text{F}_2$  and 2300 Å for  $\text{CCl}_3\text{F}$ ), with lesser effects at shorter wavelengths. Since the stratospheric absorption of ultraviolet by  $\text{CCl}_3\text{F}$  and  $\text{CCl}_2\text{F}_2$  is spread rather evenly over the wavelength range from 1900 to 2100 Å,<sup>5</sup> the variations measured at

2139 Å clearly represent more change with temperature than can be expected in the actual stratosphere. Furthermore, since ultraviolet intensity changes very rapidly with altitude in the 20–40-km region important for chlorofluoromethane photolysis, even a decrease of a factor of 3 in average cross section would lead only to an increase of about 2 km in average altitude of photolysis, and to an increase of about a factor of 1.5 in the average atmospheric residence time.<sup>6</sup>

Preliminary measurements of the temperature dependence of these ultraviolet cross sections have indeed shown that the average decrease in cross section, weighted by stratospheric ultraviolet fluxes, is much less than a factor of 3, and that the overall effect on lifetimes and altitudes of photolysis is relatively minor.<sup>7,8</sup> Although some statements to the contrary have appeared,<sup>9</sup> the primary effect of reduced stratospheric cross sections is an increase in the estimated potential for destruction of stratospheric ozone per molecule of  $\text{CCl}_2\text{F}_2$  or  $\text{CCl}_3\text{F}$ , since the  $\text{ClO}_x$  decomposition products are thereby estimated to be released at higher altitudes. In general, of course, the higher the altitude of injection of a potential stratospheric pollutant, the greater the destruction per molecule during the longer time required for diffusion to the troposphere and removal there by tropospheric processes such as rainout.<sup>2</sup> Although our preliminary estimates gave only about 10% as the overall increase in potential destructive capability of  $\text{ClO}_x$  released from  $\text{CCl}_2\text{F}_2$ ,<sup>7,8</sup> we have refined both our measurements and our calculations to provide a reasonable prototype of the importance of stratospheric temperatures on such absorption processes. The more detailed study described here confirms the semiquantitative estimates

<sup>†</sup> Alfred P. Sloan Fellow.

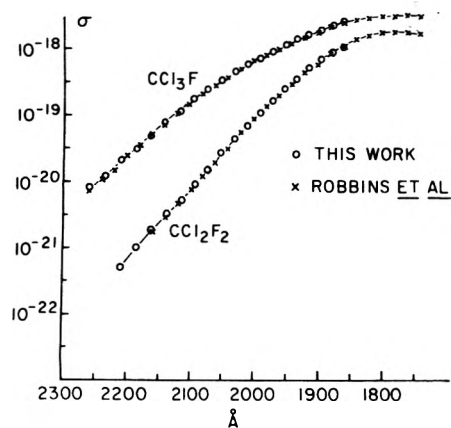


Figure 1. Ultraviolet absorption cross sections for  $\text{CCl}_2\text{F}_2$  and  $\text{CCl}_3\text{F}$  at 296 K: (O) this work; (X) measurements by Robbins and Stolarski, ref 10.

made earlier that the errors introduced by using measurements of ultraviolet absorption cross sections made at 296 K rather than 210–275 K are rather small, especially relative to the other errors inherent in such calculations.

### Experimental Section

**Absolute Cross Sections at 296 K.** Our basic absorption measurements have been made with a nitrogen-purged Cary 14 ultraviolet spectrometer and a temperature controlled absorption cell equipped with a cooling jacket and Suprasil quartz windows. The temperature of the cell was controlled by circulating refrigerated liquid (methanol or ethanol) through the cooling jacket. The temperature of the gas within the cell was measured to be within  $\pm 1$  °C of the temperature of the refrigerant at its emergence from the cooling jacket.

The absorption cross sections of these molecules vary by as much as a factor of  $10^3$  over the wavelengths investigated here, thereby requiring a range of filling pressures for optimum cross section measurements. While no difficulties are encountered at room temperature, for which both  $\text{CCl}_2\text{F}_2$  and  $\text{CCl}_3\text{F}$  have high vapor pressures, serious limitations are found (especially for  $\text{CCl}_3\text{F}$ ) in the amount of gas available at 210–240 K. (The vapor pressure of  $\text{CCl}_3\text{F}$  at 210 K is 7 Torr.) The overall procedure which was adopted involves (a) evaluation of the absolute cross section for ultraviolet absorption at 296 K for all wavelengths; and (b) evaluation of the averages of the *relative* absorption cross sections for temperature  $T$  K vs. 296 K for each particular cell-filling. Experimentally, of course, it is possible to obtain an absolute cross section at temperature  $T$  K directly from the measurement of transmitted light for a particular filling. However, the reproducibility of the *relative* cross sections at  $T$  K vs. 296 K was better, since possible errors in composition were automatically cancelled. Measurements of absolute cross sections were considerably easier at 296 K and were consequently much more numerous, leading to quite reliable estimates of absolute cross sections at that temperature.

The absolute cross sections for absorption of ultraviolet radiation between 1850 and 2272 Å are summarized in Table I, expressed as cross sections at the midpoint of 500- $\text{cm}^{-1}$  intervals. We have also included for comparison purposes the earlier values given by Rowland and Molina. Our new data are graphed in Figure 1 together with the data of Robbins and Stolarski.<sup>10</sup> Direct absorption measurements at 296 K have also been recently reported by Bass and Ledford,<sup>11</sup> with essential agreement to the data of Table I. In our earlier review article, we also

TABLE I: Absorption Cross Sections for  $\text{CCl}_2\text{F}_2$  and  $\text{CCl}_3\text{F}$  in the Wavelength Range 1850–2272 Å at 296 K (Units of  $10^{-20} \text{ cm}^2$ )

Mid-point of interval, $\lambda$ , Å	Interval boundaries, $\nu$ , $10^3 \text{ cm}^{-1}$	$\text{CCl}_2\text{F}_2$		$\text{CCl}_3\text{F}$	
		This work	ref 2	This work	ref 2
	44.0				
2260	44.5	<0.05		0.8	0.9
2235	45.0	<0.05		1.2	1.3
2210	45.5	0.05		2.1	1.8
2186	46.0	0.10		3.0	3.4
2162	46.5	0.19	<0.2	4.9	5.1
2139	47.0	0.32	0.30	7.8	8.0
2116	47.5	0.53	0.70	11.6	12.5
2094	48.0	0.90	1.36	17.3	18.5
2073	48.5	1.53	1.81	24.8	25.0
2051	49.0	2.66	3.11	34.1	34.5
2030	49.5	4.37	4.9	45.7	46.0
2010	50.0	6.96	7.2	59.0	59.0
1990	50.5	10.9	11.3	74.3	73.0
1970	51.0	16.8	16.4	93.2	88.5
1951	51.5	24.9	24.6	115	113
1932	52.0	36.7	34.5	141	137
1914	52.5	51.4	49.1	(164) <sup>a</sup>	164
1896	53.0	66.1	65.5	(197) <sup>a</sup>	197
1878	53.5	86.5	86.5	(227) <sup>a</sup>	227
1860	54.0	105	91.2	255 <sup>b</sup>	241

<sup>a</sup> Not remeasured. <sup>b</sup> Interpolated from measurement at the 1849-Å resonance line.

included the measurements by Doucet, Sauvageau, and Sandorfy, which are not in good agreement with those of Table I, and which are now excluded as inaccurate in this wavelength range. The direct measurement of absorption cross sections, as shown in Table I, is consistent with those determined by electron-scattering experiments.<sup>12</sup> The slight revisions in cross sections found between ref 2 and the present work are negligible in their stratospheric impact, as are the small differences between these results and those of ref 10 and 11.

The absolute cross section at 2139 Å has also been measured by Rebbert and Ausloos with a Zn line ultraviolet source,<sup>4</sup> who obtained a cross section of  $0.27 \times 10^{-20} \text{ cm}^2$  at 295 K. Our best current value at 296 K in Table I is  $0.32 \times 10^{-20} \text{ cm}^2$ . The discrepancy in measured cross section between the present work and that of ref 4 becomes progressively larger at lower temperatures as discussed later and shown in Figure 3.

**Relative Cross Sections at Stratospheric Temperatures.** The ratios of measured cross sections at  $T$  K to those at 296 K are shown in Figure 2 for  $\text{CCl}_2\text{F}_2$  for six different temperatures between 212 and 257 K. The absorption

TABLE II: Ratios of Absorption Cross Sections at 252 and 212 K Vs. 296 K for Different  $\text{CCl}_2\text{F}_2$  Pressures<sup>a</sup>

$\lambda$ , Å	252 K				212 K		
	19 Torr	61 Torr	149 Torr	604 Torr	19 Torr	61 Torr	149 Torr
2186				0.61			
2162			0.63	0.64			
2139		0.63	0.62	0.65			0.43
2116		0.65	0.65	0.68			0.46
2094		0.67	0.68	0.69			0.49
2073		0.68	0.70	0.74		0.54	0.52
2051	0.72	0.72	0.73		0.51	0.58	0.58
2030	0.73	0.76	0.75		0.55	0.61	0.60
2010	0.78	0.78			0.62	0.65	0.61
1990	0.79	0.80			0.64	0.68	
1970	0.82	0.82			0.70	0.71	
1951	0.85				0.74		
1932	0.87				0.80		

<sup>a</sup> Pressures are given for 296 K, and the cross sections are measured at different temperatures without changing the composition.

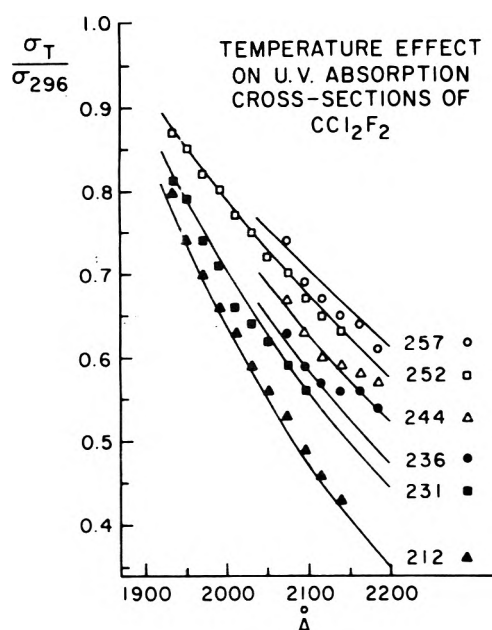


Figure 2. Temperature effect on ultraviolet absorption cross sections of  $\text{CCl}_2\text{F}_2$ . The cross sections are expressed relative to the cross section at 296 K. (O) 257 K; (□) 252 K; (Δ) 244 K; (●) 236 K; (■) 231 K; (▲) 212 K. The lines have been calculated from eq 5.

ratios measured at several pressures for two temperatures are shown in Table II, illustrating the use of different pressures for different wavelengths. The average values of the ratios are used in Figure 2.

At each temperature, the cross section ratio becomes monotonically larger as the wavelength gets shorter; at each wavelength, the ratio becomes monotonically larger as the temperature increases. All of these relative values can be fitted with reasonable accuracy by a three-parameter equation in which the ratio,  $R$ , of  $\sigma_T/\sigma_{296}$  is given by eq

$$R = \frac{\sigma_T}{\sigma_{296}} = \exp[B(\lambda - \lambda_c)(T - T_0)] \quad (5)$$

5 for wavelength,  $\lambda$  (in Ångstrom units), and absolute temperature,  $T$ . The calculated values of  $R$  for  $B = +3.6 \times 10^{-5}$ ,  $\lambda_c = 1849$ , and  $T_0 = 296$  are shown as the solid lines on Figure 2. Equation 5 is empirically based on the overall pattern of the data, and has been devised solely for convenience in providing a numerically accessible summary of  $\sigma(\lambda, T)$  in terms of the values of  $\sigma_{296}$  in Table I, and the

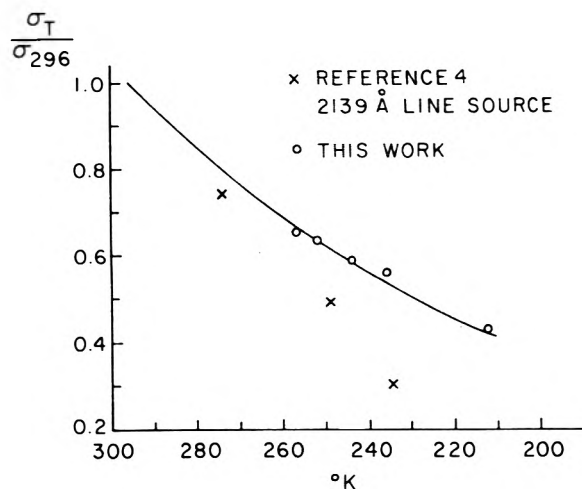


Figure 3. Temperature effect on ultraviolet absorption cross sections of  $\text{CCl}_2\text{F}_2$  at 2139 Å: (X) ref 4, using a Zn resonance lamp; (O) this work.

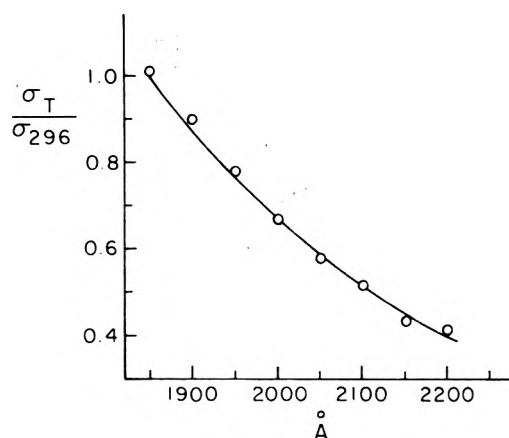


Figure 4. Temperature effect on ultraviolet absorption cross sections of  $\text{CCl}_2\text{F}_2$  at 223 K (expressed relative to cross sections at 296 K): (O) measurements of ref 11. (—) calculated in this work from eq 5 fitted to our measurements between 212 and 257 K.

three constants of eq 5 for  $\text{CCl}_2\text{F}_2$ .

A systematic discrepancy exists between the line source data at 2139 Å<sup>4</sup> and our measurements for the comparable band pass, as shown in Figure 3. The solid line is calculated from eq 5.

Bass and Ledford have measured cross sections at both 223 and 296 K.<sup>11</sup> The agreement between our eq 5 and their cross section ratios is excellent, as illustrated in Figure 4.

The ratios of measured cross sections of  $T$  K to those at 296 K are shown in Figure 5 for  $\text{CCl}_3\text{F}$  for three different temperatures between 252 and 213 K. The cross sections for  $\text{CCl}_3\text{F}$  have been measured at 223 and 296 K by Bass and Ledford, and these ratios are also shown in Figure 5.<sup>11</sup> The values of  $R$  are all closer to unity for  $\text{CCl}_3\text{F}$  than for  $\text{CCl}_2\text{F}_2$  at the same temperature and wavelength. This is expected since the stratospherically important wavelengths are further from the threshold for  $\text{CCl}_3\text{F}$  than for  $\text{CCl}_2\text{F}_2$ , and therefore less perturbed by the temperature effects on absorption. Since more than 90% of the stratospheric absorption by  $\text{CCl}_3\text{F}$  occurs with  $1950 \text{ Å} < \lambda < 2100 \text{ Å}$ , the average cross section reduction is obviously not more than a factor of 0.85–0.9. The calculation in Table III shows 0.88 at 235 K.

*Stratospheric Calculations for  $\text{CCl}_2\text{F}_2$  and  $\text{CCl}_3\text{F}$  Ultraviolet Absorption.* Earlier calculations indicated that the peak altitudes for photodissociation of  $\text{CCl}_2\text{F}_2$  and  $\text{CCl}_3\text{F}$  were about 32 and 27 km, respectively. The

TABLE III: Calculated Values for Photodissociation Coefficients,  $J$ , of CCl<sub>2</sub>F<sub>2</sub> and CCl<sub>3</sub>F at 235 K, 30 km Altitude, with Overhead Sun

Mid-point of interval, $\lambda$ , Å	Solar flux, $\phi$ , <sup>a</sup> n/cm <sup>2</sup> /s 30 km × 10 <sup>11</sup>	CCl <sub>2</sub> F <sub>2</sub>		CCl <sub>3</sub> F	
		$\phi\sigma_{296}$ , s <sup>-1</sup> × 10 <sup>-9</sup>	$\phi\sigma_{235}$ , s <sup>-1</sup> × 10 <sup>-9</sup>	$\phi\sigma_{296}$ , s <sup>-1</sup> × 10 <sup>-8</sup>	$\phi\sigma_{235}$ , s <sup>-1</sup> × 10 <sup>-8</sup>
2235	0.30	<0.01	<0.01	0.04	0.03
2210	1.1	0.06	0.03	0.23	0.19
2186	2.4	0.24	0.11	0.72	0.56
2162	5.4	1.04	0.52	2.7	2.1
2139	8.8	2.8	1.5	6.9	5.6
2116	13.2	7.0	3.9	15.3	12.7
2094	13.9	12.5	7.3	24.1	20.3
2073	9.3	14.3	8.7	23.1	19.8
2051	5.6	15.0	9.6	19.2	16.7
2030	4.1	17.9	12.1	18.8	16.7
2010	3.5	24.3	17.1	20.6	18.6
1990	2.9	31.6	23.2	21.5	19.7
1970	1.7	29.1	22.3	16.1	15.0
1951	0.85	21.3	17.0	9.8	9.3
1932	0.30	11.0	9.1	4.2	4.0
1914	0.22	11.3	9.8	3.6	3.5
1896	0.13	8.6	7.8	2.6	2.5
1878	0.03	2.2	2.1	0.58	0.58
1860	0.003	0.3	0.3	0.07	0.07
Total		210	152	190	168

weighted effect of using the cross sections at actual stratospheric temperatures is illustrated in Table III, for 30 km, 235 K, and overhead sun. For these conditions the value of  $J$  found for CCl<sub>2</sub>F<sub>2</sub> with  $\sigma_{235}$  is reduced by about 28% from that found using  $\sigma_{296}$ , while that for CCl<sub>3</sub>F is reduced by only about 12%. This calculation can then be repeated for all zenith angles and altitudes with the appropriate solar fluxes, and new average values of  $J$  obtained. These averaged photodissociation coefficients, together with the overhead sun values, are compared in Table IV.

The averaged photodissociation coefficients have then been used in a steady-state calculation of the type described in ref 2, using a variety of suggested eddy diffusion coefficients, as before. The molecules have also been assumed to be decomposed by reactions with O(<sup>1</sup>D) atoms by eq 6 and 7, using  $2.6 \times 10^{-10}$  cm<sup>3</sup>/molecule s and  $3.3$



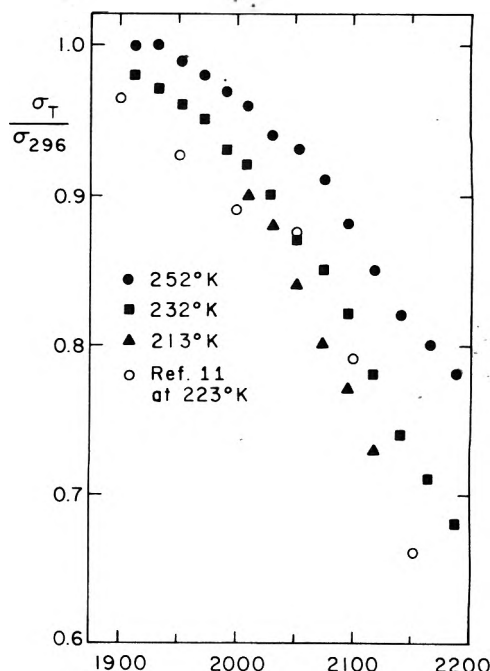
× 10<sup>-10</sup> cm<sup>3</sup>/molecule s as the respective rate constants for reactions 6 and 7.<sup>13</sup>

The overall effect on these calculations can be described by the changes in average atmospheric residence times or by the percentage reaction by photolysis, as shown in Table

TABLE IV: Calculated Values for Photodissociation Coefficients,  $J$ , for CCl<sub>2</sub>F<sub>2</sub> and CCl<sub>3</sub>F Vs. Altitude, Using Temperature Dependent Absorption Cross Sections

Altitude, km	Temp, K	Photodissociation coeff, $J$ , <sup>a</sup> s <sup>-1</sup>							
		CCl <sub>2</sub> F <sub>2</sub>				CCl <sub>3</sub> F			
		Overhead sun		Worldwide av		Overhead sun		Worldwide av	
		$\sigma_{296}$	$\sigma_T$	$\sigma_{296}$	$\sigma_T$	$\sigma_{296}$	$\sigma_T$	$\sigma_{296}$	$\sigma_T$
15	210.8	1.5(-10)	9.0(-11)	7.7(-12)	4.5(-12)	2.0(-9)	1.7(-9)	1.0(-10)	8.4(-11)
20	218.9	5.6(-9)	3.5(-9)	4.3(-10)	2.6(-10)	6.2(-8)	5.4(-8)	4.7(-9)	4.1(-9)
25	227.1	4.9(-8)	3.3(-8)	5.3(-9)	3.6(-9)	4.8(-7)	4.3(-7)	5.3(-8)	4.7(-8)
30	235.2	2.1(-7)	1.5(-7)	3.2(-8)	2.2(-8)	1.9(-6)	1.7(-6)	2.9(-7)	2.6(-7)
35	251.7	5.7(-7)	4.4(-7)	1.2(-7)	8.8(-8)	4.8(-6)	4.6(-6)	1.0(-6)	9.7(-7)
40	268.2	1.1(-6)	9.3(-7)	2.9(-7)	2.4(-7)	8.7(-6)	8.3(-6)	2.5(-6)	2.3(-6)
45	274.5	1.6(-6)	1.4(-6)	5.1(-7)	4.5(-7)	1.2(-5)	1.2(-5)	4.1(-6)	4.0(-6)

<sup>a</sup> 1.5(-10) signifies  $1.5 \times 10^{-10}$ .

Figure 5. Temperature effect on ultraviolet absorption cross sections of CCl<sub>3</sub>F (expressed relative to cross sections at 296 K), this work: (●) 252 K; (■) 232 K; (▲) 212 K; (○) ref 11 at 223 K.

V. (Since several minor procedural changes have been made in the computing process since the calculations of ref 2, all have been repeated again so that the only differences between the individual pairs of Table V are the result of using  $\sigma_{296}$  in one case and  $\sigma_T$  in the other.) As expected, the calculated altitudes for decomposition are slightly higher. Consequently, the lifetimes for CCl<sub>2</sub>F<sub>2</sub> are 8–17% longer, and for CCl<sub>3</sub>F 3–6% longer. Since the values of  $J$  are lower than before, the importance of decomposition by O(<sup>1</sup>D) atoms becomes fractionally more important. No temperature variations have been measured for O(<sup>1</sup>D) reactions with CCl<sub>2</sub>F<sub>2</sub> or CCl<sub>3</sub>F, but such effects must be very small since the collision efficiencies approach unity at room temperatures.

At steady state, the concentration of ClX, the chlorine-containing decomposition products from CCl<sub>2</sub>F<sub>2</sub> and CCl<sub>3</sub>F, will be proportional to the atmospheric lifetimes given fixed input fluxes. Since the fraction of ClX to be found as ClO, etc., is only a slowly varying function of the amount of ClX itself, the steady-state estimate of ClO concentrations from each molecule will be increased by approximately the ratios of atmospheric residence times. A reasonable estimate of the overall effect at steady state can be obtained by summing the ClX concentrations at 40 km from CCl<sub>2</sub>F<sub>2</sub> and CCl<sub>3</sub>F. The calculated percentage

TABLE V: Comparison of Atmospheric Residence Times Calculated Using Absorption Cross Sections of  $\text{CCl}_2\text{F}_2$  and  $\text{CCl}_3\text{F}$  at 296 K and at Actual Stratospheric Temperatures

Stratospheric <sup>a</sup> mixing rate					
$\text{CCl}_2\text{F}_2$	Temp	A	B	C	D
Lifetime, years	(296 K) <sup>b</sup>	71.9	98.5	155	143
	(T K)	78.0	106.7	182	157
% photolysis <sup>c</sup>	(296 K)	91.4	90.9	88.7	89.6
	(T K)	89.3	88.6	85.2	86.7
$\text{CCl}_3\text{F}$					
Lifetime, years	(296 K)	42.4	58.0	59.4	77.9
	(T K)	43.7	60.0	62.9	80.8
% photolysis	(296 K)	98.2	97.9	97.2	97.1
	(T K)	98.1	97.7	97.0	96.9

<sup>a</sup> The eddy diffusion coefficients used by stratospheric modelers are frequently adjusted to give better fits to new data as acquired. These models are those of Wofsy (A), Crutzen (B), Chang (C), and Hunten (D) as described in ref 2. Each has been modified since, but the effects are generally applicable. <sup>b</sup> All cross sections at 296 K, or at actual stratospheric temperatures. <sup>c</sup> Remainder is removed by reaction with O(<sup>1</sup>D).

TABLE VI: Calculated Percentage Increase in Steady-State ClX Concentrations at 40 km (units of  $10^6 \text{ cm}^{-3}$ )

$\text{CCl}_2\text{F}_2$	A	B	C	D
$[\text{ClX}]_{296\text{K}}$	3.08	4.39	7.30	6.72
$[\text{ClX}]_{TK}$	3.26	4.66	8.54	7.34
% increase	5.8	6.2	17.0	9.2
$\text{CCl}_3\text{F}$				
$[\text{ClX}]_{296\text{K}}$	1.35	1.85	1.90	2.54
$[\text{ClX}]_{TK}$	1.39	1.92	2.01	2.63
% increase	3.0	3.8	5.8	3.5
Total				
$[\text{ClX}]_{296\text{K}}$	4.43	6.24	9.20	9.26
$[\text{ClX}]_{TK}$	4.65	6.58	10.55	9.97
% increase	5.0	5.5	14.7	7.7

increases in ClX at 40 km for each of the eddy diffusion models is given in Table VI.

The increases in ClX range from 5 to 15% and therefore represent increases in estimated depletion of ozone at steady state by similar amounts. However, such changes are well within the estimated accuracy of such calculations, and do not materially alter the understanding of the situation. The calculated variations are of the magnitude

that is neither of major importance nor completely negligible, indicating that some assessment of temperature variations of cross section should be made for any other fluorocarbon molecule with an absorption threshold less than 2300 Å.

These calculations have also been performed without any feedback, and are actually applicable only in situations in which the stratospheric composition is essentially unperturbed from the present situation. If the current rate of release of  $\text{CCl}_2\text{F}_2$  and  $\text{CCl}_3\text{F}$  were permitted to continue to concentrations approaching steady state, then the depletion of ozone at high altitudes would be so severe that much larger amounts of 1900–2200-Å radiation would penetrate to lower altitudes and the values of the photodissociation coefficients would be appreciably increased at many altitudes. This variation in  $J$  with time is automatically programmed into most long-term estimates of ozone depletion. Typically, however, the change in stratospheric temperature with loss of ozone in the 40–50-km range is *not* included in such calculations. The stratospheric mixing processes (e.g., eddy diffusion coefficients in one-dimensional calculations) are also assumed to be unchanged despite rather drastic modifications in the physicochemical structure of the upper stratosphere.

*Acknowledgment.* This research was supported by ERDA Contract AT-(04-3)-34, P.A. 126.

#### References and Notes

- (1) M. J. Molina and F. S. Rowland, *Nature (London)*, **249**, 810 (1974).
- (2) F. S. Rowland and M. J. Molina, *Rev. Geophys. Space Phys.*, **13**, 1 (1975).
- (3) "Fluorocarbons and the Environment", Report of Federal Task Force on Inadvertent Modification of the Stratosphere (IMOS), Council on Environmental Quality, Washington, D.C., June, 1975.
- (4) R. E. Rebert and P. J. Ausloos, *J. Photochem.*, **4**, 419 (1975).
- (5) Figure 5 of ref 2, p 9.
- (6) Table 8 of ref 2, p 13.
- (7) F. S. Rowland, *New Scientist*, **68**, 8 (1975).
- (8) C. C. Chou, M. J. Molina, G. Crescentini, H. Vera Ruiz, and F. S. Rowland, Abstracts of Papers, First Chemical Congress of the North American Continent, Nov 30–Dec 5, 1975, Mexico City.
- (9) R. L. Schuyler, E. I. DuPont de Nemours and Co., Hearings before the Subcommittee on the Upper Atmosphere of the Committee on Aeronautical and Space Sciences, United States Senate, Sept 18, 1975, p 547–548.
- (10) D. Robbins and R. Stolarski, *Geophys. Res. Lett.*, **3**, 603 (1976).
- (11) A. M. Bass and A. E. Ledford, Jr., 12th Informal Conference on Photochemistry, June 28–July 1, 1976, Gaithersburg, Md.
- (12) R. H. Huebner, D. L. Bushnell, R. J. Celotte, S. R. Mielczarek, and C. E. Kuyatt, *Nature (London)*, **257**, 376 (1976).
- (13) R. K. M. Jayanty, R. Simonaitis, and J. Heicklen, *J. Photochem.*, **4**, 203 (1975).

# Flash Photolysis Resonance Fluorescence Investigation of the Temperature Dependencies of the Reactions of Cl(<sup>2</sup>P) Atoms with CH<sub>4</sub>, CH<sub>3</sub>Cl, CH<sub>3</sub>F, CH<sub>3</sub>F<sup>†</sup>, and C<sub>2</sub>H<sub>6</sub>

Ronald G. Manning<sup>†</sup> and Michael J. Kurylo\*

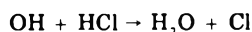
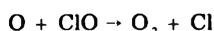
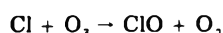
Physical Chemistry Division, National Bureau of Standards, Washington, D.C. 20234 (Received July 26, 1976)

Publication costs assisted by the National Bureau of Standards

The flash photolysis resonance fluorescence technique was employed to investigate the temperature dependencies of the reactions Cl + CH<sub>4</sub> → HCl + CH<sub>3</sub> (*k*<sub>1</sub>); Cl + CH<sub>3</sub>Cl → HCl + CH<sub>2</sub>Cl (*k*<sub>2</sub>); Cl + CH<sub>3</sub>F → HCl + CH<sub>2</sub>F (*k*<sub>3</sub>); Cl + CH<sub>3</sub>F<sup>†</sup> → HCl + CH<sub>2</sub>F (*k*<sub>3</sub><sup>†</sup>); Cl + C<sub>2</sub>H<sub>6</sub> → HCl + C<sub>2</sub>H<sub>5</sub> (*k*<sub>4</sub>). The following rate expressions were obtained in units of cm<sup>3</sup> molecule<sup>-1</sup> s<sup>-1</sup>: *k*<sub>1</sub>(218–322 K) = (7.93 ± 1.53) × 10<sup>-12</sup> exp[-(2529 ± 101)/RT]; *k*<sub>2</sub>(233–322 K) = (3.36 ± 0.71) × 10<sup>-11</sup> exp[-(2484 ± 113)/RT]; *k*<sub>3</sub>(216–296 K) = (4.79 ± 1.05) × 10<sup>-12</sup> exp[-(1535 ± 107)/RT]; *k*<sub>4</sub>(222–322 K) = (7.29 ± 1.23) × 10<sup>-11</sup> exp[-(121 ± 87)/RT] where *R* = 1.987 cal deg<sup>-1</sup> mol<sup>-1</sup>. At 227 and 296 K *k*<sub>3</sub><sup>†</sup>/*k*<sub>3</sub> was observed to be ≤ 1.3.

## Introduction

The recent inquiry into the possible role that naturally occurring or man-made chlorine containing compounds might play in determining the chemistry of the earth's stratosphere has resulted in an upsurge of interest in chlorine atom gas phase reactions.<sup>1</sup> Of principle concern is the question of the perturbation of the stratospheric ozone layer by a sequence of reactions which includes



The first two reactions represent the predominant sequence of Cl "catalyzed" processes predicted to be responsible for O<sub>3</sub> depletion following Cl production by the photolysis of chlorine containing species of either natural or anthropogenic origin (viz. CF<sub>2</sub>Cl<sub>2</sub> and CFCl<sub>3</sub>). Interruption of the Cl-ClO chain can occur via the third reaction, the reaction of Cl atoms with organic or inorganic hydrogen containing species, whereby Cl is converted into less reactive HCl. The chain is thus disrupted until HCl is reconverted into Cl (predominantly by reaction with OH). Since in any chain reaction sequence, determination of chain length requires accurate knowledge of the rate of termination, any loss of stratospheric ozone is quantitatively dependent on the rate constants for those reactions which destroy or "tie up" Cl. The most logical candidate for a reactant (RH) is methane which is abundant at midstratospheric levels with a mixing ratio (v/v) of 10<sup>-6</sup>.<sup>2</sup> CH<sub>3</sub>Cl, the most abundant natural halocarbon, is thought to be considerably less important due to its much lower mixing ratio (some three orders of magnitude smaller). Until recently, however, the only direct reaction rate data for Cl atoms with either of these species were obtained for temperatures at or above 298 K.<sup>3,4</sup> Unlike the reactions of O atoms with CH<sub>4</sub> and CH<sub>3</sub>Cl,<sup>5</sup> the Cl reactions were observed to have vastly different Arrhenius *A* factors and equal activation energies. A very recent study<sup>6</sup> of Cl + CH<sub>4</sub> from 218 to 401 K is in reasonable agreement with the two earlier studies at 298 K but differs significantly from the

values predicted by the only other published temperature-dependent study. For these reasons we decided to undertake a systematic study of H atom metathesis by Cl atoms for a series of halogenated methanes with particular emphasis on conditions applicable to stratospheric modeling. We report herein the results of our studies of reactions 1 (218–322 K), 2 (233–322 K), and 3 (216–296 K).



In the investigation of reaction 1 it was observed that C<sub>2</sub>H<sub>6</sub> impurities in 100 ppm range could result in major differences in the measured rate constant. Hence reaction



4 was studied from 222 to 322 K. The effect of reactant vibrational energy on the rate of reaction 3 was investigated at 227 and 296 K.

## Experimental Section

All experiments were performed using the flash photolysis resonance fluorescence technique. Procedural descriptions as well as details concerning the flash lamp, resonance lamp, and reaction cell are given in earlier publications.<sup>7</sup> Chlorine atoms were produced via the flash photolysis of 13 mTorr of CCl<sub>4</sub> (1 mTorr = 0.133 Pa = 9.6587 × 10<sup>15</sup>/T(K) molecules cm<sup>-3</sup>) at wavelengths above either the Suprasil (165 nm) or barium fluoride (135 nm) cutoff. In the initial experiments the flash lamp output intensity was varied from 3 × 10<sup>12</sup> to 3 × 10<sup>13</sup> quanta/flash producing initial Cl atom concentrations, [Cl]<sub>0</sub>, of 3 × 10<sup>10</sup> to 3 × 10<sup>11</sup> cm<sup>-3</sup>. The absence of any perceptible dependence of the atom decay rate on initial atom concentration was viewed as evidence for the lack of interference from secondary atom-radical reactions and the majority of the experiments were conducted with a flash intensity of 1 × 10<sup>13</sup> quanta/flash ([Cl]<sub>0</sub> = 1 × 10<sup>11</sup> cm<sup>-3</sup>). Reactions mixtures were flowed through the cell at 5 Torr total pressure with a flow rate of approximately 150 cm<sup>3</sup>

<sup>†</sup> NRC-NBS Postdoctoral Associate, 1975–present.

TABLE I: Rate Constants for the Reaction  $\text{Cl} + \text{CH}_4 \rightarrow \text{HCl} + \text{CH}_3$ 

Temp, K	$10^{14} k_1, {}^a \text{cm}^3 \text{ molecule}^{-1} \text{ s}^{-1}$			
	Measured <sup>b</sup>	Corrected <sup>b</sup>	Measured <sup>c</sup>	Corrected <sup>c</sup>
218	2.68 ± 0.14	2.49 ± 0.18		
224			5.51 ± 0.60	2.73 ± 1.40
235	3.69 ± 0.38	3.49 ± 0.42		
250	5.04 ± 0.36	4.83 ± 0.40		
254			7.43 ± 0.40	4.56 ± 1.40
263	6.36 ± 0.36	6.15 ± 0.40		
277	7.56 ± 0.62	7.35 ± 0.66		
285	8.79 ± 0.52	8.58 ± 0.56		
296	10.62 ± 1.02	10.39 ± 1.06	12.64 ± 0.38	9.68 ± 1.35
313	14.28 ± 0.96	14.08 ± 1.00		
322	16.86 ± 0.45	16.66 ± 0.49		

<sup>a</sup> Uncertainties expressed are  $\pm 2\sigma$  bands (i.e., 95% confidence limits). <sup>b</sup>  $\text{CH}_4$  containing 34 ppm of  $\text{C}_2\text{H}_6$ . Corrected using data in Table IV. <sup>c</sup>  $\text{CH}_4$  containing 500 ppm of  $\text{C}_2\text{H}_6$ . Corrected using data in Table IV.

TABLE II: Rate Constants for the Reaction  $\text{Cl} + \text{CH}_3\text{Cl} \rightarrow \text{HCl} + \text{CH}_2\text{Cl}$ 

Temp, K	$10^{13} k_1, {}^a \text{cm}^3 \text{ molecule}^{-1} \text{ s}^{-1}$	Temp, K	$10^{13} k_1, {}^a \text{cm}^3 \text{ molecule}^{-1} \text{ s}^{-1}$
233	1.67 ± 0.14	278	3.86 ± 0.30
244	2.00 ± 0.08	296	5.10 ± 0.14
256	2.49 ± 0.18	308	5.86 ± 0.54
263	2.62 ± 0.21	322	6.93 ± 0.40

<sup>a</sup> Uncertainties expressed are  $\pm 2\sigma$  bands (i.e., 95% confidence limits).

$\text{s}^{-1}$ . In this way the reaction cell was flushed every three flashes thereby avoiding any substantial decomposition of reactants or buildup of products.

The chlorine atom fluorescence resonantly scattered from the microwave discharge resonance lamp was viewed without wavelength resolution and was assumed to be linearly proportional to the atom concentration.<sup>8</sup> Analysis of the atom decay curves assumed pseudo-first-order kinetics since  $30 \leq [\text{reagent}]_0/[\text{Cl}]_0 \leq 10^5$ . First-order decay rates were calculated to have less than a 5% standard deviation from an experimental least-squares analysis of these curves. Second-order rate constants were then obtained from a linear least-squares fit of the first-order decay rate vs. substrate concentration plots. These fits were determined taking into account a  $\pm 2\sigma$  error band for each first-order decay rate.

Temperature of the reaction mixtures was controlled and measured to within 0.5 K. Gas mixtures were prepared in glass bulbs using calibrated capacitance manometers and Bourdon pressure gauges. Reaction concentrations during an actual experiment were thus determined to within 1–2% for all four systems studied. Any possible systematic error is smaller than the 5–10% ( $\pm 2\sigma$ , 95% confidence limits) uncertainties expressed for each bimolecular rate constant in Tables I–IV (see paragraph at end of text regarding supplementary material).

The effect of vibrational energy in  $\text{CH}_3\text{F}$  on  $k_3$  was determined using a procedure outlined in a previous

TABLE III: Rate Constants for the Reaction  $\text{Cl} + \text{CH}_3\text{F} \rightarrow \text{HCl} + \text{CH}_2\text{F}$ 

Temp, K	$10^{13} k_3, {}^a \text{cm}^3 \text{ molecule}^{-1} \text{ s}^{-1}$	Temp, K	$10^{13} k_3, {}^a \text{cm}^3 \text{ molecule}^{-1} \text{ s}^{-1}$
216	1.35 ± 0.12	264	2.29 ± 0.10
227	1.55 ± 0.08	278	3.12 ± 0.18
227 <sup>b</sup>	1.68 ± 0.06	296	3.61 ± 0.10
233	1.85 ± 0.10	296 <sup>b</sup>	3.82 ± 0.16
245	2.07 ± 0.12		

<sup>a</sup> Uncertainties expressed as  $\pm 2\sigma$  bands (i.e., 95% confidence limits). <sup>b</sup> Value obtained using infrared laser excitation of  $\text{CH}_3\text{F}$ . See text for details.

TABLE IV: Rate Constants for the Reaction  $\text{Cl} + \text{C}_2\text{H}_6 \rightarrow \text{HCl} + \text{C}_2\text{H}_5$ 

Temp, K	$10^{11} k_4, {}^a \text{cm}^3 \text{ molecule}^{-1} \text{ s}^{-1}$	Temp, K	$10^{11} k_4, {}^a \text{cm}^3 \text{ molecule}^{-1} \text{ s}^{-1}$
222	5.45 ± 0.46	267	6.11 ± 0.36
232	5.48 ± 0.46	280	5.74 ± 0.28
243	5.76 ± 0.24	296	5.93 ± 0.44
255	5.90 ± 0.28	322	5.92 ± 0.50

<sup>a</sup> Uncertainties expressed are  $\pm 2\sigma$  bands (i.e., 95% confidence limits).

publication.<sup>9</sup> Briefly, a continuous wave  $\text{CO}_2$  laser tuned to the P(20) 9.6- $\mu$  line was used to excite  $\text{CH}_3\text{F}$  into the  $\nu_3$  normal mode. Under conditions of minimal deactivation up to 30% of the  $\text{CH}_3\text{F}$  could be maintained as  $\text{CH}_3\text{F}^+$ . The decay rate of Cl atoms was then observed in this non-Boltzmann mixture at 296 and 227 K and compared with the thermal rate.

The purities of all gases used were as follows: argon (99.999%) used directly from cylinder;  $\text{CH}_4$  (99.8 and 99.97%) analyzed by gas chromatography to contain 500 ± 75 ppm of  $\text{C}_2\text{H}_6$  and 34 ± 5 ppm of  $\text{C}_2\text{H}_2$ , respectively, and used after degassing at 78 K;  $\text{CH}_3\text{Cl}$  (99.5% min) analyzed to contain 20 ± 5 ppm of  $\text{CH}_4$  + air, 15 ± 5 ppm of  $\text{C}_2\text{H}_3\text{Cl}$ , and 30 ± 5 ppm of  $\text{CH}_3\text{Br}$  used after degassing at 78 K;  $\text{CH}_3\text{F}$  (99.0% min) analyzed to contain 20 ± 10 ppm of  $\text{CH}_4$  + air and 35 ± 10 ppm of  $\text{C}_2\text{H}_5\text{F}$  used after degassing at 78 K;  $\text{C}_2\text{H}_6$  (99.9% min) analyzed to contain 10 ± 3 ppm of  $\text{CH}_4$  and 8 ± 3 ppm of  $\text{C}_2\text{H}_4$  used after degassing at 78 K.

## Results and Discussion

(a)  $\text{Cl} + \text{CH}_4$ . The values of  $k_1$  obtained for the two purities of  $\text{CH}_4$  used in these studies are tabulated vs. temperature in Table I. At each temperature a correction has been applied to account for reaction of Cl with the  $\text{C}_2\text{H}_6$  impurity using the values of  $k_4$  obtained in this study. As can be seen, these corrections are more significant at the lower temperatures and can be as high as 25% for 100 ppm of  $\text{C}_2\text{H}_6$  at stratospheric temperatures. The corrected rate constants obtained using the less pure  $\text{CH}_4$  compare reasonably well with those calculated from the purer methane data indicating the validity of the correction procedure. However due to the larger uncertainties in the corrected values from the less pure methane these points were not used in the Arrhenius fit of the data.

The corrected values of  $k_1$  are plotted in Arrhenius form in Figure 1. The solid line represents a least-squares analysis of all the data and is given by

$$k_1 = (7.93 \pm 1.53) \times 10^{-12} \exp[-(2529 \pm 101)/RT]$$

in units of  $\text{cm}^3 \text{ molecule}^{-1} \text{ s}^{-1}$ . The uncertainties are one standard deviation, taking into account the  $\pm 2\sigma$  associated with each individual point in Table I. Within the experimental uncertainties, all points seem to be fairly well

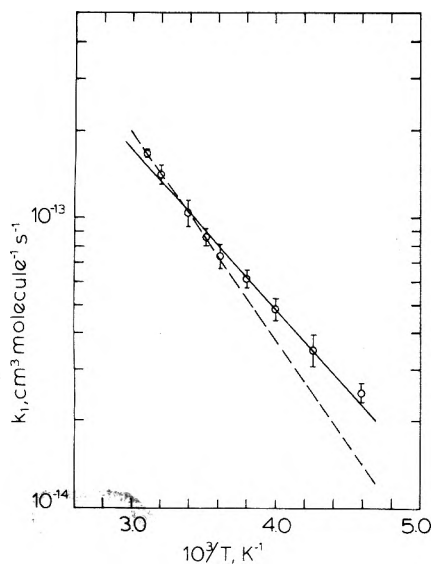


Figure 1. Arrhenius plot of the rate constants for the reaction  $\text{Cl} + \text{CH}_4$  measured in this study: (—) Arrhenius fit of all data; (---) Arrhenius fit of four highest temperature points.

represented by the exponential fit. The observation that the highest and lowest temperature points lie above the line whereas the midrange points lie below it does however suggest the possibility of slight curvature. Indeed if only the four highest temperature points are analyzed one finds (dashed line in Figure 1)

$$k_1(277\text{--}322 \text{ K}) = (2.77 \pm 1.28) \times 10^{-11} \times \exp\left[-\frac{(3273 \pm 274)}{RT}\right] \text{ cm}^3 \text{ molecule}^{-1} \text{ s}^{-1}$$

Although the slight scatter (or trend) in our data is really too small to justify any claim about this change in the regression parameters, the observation is interesting in light of the current controversy over the temperature dependence of  $k_1$ . A review of all studies of reaction 1 (both published and unpublished) has recently been prepared by Watson.<sup>10</sup> All of the absolute data from this compilation are shown on an Arrhenius plot in Figure 2. One's initial inclination might be to average the data according to a simple Arrhenius fit. However, such an averaging would neglect the estimated confidence limits of the various studies. The seven absolute rate determinations (six as a function of temperature) divide into two groupings: those performed in the presence of excess methane,  $[\text{CH}_4]_0$ , and those with  $[\text{Cl}]_0/[\text{CH}_4]_0 \gg 1$ . In the first group are the present work, Watson et al.,<sup>6</sup> Davis et al.<sup>3</sup> (all by flash photolysis resonance fluorescence), and Zahniser and Kaufman<sup>11</sup> (by discharge flow resonance fluorescence). While these techniques have in recent years yielded the most precise kinetic data available, one must consider both systematic errors and hydrocarbon impurity levels in the  $\text{CH}_4$ . At 298 K the first three of these studies give corrected values of 1.07, 1.15, and  $\leq 1.28$  ( $\text{C}_2\text{H}_6$  and  $\text{C}_3\text{H}_8$  impurities were not totally accounted for)  $\times 10^{-13} \text{ cm}^3 \text{ molecule}^{-1} \text{ s}^{-1}$ . The fourth study reports a value of  $k_1 = 0.99 \times 10^{-13} \text{ cm}^3 \text{ molecule}^{-1} \text{ s}^{-1}$ .<sup>11</sup> Thus, all four determinations agree quite well and point to an average value very close to that measured in this study.

The three investigations performed under "Cl rich" conditions<sup>4,12,13</sup> all involved discharge flow mass spectrometric techniques. The values reported for  $k_1$  at 298 K are from 10 to 20% higher than the resonance fluorescence data. Typically, fewer data points were accumulated for the rate constant determinations, resulting

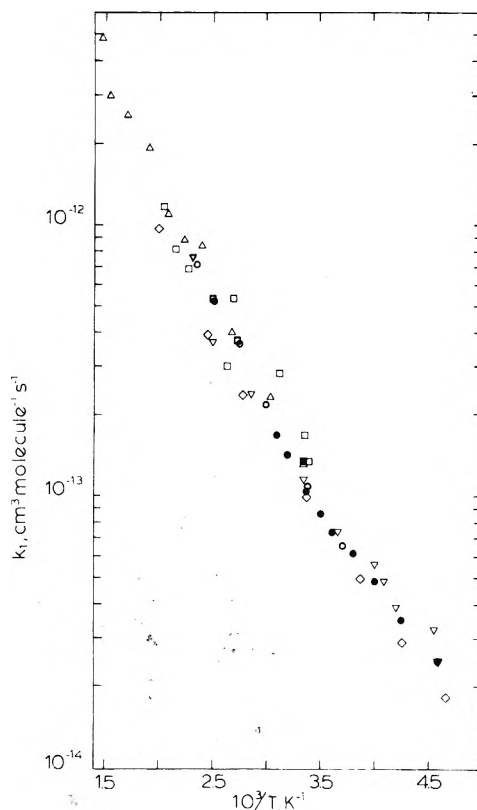


Figure 2. Arrhenius plot of all absolute rate constants for the reaction  $\text{Cl} + \text{CH}_4$ : (●) this work, (□) Zahniser and Kaufman (ref 11), (▽) Watson et al. (ref 6), (■) Davis et al. (ref 3), (○) Leu and De More (ref 12), (△) Clyne and Walker (ref 4), (□) Poulet et al. (ref 13).

in lower precision. In addition, heterogeneous loss of Cl can be a problem. A third consideration, indicated in the study of Poulet et al.,<sup>13</sup> is the necessity to employ second-order kinetic analysis to the data for  $[\text{Cl}]_0/[\text{CH}_4]_0$  ratios as high as 20/1 due to high reaction stoichiometries. Unfortunately any second-order correction procedure used for these studies raises  $k_1$  at 298 K even higher. In any case, initial Cl concentrations were specified only in the study of Poulet et al. whose data appear to be of the poorest precision of the three. The room temperature data nevertheless do overlap the resonance fluorescence results within reported uncertainties. Thus a recommended value of  $k_1$  at 298 K would weight predominantly the present work, Watson et al., and Zahniser and Kaufman to give

$$k_1^{298} = (1.07 \pm 0.20) \times 10^{-13} \text{ cm}^3 \text{ molecule}^{-1} \text{ s}^{-1}$$

A comparative analysis becomes more complex when one considers the temperature dependence of  $k_1$ . The level of agreement (or disagreement) of the six absolute temperature-dependent studies is not entirely evident from the calculated values of the Arrhenius parameters. This is principally due to the small temperature overlap between the mass spectrometric and optical techniques. Between 200 and 300 K the results of the present study agree very well with those of Watson et al. and Zahniser and Kaufman, with the total spread in the data being 20% at 300 K and 30% at 218 K (the lowest overlap temperature). This agreement argues strongly against systematic error in any one of the studies (particularly since the data at the temperature extremes of most kinetic studies tend to be the least certain). The current results lie virtually midway between these other two studies and data averaging procedures would yield the herein reported Arrhenius parameters over this temperature range.

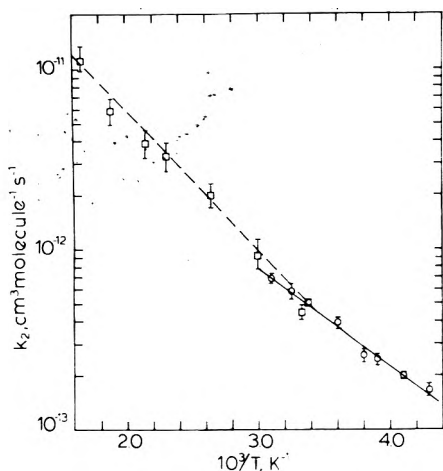


Figure 3. Arrhenius plot of the rate constants for the reaction  $\text{Cl} + \text{CH}_3\text{Cl}$ : (O and —) this work, (□ and —) Clyne and Walker (ref 4).

Above 300 K these three studies predict values of  $k_1$  significantly lower than the results of the three mass spectrometric investigations (although, as mentioned, the precision of Poulet et al. is not good enough to make a strict quantitative comparison). The excellent agreement between the studies of Clyne and Walker and Leu and De More indicates the absence of any systematic error in the mass spectrometric experiments. Some insight into the variation in the reported activation energies is given by the study of Zahniser and Kaufman in which nonlinear Arrhenius behavior was observed. Their data between 300 and 500 K curve upward and yield the somewhat steeper Arrhenius expression

$$k_1(300\text{--}500 \text{ K}) = 2.25 \times 10^{-11} \exp(-3225/RT) \text{ cm}^3 \text{ molecule}^{-1} \text{ s}^{-1}$$

(which is close to that derived from our data between 277 and 322 K). However, while curvature over the 200–500 K temperature range is not unexpected for a reaction of small effective activation energy, the rate constants in the high temperature region of overlap still do not agree within the quoted confidence limits of the individual studies. It is possible that a changing mechanism could result in discrepancies between the experimental methods outside of these estimated confidence limits. Until a single study of sufficient precision is performed spanning the 200–800 K temperature range the absolute magnitude of the Arrhenius curvature remains uncertain.<sup>18</sup> Below 300 K there is, as mentioned, excellent agreement of all studies with the data of the present study seeming to represent the mean. Between 300 and 500 K a reasonable choice of  $k_1$  would be bracketed by the expressions of Zahniser and Kaufman<sup>11</sup> and Leu and De More.<sup>12</sup>

(b)  $\text{Cl} + \text{CH}_3\text{Cl}$ . The temperature data for  $k_2$  are listed in Table II and plotted in Arrhenius form in Figure 3. The rate constants are fit by the expression

$$k_2 = (3.36 \pm 0.71) \times 10^{-11} \exp[-(2484 \pm 113)/RT] \text{ cm}^3 \text{ molecule}^{-1} \text{ s}^{-1}$$

taking into account the  $\pm 2\sigma$  uncertainty in each point. The equation is virtually identical with the fit of Watson et al.<sup>14</sup>

$$(3.7 \pm 0.4) \times 10^{-11} \exp[-(2557 \pm 300)/RT] \text{ cm}^3 \text{ molecule}^{-1} \text{ s}^{-1}$$

obtained from 245–350 K but significantly different from the expression given by Clyne and Walker<sup>4</sup> of

$$(2.1 \pm 0.4) \times 10^{-10} \exp[-(3551 \pm 140)/RT] \text{ cm}^3 \text{ molecule}^{-1} \text{ s}^{-1}$$

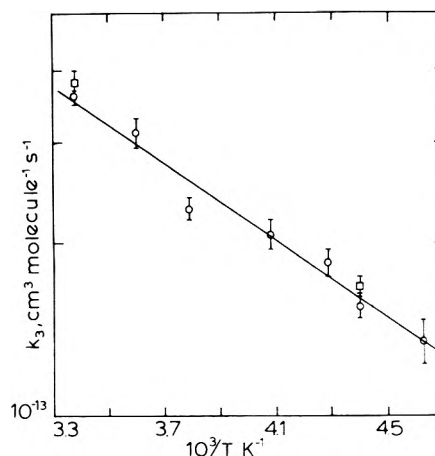


Figure 4. Arrhenius plot of the rate constants for the reaction  $\text{Cl} + \text{CH}_3\text{F}$  measured in this study: (O) laser off, (□) laser on.

from 300 to 604 K. All three studies agree within the cited error limits around 300 K. The data of Clyne and Walker may be contrasted with our resonance fluorescence data in Figure 3. (The data of Watson et al. were not included in this plot due to their virtual superposition on the present data.) While there is no immediately obvious explanation for the differences, it is rather interesting that all three absolute studies obtain over their respective temperatures

$$k_2/k_1 = (4.5 \pm 0.45) \exp[60 \pm 65/RT]$$

ranges. This result may suggest an inherent error in one of the two techniques. Nonlinear Arrhenius behavior similar to that indicated by temperature dependence of  $k_1$  might be involved for the present reaction but would require an Arrhenius A factor at high temperature much larger than the  $2.1 \times 10^{-10} \text{ cm}^3 \text{ molecule}^{-1} \text{ s}^{-1}$  already reported in the mass spectrometric study. Until a detailed systematic study is performed over a wide range of temperature, no confirmation of curvature can be made nor can a recommendation for  $k_2$  above 350 K be proposed. Below this temperature the flash photolysis resonance fluorescence data can be subjected to a common least-squares fit to give a preferred value of

$$(3.4 \pm 0.8) \times 10^{-11} \exp[-(2496 \pm 120)/RT] \text{ cm}^3 \text{ molecule}^{-1} \text{ s}^{-1}$$

from 233 to 350 K.

(c)  $\text{Cl} + \text{CH}_3\text{F}$ . The results obtained for reaction 3 are listed in Table III and plotted in Arrhenius form in Figure 4. A linear least-squares analysis of the Arrhenius fit gives

$$k_3 = (4.79 \pm 1.05) \times 10^{-12} \exp[-(1535 \pm 107)/RT] \text{ cm}^3 \text{ molecule}^{-1} \text{ s}^{-1}$$

There are no other absolute rate measurements with which we can compare our results for this reaction. It is interesting to note, however, that the Arrhenius A factor for reaction 3 is quite low (similar to that associated with the data for reaction 1 over the same temperature range). While this observation could once again imply curvature in the Arrhenius plot, one might alternatively suggest that within this range of temperature the reaction intermediate is different from that associated with simple H atom abstraction from  $\text{CH}_3\text{Cl}$  and  $\text{C}_2\text{H}_6$  which exhibit larger A factors.

In an attempt to gain further insight into the reaction energetics, the effect of excess vibrational energy in  $\text{CH}_3\text{F}$  on  $k_3$  was investigated at 227 and 296 K. The values obtained for the bimolecular rate constant under laser-on conditions are also plotted in Figure 4. The complete

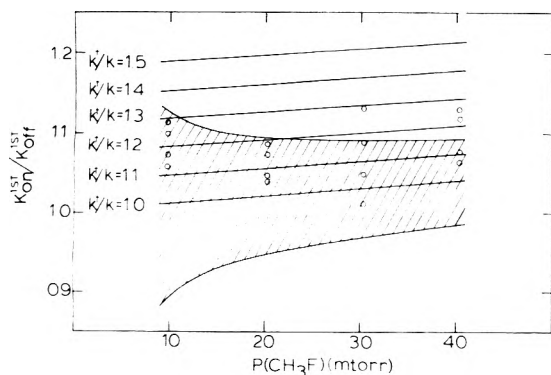
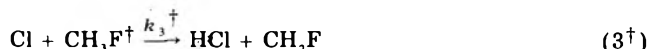


**Figure 5.** Plot of the measured and calculated  $R$ -ratio values (eq I) vs.  $\text{CH}_3\text{F}$  pressure for the reaction  $\text{Cl} + \text{CH}_3\text{F}^\ddagger$ ; 13 mTorr of  $\text{CCl}_4$  to 5 Torr total pressure with Ar. Laser power of 5.1 W at P20 line, 9.6- $\mu$  band.

analysis for the laser enhanced rate data has been given in a previous paper. Briefly, at any given concentration of  $\text{CH}_3\text{F}$ , the ratio of laser-on to laser-off first-order atom decay rates (corrected for the decay at  $[\text{CH}_3\text{F}] = 0$ ) is given by

$$R = \exp\left(\frac{-E(T_1 - T_2)}{R T_1 T_2}\right) \times \left(1 + \frac{[\text{CH}_3\text{F}^\ddagger]}{[\text{CH}_3\text{F}]} \frac{(k_3^\ddagger - k_3)}{k_3}\right) \quad (\text{I})$$

where  $E$  is the activation energy (assumed to be unaltered by vibrational excitation),  $T_1$  is the temperature of the reaction mixture when the laser is off,  $T_2$  is the temperature of the mixture when the laser is on (laser heating produced by V-T deactivation), and  $k_3^\ddagger$  is the actual bimolecular rate constant for the process



The value of  $T_2$  was determined relative to the known temperature rise in a laser pumped  $\text{CH}_2\text{F}_2$  system using the known ratios of laser power, absorbant concentrations, and absorption coefficients. The experimental points (at 296 K) and theoretical curves (from eq I) are presented in Figure 5. The  $k^\ddagger/k_3 = 1.0$  line defines the case of purely thermal heating. The flared shaded area represents the  $\pm\sigma_R$  (standard deviation of  $R$ ) error bands. At the lower  $\text{CH}_3\text{F}$  pressures, the uncertainty in the atom decay rate due to diffusion contributed significantly to the error in  $R$  resulting in the flaring outward of the error curves. At higher  $[\text{CH}_3\text{F}]$  the error in  $R$  is determined primarily by the least-squares error in decay curves. Other parallel lines are drawn for the various rate constant enhancements. As is evident from Figure 5 a ratio  $k_3^\ddagger/k_3 = 1.3$  would be clearly discernible outside of the error bands. Unfortunately, however, all the data points lie below this and in fact the majority of them are indistinguishable from the boundaries associated with a purely heating phenomenon. Thus we can confidently place an upper limit of 30% on the increase in  $k_3$  due to vibrational excitation of  $\text{CH}_3\text{F}$ . The analysis at 227 K is nearly identical with that for 296 K and again an upper limit of  $k_3^\ddagger/k_3 \leq 1.3$  can be set. These results can be compared with some recent results on the reaction<sup>15</sup>



which report that over the temperature range 148–298 K  $k_1^\ddagger/k_1 \leq 30$

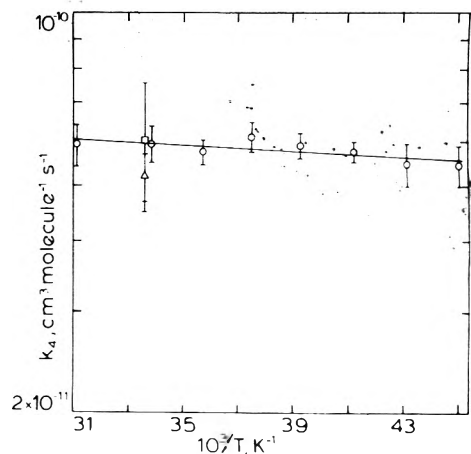


**Figure 6.** Arrhenius plot of the rate constants for the reaction  $\text{Cl} + \text{C}_2\text{H}_6$ : (O and —) this work, ( $\Delta$ ) Davis et al. (ref 3), ( $\square$ ) Watson et al. (ref 14).

Even more recently it was observed that in the reaction of Cl with  $\text{CH}_3\text{Br}$  only a 2–3% isotopic enrichment of brominated hydrocarbon products was observed when the  $\text{CH}_3\text{Br}$  was excited with a  $\text{CO}_2$  laser.<sup>16</sup> All of these results are consistent with our earlier observations that there is little effect of reactant vibrational energy on the rate of reactions having “early” activation barriers.<sup>9</sup>

(d)  $\text{Cl} + \text{C}_2\text{H}_6$ . The values obtained for  $k_4$  in this study are tabulated vs. temperature in Table IV and plotted in Arrhenius form in Figure 5. The data can be fit to the equation

$$k_4 = (7.29 \pm 1.23) \times 10^{-11} \exp[-(121 \pm 87)/RT] \text{ cm}^3 \text{ molecule}^{-1} \text{ s}^{-1}$$

The result obtained in this study at 296 K of  $5.93 \times 10^{-11} \text{ cm}^3 \text{ molecule}^{-1} \text{ s}^{-1}$  is in excellent agreement with the only other measured values at 298 K of  $6.0^3$  and  $5.5 \times 10^{-11}$ .<sup>14</sup> No other absolute determinations of the activation energy of reaction 4 have been made. The low value reported here seems more reasonable than the 1 kcal determined via competitive chlorination techniques<sup>10</sup> since this higher number, when coupled with the confirmed room temperature rate constant, yields an unusually high Arrhenius  $A$  factor.

### Summary

The rate constants reported herein for the  $\text{Cl} + \text{CH}_4$  reaction are consistent with Arrhenius  $A$  and  $E$  parameters significantly lower than those calculated from mass spectrometric flow data above room temperature. These differences can be explained at least in part by curvature in the Arrhenius plot. Below room temperature there is substantial agreement among the data from a number of experiments employing optical detection of Cl.

Because of the possibility of curvature in the Arrhenius plots for reactions having low effective activation barriers, comparison of the  $A$ 's and  $E$ 's for reactions 1–4 can be misleading. Nevertheless, the  $A$  factors for  $\text{CH}_3\text{Cl}$  and  $\text{C}_2\text{H}_6$  are in the ratio of approximately 1:2 (the ratio of the number of abstractable hydrogens) and are of comparable magnitude to the  $A$  factors obtained for the corresponding reaction with O atoms. It is expected that the limiting high temperature  $A$  factors for reaction of Cl with  $\text{CH}_4$  and  $\text{CH}_3\text{F}$  would also fall in line with the O atom values. The lack of a rate enhancement from vibrational excitation in  $\text{CH}_3\text{F}$  is consistent with the exothermicity of the reaction.

*Acknowledgment.* The authors wish to express their appreciation to Drs. R. T. Watson, F. Kaufman, W. B. De More, and J. V. Michael for relating the results of their

studies prior to publication. This work was supported in part by the Office of Air and Water Measurement, National Bureau of Standards.

**Supplementary Material Available:** Supplementary Tables I–IV contain the first-order decay rate data from which  $k_1$ ,  $k_2$ ,  $k_3$ , and  $k_4$  are calculated (13 pages). Ordering information is available on any current masthead page.

## References and Notes

- (1) F. S. Rowland and M. J. Molina, *Rev. Geophys. Space Phys.*, **13**, 1 (1975).
- (2) CIAP Monograph I, "The Natural Stratosphere of 1975", DOT-TST-75-51, Department of Transportation, Washington, D.C.
- (3) D. D. Davis, W. Braun, and A. M. Bass, *Int. J. Chem. Kinet.*, **2**, 101 (1970).
- (4) M. A. A. Clyne and R. F. Walker, *J. Chem. Soc., Faraday Trans. 1*, **69**, 1547 (1973).
- (5) R. E. Huie and J. T. Herron, *Prog. React. Kinet.*, **8**, 1 (1975).
- (6) R. T. Watson, G. Machado, S. Fischer, and D. D. Davis, *J. Chem. Phys.*, **65**, 2126 (1976).
- (7) (a) M. J. Kurylo, N. C. Peterson, and W. Braun, *J. Chem. Phys.*, **53**, 2776 (1970); (b) D. D. Davis, R. E. Huie, J. T. Herron, M. J. Kurylo, and W. Braun, *ibid.*, **56**, 4868 (1972); (c) M. J. Kurylo and W. Braun, *Chem. Phys. Lett.*, **37**, 232 (1976).
- (8) (a) P. O. Bernand and M. A. A. Clyne, *J. Chem. Soc., Faraday Trans. 2*, **71**, 1132 (1975); (b) M. S. Zahniser, F. Kaufman, and J. G. Anderson, *Chem. Phys. Lett.*, **37**, 226 (1976).
- (9) R. G. Manning, W. Braun, and M. J. Kurylo, *J. Chem. Phys.*, **65**, 2609 (1976).
- (10) R. T. Watson, *J. Phys. Chem. Ref. Data*, to be published.
- (11) M. S. Zahniser and F. Kaufman, private communication. Ethane impurities were analyzed by gas chromatography to be <25 ppm.
- (12) M.-T. Leu and W. B. De More, private communication.
- (13) G. Poulet, C. LeBras, and J. Combourieu, *J. Chim. Phys.*, **71**, 101 (1974).
- (14) R. T. Watson, D. D. Davis, E. S. Machado, B. C. Conway, and Y. Oh, to be published.
- (15) E. N. Chesnokov, V. P. Strunin, N. K. Serdyuk, and V. N. Panfilov, *React. Kinet. Catal. Lett.*, **3**, 131 (1975).
- (16) T. J. Manuccia, M. D. Clark, and E. R. Lory, presented at 12th Informal Conference on Photochemistry, National Bureau of Standards, Gaithersburg, Md, July 1976.
- (17) J. V. Michael, National Bureau of Standards, Physical Chemistry Division Seminar, July 29, 1976.
- (18) Subsequent to the submission of this manuscript for publication the results of an additional determination of  $k_1$  were conveyed to the authors.<sup>17</sup> This study employed the same flash photolysis resonance fluorescence technique used in the present work and spanned the temperature range 200–500 K. The results are in excellent quantitative agreement with our own and indicate the same curvature in the Arrhenius plot observed by Zahniser and Kaufman.

# Kinetics and Mechanism of the Gas Phase Reaction of OH Radicals with Aromatic Hydrocarbons Over the Temperature Range 296–473 K

R. A. Perry, R. Atkinson,\* and J. N. Pitts, Jr.

Department of Chemistry and Statewide Air Pollution Research Center, University of California, Riverside, California 92502  
(Received July 19, 1976)

Publication costs assisted by the University of California, Riverside

Absolute rate constants for the reaction of OH radicals with a series of aromatic hydrocarbons in the gas phase have been determined over the temperature range 296–473 K using a flash photolysis-resonance fluorescence technique. In all cases it was observed that for temperatures between ~325 and ~380 K the OH decays were nonexponential. For the temperature regions  $380 \text{ K} \leq T < 473 \text{ K}$  and  $296 \text{ K} < T \leq 325 \text{ K}$  the OH decays were exponential, with the rate constants at ~380 K being a factor of 4–12 lower than those at ~298 K. The observed behavior is explained by the occurrence of both OH radical addition to the aromatic ring and H atom abstraction at room temperature, while the abstraction reaction is the sole reaction observed above ~380 K due to the rapid decomposition of the OH–aromatic adduct within the time scale of the observations. In the temperature region where nonexponential decays are observed it is postulated that the OH–aromatic adduct, formed by OH radical addition to the ring, is decomposing back to reactants. The rate constants for the reaction of OH radicals with toluene- $d_8$  substantiates this reaction scheme, being within 5% of that for toluene at 298 K, but being a factor of ~2.5 lower at 432 K than that for toluene. The overall room temperature rate constants determined ranged from  $1.20 \times 10^{-12} \text{ cm}^3 \text{ molecule}^{-1} \text{ s}^{-1}$  for benzene to  $6.24 \times 10^{-11} \text{ cm}^3 \text{ molecule}^{-1} \text{ s}^{-1}$  for 1,3,5-trimethylbenzene. Rate constants for both addition and abstraction for benzene, toluene, toluene- $d_8$ , *o*-, *m*-, and *p*-xylene, and 1,2,3-, 1,2,4-, and 1,3,5-trimethylbenzene are given. Heats of formation of the OH–aromatic adduct are derived, leading to a calculated stabilization energy of the OH–aromatic adduct (if a  $\sigma$  bonded moiety) of  $16.5 \pm 5 \text{ kcal mol}^{-1}$ .

## Introduction

The reactions of the hydroxyl radical with aromatic hydrocarbons are of fundamental interest as well as being of importance in chemical models of photochemical air pollution.<sup>1,2</sup> Absolute rate constants have recently been determined at room temperature for the reaction of OH radicals with benzene and toluene<sup>3,4</sup> and with a series of aromatic hydrocarbons<sup>4</sup> using flash photolysis-resonance fluorescence techniques. In addition, rate constants for the reaction of OH radicals with aromatic hydrocarbons have been obtained from the initial rates of disappearance of the aromatic hydrocarbons relative to that of *n*-butane

in an environmental chamber<sup>5,6</sup> at 304–305 K.

However, rate constants for these reactions are not known as a function of temperature, nor are there direct product studies of the reaction of OH radicals with aromatic hydrocarbons. However, the rate constant data for benzene and toluene obtained by Davis, Bollinger, and Fischer<sup>3</sup> indicated that at room temperature in the limiting high pressure region OH radical addition to the aromatic ring is at least as important a reaction pathway as that of abstraction.

In this work absolute rate constants for the reaction of OH radicals with a series of aromatic hydrocarbons have

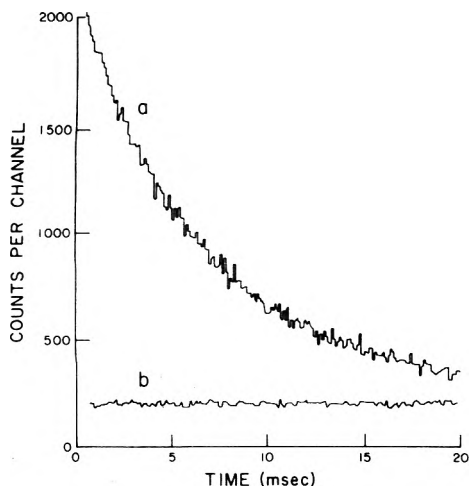


**Figure 1.** Time dependence of the OH radical resonance fluorescence signal intensity accumulated from 400 flashes of a benzene (0.002 25 Torr)-H<sub>2</sub>O (0.021 Torr)-argon (101.1 Torr) mixture at 322.7 K with a multichannel scaler width of 100  $\mu$ s and a flash energy of 50 J per flash. (a) Observed OH resonance fluorescence signal intensity for the first 20 ms after the flash. (b) Scattered light signal from the OH resonance lamp.

been determined over the temperature range 296–473 K using a flash photolysis-resonance fluorescence technique.

### Experimental Section

The apparatus and techniques used have been described previously,<sup>4,7</sup> and hence only a brief summary will be given here. OH radicals were produced by the pulsed vacuum ultraviolet photolysis of H<sub>2</sub>O at wavelengths longer than the LiF cutoff ( $\geq 1050$  Å). OH radical concentrations were monitored as a function of time after the flash by resonance fluorescence using a cooled EMI 9659QA photomultiplier fitted with an interference filter transmitting the 3064-Å band of OH(A<sup>2</sup> $\Sigma^+$ ,  $\nu' = 0 \rightarrow X^2\Pi$ ,  $\nu'' = 0$ ). The intersection of the detection system aperture and the resonance radiation beam defined a fluorescence viewing zone at the center of the reaction vessel, whose cross section was  $\sim 2$  cm in diameter. This region was well separated from the reaction vessel walls, thus minimizing wall losses of the OH radicals. The reaction cell was enclosed in a furnace which could be held constant to better than  $\pm 1$  K over the temperature range 295–475 K. The gas temperature was measured by a chromel/alumel thermocouple mounted inside the reaction vessel.

The flash lamp was typically operated at discharge energies of 25–50 J per flash at repetition rates of one flash every 3 s. Signals were obtained by photon counting in conjunction with multichannel scaling. OH radical decay curves such as that shown in Figure 1 were accumulated from 20–1200 flashes, depending on the signal strengths. OH half-lives ranged from 1.54 to 161 ms, and the OH radical concentrations were followed over at least three half-lives. In all cases the flash duration was negligible in comparison to the OH radical half-lives encountered.

In order to avoid the accumulation of photolysis or reaction products, all experiments were carried out under flow conditions so that the gas mixture in the reaction vessel was replenished every few flashes. The partial pressure of H<sub>2</sub>O in the reaction cell was  $\sim 0.02$  Torr. The argon and oxygen used had purity levels of  $\geq 99.998$  and  $\geq 99.99\%$ , respectively, according to the manufacturers. Gas chromatographic analyses of the aromatic hydrocarbons used showed<sup>4,8</sup> them to have purity levels of  $\geq 99.0\%$ , except for *m*-xylene (98.6%) and 1,2,3-trimethylbenzene (97.6%). The impurities observed<sup>4,8</sup> were

other aromatic hydrocarbons, and for the xylenes and trimethylbenzenes were mainly their isomers. The toluene-*d*<sub>8</sub> had a stated D atom purity level of  $\geq 99\%$ .

A known fraction of the total flow was saturated with the aromatic vapor at 251–293 K, depending on the aromatic hydrocarbon used. Aromatic hydrocarbon partial pressures in this fraction of the total flow were determined by their ultraviolet absorption using a 9.0-cm pathlength cell and a Cary 15 spectrophotometer. The absorption cell was calibrated using known pressures of the aromatic hydrocarbons as measured by an MKS Baratron capacitance manometer. All flows were monitored by calibrated flowmeters and the gases were premixed before entering the reaction vessel.

### Results

Under the conditions used, the aromatic hydrocarbon concentrations were in large excess of the initial OH radical concentrations ( $\sim 10^{11}$  molecule cm<sup>-3</sup>). If the products of the reaction of OH radicals with the aromatic hydrocarbons are stable, or if they decompose to fragments other than OH radicals, then the OH concentration is given by

$$-d[\text{OH}]/dt = (k_0 + k[\text{aromatic}])[\text{OH}] \quad (\text{I})$$

and

$$\begin{aligned} [\text{OH}]_{t_0}/[\text{OH}]_t &= S_0/S_t \\ &= \exp[(k_0 + k[\text{aromatic}])(t - t_0)] \end{aligned} \quad (\text{II})$$

where  $[\text{OH}]_{t_0}$  and  $[\text{OH}]_t$  are the concentrations of OH at times  $t_0$  and  $t$ , respectively,  $S_0$  and  $S_t$  are the corresponding resonance fluorescence intensities,  $k_0$  is the first-order rate constant for removal of OH in the absence of added reactant (primarily attributed to diffusion out of the viewing zone and to reaction with impurities), and  $k$  is the rate constant for the reaction



However, if this reaction is reversible then, depending on the half-life of the product with respect to reformation of OH and the time scale that OH radicals are being observed over, the OH decays will no longer be exponential (vide infra).

OH radical decays were determined for the reaction of OH radicals with benzene, toluene, toluene-*d*<sub>8</sub>, *o*-, *m*-, and *p*-xylene, and 1,2,3-, 1,2,4-, and 1,3,5-trimethylbenzene over the temperature range 296–473 K at a total pressure of  $\sim 100$  Torr of argon (total pressures up to 200 Torr of argon were used in the case of toluene). In all cases, as the temperature was increased from  $\sim 298$  K the following characteristics were observed:

At room temperature ( $\sim 298$  K) the OH radical decays were exponential over at least three half-lives and the decay rates  $R$ , defined as  $R = (t - t_0)^{-1} \ln S_0/S_t$ , were a linear function of the aromatic hydrocarbon concentration:

$$R = k_0 + k[\text{aromatic}] \quad (\text{III})$$

Similar behavior was observed up to  $\sim 325$  K with the rate constant  $k$  changing only slightly with the increasing temperature.

For temperatures between  $\sim 325$  and 380 K the OH decays were no longer exponential, with the decay rate decreasing with time after the flash (Figure 2). The rate constants  $k$  obtained at  $\sim 380$  K from the initial OH decay rates were a factor of 4–12 lower than those at  $\sim 298$  K.

For temperatures  $\geq 380$  K the OH decays were again exponential with a linear dependence of the decay rates on aromatic hydrocarbon concentration. The rate constants  $k$  obtained in this temperature regime generally

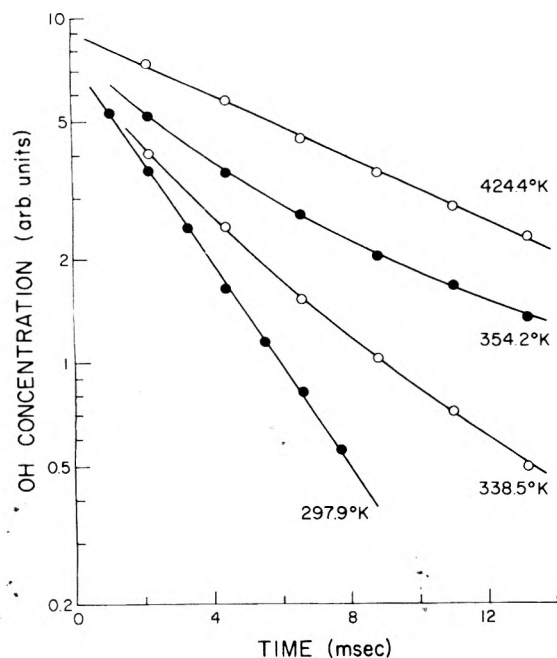


**Figure 2.** OH radical decays, plotted as  $\ln [\text{OH}]_t$  against time after the flash, for the reaction of OH radicals with toluene at 297.9, 338.5, 354.2, and 424.4 K with  $\sim 100$  Torr total pressure of argon diluent. Data points are plotted at every eleventh channel (100- or 200- $\mu\text{s}$  channel widths). The toluene concentrations are: 297.9 K,  $4.95 \times 10^{13}$  molecule  $\text{cm}^{-3}$ ; 338.5 K,  $4.68 \times 10^{13}$  molecule  $\text{cm}^{-3}$ ; 354.2 K,  $6.11 \times 10^{13}$  molecule  $\text{cm}^{-3}$ ; 424.4 K,  $5.22 \times 10^{13}$  molecule  $\text{cm}^{-3}$ .

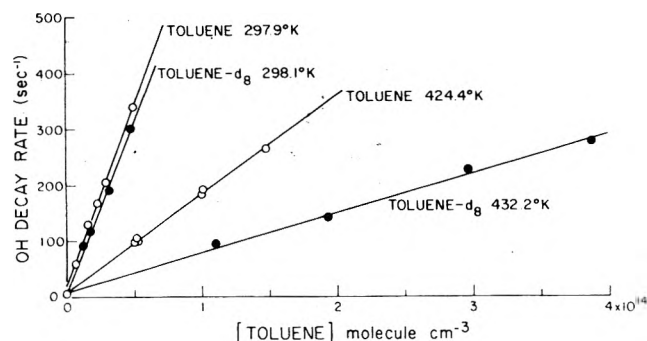


**Figure 3.** Plots of the OH radical decay rate against aromatic hydrocarbon concentration for toluene at 297.9 and 424.4 K and for toluene- $d_8$  at 298.1 and 432.2 K. Total pressure  $\sim 100$  Torr of argon.

increased with temperature up to the highest temperatures used (420–470 K).

This behavior is illustrated by Figures 2 and 3. Figure 2 shows OH radical decays, plotted as  $\ln [\text{OH}]_t$  against  $t$ , for a toluene concentration of  $\sim 5 \times 10^{13}$  molecule  $\text{cm}^{-3}$  at 297.9, 338.5, 354.2, and 424.4 K, while Figure 3 shows plots of the OH decay rate against toluene concentration for the temperatures 297.9 and 424.4 K.

Rate constants  $k$  were determined as a function of temperature from either (a) the dependence of the OH radical decay rate on the aromatic hydrocarbon concentration, as shown in Figure 3 for toluene, or (b) a single OH decay rate  $R$  at a known aromatic hydrocarbon concentration using eq III. The latter method obviously has a somewhat larger degree of uncertainty, partially associated with the estimation of the OH decay rate in the absence of reactant,  $R = k_0$ . However, for OH decay rates  $\geq 200 \text{ s}^{-1}$ , any error associated with the estimation of  $k_0$  (which was typically  $\sim 10\text{--}20 \text{ s}^{-1}$ ) was  $\leq 5\%$ . Values of  $k_0$  were estimated using values obtained by method (a) for the same aromatic hydrocarbon at similar temperatures. The error limits given in Table I (see paragraph at end of

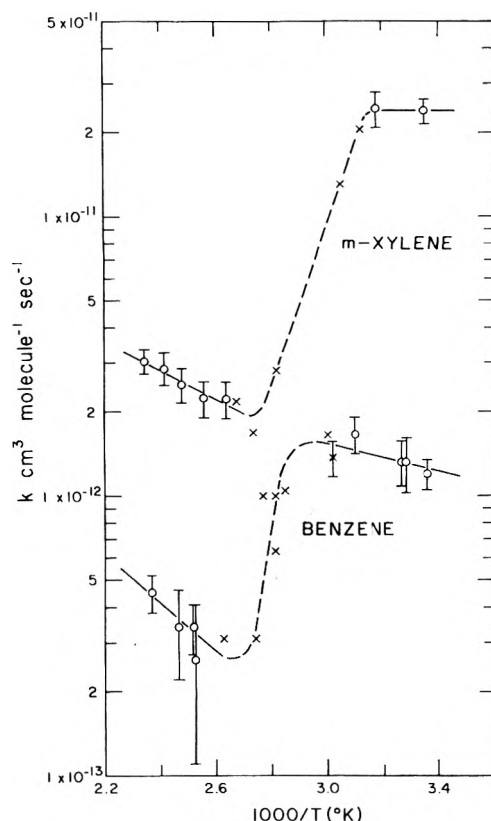


**Figure 4.** Arrhenius plots of  $\log k$  against  $1000/T$  for benzene and *m*-xylene: (O) exponential OH radical decays observed; (X) nonexponential OH radical decays observed. The dashed lines merely reflect the trend of the data in temperature regions where nonexponential decays are observed.

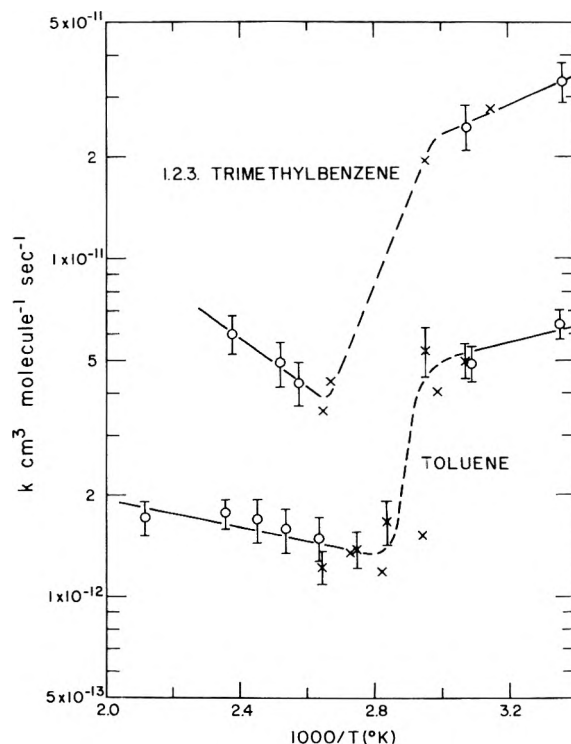


**Figure 5.** Arrhenius plots of  $\log k$  against  $1000/T$  for toluene and 1,2,3-trimethylbenzene: (O) exponential OH radical decays observed; (X) nonexponential OH radical decays observed. The dashed lines merely reflect the trend of the data in temperature regions where nonexponential decays are observed.

text regarding supplementary material) and shown in Figures 4–7 are the estimated overall error limits, which, for method (a), include the least-squares standard devi-

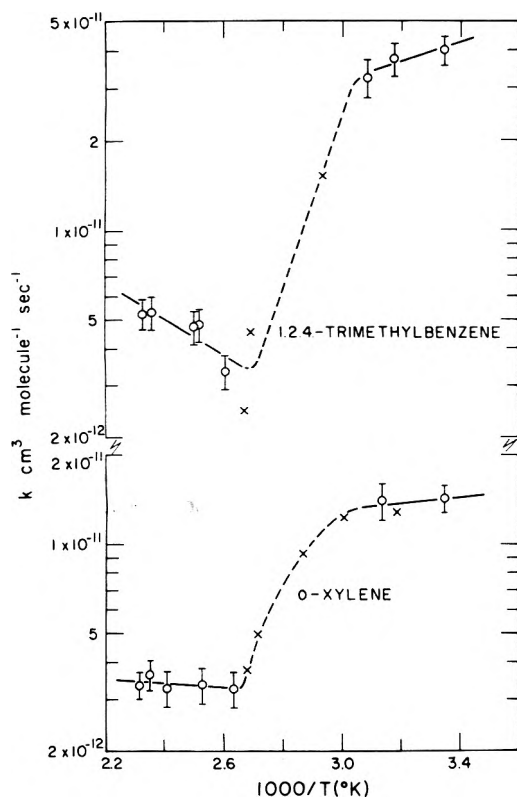


**Figure 6.** Arrhenius plots of  $\log k$  against  $1000/T$  (°K) for *o*-xylene and 1,2,4-trimethylbenzene: (O) exponential OH radical decays observed; (X) nonexponential OH radical decays observed. The dashed lines merely reflect the trend of the data in temperature regions where nonexponential decays are observed.

ations (1–7%) as well as the estimated accuracy limits of other parameters such as total pressure and the aromatic hydrocarbon concentrations in the reactant mixture. In all cases using method (a), the experimental decay rates in the range typically used for method (b) ( $R \geq 200 \text{ s}^{-1}$ ) were within 5% of those calculated from least-squares analysis of the data. Hence this spread is indicative of the random errors associated with method (b), and is included in the overall error limits for method (b) (Table I and Figures 4–7). For benzene at temperatures  $\geq 380 \text{ K}$  the experimental conditions were limited by the low rate constants so that the OH decay rates were  $< 100 \text{ s}^{-1}$  and hence the error limits for benzene above  $\sim 380 \text{ K}$  are much higher than those for the other aromatic hydrocarbons.

For the reaction of OH radicals with toluene, additional experiments were carried out to verify the observed behavior. A variation in the flash energy by a factor of 2 had no effect on the rate constants within the experimental errors, indicating that secondary reactions of the OH radicals with reaction products were negligible, as expected from the initial OH concentrations ( $\sim 10^{11} \text{ molecule cm}^{-3}$ ) and the aromatic hydrocarbon concentrations used. Similarly, an increase in the total pressure (argon diluent) from  $100 \pm 2$  to  $200 \pm 2$  Torr at 325.3, 378.4, and 424.4 K had no effect on the rate constants within the experimental errors ( $\pm 5$ –10%) when the OH decay rates at 325.3 and 378.4 K were determined from the initial OH decays. Furthermore, the addition of 2.0 Torr of  $\text{O}_2$  at 397.4 K and 2.3 Torr of  $\text{O}_2$  at 352.6 K had no effect (within  $\pm 10$ –15%) on the rate constants. In these cases the presence of  $\text{O}_2$  markedly reduced the OH resonance fluorescence signal, presumably due to quenching of the  $\text{OH}(A^2\Sigma^+)$  state. Less extensive rate data for the reaction of OH radicals with toluene- $d_8$  showed similar behavior. Thus the rate constant at room temperature was within 5% of that for

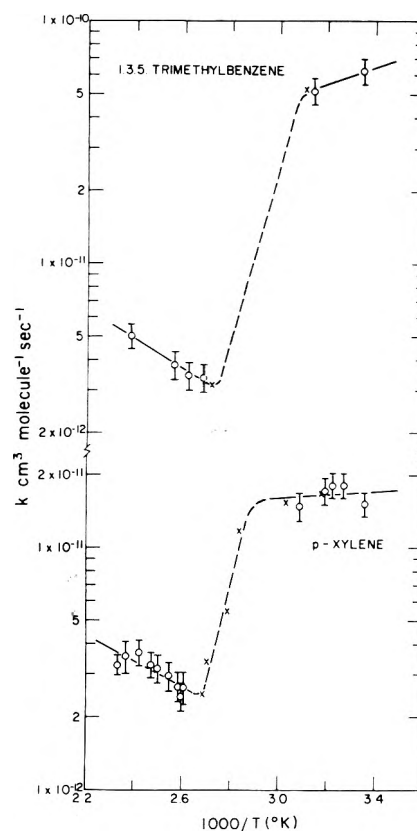


**Figure 7.** Arrhenius plots of  $\log k$  against  $1000/T$  (°K) for *p*-xylene and 1,3,5-trimethylbenzene: (O) exponential OH radical decays observed; (X) nonexponential OH radical decays observed. The dashed lines merely reflect the trend of the data in temperature regions where nonexponential decays are observed.

toluene, while the rate constant determined for toluene- $d_8$  at 432.2 K was a factor of 2.5 lower than that for toluene at 424.4 K. The rate constants obtained for toluene- $d_8$  are given in Table I, while Figure 3 shows plots of the OH decay rate against toluene and toluene- $d_8$  at room temperature and at  $\sim 428 \text{ K}$ .

Table I gives the rate constants obtained at the temperatures used for the aromatic hydrocarbons studied, while Figures 4–7 show the data plotted in Arrhenius form. The solid lines for  $\leq 325 \text{ K}$  and for  $\geq 380 \text{ K}$  were obtained from least-squares fitting of the data in these temperature regimes, while the dashed lines between these temperature regions merely reflect the trend of the data.

## Discussion

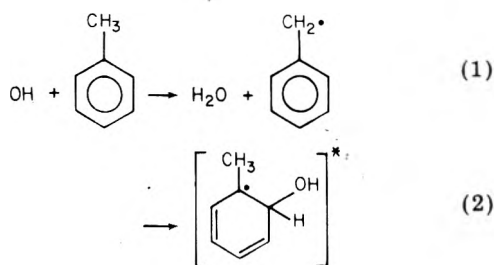
From the initial OH radical concentrations and the aromatic hydrocarbon concentrations used, it can be estimated<sup>4</sup> that errors in the measured rate constants due to reaction of OH radicals with reaction products would be typically  $< 5$ –10%, using an assumed rate constant of  $10^{-10} \text{ cm}^3 \text{ molecule}^{-1} \text{ s}^{-1}$  for the reaction of OH radicals with all reaction products. This conclusion was substantiated by the fact that a variation of a factor of 2 in the flash energy had no effect, within the experimental errors, on the rate constants. Similarly, the reaction of OH radicals with reactant impurities can be calculated to cause errors in the measured rate constants of  $\leq 5\%$ .

**Kinetics and Mechanism.** For the reactions of OH radicals with an aromatic hydrocarbon the initial reaction can be (using toluene as an example) either abstraction (reaction 1) or addition to the aromatic ring (reaction 2). The rate constants  $k$  obtained for benzene and the substituted benzenes at temperatures of  $\sim 380$ –470 K indicate (see below) that at these temperatures H atom abstraction

TABLE II: Comparison of the Room Temperature Rate Constants,  $k$ , for the Reaction of OH Radicals with Aromatic Hydrocarbons from the Present Work with Literature Values

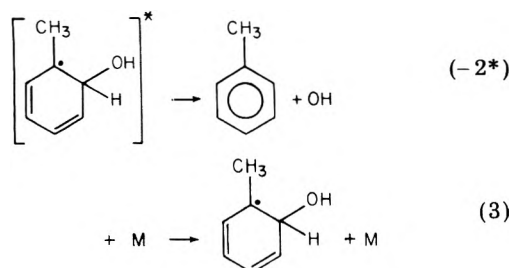
Aromatic hydrocarbon	$10^{12}k \text{ cm}^3 \text{ molecule}^{-1} \text{ s}^{-1}$					
	This work <sup>a</sup>	Ref 4 <sup>b</sup>	Ref 5 <sup>c</sup>	Ref 6 <sup>c</sup>	Ref 3 <sup>d</sup>	Ref 14 <sup>e</sup>
Benzene	$1.20 \pm 0.15$	$1.24 \pm 0.12$	$\leq 3.8$		$1.59 \pm 0.12$	
Toluene	$6.40 \pm 0.64$	$5.78 \pm 0.58$	$4.2 \pm 1.5$		$6.11 \pm 0.40$	
Toluene- $d_8$	$6.13 \pm 0.63$					
<i>o</i> -Xylene	$14.3 \pm 1.5$	$15.3 \pm 1.5$	$12.8 \pm 3.8$			} 18.7
<i>m</i> -Xylene	$24.0 \pm 2.5$	$23.6 \pm 2.4$	$23.2 \pm 1.7$	$21.5 \pm 4.3$		
<i>p</i> -Xylene	$15.3 \pm 1.7$	$12.2 \pm 1.2$	$12.3 \pm 2.5$			
1,2,3-Trimethylbenzene	$33.3 \pm 4.5$	$26.4 \pm 2.6$	$23 \pm 5$			
1,2,4-Trimethylbenzene	$40.0 \pm 4.5$	$33.5 \pm 3.4$	$33 \pm 5$			
1,3,5-Trimethylbenzene	$62.4 \pm 7.5$	$47.2 \pm 4.8$	$51.5 \pm 6.5$			

<sup>a</sup> Total pressure  $100 \pm 2$  Torr (Ar). <sup>b</sup> Total pressure  $\geq 50$  Torr (Ar). <sup>c</sup> Total pressure 1 atm of air at  $304 \pm 1$  K (ref 5) or  $305 \pm 2$  K (ref 6); rate constants placed on an absolute basis using a rate constant for OH + *n*-butane of  $3.0 \times 10^{-12} \text{ cm}^3 \text{ molecule}^{-1} \text{ s}^{-1}$ . <sup>d</sup> Total pressure 100 Torr (He). <sup>e</sup> Total pressure  $\sim 1$  Torr (He), mixture of isomers.

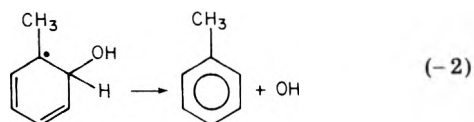


occurs mainly from the substituent  $\text{CH}_3$  groups rather than from the aromatic ring. Addition of the OH radical is shown for attack at the ortho position by analogy with the reaction of  $\text{O}(^3\text{P})$  atoms with aromatic hydrocarbons;<sup>9-11</sup> obviously addition of OH radicals may occur at any of the carbon atoms of the aromatic ring, forming a variety of OH-aromatic adducts which initially contain the excess energy due to the exothermicity of the reaction.

Such an energy-rich OH-aromatic adduct can either decompose or be stabilized, as was observed by Davis, Bollinger, and Fischer<sup>3</sup> for benzene and toluene:



A further reaction step is that the *thermalized* OH-aromatic adduct could unimolecularly decompose back to the reactants



However, it is also possible that the initial reaction could involve the formation of a  $\pi$  complex, which could either decompose back to the reactants or evolve to a  $\sigma$  bonded OH-aromatic adduct such as shown above.

An analogous reaction system has been studied by Majer, Phillips, and Robb<sup>12</sup> who investigated the reaction of  $\text{CF}_2\text{Cl}$  radicals with benzene. The  $\text{CF}_2\text{Cl}$ -benzene adduct was observed to decompose back to reactants above 373 K with an activation energy of  $11.4 \pm 0.8 \text{ kcal mol}^{-1}$ , while the activation energy for the addition of  $\text{CF}_2\text{Cl}$  radicals to benzene was determined to be  $5.3 \pm 0.4 \text{ kcal mol}^{-1}$ . Similar results were obtained for the reaction of  $\text{CF}_2\text{Cl}$  radicals with benzene- $d_6$ ,<sup>13</sup> for which an activation

energy for the decomposition of the adduct of  $10.7 \pm 0.4 \text{ kcal mol}^{-1}$  was obtained.

In a previous determination<sup>4</sup> of the rate constants for the reaction of OH radicals with a series of aromatic hydrocarbons, it was observed that the rate constants for benzene and toluene were independent of the total pressure (argon diluent) over the ranges 50–600 and 100–620 Torr, respectively. This was in agreement with the data of Davis, Bollinger, and Fischer<sup>3</sup> who observed a pressure dependence of  $k$  for benzene and toluene over the range 3–100 Torr of helium, but concluded from Lindemann plots that the rate constants measured at 100 Torr of helium were essentially the high pressure limiting values. Davis, Bollinger, and Fischer<sup>3</sup> deduced from this pressure dependence that over half of the total reaction at room temperature proceeds via addition ( $k_2 > k_1$ ).

Table II compares the present room temperature rate constants  $k$  with literature values.<sup>3-6,14</sup> It can be seen that the agreement with the literature data is generally good and that the present rate constants are in general agreement, within the experimental error limits, with those obtained previously<sup>4</sup> in this laboratory. The agreement between the rate constants from this and the previous study<sup>4</sup> for benzene, toluene, and *o*- and *m*-xylene is seen to be excellent. The present rate constants for *p*-xylene and 1,2,3-, 1,2,4-, and 1,3,5-trimethylbenzene are, however,  $\sim 20$ –30% higher than those determined previously,<sup>4</sup> and this may reflect a systematic error in the previous calibration of the aromatic absorption, which was weak under the conditions used. The somewhat increased overall error limits quoted in the present work (10–14%) take into account more realistically the higher errors associated with such calibrations. However, the reproducibility of the data from the two studies is indicative of the likely overall error limits as the studies were performed independently, with complete recalibrations of flowmeters and the absorption cell-Cary 15 spectrophotometer combination.

The fact that the previous<sup>4</sup> and present absolute rate constants  $k$  for the xylenes determined at  $\sim 100$  Torr total pressure of argon are consistent with that obtained by Morris and Niki<sup>14</sup> for a mixture of isomers at  $\sim 1$  Torr total pressure of helium shows that  $k$  for the xylenes must be at, or close to, the limiting high pressure region at  $\sim 1$  Torr total pressure. This is consistent with unimolecular theory which predicts that the falloff region should shift to lower total pressures as the complexity, or number of vibrational degrees of freedom, of the OH-aromatic adduct increases. As has been noted previously,<sup>4-6</sup> the rate constants  $k$  at room temperature show the same trend with degree and position of alkylation as for  $\text{O}(^3\text{P})$  atom reaction,<sup>8</sup> demonstrating the electrophilic character of the OH radical. This further suggests that at room temperature the major

reaction path is one of addition to the aromatic ring.

The lack of a dependence of  $k$  for toluene on total pressure of argon over the range 100–200 Torr at 325.3, 378.4, and 424.4 K in the present work further indicates that the initially energy rich OH–toluene adduct is rapidly thermalized under these conditions.

The experimental results are thus consistent with the occurrence of reactions 1–3 with the OH–aromatic adducts being stable within the time frame of the OH radical observations ( $\sim 1$ –30 ms) at room temperature, and being unstable for temperatures  $\geq 380$  K. Hence at room temperature the measured rate constants are those for both addition and abstraction,  $k = k_1 + k_2$ , while at  $\geq 380$  K only  $k_1$ , the rate constant for abstraction, is measured. These conclusions are confirmed from the reaction of OH radicals with toluene- $d_8$ : at room temperature the rate constant  $k$  for toluene- $d_8$  is within 5% of that for toluene, while at 432 K the rate constant for toluene- $d_8$  is a factor of  $\sim 2.5$  lower than that for toluene. These observations are in accord with mainly OH radical addition to the aromatic ring at room temperature, as a small isotope effect is expected for addition (thus rate constants at room temperature for the reactions of OH radicals with propylene- $d_6$ ,<sup>14,15</sup> of  $O_3$  with ethylene- $d_4$ <sup>16</sup> and propylene- $d_6$ ,<sup>16</sup> and of  $O(^3P)$  atoms with acetylene- $d_2$ ,<sup>17</sup> ethylene- $d_4$ ,<sup>18,19</sup> isobutene- $d_8$ ,<sup>20</sup> and benzene- $d_6$ <sup>21</sup> are all within  $\sim 20\%$  of those for the hydrogen isotope species). However, for abstraction a significant isotope effect is expected with the deuterium isotope reacting slower than the hydrogen isotope, as has been observed previously for the reaction of OH radicals with  $D_2$ <sup>22–24</sup> and  $DCI$ <sup>24</sup> as compared to  $H_2$  and  $HCl$ , respectively, and for the reaction of  $CH_3$  radicals with toluene- $\alpha$ - $d_3$ , toluene- $d_8$ , and toluene- $d_5$ .<sup>25</sup>

As the OH–aromatic adduct is deactivated to an essentially thermal energy population at the total pressures used in this study, then the rate constant  $k_2$  is given by

$$k_{-2} = A_{-2} e^{-E_{-2}/RT} \quad (IV)$$

With the present experimental technique OH radicals are monitored for  $\sim 1$ –30 ms after the flash. Significant nonexponentiality of the OH decay curves was observed at temperatures from  $\sim 325$  to 380 K and hence the half-life of the OH–aromatic adduct must be of the order of  $\sim 5$ –10 ms in this temperature range, corresponding to  $k_{-2} \sim 100 \text{ s}^{-1}$  at 350 K. For  $A_{-2} \sim 3 \times 10^{13} \text{ s}^{-1}$  (of the same order of magnitude as the  $A$  factors for decomposition of the cyclohexadienyl<sup>26</sup> and methylcyclohexadienyl radicals<sup>27</sup>) the activation energy for reaction  $-2$  can be calculated to be  $E_{-2} \approx 18 \text{ kcal mol}^{-1}$ . (Data for the individual aromatic hydrocarbons are given in Table V.) The initially formed OH–aromatic adduct will contain approximately this amount of excess energy and should thus be readily thermalized in a time scale shorter than 1–30 ms by  $\sim 100$  Torr of argon as argon has been shown to remove vibrational energy of the order of 1 kcal mol<sup>-1</sup> per collision with a number of photochemically and chemically activated molecules.<sup>28</sup>

From eq IV with  $A_{-2} = 3 \times 10^{13} \text{ s}^{-1}$  and  $E_{-2} = 18 \text{ kcal mol}^{-1}$  the half-lives of the OH–aromatic adduct can be estimated to be 0.37 s at 298 K, 29 ms at 325 K, 0.52 ms at 380 K, and 0.16 ms at 400 K. These values of  $A_{-2}$  and  $E_{-2}$  thus give half-lives of the OH–aromatic adducts which are totally consistent with both the reaction scheme discussed above and the experimental observations. Thus the temperatures at which the appearance of nonexponential behavior in the OH radical decays occur will depend on the technique used and the observational time scale employed. For instance, if the OH radicals were

TABLE III: Abstraction Rate Constants  $k_1$  and the Ratio  $k_1/(k_1 + k_2)$  for the Reaction of OH Radicals with Aromatic Hydrocarbons at Room Temperature

Aromatic hydrocarbon	$10^{12} k_1 \text{ cm}^3 \text{ molecule}^{-1} \text{ s}^{-1} \text{ }^a$	$k_1/(k_1 + k_2)$
Benzene	$0.06^{+0.10}_{-0.05}$	$0.05^{+0.08}_{-0.04}$
Toluene	$1.0^{+0.5}_{-0.3}$	$0.16^{+0.07}_{-0.05}$
Toluene- $d_8$	$\leq 0.5^b$	$\leq 0.08^b$
o-Xylene	$2.9^{+2.1}_{-1.4}$	$0.20^{+0.15}_{-0.10}$
m-Xylene	$0.9^{+0.4}_{-0.4}$	$0.04^{+0.03}_{-0.02}$
p-Xylene	$1.1^{+1.1}_{-0.5}$	$0.07^{+0.07}_{-0.03}$
1,2,3-Trimethylbenzene	$1.2^{+0.7}_{-0.8}$	$0.035^{+0.08}_{-0.02}$
1,2,4-Trimethylbenzene	$1.3^{+1.2}_{-0.4}$	$0.03^{+0.03}_{-0.01}$
1,3,5-Trimethylbenzene	$1.3^{+0.7}_{-0.6}$	$0.02^{+0.02}_{-0.01}$

<sup>a</sup> Extrapolated from  $T \geq 380$  to 298 K using the Arrhenius lines in Figures 4–7 and given in Table IV.

<sup>b</sup> Upper limit from the rate constants obtained at 432.2 and 298.1 K, as the rate constants for  $T > 380$  K increase with increasing temperature (Table I).

observed over a time scale of  $\sim 10$ –100  $\mu\text{s}$ , as is typically the case with flash photolysis-resonance absorption systems (rather than over the time scale  $\sim 1$ –30 ms used in the present work), then the low temperature onset of nonexponential behavior would move up from  $\sim 325$  to  $\sim 400$  K.

The rate constant data of Doyle et al.<sup>5</sup> and Lloyd et al.<sup>6</sup> are in good agreement with those obtained by the flash photolysis-resonance fluorescence techniques<sup>3,4</sup> showing that the OH–aromatic adduct must react, presumably with  $O_2$ , NO, or  $NO_2$ , in their system before decomposition. However, the present lack of an effect of  $O_2$  at 397.4 and 352.6 K allows an upper limit of  $1 \times 10^{-15} \text{ cm}^3 \text{ molecule}^{-1} \text{ s}^{-1}$  to be set, at these temperatures, for the apparent rate constant for the reaction of  $O_2$  with the OH–toluene adduct. However, the  $CH_3C_6H_5(OH)(O_2)$  radical may decompose at elevated temperatures which would give a low apparent rate constant for the addition of  $O_2$  to the OH–toluene adduct.

Table III gives room temperature values of  $k_1$ , obtained by extrapolation of the data above  $\sim 380$  K, and the fraction of the reaction proceeding via H (or D) atom abstraction,  $k_1/(k_1 + k_2)$ , for the aromatic hydrocarbons studied. It can be seen that the amount of reaction at room temperature proceeding via abstraction is of the order of 2–20% depending on the individual hydrocarbon. The values of  $k_1$  and  $k_1/(k_1 + k_2)$  given for benzene are subject to large uncertainties, but the extrapolated value of  $k_1 \approx (6^{+10}) \times 10^{-14} \text{ cm}^3 \text{ molecule}^{-1} \text{ s}^{-1}$  at 298 K can be compared with room temperature rate constants for the reaction of OH radicals with  $CH_4$  and  $NH_3$  of  $\sim 8 \times 10^{-15}$ <sup>29–35</sup> and  $\sim 1.6 \times 10^{-13} \text{ cm}^3 \text{ molecule}^{-1} \text{ s}^{-1}$ ,<sup>36–41</sup> respectively.  $CH_4$  and  $NH_3$  have C–H and N–H bond energies of  $104 \pm 1$  and  $110 \pm 2 \text{ kcal mol}^{-1}$ , respectively,<sup>42</sup> compared to  $110.2 \pm 2.0 \text{ kcal mol}^{-1}$  for the C–H bond energy in benzene,<sup>42</sup> and hence a rate constant  $k_1$  of the magnitude observed is reasonably in line with the respective bond energies. For the alkylated benzenes, other than toluene- $d_8$ , the rate constants  $k_1$  at 298 K are much larger than  $k_1$  for benzene, which is to be expected due to the lower C–H bond energies in the methyl groups [ $(85 \pm 1) \text{ kcal mol}^{-1}$  for  $C_6H_5CH_2-H$ ].<sup>42</sup> For the temperature ranges used in this study, abstraction from these alkylated aromatic hydrocarbons occurs, as can be seen from the data in Table I and Figures 4–7, mainly from the substituent  $CH_3$  groups rather than from the aromatic ring due to the differences in C–H bond energies.

Table IV gives the Arrhenius parameters for reactions 1 and 2 for the temperature ranges  $298 \text{ K} < T \leq 325 \text{ K}$  and  $T \geq 380 \text{ K}$  as determined from the data in Table I and

TABLE IV: Arrhenius Parameters for the Reaction of OH Radicals with a Series of Aromatic Hydrocarbons<sup>a</sup>

Aromatic hydrocarbon	$12 + \log A_1$ (cm <sup>3</sup> molecule <sup>-1</sup> s <sup>-1</sup> )	$E_1$ , kcal mol <sup>-1</sup>	$13 + \log A_2$ (cm <sup>3</sup> molecule <sup>-1</sup> s <sup>-1</sup> )	$E_2$ , kcal mol <sup>-1</sup>
Benzene	1.6 ± 1.6	4 ± 3	1.7 ± 0.7	0.9 ± 1.0
Toluene	0.7 ± 0.5	0.9 ± 1.0	0.5 ± 0.7	-1.6 ± 1.0
<i>o</i> -Xylene	0.7 ± 0.8	0.3 ± 1.5	1.6 ± 1.4	-0.7 ± 2.0
<i>m</i> -Xylene	1.7 ± 0.8	2.3 ± 1.5	2.3 ± 1.4	-0.1 ± 2.0
<i>p</i> -Xylene	1.8 ± 0.8	2.4 ± 1.5	1.8 ± 0.7	-0.6 ± 1.0
1,2,3-Trimethylbenzene	2.5 ± 1.3	3.3 ± 2.5	0.8 ± 1.4	-2.3 ± 2.0
1,2,4-Trimethylbenzene	2.2 ± 0.8	2.8 ± 1.5	1.3 ± 1.4	-1.7 ± 2.0
1,3,5-Trimethylbenzene	2.1 ± 0.8	2.7 ± 1.5	1.6 ± 1.4	-1.7 ± 2.0

<sup>a</sup> The indicated errors are the estimated overall error limits derived from Figures 4-7.

TABLE V: Activation Energies for Reactions 2 and -2 and Heats of Formation  $\Delta H_f$  for the OH-Aromatic and CF<sub>2</sub>Cl-Aromatic Adducts

Aromatic hydrocarbon	$E_2$ , kcal mol <sup>-1</sup>	$E_{-2}$ , <sup>a</sup> kcal mol <sup>-1</sup>	Aromatic hydrocarbon <sup>b</sup>	$\Delta H_f$ , kcal mol <sup>-1</sup>	
				OH-aromatic adduct	OH-CF <sub>2</sub> Cl adduct
				Expt <sup>c</sup>	Calcd <sup>d</sup>
Benzene	0.9 ± 1	18.7 ± 2	19.82 ± 0.12	10.5 ± 3	11.8
Toluene	-1.6 ± 1	18.1 ± 2	11.95 ± 0.15	0.8 ± 3	1.5
<i>o</i> -Xylene	-0.7 ± 2	18.4 ± 2	4.54 ± 0.26	-6.1 ± 4	-6.8
<i>m</i> -Xylene	-0.1 ± 2	17.9 ± 2	4.12 ± 0.18	-5.4 ± 4	-6.8
<i>p</i> -Xylene	-0.6 ± 1	18.7 ± 2	4.29 ± 0.24	-6.5 ± 3	-6.4
1,2,3-Trimethylbenzene	-2.3 ± 2	18.6 ± 2	-2.29 ± 0.30	-14.7 ± 4	-14.7
1,2,4-Trimethylbenzene	-1.7 ± 2	18.3 ± 2	-3.33 ± 0.27	-14.8 ± 4	-15.0
1,3,5-Trimethylbenzene	-1.7 ± 2	18.1 ± 2	-3.84 ± 0.34	-15.1 ± 4	-14.7
				OH-CF <sub>2</sub> Cl adduct	
				Expt <sup>f</sup>	Calcd <sup>d</sup>
Benzene	5.3 ± 0.4 <sup>e</sup>	11.4 ± 0.8 <sup>e</sup>	19.82 ± 0.12	-51.3 ± 2	-51.1

<sup>a</sup>  $E_{-2}$  obtained using  $A_{-2} = 3 \times 10^{13} \text{ s}^{-1}$ ,  $k_{-2} = 100 \text{ s}^{-1}$  at the temperature corresponding to the midpoint of the dashed lines in Figures 4-7. Indicated error limits are equivalent to a factor of 100 in  $A_{-2}/k_{-2}$  at the temperature of the midpoint of the dashed lines of Figures 4-7. <sup>b</sup> Reference 56. <sup>c</sup> Calculated using  $\Delta H_f(\text{OH}) = 9.2 \pm 1 \text{ kcal mol}^{-1}$ <sup>42</sup> and  $\Delta H_f(\text{OH-aromatic adduct}) = \Delta H_f(\text{aromatic}) + \Delta H_f(\text{OH}) - (E_{-2} - E_2 + RT)$ . <sup>d</sup> Calculated from group additivity rules, using a stabilization energy for the radical of 16.5 kcal mol<sup>-1</sup>. The calculated values of  $\Delta H_f$  refer to the following cyclohexadienyl radicals: for toluene, 1-methyl-2-hydroxy; *o*-xylene, 1,2-dimethyl-3-hydroxy; *m*-xylene, 1,3-dimethyl-2-hydroxy; *p*-xylene, 1,4-dimethyl-2-hydroxy; 1,2,3-trimethylbenzene, 1,2,3-trimethyl-4-hydroxy; 1,2,4-trimethylbenzene, 1,2,4-trimethyl-3-hydroxy; 1,3,5-trimethylbenzene, 1,3,5-trimethyl-2-hydroxy. These radicals were obtained by assuming that OH radical attack occurs ortho to the substituent methyl groups, analogous to O(<sup>3</sup>P) atom reactions.<sup>9-11</sup> <sup>e</sup> Reference 12. <sup>f</sup> Calculated using  $\Delta H_f(\text{CF}_2\text{Cl}) = -64.3 \pm 2 \text{ kcal mol}^{-1}$ .<sup>57</sup>

Figures 4-7. Because of the small temperature ranges in each region the error limits are large and extrapolation outside of the quoted temperature ranges will give large uncertainties in the values obtained. Discussion of the individual values of the preexponential factors and Arrhenius activation energies has little merit in view of the large error limits, except to point out that reaction 1 has in all cases a positive activation energy of ~0-4 kcal mol<sup>-1</sup>, while reaction 2 has, except in the case of benzene, an essentially zero or slightly negative temperature dependence, as has been previously observed for the addition of O(<sup>3</sup>P)<sup>43-46</sup> and S(<sup>3</sup>P)<sup>47</sup> atoms, and OH radicals,<sup>48-51</sup> to olefins. It can also be seen from Table I and Figures 4-7 that at ~380-470 K the values of  $k_1$  obtained increase approximately linearly with the number of substituent methyl groups, being similar for the three xylenes and for the three trimethylbenzenes.

**Thermochemistry.** Knowing the activation energies for reactions 2 and -2, the heats of formation of the OH-aromatic adducts can be obtained as<sup>52</sup>

$$\Delta H_f(\text{OH-aromatic adduct}) = \Delta H_f(\text{aromatic}) + \Delta H_f(\text{OH}) - \Delta H_2$$

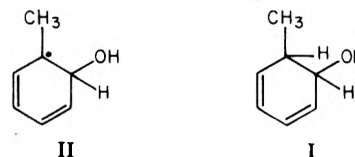
where  $\Delta H_2$  is the enthalpy of reaction 2 and

$$\Delta H_2 = E_{-2} - E_2 + RT$$

where  $E_{-2}$  and  $E_2$  are the activation energies for reactions -2 and 2, respectively. Except for benzene, the experi-

mental Arrhenius activation energies for reaction 2 are zero or negative. However, the observed Arrhenius activation energies are not necessarily equivalent to the activation energies  $E_2$  for the addition reaction as the preexponential factors may be temperature dependent<sup>43-45,47,49-51,53</sup> and it is in fact likely that observed negative temperature dependencies have a zero activation energy with a temperature-dependent preexponential factor. In the absence of a knowledge of any temperature dependence of the preexponential factors for reaction 2 the activation energies  $E_2$  have been set equal to the experimental Arrhenius activation energies for reaction 2.

Table V gives the Arrhenius activation energies  $E_2$  and  $E_{-2}$  used, together with the experimental and calculated heats of formation  $\Delta H_f$  of the OH-aromatic adduct. The calculated values of  $\Delta H_f$  (OH-aromatic adduct) were obtained as follows (using II as an example):  $\Delta H_f$  of I was



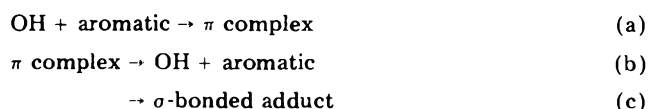
calculated using group additivity rules,<sup>52</sup> and that for the radical II was derived from<sup>27,52</sup>

$$\Delta H_f(\text{II}) = \Delta H_f(\text{I}) + D(\text{tertiary C-H}) - \Delta H_f(\text{H}) - \text{SE}$$

where  $D$ (tertiary C–H) is the tertiary C–H bond energy and SE is the stabilization energy of radical II.

Table V shows that there is good agreement between calculated and experimental values of  $\Delta H_f$ (OH–aromatic adduct) within the experimental error limits of  $\pm 3$  kcal mol<sup>-1</sup> using a best fit value of the stabilization energy of 16.5 kcal mol<sup>-1</sup>. Furthermore, as also shown in Table V, the data of Majer, Phillips, and Robb<sup>12</sup> on the addition of CF<sub>2</sub>Cl radicals to benzene ( $E = 5.3 \pm 0.4$  kcal mol<sup>-1</sup>) and the decomposition of the CF<sub>2</sub>Cl–benzene adduct ( $E = 11.4 \pm 0.8$  kcal mol<sup>-1</sup>) at  $\geq 373$  K leads to equally good agreement between calculated and experimental values of  $\Delta H_f$  for the CF<sub>2</sub>Cl–benzene radical using SE = 16.5 kcal mol<sup>-1</sup>. Hence the present work leads to a stabilization energy for these substituted cyclohexadienyl radicals of  $16.5 \pm 5$  kcal mol<sup>-1</sup> where the error limit includes the experimental error limits as well as an estimate of  $\pm 2$  kcal mol<sup>-1</sup> for the calculated values of  $\Delta H_f$ (OH–aromatic adduct).

This stabilization energy is very close to the value of  $15.4 \pm 1$  kcal mol<sup>-1</sup> obtained for the pentadienyl radical by Egger and Benson.<sup>54</sup> However, James and Suart<sup>26</sup> reported a stabilization energy for the cyclohexadienyl radical of 25 kcal mol<sup>-1</sup> from a study of mutual interaction and thermal decomposition of cyclohexadienyl radicals, while Shaw, Cruickshank, and Benson<sup>55</sup> quote a value of  $24.6 \pm 0.7$  kcal mol<sup>-1</sup>. It has been suggested<sup>12,26</sup> that the temperature dependence of the addition of CF<sub>2</sub>Cl to benzene can be interpreted as a  $\pi$  complex which could either dissociate back to the reactants or evolve to a more closely bonded  $\sigma$  complex. If the addition of OH radicals to aromatic hydrocarbons proceeds via  $\pi$  complex formation



and if back dissociation to reactants is rapid at room temperature, the observed  $\sim 18$  kcal mol<sup>-1</sup> activation energy for decomposition must refer to the  $\sigma$ -bonded complex. However, if  $k_b \gg k_c$  the observed activation energy of addition is given by ( $E_a + E_c - E_b$ ) and would not refer to the reverse of reaction -2. However, if the 18 kcal mol<sup>-1</sup> decomposition activation energy refers to the  $\pi$  complex, then both  $k_b$  and  $k_c$  must be slow at room temperature and the activation energy of addition is given by  $E_a$ . In this case the  $\pi$  complex would be a stable entity (only some 8–10 kcal mol<sup>-1</sup> less stable than the  $\sigma$ -bonded adduct, calculated using a stabilization energy of the  $\sigma$ -bonded adduct of 25 kcal mol<sup>-1</sup>).<sup>26,55</sup>

Obviously, further work is needed to more precisely determine such stabilization energies, in view of the rather substantial uncertainties inherent in the present determinations.

## Conclusions

The reaction of OH radicals with a series of aromatic hydrocarbons proceeds via two pathways: (a) abstraction of an H atom from the aromatic ring or (except for benzene) from the substituent CH<sub>3</sub> groups, and (b) addition to the aromatic ring to form an adduct which is readily thermalized at total pressures of  $\sim 100$  Torr of argon but which can, in the absence of other competing reactions, decompose back to reactants at  $\geq 325$  K in the time scale  $\leq 30$  ms. For substituted benzenes, the rate constants extrapolated to room temperature for abstraction show (Table III) that abstraction occurs mainly from the CH<sub>3</sub> groups at room temperature but that abstraction from the ring becomes more important at elevated temperatures.

The present data enable an estimate of  $16.5 \pm 5$  kcal mol<sup>-1</sup> to be made for the stabilization energy of the OH–aromatic (or CF<sub>2</sub>Cl–benzene) adducts, which is lower than previously reported values of  $\sim 25$  kcal mol<sup>-1</sup><sup>26,55</sup> but is close to the stabilization energy reported for the pentadienyl radical.<sup>54</sup>

At room temperature under simulated atmospheric conditions the OH–aromatic adduct reacts further, presumably with O<sub>2</sub>, NO, or NO<sub>2</sub>, as shown by the good agreement between the rate constants obtained from relative rate studies in an environmental chamber<sup>5,6</sup> with those obtained by flash photolysis-resonance fluorescence.<sup>3,4</sup> However, at elevated temperatures (for instance,  $\geq 400$  K) it appears that, unless the adduct can react further in  $\leq 1$  ms, the reaction will proceed via abstraction on account of the short lifetime of the OH–aromatic adduct with respect to decomposition back to reactants.

**Acknowledgment.** The authors gratefully acknowledge the financial support of NSF Grants MPS73-08638-A03 and CHE 76-10447 and thank Dr. A. C. Lloyd and Dr. W. P. L. Carter for helpful discussions.

**Supplementary Material Available:** Table I containing rate constants obtained at the temperatures used for the aromatic hydrocarbons studied (6 pages). Ordering information is available on any current masthead page.

## References and Notes

- (1) M. C. Dodge, Workshop on Mathematical Modeling of Photochemical Smog, Summary Proceedings, Report EPA-R4-73-010, Environmental Protection Agency, Washington, D.C., 1973.
- (2) B. J. Finlayson and J. N. Pitts, Jr., *Science*, **192**, 111 (1976).
- (3) D. D. Davis, W. Bollinger, and S. Fischer, *J. Phys. Chem.*, **79**, 293 (1975).
- (4) D. A. Hansen, R. Atkinson, and J. N. Pitts, Jr., *J. Phys. Chem.*, **79**, 1763 (1975).
- (5) G. J. Doyle, A. C. Lloyd, K. R. Darnall, A. M. Winer, and J. N. Pitts, Jr., *Environ. Sci. Technol.*, **9**, 237 (1975).
- (6) A. C. Lloyd, K. R. Darnall, A. M. Winer, and J. N. Pitts, Jr., *J. Phys. Chem.*, **80**, 789 (1976).
- (7) R. Atkinson, D. A. Hansen, and J. N. Pitts, Jr., *J. Chem. Phys.*, **62**, 3284 (1975); **63**, 1703 (1975).
- (8) R. Atkinson and J. N. Pitts, Jr., *J. Phys. Chem.*, **78**, 1780 (1974).
- (9) G. R. H. Jones and R. J. Cvetanovic, *Can. J. Chem.*, **39**, 2444 (1961).
- (10) E. Grovenstein, Jr., and A. J. Mosher, *J. Am. Chem. Soc.*, **92**, 3810 (1970).
- (11) J. S. Gaffney, R. Atkinson, and J. N. Pitts, Jr., *J. Am. Chem. Soc.*, **98**, 1828 (1976).
- (12) J. R. Majer, D. Phillips, and J. C. Robb, *Trans. Faraday Soc.*, **61**, 110 (1965).
- (13) J. R. Majer, D. Phillips, and J. C. Robb, *Trans. Faraday Soc.*, **61**, 122 (1965).
- (14) E. D. Morris, Jr., and H. Niki, *J. Phys. Chem.*, **75**, 3640 (1971).
- (15) F. Stuhl, *Ber. Bunsenges, Phys. Chem.*, **77**, 674 (1973).
- (16) S. M. Japar, C. H. Wu, and H. Niki, *J. Phys. Chem.*, **78**, 2318 (1974).
- (17) F. Stuhl and H. Niki, *J. Chem. Phys.*, **55**, 3954 (1971).
- (18) F. Stuhl and H. Niki, *J. Chem. Phys.*, **57**, 5403 (1972).
- (19) M. J. Kurylo and R. E. Huie, *J. Chem. Phys.*, **58**, 1258 (1973).
- (20) J. J. Havel and C. J. Hunt, *J. Phys. Chem.*, **80**, 779 (1976).
- (21) R. A. Bonanno, P. Kim, J. H. Lee, and R. B. Timmons, *J. Chem. Phys.*, **57**, 1377 (1972).
- (22) N. R. Greiner, *J. Chem. Phys.*, **48**, 1413 (1968).
- (23) F. Stuhl and H. Niki, *J. Chem. Phys.*, **57**, 3671 (1972).
- (24) I. W. M. Smith and R. Zellner, *J. Chem. Soc., Faraday Trans. 2*, **70**, 1045 (1974).
- (25) M. Cher, *J. Phys. Chem.*, **68**, 1316 (1964).
- (26) D. G. L. James and R. D. Suart, *Trans. Faraday Soc.*, **64**, 2752 (1968).
- (27) A. Amano, O. Horie, and N. H. Hanh, *Int. J. Chem. Kinet.*, **8**, 321 (1976).
- (28) S. W. Orchard and B. A. Thrush, *Proc. R. Soc. London, Ser. A*, **329**, 233 (1972), and references therein.
- (29) W. E. Wilson and A. A. Westenberg, *Symp. (Int.) Combust. [Proc.]*, **11th**, 1966, 1143 (1967).
- (30) N. R. Greiner, *J. Chem. Phys.*, **53**, 1070 (1970).
- (31) D. D. Davis, S. Fischer, and R. Schiff, *J. Chem. Phys.*, **61**, 2213 (1974).
- (32) J. J. Margitan, F. Kaufman, and J. G. Anderson, *Geophys. Res. Lett.*, **1**, 80 (1974).
- (33) R. P. Overend, G. Paraskevopoulos, and R. J. Cvetanovic, *Can. J. Chem.*, **53**, 3374 (1975).
- (34) C. J. Howard and K. M. Evenson, *J. Chem. Phys.*, **64**, 197 (1976).
- (35) R. Zellner and W. Steinert, *Int. J. Chem. Kinet.*, **8**, 397 (1976).

- (36) F. Stuhl, *J. Chem. Phys.*, **59**, 635 (1973).  
 (37) R. Zellner and I. W. M. Smith, *Chem. Phys. Lett.*, **26**, 72 (1974).  
 (38) I. W. M. Smith and R. Zellner, "Symposium on Chemical Kinetics Data for the Lower and Upper Atmosphere", Warrenton, Va., Sept 1974; *Int. J. Chem. Kinet., Symp.*, **1**, 341 (1975).  
 (39) W. Hack, K. Hoyerman, and H. Gg. Wagner, *Ber. Bunsenges. Phys. Chem.*, **78**, 386 (1974).  
 (40) R. A. Cox, R. G. Derwent, and P. M. Holt, *Chemosphere*, **4**, 201 (1975).  
 (41) R. A. Perry, R. Atkinson, and J. N. Pitts, Jr., *J. Chem. Phys.*, **64**, 3237 (1976).  
 (42) J. A. Kerr, M. J. Parsonage, and A. F. Trotman-Dickenson, "Strengths of Chemical Bonds", in "Handbook of Chemistry and Physics", 56th ed, The Chemical Rubber Company, Cleveland, Ohio, 1975-1976.  
 (43) D. D. Davis, R. E. Huie, and J. T. Herron, *J. Chem. Phys.*, **59**, 628 (1973).  
 (44) D. L. Singleton, S. Furuyama, R. J. Cvetanovic, and R. S. Irwin, *J. Chem. Phys.*, **63**, 1003 (1975).  
 (45) J. S. Gaffney, R. Atkinson, and J. N. Pitts, Jr., *J. Am. Chem. Soc.*, **97**, 6481 (1975).  
 (46) D. L. Singleton and R. J. Cvetanovic, *J. Am. Chem. Soc.*, **98**, 6812 (1976).  
 (47) D. D. Davis and R. B. Klemm, *Int. J. Chem. Kinet.*, **5**, 841 (1973).  
 (48) N. R. Greiner, *J. Chem. Phys.*, **53**, 1284 (1970).  
 (49) R. Atkinson and J. N. Pitts, Jr., *J. Chem. Phys.*, **63**, 3591 (1975).  
 (50) R. Atkinson, R. A. Perry, and J. N. Pitts, Jr., *Chem. Phys. Lett.*, **38**, 607 (1976).  
 (51) R. Atkinson, R. A. Perry, and J. N. Pitts, Jr., *J. Chem. Phys.*, in press.  
 (52) S. W. Benson, "Thermochemical Kinetics: Methods for the Estimation of Thermochemical Data and Rate Parameters", Wiley, New York, N.Y., 1968.  
 (53) R. Atkinson and R. J. Cvetanovic, *J. Chem. Phys.*, **56**, 432 (1972).  
 (54) K. N. Egger and S. W. Benson, *J. Am. Chem. Soc.*, **88**, 241 (1966).  
 (55) R. Shaw, F. R. Cruickshank, and S. W. Benson, *J. Phys. Chem.*, **71**, 4538 (1967).  
 (56) E. J. Prosen, W. H. Johnson, and F. D. Rossini, *J. Res. Natl. Bur. Stand.*, **36**, 455 (1946).  
 (57) L. M. Leyland, J. R. Majer, and J. C. Robb, *Trans. Faraday Soc.*, **66**, 898 (1970).

## Radiolysis of Adenine in Dilute Neutral Aqueous Solution

George Gorin,\* C. Lehman, C. A. Mannan, L. M. Raff, and S. E. Scheppele

Department of Chemistry, Oklahoma State University, Stillwater, Oklahoma 74074 (Received August 16, 1976)

Publication costs assisted by the National Institutes of Health

Solutions of adenine, 0.2 to 2 mM, have been radiolyzed at constant dose rate in air-equilibrated and in oxygen-saturated phosphate buffer, pH 7. The radiochemical decomposition yield is  $1.9, \pm 0.1$  molecules/(100 eV). The progress of the radiolysis was monitored by a highly specific colorimetric method for determining the adenine, and by measurements of the absorption spectrum at wavelengths between 290 and 220 nm. The results show that the radiolysis products absorb in the wavelength range investigated; this explains why previously reported values of  $G(-Ade)$ , which had been calculated from the rate of decrease of the absorbance with dose, are lower than that reported here. The spectra are unusual in that isobestic points develop at 280 and 238 nm and persist to >50% decomposition. Analysis by thin-layer chromatography and mass spectrometry shows that urea is one of the products, and it confirms the formation of 8-hydroxyadenine and of 4,6-diamino-5-formamidopyrimidine, which had been reported previously. None of these products interfere with the colorimetric determination of adenine.

### Introduction

This investigation is one of a series aimed at elucidating the chemical reactions that take place when ionizing radiation interacts with living organisms.<sup>1,2</sup> Our attention has been directed, in particular, to the bases which occur in DNA, inasmuch as this substance indubitably plays an important role in the development of radiation injuries.<sup>3</sup> A previous paper<sup>2</sup> describes our general approach and methods, and their application to the radiolysis of cytosine; here we report their extension to the radiolysis of adenine.

Adenine possesses an intense and fairly sharp absorption maximum at 260 nm, which decreases on irradiation. The changes can be easily measured with relatively good accuracy, and such measurements thus provide a very convenient means of following the progress of the reaction. This approach was first utilized by Scholes et al.,<sup>4</sup> who came to the conclusion that the products of radiolysis did not absorb at 260 nm; on that basis they calculated the radiolytic decomposition yield,  $G(-Ade)$ , to be 1.1 molecules/(100 eV).  $G$  values ranging from 0.65 to 1.2 have been reported subsequently by other investigators.<sup>5-7</sup>

However, these results are inconsistent with the reports that some of the radiation products have a substantial absorbance at 260 nm.<sup>5,6,8</sup> As we have shown in a previous paper,<sup>2</sup> if the products have an appreciable absorbance and this fact is neglected in calculating the value of  $G$  from spectrophotometric measurements, the result inevitably will be lower than the true value.

These considerations prompted us to reinvestigate the question, and to use a highly specific colorimetric method to determine the adenine.<sup>9</sup> Moreover, we undertook to measure the complete spectrum of the irradiated solutions, not only the absorbance at the maximum. The results show that the radiolysis products do indeed absorb at 260 nm, so that the decrease in absorbance does not measure the amount of adenine decomposed.

The spectra of the irradiated solutions exhibit a rather strange and interesting feature, namely, two isobestic points, at which the absorbance remains sensibly constant, to at least 50% decomposition. The development of one isobestic point at 236 nm had been noted earlier by Uliana and Creac'h,<sup>10</sup> but they did not offer an explanation of the phenomenon. We shall show what conditions are necessary for this phenomenon to develop.

### Experimental Section

Adenine (Sigma and Schwarz Biochemicals), [8-<sup>14</sup>C]-adenine (New England Nuclear), and isoguanine (Sigma) were commercial samples. 8-Hydroxyadenine and 4,6-diamino-5-formamidopyrimidine were synthesized.<sup>11</sup> The solutions were prepared in 0.05 M phosphate buffer, pH 7.0. The radiation source was a <sup>60</sup>Co Gammacell-200 (Atomic Energy of Canada); dose rates were 3300-2800 rads/min.<sup>12</sup>

The course of the radiolysis depended on the adenine/oxygen ratio. In air-equilibrated solutions, the

concentration of oxygen is about 0.25 mM, in solutions saturated with oxygen at 1 atm it is 1.3 mM.<sup>13</sup> The solutions containing 2 mM adenine were saturated with oxygen by bubbling the gas continuously through them, at the rate of 1–2 mL/s;<sup>14</sup> the spectra obtained under these conditions differed substantially from those which developed in initially air-equilibrated solutions without replenishing the oxygen. In solutions containing 0.2 mM adenine, the same results were obtained for air-equilibrated samples as in those saturated with oxygen. Usually, the volume of the irradiated samples was 5 mL, the surface area 2 cm<sup>2</sup>.

The adenine concentration was determined by the colorimetric method developed by Davis and Morris.<sup>9</sup> The procedure is as follows: to a 3-mL sample containing <3 μmol of adenine add 400 μL of 9 M H<sub>2</sub>SO<sub>4</sub>, shake, add 200 μL of 0.2 M KBr, shake again, add 600 μL of 0.2 M KMnO<sub>4</sub>, wait 5 min, remove excess MnO<sub>4</sub><sup>-</sup> with 200 μL of 6% H<sub>2</sub>O<sub>2</sub>, add some H<sub>2</sub>O, shake well to expel gas bubbles, adjust the volume to exactly 6.00 mL, and measure the absorbance within 15 min against a reagent blank. The adenine concentration is estimated from a calibration curve, which is established with the same reagents.

Chromatographic analysis of the radiolysis products was done on samples of 2 mM [8-<sup>14</sup>C]-adenine, 1–2 μCi/mL, which had been exposed to 135–800 krad. A microcrystalline cellulose plate; 10 × 10 cm, was used (Brinkmann Avicell Plate No. 22). A 50-μL aliquot of the irradiated solution was spotted on the plate, developed first with solvent system A (14:9:10 1-butanol:propanoic acid:H<sub>2</sub>O) and then orthogonally with system B (6:3:1 2-propanol:NH<sub>4</sub>OH:H<sub>2</sub>O).<sup>15</sup> The plate was radioautographed with GAF nonscreen X-ray film, exposed for 24–48 h. Finally, the radioactive spots were scraped off the plate and their radioactivity was measured with a Tri-Carb liquid scintillation counter (Packard Instrument Co., Model 3200).

The mass spectra were determined by evaporating a 1-μL aliquot of solution on a 3 × 5 cm stainless steel gauze, which was then introduced into the direct probe of the mass spectrometer (LKB, Model 9000). The temperature was raised from 25 to 250 °C, and the mass spectra were recorded at appropriate intervals; the nominal electron energy was 10 eV, the trap current 20 μA, and the ion-source temperature 180–230 °C.

## Results and Discussion

The basic equation which relates the initial absorbance of a solution of some substance S at wavelength λ, A<sub>0</sub><sup>λ</sup>, to the absorbance after some given dose, A<sub>D</sub><sup>λ</sup>, is

$$A_D^\lambda = A_0^\lambda - G(-S)E_V(\epsilon_S^\lambda - \epsilon_\Sigma^\lambda) \quad (1)$$

where G(-S) is the radiochemical yield for decomposition of S, E<sub>V</sub> the energy absorbed per unit volume, ε<sub>S</sub><sup>λ</sup> the molar absorption coefficient of S, and ε<sub>Σ</sub><sup>λ</sup> the "equivalent absorption coefficient" of the products U<sub>i</sub>:

$$\epsilon_\Sigma^\lambda = \sum_i G(U_i)\epsilon_i^\lambda / G(-S) \quad (2)$$

Clearly, G(-S) can be calculated from (1) for any wavelength at which ε<sub>Σ</sub><sup>λ</sup> = 0; and, conversely, if ε<sub>Σ</sub><sup>λ</sup> > 0, the fractional change in absorbance will define the lower limit to G(-S):

$$G(-S) > (A_0^\lambda - A_D^\lambda) / E_V \epsilon_S^\lambda \quad (3)$$

In order to interpret the spectra of a system in which only some, or possibly none, of the radiolysis products are known, the above relationships must be applied in reverse. If it is found experimentally that, over some wavelength

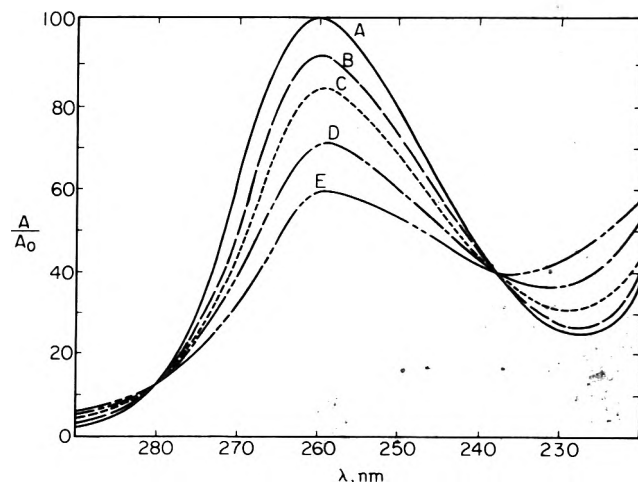


Figure 1. Spectra of irradiated 0.2 mM adenine solutions, air equilibrated: (curve A) 0 krad; (B) 15.5 krad; (C) 31.0 krad; (D) 62.0 krad; (E) 93.0 krad.

TABLE I: Fractional Change in Absorbance at Various Wavelengths (0.2 mM Adenine after 62.0 krad)

Wave-length, nm	$(A_0^\lambda - A_{62}^\lambda) / A_0^\lambda$	Wave-length, nm	$(A_0^\lambda - A_{62}^\lambda) / A_0^\lambda$
280	0.0	245	0.177
260	0.288	240	0.050
255	0.275	238	0.0
250	0.238		

range, the fractional absorbance is independent of λ, i.e.

$$(A_0^\lambda - A_D^\lambda) / A_0^\lambda \neq f(\lambda) \quad (4)$$

it can be inferred to a very high degree of probability that ε<sub>Σ</sub><sup>λ</sup> = 0. This condition was fulfilled in the case of cytosine,<sup>2</sup> which is therefore especially favorable, but rather special.

Figure 1 and Table I show representative results, obtained by irradiating 0.2 mM adenine. It may be seen that two well-defined isosbestic points develop at 280 and 238 nm. Clearly, the fractional change in absorbance varies strongly with λ, and eq 4 does not hold in the present case.

It follows immediately from eq 1 that the condition for an isosbestic point is

$$\epsilon_S^\lambda = \epsilon_\Sigma^\lambda \quad (5)$$

It should be noted that eq 5 is equivalent to that derived by Cohen and Fischer<sup>16</sup> in their general treatment of the isosbestic phenomenon; radiolytic reactions are a special case.

The development of (one or more) isosbestic points constitutes by itself unequivocal proof that the radiolysis products absorb. Moreover, it defines the values of ε<sub>Σ</sub><sup>λ</sup> at the isosbestic wavelengths; they are 1100 at 280 nm, and 5600 at 238 nm, respectively.

However, the results so far discussed do not allow us to determine the value of G(-Ade). Obviously nothing can be learned about this value from measurements at the isosbestic points, and at the other wavelengths the value of ε<sub>Σ</sub><sup>λ</sup> is not known; as was shown above, all one can obtain from such data is the lower limit to G(-Ade). The results of this analysis are shown in Figure 2, line C; the apparent values of G extrapolate to about 1 molecule/(100 eV) at zero dose.

As we have mentioned, Scholes et al.<sup>4</sup> obtained, by the same method of analysis, a G value of 1.1. In other words, our experimental results are in close agreement with theirs, and we differ only in the interpretation; this hinges entirely on the question of how strongly the products absorb at 260

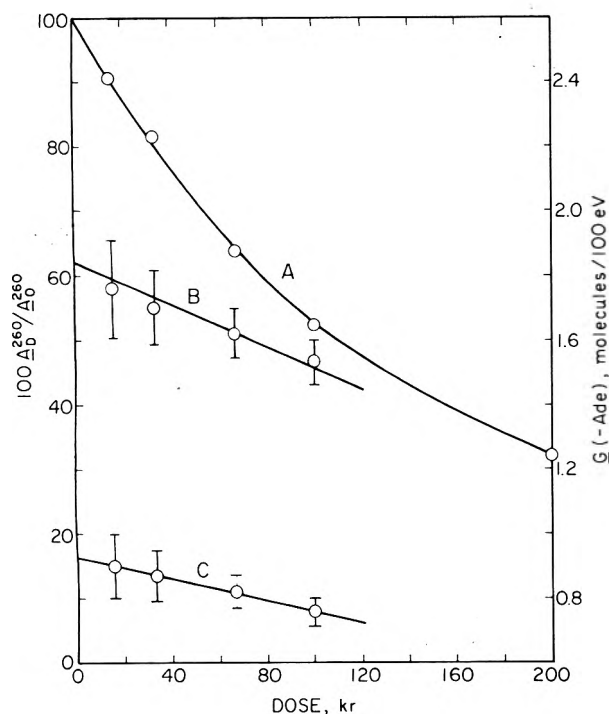


**Figure 2.** (Left ordinate, curve A) Absorbance of irradiated 0.2 mM adenine solution at 260 nm. (Right ordinate, line B)  $G(-Ade)$  calculated from results of the Davis–Morris method; (line C) apparent  $G(-Ade)$  calculated from  $(dA^{260}/dD)$  assuming  $\epsilon_{\Sigma}^{260} = 0$ .

nm.

In order to resolve this question, we took recourse in an independent, highly specific method for determining adenine, the colorimetric test devised by Davis and Morris.<sup>9</sup> The inventors of this procedure demonstrated that 14 purine and pyrimidine derivatives did not interfere with the determination of adenine, and we have ascertained in this work that this also is the case for three additional compounds, 8-hydroxyadenine, 4,6-diamino-5-formamidopyrimidine, and isoguanine.

The results of applying the Davis–Morris procedure to irradiated adenine solutions are illustrated by line B in Figure 2, which is a linear least-squares fit to the calculated values of  $G(-Ade)$ . In this instance, extrapolation to zero dose gives the value  $G_0(-Ade) = 1.84$  molecules/(100 eV). Eight independent determinations of  $G_0(-Ade)$  averaged  $1.94 \pm 0.1$ ; i.e., the reproducibility is quite satisfactory. It is of course to be expected that this result should be larger than the values reported previously.

Equation 2 can now be employed to determine the value of  $\epsilon_{\Sigma}^{260}$ , the average of some 40 determinations was  $5500 \pm 1100$ . This result is not very precise because it had to be derived from measurements of  $(A_0 - A_D)$  at low doses, which are inevitably subject to large errors. However the data leave no doubt that  $\epsilon_{\Sigma}^{260}$  is much greater than zero.

Our general approach to the study of the radiolysis of biologically important compounds has been to focus attention on the decomposition yield of the original substance, because that is the phenomenon of critical importance from the biological point of view.<sup>1,2</sup> The identity of the products is of lesser importance, although in some cases they may have a biological effect of their own.<sup>17</sup> In the present context, it was also pertinent to know whether the products might interfere with the Davis–Morris test. For these reasons, a partial analysis of the products was carried out by thin-layer chromatography and by mass spectrometry. The results are summarized in Table II.

Chromatography gave eight well-defined spots, besides that of adenine (spot 1). The observation confirms our

**TABLE II: Chromatography and 10-eV Mass Spectra of Radiolysis Products**

Spot no.	Thin-layer chromatography		Yield <sup>a</sup>	Mass Spectrometry	
	$R_f$ value			Mass/charge	Probe temp, °C <sup>b</sup>
	System A	System B			
1 <sup>g</sup>	0.70	0.51	$-3 \pm 1$	17 <sup>g</sup>	30
2 <sup>g</sup>	0.61	0.63	0.15	45	30
3 <sup>g</sup>	0.58	0.42	0.5	46	30
4	0.54	0.52	0.15	60 <sup>g</sup>	55
5	0.51	0.51	0.3	86	130
6 <sup>g</sup>	0.43	0.50	0.4	88	130
7	0.39	0.32	0.3	96	130
8	0.38	0.55	0.2	108 <sup>g</sup>	130
9	0.35	0.27	0.2	111	210
				125 <sup>g</sup>	120
				129	130
				135 <sup>g</sup>	130
				151 <sup>g</sup>	150
				153 <sup>g</sup>	140

Compound	$R_f$ value		$\epsilon^{260}$	Principal ions <sup>c</sup>	
	Sys-tem A	Sys-tem B		$m/e$	Probe temp, °C <sup>d</sup>
Adenine	0.70	0.51	13400	135 (100) 108 (31)	130
Urea	0.61	0.63		60 (100) 17 (15)	55
8-Hydroxy-adenine	0.58	0.42	10100 <sup>e</sup>	151 (100)	220
II <sup>f</sup>	0.43	0.50	4600 <sup>e</sup>	153 (100) 125 (32)	170

<sup>a</sup> (Counts in spot)/(change in counts in adenine spot); approximate values, averaged over the range 130–540 krad. <sup>b</sup> Temperature at which ion first appears. <sup>c</sup> Number in parentheses is the abundance of the ion relative to the principal peak; only ions with relative abundance >10 are listed. <sup>d</sup> Temperature at which the molecular ion is most intense. <sup>e</sup> In agreement with Cavalieri and Bendich.<sup>11</sup> <sup>f</sup> 4,6-Diamino-5-formamidopyrimidine. <sup>g</sup> Identified with known compound in bottom part of table.

supposition that to determine all the radiolysis products would be a laborious undertaking. We have identified one of the products (spot 2) as urea; to our knowledge, this product had not been reported previously. Since the urea is radioactive, it must come, at least in part, from the C-8 atom of adenine. Two other products are 8-hydroxyadenine (I, spot 3), and 4,6-diamino-5-formamidopyrimidine (II, spot 6); these products have been reported previously.<sup>5,6</sup> As noted above, I and II do not interfere with the Davis–Morris test.

The mass spectrophotometric results cannot be interpreted unambiguously. However the mass spectra are consistent with the presence of the aforementioned products, and of some additional ones which we have not identified.

I and II account for a major fraction of  $\epsilon_{\Sigma}^{260}$ . Their contribution can be estimated by substituting the appropriate values of  $G(U_i)$  and  $\epsilon_i^{260}$  from Table II and the value of  $G(-Ade) = 1.9$  into eq 2, as follows:

$$\epsilon^{260}(I + II) = (1/1.9)(0.5 \times 10100 + 0.4 \times 4600) = 3600 \quad (6)$$

This leaves a remainder of some 1900 for the equivalent absorbance of all the other products, which account for about half of the adenine decomposed.

The results thus provide a self-consistent and largely unambiguous interpretation of the radiolysis process. The

only uncertainty concerns the identity of some of the products. It should be noted that, if any of the unidentified products gave some color in the Davis-Morris test, the value of  $G(-Ade)$  would be even higher than that which has been quoted above. This possibility cannot be absolutely excluded, but it is very unlikely in view of what is known about the radiolysis process and the unidentified products.

**Acknowledgment.** The work described above was aided by a Biomedical Sciences Support Grant from the National Institutes of Health to the Research Foundation, Oklahoma State University, and by NSF Grant MPS 75-18967 to L.M.R.

### References and Notes

- (1) R. N. Rice, G. Gorin, and L. M. Raff, *J. Phys. Chem.*, **79**, 2717 (1975).
- (2) G. Gorin, N. Ohno, and L. M. Raff, *J. Phys. Chem.*, **80**, 112 (1976).
- (3) D. T. Kanazir, *Prog. Nucl. Acid Res. Mol. Biol.*, **9**, 117 (1969).
- (4) G. Scholes, J. F. Ward, and J. Weiss, *J. Mol. Biol.*, **2**, 379 (1960).
- (5) J. J. Conlay, *Nature (London)*, **197**, 555 (1963).
- (6) J. J. van Hemmen and J. F. Bleichrodt, *Radiat. Res.*, **46**, 444 (1971).
- (7) J. F. Ward in "Advances in Radiation Research", Vol. 5, J. T. Lett and H. Adler, Ed., Academic Press, New York, N.Y., 1975, p 207.
- (8) H. J. Rhaese, *Biochim. Biophys. Acta*, **166**, 311 (1968).
- (9) J. R. Davis and R. N. Morris, *Anal. Biochem.*, **5**, 64 (1963).
- (10) R. Uliana and P. V. Creac'h, *Bull. Soc. Chim. Fr.*, 2904 (1969).
- (11) L. F. Cavalieri and A. Bendich, *J. Am. Chem. Soc.*, **72**, 2587 (1950).
- (12) "Radiation Dosimetry: X-Rays and Gamma Rays with Maximum Photon Energies Between 0.6 and 60 MeV" (ICRU Report No. 14), International Commission on Radiation Units and Measurements, Washington, D.C., 1969.
- (13) H. Stephen and T. Stephen, "Solubilities of Inorganic and Organic Compounds", Vol. 1, Pergamon Press, Oxford, 1963, part 1, pp 87-88; W. F. Linke, Ed., "Solubilities", Vol. II, American Chemical Society, Washington, D.C., 1965, p 1228.
- (14) C. A. Mannan, M.S. Thesis, Oklahoma State University, 1972.
- (15) L. Josefsson, *Biochim. Biophys. Acta*, **72**, 133 (1963); P. Grippo, M. Iaccarino, M. Rossi, and E. Scarano, *ibid.*, **95**, 1 (1965).
- (16) M. D. Cohen and E. Fischer, *J. Chem. Soc.*, 3044 (1962).
- (17) E.g., M. Poverelli and R. Teoule, *C. R. Acad. Sci. Paris, Ser. C*, **277**, 747 (1973).

## A Chromatographic Investigation of Ternary Nonelectrolyte Systems

Jon F. Parcher\* and Theodore N. Westlake

Chemistry Department, University of Mississippi, University, Mississippi 38677 (Received May 17, 1976; Revised Manuscript Received November 8, 1976)

Publication costs assisted by the University of Mississippi and the National Science Foundation

The "chromatographic" partition coefficients of eleven solutes at infinite dilution were measured as a function of composition in four binary solvents at 45 °C. The binary liquid phases were formed by utilizing a condensable component in the carrier gas. The molecular sizes of the components were disparate and the systems were used to test several nonelectrolyte solution theories. It is shown that Purnell's "microscopic partitioning theory" was inadequate for most of the systems studied and that the Flory-Huggins theory provides a much better, although imperfect, description of the particular systems investigated.

In the last decade, gas-liquid chromatography has proven to be an accurate and convenient technique for measuring vapor-liquid equilibria data for nonelectrolyte systems. This is especially true in the low concentration ranges (infinite dilution) normally inaccessible by static vapor pressure measurements. The primary data usually obtained are the "chromatographic" partition coefficient and the Raoult's law activity coefficient of the volatile solute in the stationary liquid phase.

Binary liquid phases have also been investigated by several authors. There are two main purposes for this type of investigation. One is the attempt to control the selectivity of a chromatographic column by using mixed liquid phases and the other is an attempt to measure the equilibrium constants for the weak type of complexes, such as charge transfer,  $\pi$  bonding, or H bonding complexes, between the solute and one component of a binary liquid phase. The latter type of investigation has invoked a great deal of controversy, especially involving the comparison of complex formation constant data from chromatography, UV-visible spectrophotometry, and nuclear magnetic resonance spectrometry.

Pilgrim and Keller<sup>1</sup> reviewed the general area of mixed liquid phases in 1973 and pointed out the multiplicity of empirical and theoretical equations which "fit" the partition coefficient data.

Dal Nogare and Juvet<sup>2</sup> first suggested a simple relation between the "chromatographic" partition coefficient of a

solute,  $i$ , in a binary solvent, A + S, and the composition of the liquid phase. Several authors<sup>3-5</sup> have used the equation

$$(t_{Ri})_{A+S} = (t_{Ri})_A \left\{ \frac{W_A}{W_A + W_S} \right\} + (t_{Ri})_S \left\{ \frac{W'_S}{W_A + W'_S} \right\} \quad (1)$$

where  $(t_{Ri})_j$  is the retention time of solute  $i$  in liquid phase  $j$  and  $W_j$  is the weight of component  $j$  in the mixed liquid phase. This equation was shown to be accurate for over 100 chromatographic systems by plotting  $(t_{Ri})_{A+S}$  vs. the weight percentage of one of the liquid phase components.

Waksmundzki, Soczewinski, and Supryniewicz<sup>6,7</sup> proposed an equation of the form

$$\ln (k_{iA+S}) = \phi_A \ln (k_{iA}) + \phi_S \ln (k_{iS}) \quad (2)$$

where  $(k_{i})_j$  is the partition ratio (moles of  $i$  in the liquid phase per mole of  $i$  in the gas phase) of solute,  $i$ , in solvent  $j$ , and  $\theta_j$  is the volume fraction of component  $j$  in the liquid phase. The partition ratio is equal to the ratio of the retention time of a solute to the retention time of air or another inert solute. Thus, eq 2 predicts a linear relation between  $\ln t_{Ri}$  and the volume fraction of one of the liquid phase components. This equation was shown to be accurate for 17 chromatographic systems, although the authors later<sup>8</sup> modified eq 2 to include a term to account

for the excess free energy of the solvent mixture.

A third form of equation was derived by Reznikov<sup>9,10</sup> from the Van Laar equation for the activity coefficient as a function of solvent composition. This author used a form of relative partition coefficient and utilized the following expression

$$\ln (K_{REL})_{A+S} = \phi'_A \ln (K_{REL})_A + \phi'_S \ln (K_{REL})_S + \phi'_A \phi'_S \ln (\gamma_A)_S \frac{v_i - v_{STD}}{v_A} \quad (3)$$

where  $(\gamma_A)_S$  is the activity coefficient of A in S and  $v_j$  is the molar volume of component j and the subscript STD is used to denote the standard.  $\theta'_j$  is an "effective" volume fraction. If  $v_i$  and  $v_{STD}$  are small relative to  $v_A$ , the correlation term of eq 3 can be neglected and Reznikov showed that this simplified version of eq 3 is valid for 75 chromatographic system.

Recently, Purnell<sup>11-14</sup> investigated a large number of systems and found that a simple equation was adequate to describe the vast majority of the systems involving two nonvolatile liquid phases over the entire range of composition

$$(K_{Ri}^0)_M = \phi_A (K_{Ri}^0)_A + \phi_S (K_{Ri}^0)_S \quad (4)$$

where  $(K_{Ri}^0)_j$  is the chromatographic partition coefficient of solute i at infinite dilution in solvent j. Purnell postulated a model to explain this type of behavior which involved the idea that the two liquid phases "exist in their macroscopic solutions as microscopically immiscible groups of like molecules."<sup>13</sup>

Martire<sup>15</sup> has criticized Purnell's "Microscopic Partitioning Theory" and proposed an alternate model for complexing systems.<sup>16,17</sup> Martire suggested that the association constants measured chromatographically were actually a combination of terms measuring both chemical (complexing) and physical (solution) effects. This resulted in an equation of the form

$$\ln \left[ \frac{(\gamma_i^\infty)_{SUS}}{(\gamma_i^\infty)_{MUM}} \right] = \alpha_1 C_A + \alpha_2 C_A^2 \quad (5)$$

$$\alpha_1 = \frac{v_i}{v_S} (v_S - v_A) + v_A (\chi_i)_S - v_A (\chi_i)_A + \alpha_2$$

$$\alpha_2 = -v_i v_A (\chi_A)_S$$

$(\gamma_i^\infty)_j$  is the infinite dilution activity coefficient of the solute i in solvent j;  $C_A$  is the molar concentration of the moderator or additive, A, and  $(\chi_i)_j$  is the Flory-Huggins interaction parameter for component i in solvent j. The partition coefficients are related to the activity coefficients and complex formation constant,  $K_1$ , by the equation

$$\frac{(K_{Ri}^0)_M}{(K_{Ri}^0)_S} = \frac{(\gamma_i^\infty)_{SUS}}{(\gamma_i^\infty)_{MUM}} [1 + K_1 (\gamma_A)_M C_A] \quad (6)$$

In systems where strong chemical interactions or complex formation is not favored the partition coefficients can be related directly to  $\alpha_1$  and  $\alpha_2$ .

Under certain conditions, Martire's equations (eq 5 and 6) will reduce to an equation of the same form as Purnell's equation (eq 4). If  $(\alpha_1 C_A + \alpha_2 C_A^2) \ll 1$  and  $(\gamma_A)_M$  is a linear function of  $C_A$ , i.e.,  $(\gamma_A)_M = 1 + \beta_1 C_A$ , then eq 5 and 6 reduce to

$$\frac{(K_{Ri}^0)_M}{(K_{Ri}^0)_S} = 1 + (K_1 + \alpha_1) C_A + \left[ K_1 (\alpha_1 + \beta_1) + \frac{\alpha_1^2}{2} + \alpha_2 \right] C_A^2 \quad (7)$$

TABLE I: Physical Characteristics of the Chromatographic Columns

Liquid phase	Solid support	% Coating	Liquid phase vol, ml
1. Dinonyl-phthalate	Gas Chrom Z (60/80)	11.5	2.36
2. Squalane	Gas Chrom Q (60/80)	13.4	2.59
3. Squalane	Gas Chrom Z (60/80)	10.7	2.28

TABLE II: Molar Volumes and Partition Coefficients of the Solutes in Pure Benzene and *n*-Heptane at 45 °C

Solutes	Molar vol, M <sup>-1</sup>	Partition coefficients	
		Benzene	<i>n</i> -Heptane
<i>n</i> -Pentane	0.120	122 <sup>a</sup>	
<i>n</i> -Hexane	0.135	345 <sup>b</sup>	
<i>n</i> -Heptane	0.151	977 <sup>c</sup>	1,140
Ethanol	0.060	136 <sup>d</sup>	28.7 <sup>f</sup>
Acetone	0.076	295 <sup>d</sup>	45
Acetonitrile	0.054	326 <sup>d</sup>	24.8 <sup>g</sup>
Nitromethane	0.055	763 <sup>d</sup>	53
2-Butanone	0.092		
Cyclohexene	0.110	521 <sup>e</sup>	540
Cyclohexane	0.104		545
Benzene	0.091		402.8 <sup>g</sup>

<sup>a</sup> Reference 20. <sup>b</sup> Reference 21. <sup>c</sup> Reference 22. <sup>d</sup> Reference 23. <sup>e</sup> Reference 24. <sup>f</sup> Reference 25. <sup>g</sup> Reference 26.

If the term involving  $C_A^2$  is small and the volume of mixing is zero, so that  $\theta_A = C_A v_A$ , then eq 7 becomes identical in form with eq 4.

$$\frac{(K_{Ri}^0)_M}{(K_{Ri}^0)_S} = 1 + \left[ \frac{K_1 + \alpha_1}{v_A} \right] \phi_A \quad (8)$$

Because of the fact that both the microscopic partitioning theory of Purnell and Martire's additive contribution model predict a linear variation of  $(K_{Ri}^0)_M$  with  $\theta_A$ , under the conditions given above, it has not been possible to test these two models by chromatographic studies alone.

Previous gas chromatographic investigations of this nature have always involved the use of two high molecular weight, nonvolatile liquid phases as components A and S so that  $v_i \ll v_A \approx v_S$  so the combinatorial contribution to  $\alpha_1$  is small. The interaction parameter contributions to  $\alpha_1$  and  $\alpha_2$  are also small for mixed liquid phases<sup>15</sup> and  $(K_{Ri})_m$  is generally observed to be a linear function of  $C_A$  or  $\theta_A$ .

A chromatographic investigation could be used to distinguish between the two models if the conditions were removed which allow the reduction of eq 7 to a linear form (eq 8). This can be done by utilizing a low molecular weight, volatile component along with a normal chromatographic liquid phase to form the binary solvent.<sup>18</sup> In this case  $v_i \approx v_A \ll v_S$ , and both the combinatorial and interaction parameter contributions to  $\alpha_1$  and  $\alpha_2$  are larger than for mixed liquid phases.

### Experimental Section

The experiments were carried out by normal frontal chromatographic techniques<sup>19</sup> using different mole fractions of benzene or *n*-heptane in helium as the binary carrier gas. The physical characteristics of the packed columns are given in Table I. The partition coefficients of the solutes in pure benzene and *n*-heptane along with the molar volumes of the solutes are given in Table II. The molar volumes were calculated from the density-temperature relations given by Dreisback<sup>27</sup> and others.<sup>28</sup>

TABLE III: "Chromatographic" Partition Coefficients for a Series of Solutes in Squalane Plus Benzene at 45 °C

Solute	Partition coefficient							
<i>n</i> -Pentane	60.7	64.4	70.8	74.0	72.4	81.2	87.4	87.1
<i>n</i> -Hexane	171.7	183.2	190.2	213.1	208.7	236.2	240.8	258.1
<i>n</i> -Heptane	481.5	511.0	571.4	603.6	575.8	666.4		
Ethanol	19.7	21.5	26.6	27.6	29.0		36.5	43.2
Acetone	28.8	33.1	40.2	45.3	48.0	66.0	66.9	80.9
Acetonitrile	20.7	22.5	30.5	34.9	39.4		60.6	81.9
Nitromethane	37.2	46.5	62.9	72.3	82.0	127.3	128.5	171.0
2-Butanone	86.9	100.5	122.7	138.4	145.7		207.7	751.6
$C_A, M$	0.0	0.55	1.31	2.13	2.55	5.04	5.12	7.22
$C_A$ (Lit.), $M$	0.0	0.55	1.20	1.90	2.42	5.05	4.75	7.45
$\phi_A$	0.0	0.05	0.11	0.16	0.19	0.31	0.32	0.40
$X_A$	0.0	0.23	0.41	0.53	0.58	0.73	0.73	0.79
$V_L, ml$	2.59	2.72	2.90	3.09	3.19	3.78	3.80	4.30
$Y_A$	0.0	0.04	0.07	0.09	0.11	0.18	0.17	0.18

TABLE IV: Partition Coefficients in Squalane Plus *n*-Heptane at 45 °C

Solute	Partition coefficient						
<i>n</i> -Pentane	60.7	68.1	73.4	75.1	78.7		85.6
<i>n</i> -Hexane	171.7	193.8	211.6	215.1	227.6		248.4
<i>n</i> -Heptane	481.5						
Ethanol	19.7	20.3	20.3	21.6	20.7		20.0
Acetone	28.8	28.6	31.6	32.2	32.4		34.0
Acetonitrile	20.7	19.1	19.9	20.4	20.4		20.2
Nitromethane	37.2	38.8	40.2	41.1	41.4		41.1
2-Butanone	86.9	93.1	98.6	100.3	102.8		110.4
Cyclohexane	322.9	356.8	375.9	382.6	393.7		409.2
Cyclohexene	353.9	386.6	406.8	415.2	423.0		436.2
Benzene	248.9	272.9	283.7	289.7	296.9		308.0
$C_A, M$	0.0	0.73	1.96	2.07	3.29		6.64
$C_A$ (Lit.), $M$	0.0	0.69	1.89	1.98	3.22		6.75
$\phi_A$	0.0	0.10	0.23	0.24	0.33		0.50
$X_A$	0.0	0.28	0.51	0.53	0.64		0.78
$V_L, ml$	2.28	2.52	2.95	2.99	3.41		4.56
$Y_A$	0.0	0.02	0.05	0.05	0.06		0.08

The partition coefficients of the solutes in pure benzene were calculated from published activity coefficient data<sup>20-24</sup> from the simple relation

$$(K_{Ri}^0)_A = \frac{RT}{(\gamma_i^\infty)_A P_i^0 v_A} \quad (9)$$

There is little data in the literature for systems involving *n*-heptane at 45 °C. van Ness et al.<sup>25</sup> studied ethanol in *n*-heptane and Palmer and Smith<sup>26</sup> presented data for acetonitrile and benzene in *n*-heptane. The additional partition coefficients in Table II were estimated from the relative retention volumes (based on benzene) of the solutes on a column of uncoated solid support with a binary carrier gas containing *n*-heptane. At high *n*-heptane pressures an unknown amount of *n*-heptane condensed on the uncoated support and the ratio of partition coefficients could be estimated from the relative retention times of the solutes compared to benzene or any of the other solutes for which an independent measurement of the partition coefficient was available.

The amount of additive (benzene or *n*-heptane) dissolved in the nonvolatile stationary liquid phase was calculated<sup>29</sup> from the retention volume of the sharp boundary or "break through curve". After the columns had equilibrated with the binary carrier gas, the solutes were injected in the normal elution mode with sample sizes in the range 0.2–0.5  $\mu$ l. The partition coefficients were calculated from the net retention volumes by the relation  $K_{Ri}^0 = V_N/V_L$ . The flow rate of the binary carrier gas was measured from the residence time of an air peak in an empty column.<sup>30</sup>

The gas chromatograph was a Beckman GC-65 modified for frontal chromatography.<sup>31</sup> A thermal conductivity

detector was used for all the studies and the sensitivity loss was not serious because the mole fraction of additive in the carrier gas never exceeded 0.2. The nonvolatile component was not stripped from the column by repeated saturation and the HEPT values for the solutes with a binary carrier gas were very close to the values at the same velocity for pure helium as the carrier. The instrument was equipped with a detector at the inlet of the column and another at the outlet so the detector response was negligible when there was no concentration gradient in the column.

## Results

The partition coefficients of eleven solutes at 45 °C in four binary liquid phases are given in Tables III–VI. These tables also give the measured values of the concentration of moderator in the binary liquid,  $C_A$ , in units of moles per liter of component S; the volume fraction,  $\theta_A$ , and mole fraction,  $X_A$ , of the moderator; the total volume of the binary solvent; and the mole fraction of component A in the gas phase,  $Y_A$ . The range of mole fraction,  $X_A$ , covered in the experiments was relatively high,  $0 \leq X_A \leq 0.8$ , however, the range of volume fraction was much lower due to the low molar volumes of the moderators compared to the nonvolatile chromatographic liquid phases. The total volume,  $V_L$ , was calculated on the assumption that the volume of mixing of the solvent was negligible, i.e.,  $V_L = n_A v_A + n_S v_S$ .

The net retention volumes could be accurately measured with a precision of about 1–3%. However, the value of  $C_A$ , measured from the retention time of a sharp front, was less precise. Ashworth and Everett<sup>32</sup> studied the same systems, i.e., benzene and *n*-heptane in squalane and dinonylphthalate at 20, 30, and 40 °C in a static system. These

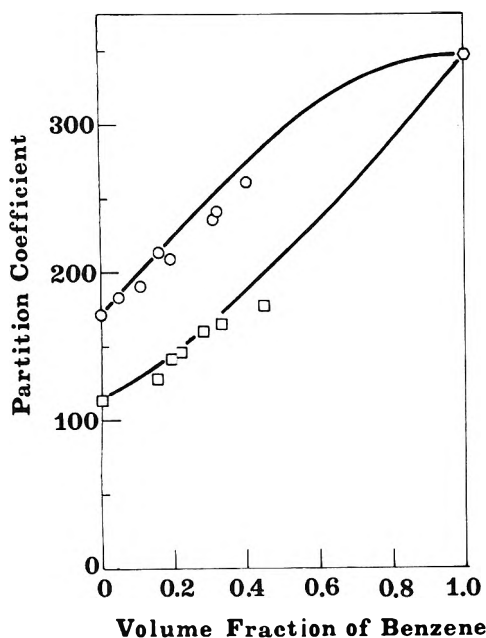


Figure 1. Chromatographic partition coefficient of *n*-hexane as a function of liquid phase composition: (O) squalane; (□) dinonylphthalate; (○) value calculated from the infinite dilution activity coefficient of *n*-hexane in benzene.

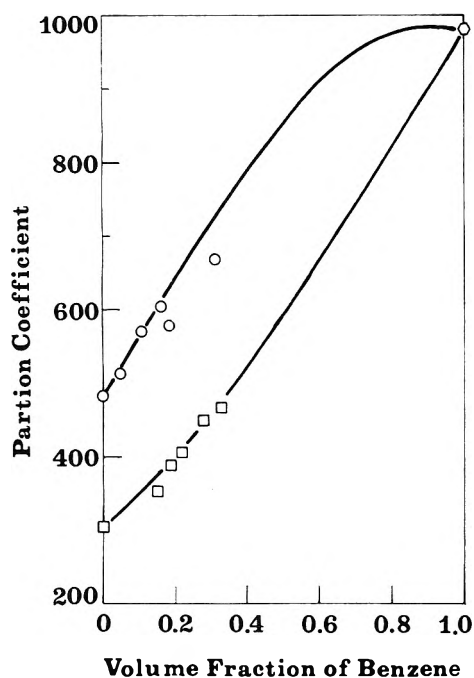


Figure 2. Chromatographic partition coefficient of *n*-heptane as a function of liquid phase composition: (O) squalane; (□) dinonylphthalate; (○) value calculated from the infinite dilution activity coefficient of *n*-heptane in benzene.

data extrapolated to 45 °C are included in Tables III-VI and the deviation of the chromatographic and static  $C_A$  values is usually less than 5% with a maximum deviation of 12%.

Both Purnell's microscopic partitioning theory (eq 4) and the simplified version of Martire's additive contribution theory (eq 8) predict a linear variation of  $(K_{Ri})_M$  with the volume fraction of the moderator,  $\phi_A$ . The experimental data are limited to  $\phi_A \leq 0.5$  because of the basic limitations of frontal chromatography. In this range, most of the systems exhibit a linear or nearly linear variation of the partition coefficient with  $\phi_A$ . There are some systems which are obviously nonlinear even over this

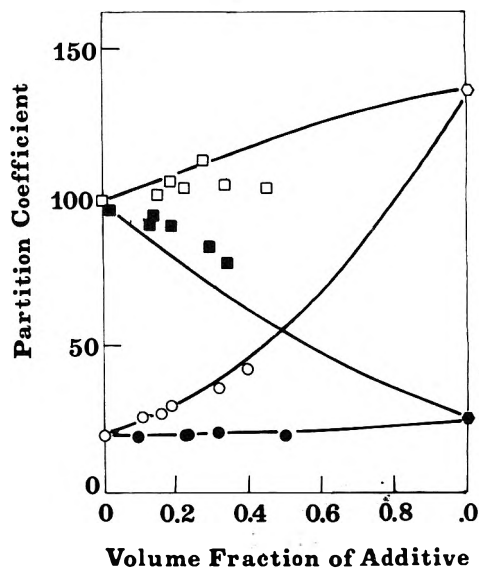


Figure 3. Chromatographic partition coefficient of ethanol as a function of liquid phase composition: (□) benzene in dinonylphthalate; (○) benzene in squalane; (■) *n*-heptane in dinonylphthalate; (●) *n*-heptane in squalane; (○) value calculated from the infinite dilution activity coefficient of ethanol in benzene; (●) value calculated from the infinite dilution activity coefficient of ethanol in *n*-heptane.

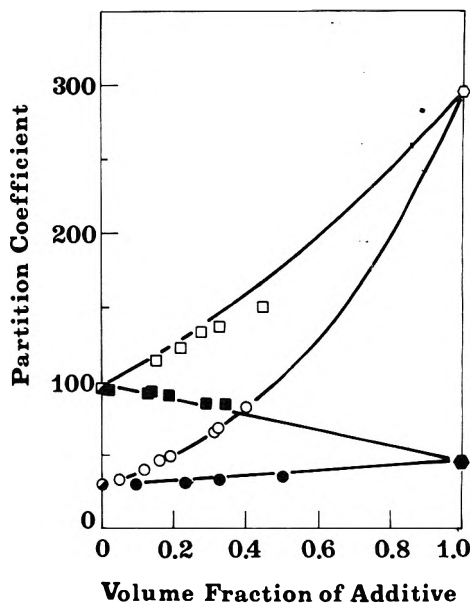


Figure 4. Chromatographic partition coefficient of acetone as a function of liquid phase composition. The symbols are the same as in Figure 3.

restricted range, e.g., most of the solutes in the system benzene/squalane.

It is obvious that, even though the systems may be linear at  $\theta \leq 0.5$ , most of the experimental data do not follow eq 4 and 8, because the linear relation at low concentrations does not extrapolate to the correct value at  $\phi_A = 1$ , as shown in Figures 1-6.

### Theory

For noncomplexing systems, the ratio of the partition coefficient of an infinitely dilute solute in a binary solvent, M, to that in a pure nonvolatile liquid phase, S, is given by

$$\frac{(K_{Ri})_M}{(K_{Ri})_S} = \frac{(\gamma_i^\infty)_S v_S}{(\gamma_i^\infty)_M v_M} \quad (10)$$

As long as the concentration of solute in the solvent is very

TABLE V: Partition Coefficients in Dinonylphthalate Plus Benzene at 45 °C

Solute	Partition Coefficient						
<i>n</i> -Pentane	41.4	46.2	50.1	52.1	56.5	58.9	61.7
<i>n</i> -Hexane	112.2	127.8	140.2	144.6	159.9	164.8	175.7
<i>n</i> -Heptane	303.8	351.1	387.3	399.9	447.0	465.7	
Ethanol	98.9	101.1	105.6	103.2	113.0	104.3	102.8
Acetone	96.5	113.1	120.9	121.5	131.2	134.2	148.6
Acetonitrile	150.6	166.1	180.2	186.9	201.2	193.0	206
Nitromethane	378.3	533.2	618.4			483.2	
2-Butanone	255.1	305.8	329.0	335.2	368.4	365.9	411.0
Cyclohexane	219.0	261.1	278.2	286.5	305.7	310.3	339.6
Cyclohexene	299.4	352.2	375.6	385.6	411.4	417.4	458.7
Benzene	354.5	526.1	631.0				
$C_A, M$	0.0	1.87	2.52	3.15	4.15	5.50	8.81
$C_A(\text{Lit.}), M$	0.0	1.78	2.45	3.03	3.62	5.54	8.80
$\phi_A$	0.0	0.15	0.19	0.22	0.28	0.33	0.45
$X_A$	0.0	0.45	0.53	0.58	0.65	0.71	0.80
$V_L, \text{ml}$	2.36	2.76	2.90	3.04	3.25	3.53	4.26
$Y_A$	0.0	0.07	0.08	0.09	0.11	0.13	0.15

TABLE VI: Partition Coefficients in Dinonylphthalate Plus *n*-Heptane at 45 °C

Solute	Partition coefficients						
<i>n</i> -Pentane	41.4	42.1	50.4	50.8	55.3	57.9	66.2
<i>n</i> -Hexane	112.2	116.2	138.9	143.6	154.3	164.4	188.6
<i>n</i> -Heptane	303.8	329.5	542.5	581.0			
Ethanol	98.9	97.0	91.7	94.8	91.2	82.8	78.1
Acetone	96.5	94.4	92.4	94.9	91.6	85.2	84.7
Acetonitrile	150.6	146.9	134.4	137.0	130.1	114.6	108.1
Nitromethane	378.3	375.5	343.3	339.9	323.2	284.1	276.4
2-Butanone	255.1	256.3	253.8	259.6	256.4	243.9	240.7
Cyclohexane	219.0	229.0	261.1	269.2	281.1	296.4	330.2
Cyclohexene	299.4	324.7	337.7	347.1	358.7	368.8	407.9
Benzene	354.5	368.1	378.2	386.3	386.1	380.2	390.8
$C_A, M$	0.0	0.15	1.00	1.04	1.51	2.74	3.40
$C_A(\text{Lit.}), M$	0.0	0.15	0.90	0.95	1.30	2.40	3.00
$\phi_A$	0.0	0.02	0.13	0.14	0.19	0.29	0.34
$X_A$	0.0	0.06	0.31	0.32	0.40	0.55	0.60
$V_L, \text{ml}$	2.36	2.41	2.72	2.73	2.90	3.33	3.57
$Y_A$	0.0	0.01	0.04	0.04	0.05	0.07	0.07

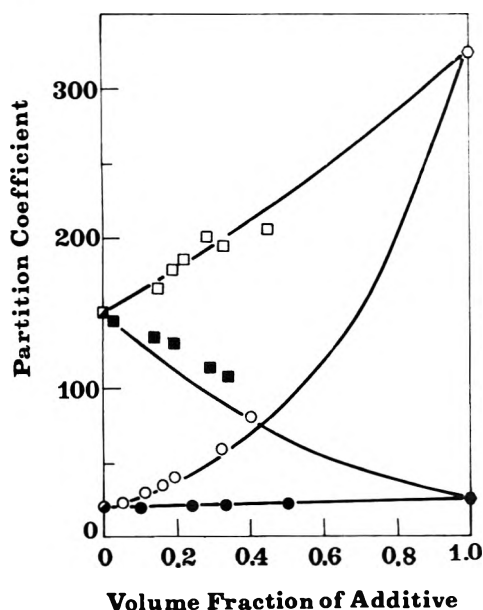


Figure 5. Chromatographic partition coefficient of acetonitrile as a function of liquid phase composition. The symbols are the same as in Figure 3.

low, i.e., infinitely dilute, the Flory-Huggins theory<sup>32</sup> can be used to describe the activity coefficient even for systems which may have very complex free energy relations at higher concentrations.

$$\ln(\gamma_i^\infty)_S = \ln \frac{v_i}{v_S} + 1 - \frac{v_i}{v_S} + (\chi_i)_S \quad (11)$$

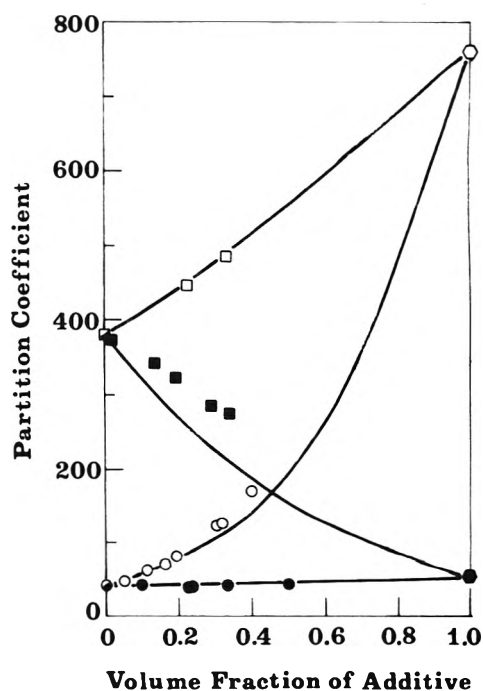


Figure 6. Chromatographic partition coefficient of nitromethane as a function of liquid phase composition. The symbols are the same as in Figure 3.

If a similar relation holds for the binary solvent

$$\ln \frac{(K_{Ri}^0)_M}{(K_{Ri}^0)_S} = \left[ \frac{v_i}{v_A} - \frac{v_i}{v_S} \right] \phi_A + (\chi_i)_S - (\chi_i)_M \quad (12)$$

Tompa<sup>33</sup> has suggested that  $(\chi_i)_M$  is a simple function of  $\theta_A$  and  $\theta_S$  for systems in which  $v_S \geq v_A$

$$(\chi_i)_M = (\chi_i)_S \phi_S + (\chi_i)_A \phi_A - \frac{v_i}{v_A} (\chi_A)_S \phi_A \phi_S \quad (13)$$

Substitution of eq 13 in eq 12 gives

$$\ln \frac{(K_{Ri})_M}{(K_{Ri})_S} = \alpha_1' \phi_A + \alpha_2' \phi_A^2 \quad (14)$$

$$\alpha_1' = \frac{v_i}{v_A} - \frac{v_i}{v_S} + (\chi_i)_S - (\chi_i)_A - \alpha_2'$$

$$\alpha_2' = \frac{-v_i}{v_A} (\chi_A)_S$$

Equation 14 has been derived previously by Martire<sup>15</sup> in a slightly different form.

The experimental data are not sufficiently precise to evaluate  $\alpha_1'$  and  $\alpha_2'$ . However, all of the experimental parameters necessary for the calculation of  $\alpha_1'$  and  $\alpha_2'$  are available in this case. The interaction parameters  $(\chi_i)_S$  can be obtained from the retention volumes of the solutes on a column containing only pure S. The  $(\chi_i)_A$  values can be obtained from the static activity coefficient data, and  $(\chi_A)_S$  can be obtained from the retention volumes of benzene and *n*-heptane on pure squalane and dinonylphthalate. The parameter  $(\chi_A)_S$  is very difficult to directly evaluate for systems involving two nonvolatile components in the liquid phase.

The interaction parameters of the solutes on each of the pure liquid phases were calculated from eq 9 and 11, and are presented in Table VII. The data from Tables II and VII can be used to calculate the  $(K_{Ri})_M = f(\theta_A)$  data for those systems for which  $(\gamma_i^\infty)_A$  is known. The results of these calculations are shown as the solid lines in Figures 1-6. These figures show that eq 14 is a relatively good representation of the observed data although there are obviously systematic deviations. However, there is little doubt that the simple relation given by eq 4 or 8 is not adequate for these systems. The data can be fit exactly to an expression of the form of eq 14, by using  $\alpha_2'$  as an adjustable parameter, however, this term then loses its physical significance. Because of the limited range of volume fraction, the values of  $\alpha_2'$  obtain by curve fitting techniques are very imprecise and of questionable value. Although eq 14 is not exact it is a far better model than any previously proposed.

The use of relative partition coefficients as suggested by Reznikov<sup>9,10</sup> can be very useful and the system can be described by a much simpler model. The expression for the relative partition coefficients is

$$\ln \frac{(K_{Ri})_M}{(K_{Rj})_M} = \ln \frac{(K_{Ri})_S}{(K_{Rj})_S} + (\alpha_{1,i} - \alpha_{1,j}) \phi_A + (\alpha_{2,i} - \alpha_{2,j}) \phi_A^2 \quad (15)$$

$$\alpha_{1,i} - \alpha_{1,j} = (v_i - v_j) \left[ \frac{1}{v_A} - \frac{1}{v_S} \right] + (\chi_i)_S - (\chi_j)_S - (\chi_i)_A + (\chi_j)_A + (\alpha_{2,i} - \alpha_{2,j})$$

$$\alpha_{2,i} - \alpha_{2,j} = \frac{(v_j - v_i)}{v_A} (\chi_A)_S$$

In a case where  $v_i \approx v_j$  or if  $(\chi_A)_S$  is small, the term involving  $\theta_A^2$  is negligible and eq 15 reduces to a linear equation. In particular, if the partition coefficients are measured relative to a series of normal hydrocarbon solutes, the retention index<sup>34</sup> of a solute should be a linear function of  $\theta_A$  and extrapolate to the value calculated for pure benzene or heptane, if  $\alpha_{2,i} - \alpha_{2,j}$  is small compared to

TABLE VII: Interaction Parameters of the Solutes in the Pure Liquid Phases and Pure Additives

Solutes	Squalane	Dinonylphthalate	Benzene	Heptane
<i>n</i> -Pentane	0.205	0.635	0.591	
<i>n</i> -Hexane	0.183	0.661	0.707	
<i>n</i> -Heptane	0.147	0.667	0.307	0.0
Ethanol	3.81	2.22	2.42	3.83
Acetone	2.14	0.958	0.505	2.03
Acetonitrile	3.53	1.56	1.27	3.53
Nitromethane	3.78	1.48	1.26	3.67
2-Butanone	1.55	0.507		
Cyclohexane	0.116	0.547		0.112
Cyclohexene				0.211
Benzene	0.536	0.218	0.0	0.484

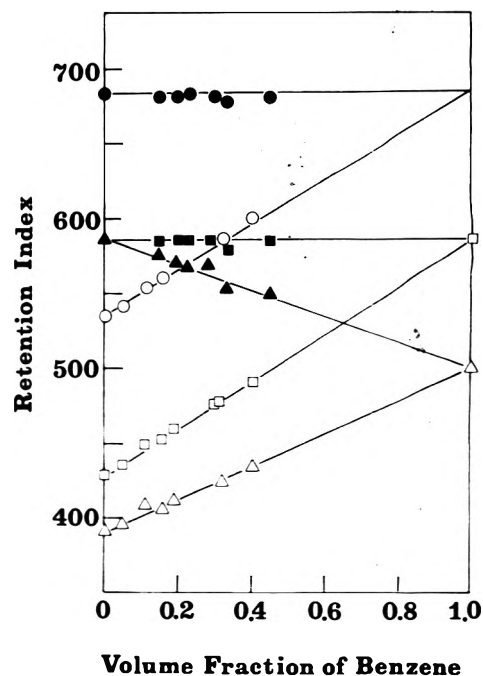


Figure 7. Plot of the retention index of three solutes as a function of the volume fraction of benzene in squalane: (O) 2-butanone; ( $\Delta$ ) ethanol; ( $\square$ ) acetone. Open symbols for squalane. Closed symbols for dinonylphthalate.

$\alpha_{1,i} - \alpha_{1,j}$ . Figure 7 is a plot of the retention indices of three polar solutes as a function of the volume fraction of benzene as the additive. In all three cases the plots are linear, however, this is not generally observed. The same type of plots for the other solutes and moderator were generally not linear.

The fact that the retention index is a linear function of  $\theta_A$  in some cases suggests a very convenient method for measuring partition isotherms. The retention index is a very easy parameter to measure experimentally and could be used to measure the concentration of the additive in the liquid phase from data for the solute in the two pure components (liquid phase and additive).

## Discussion

The main difference between binary liquid phases with two nonvolatile components and those with one volatile component is the significant disparity of the molar volumes of the liquid phase components. This causes a large contribution to the configurational or athermal portion of the activity coefficient of the solute, which will be a sensitive function of the liquid phase composition. In the case of mixed (nonvolatile) liquid phases,  $v_A \approx v_S$ , and the configurational contribution to the solute activity coefficient will not vary significantly with  $\theta_A$ . This means that

$\alpha_1'$  will be smaller and  $\alpha_2'$  will not be significant because  $v_A \gg v_i$ . Also, the distinction between weight, mole, and volume fractions is obscured in the case of binary solvents with components of similar molecular weight and size.

The mathematics is simplified considerably by the use of mixed (nonvolatile) liquid phases and this may be the reason for the many reported cases of the successful application of the "microscopic partitioning" model,<sup>11-14</sup> and other solution theories.<sup>2-10</sup>

In this study the molar volumes of the solutes and the volatile component of the liquid phase were comparable and much smaller than the molar volume of the nonvolatile liquid phase, i.e.,  $v_i \approx v_A \ll v_S$ . In several cases,  $v_i > v_A$ , and  $\alpha_2' > (\chi_A)_S$ . The  $\alpha_2'$  term is significant in this case and the plot of  $\ln(K_{Ri}^0)_M/(K_{Ri}^0)_S$  will be nonlinear. A distinct advantage of this type of experimental approach is the ability to measure  $(\chi_A)_S$  directly which is difficult, if not impossible, for mixed (nonvolatile) liquid phases. However, it is only possible to measure an unambiguous value of  $\chi_i$  for systems in which the solute exists in an uncomplexed form in the pure solvent or additive. If the solute exists in a complexed form, then it is impossible to separate  $(\chi_i)_A$  for the uncomplexed solute from the formation constant for the complex and the measured  $(\chi_i)_A$  will be a function of both as pointed out by Martire.<sup>17</sup>

There is an obvious, systematic deviation of the data from the line predicted by eq 14 in several cases where  $\alpha_1' < 0$ , i.e., for ethanol, acetonitrile, and nitromethane. In these cases the  $\alpha_2'$  value calculated is too large and the experimental data appear to fit a linear equation in which  $\alpha_2' = 0$ . However, in many other cases it is obvious that  $\alpha_2'$  is finite and the linear relation between the partition coefficient and volume fraction composition observed by Purnell is not a universal characteristic of nonelectrolyte solutions. The binary liquid phases composed of two high molecular weight, nonvolatile components are a special class of solutions in which  $\alpha_2'$  is negligible. The well-studied Flory-Huggins theory provides a reasonable model for nonelectrolyte solutions and can be used to interpret all of the observed data. It is not necessary to invoke a model involving "micro-immiscibility" of the components of a binary liquid phase.

**Acknowledgment.** This research was supported by Grant No. CHE73-08458 A03 from the National Science

Foundation. The authors thank Dr. J. H. Purnell of University College at Swansea, Wales, for helpful discussions and corrections to the manuscript.

## References and Notes

- (1) G. W. Pilgrim and R. A. Keller, *J. Chromatogr. Sci.*, **11**, 207 (1973).
- (2) S. Dal Nogare and R. S. Juvet, "Gas-Liquid Chromatography", Interscience, New York, N.Y., 1962.
- (3) M. J. Molera, J. A. Garcia Dominguez, and J. Fernandez Biarge, *J. Chromatogr. Sci.*, **7**, 305 (1969).
- (4) J. C. Touchstone, C. H. Wu, A. Nikolski, and T. Murawec, *J. Chromatogr.*, **29**, 235 (1967).
- (5) J. C. Touchstone, T. Murawec, and A. Nikolski, *J. Chromatogr. Sci.*, **8**, 221 (1970).
- (6) E. Soczewinski and C. A. Wachtmeister, *J. Chromatogr.*, **7**, 311 (1962).
- (7) A. Waksmundzki, E. Soczewinski, and Z. Suprynowicz, *Collect. Czech. Chem. Commun.*, **27**, 2001 (1962).
- (8) A. Waksmundzki and Z. Suprynowicz, *J. Chromatogr.*, **18**, 232 (1965).
- (9) S. A. Beznikov, *Russ. J. Phys. Chem.*, **42**, 906 (1962).
- (10) S. A. Reznikov, I. N. Agapova, and R. I. Siclovov, *Russ. J. Phys. Chem.*, **44**, 702 (1970).
- (11) J. H. Purnell and J. M. Vargas de Andrade, *J. Am. Chem. Soc.*, **97**, 3585 (1975).
- (12) J. H. Purnell and J. M. Vargas de Andrade, *J. Am. Chem. Soc.*, **97**, 3590 (1975).
- (13) R. J. Laub and J. H. Purnell, *J. Am. Chem. Soc.*, **98**, 30 (1976).
- (14) R. J. Laub and J. H. Purnell, *J. Am. Chem. Soc.*, **98**, 35 (1976).
- (15) D. E. Martire, *Anal. Chem.*, **48**, 398 (1976).
- (16) H. L. Liao, D. E. Martire, and J. P. Sheridan, *Anal. Chem.*, **45**, 2087 (1973).
- (17) D. E. Martire, *Anal. Chem.*, **46**, 1712 (1974).
- (18) J. F. Parcher and T. N. Westlake, *J. Chromatogr. Sci.*, **14**, 343 (1976).
- (19) D. H. James and C. S. G. Phillips, *J. Chem. Soc.*, 1066 (1954).
- (20) J. L. H. Wang and B. C. Y. Lu, *J. Appl. Chem. Biotechnol.*, **21**, 297 (1971).
- (21) I. P. C. Li, Y.-W. Wong, S.-D. Chang, and B. C.-Y. Lu, *J. Chem. Eng. Data*, **17**, 492 (1972).
- (22) D. V. S. Jain, V. K. Gupta, and B. S. Lark, *J. Chem. Thermodyn.*, **5**, 451 (1973).
- (23) L. B. Schreiber and C. A. Eckert, *Ind. Eng. Chem., Process Des. Develop.*, **10**, 572 (1971).
- (24) I. P.-C. Li and B. C.-Y. Lu, *J. Chem. Eng. Data*, **18**, 305 (1973).
- (25) H. C. van Ness, C. A. Soczek, and N. K. Kochar, *J. Chem. Eng. Data*, **12**, 346 (1967).
- (26) D. A. Palmer and B. D. Smith, *Ind. Eng. Chem., Process Des. Develop.*, **11**, 114 (1972).
- (27) R. R. Dreisbach, "Physical Properties of Chemical Compounds", Vol. II, American Chemical Society, Washington, D.C., 1959.
- (28) "International Critical Tables", Vol. III, McGraw-Hill, New York, N.Y., p 27.
- (29) C. L. Hussey and J. F. Parcher, *Anal. Chem.*, **46**, 2237 (1974).
- (30) J. F. Parcher and C. L. Hussey, *Anal. Chem.*, **44**, 1102 (1972).
- (31) C. L. Hussey and J. F. Parcher, *J. Chromatogr.*, **42**, 47 (1974).
- (32) A. J. Ashworth and D. H. Everett, *Trans. Faraday Soc.*, **56**, 1609 (1960).
- (33) H. Tompa, "Polymer Solutions", Butterworths, London, 1956, p 182.
- (34) E. Kovats, *Helv. Chim. Acta*, **41**, 1915 (1958).

# Predictive Scheme for Thermochemical Properties of Polycyclic Aromatic Hydrocarbons<sup>§</sup>

S. E. Stein,<sup>†</sup> D. M. Golden,\* and S. W. Benson<sup>‡</sup>

Department of Thermochemistry and Chemical Kinetics, Stanford Research Institute, Menlo Park, California 94025  
(Received August 20, 1976)

Publication costs assisted by the Stanford Research Institute

An extension of group additivity techniques has been applied to the prediction of standard gas-phase heats of formation, intrinsic entropies, and heat capacities for polycyclic aromatic hydrocarbons (PAHs) consisting of six-membered rings. The proposed method is easy to apply, is more accurate than previous estimation methods, and converges to known thermochemical properties of graphite for very large, highly condensed PAHs. The average difference between predicted and measured  $\Delta H_f^\circ$  for eleven PAHs is  $<2 \text{ kcal mol}^{-1}$  and generally falls within experimental uncertainties. The largest deviation,  $6.7 \text{ kcal mol}^{-1}$ , occurs for perylene; this may be due to the inability of the proposed scheme to account for "destabilization" of aromatic systems due to the presence of rings that contain only exo-type bonds. The group additivity method has also been shown to reproduce measured  $\Delta H_f^\circ$  values for substituted naphthalenes with an average deviation of  $1.2 \text{ kcal mol}^{-1}$  compared with an average experimental uncertainty of  $1.4 \text{ kcal mol}^{-1}$ . Predicted entropies for gas-phase species agree with the rather limited existing data.

## Introduction

The chemistry and properties of polycyclic aromatic hydrocarbons (PAHs) have been of practical and theoretical importance for many years. These compounds are of special current interest as key intermediates and products in carcinogen and soot formation processes and in coal conversion processes.

To begin to develop mechanistic models for these processes, we must have reliable values for standard gas-phase heats of formation ( $\Delta H_f^\circ$ ), intrinsic entropies ( $S_{\text{int}}^\circ$ ), and heat capacities ( $C_p^\circ$ ). Gaseous heat of formation data are available for a number of ortho-fused PAHs (rings oriented as chains, as in chrysene), and for two peri-fused PAHs (pyrene and perylene). Accurate  $S_{\text{int}}^\circ$  and  $C_p^\circ$  values are available for very few PAHs.

Several schemes of varying accuracy and complexity are available for estimating  $\Delta H_f^\circ$  for substituted and unsubstituted PAHs,<sup>2-5</sup> none of which can be used to determine  $S_{\text{int}}^\circ$  and  $C_p^\circ$ . We report here an extension of group additivity (GA) methods<sup>6,7</sup> for estimating the above three thermochemical parameters. This extended GA method not only allows a straightforward prediction of entropy and heat capacity of PAHs, but also reproduces known  $\Delta H_f^\circ$  values with smaller average deviation than any other comparable method.

## Method

The present GA scheme uses four groups for unsubstituted PAHs.<sup>8</sup> The C-H group in benzene [ $C_B\text{-(H)}$ ] is used unchanged from previous group values.<sup>9</sup> Three groups associated with carbon atoms located at the border of two or three fused rings,  $C_{BF}$ , are distinguished;<sup>10</sup> these are [ $C_{BF}\text{-(C}_B)_2\text{(C}_{BF})$ ], [ $C_{BF}\text{-(C}_B\text{)(C}_{BF})_2$ ], and [ $C_{BF}\text{-(C}_{BF})_3$ ]. The first  $C_{BF}$  group may be recognized as the unsubstituted carbon in naphthalene and anthracene and inherently contains 1,5 H,H repulsion energy. The simplest

illustration of the second  $C_{BF}$  group is found in phenanthrene; each of these groups contains half of the 1,6 H,H repulsion energy. The third  $C_{BF}$  group is identical with a carbon atom present in a layer of graphite, free of interplanar interactions; each of the two interior carbons in pyrene are members of this group.

Additivity values for these three groups, presented in Table I, were based on thermochemical data reported in or derived from the literature. Figure 1 illustrates these groups in benzo[a]pyrene.

For the [ $C_{BF}\text{-(C}_B)_2\text{(C}_{BF})$ ] and [ $C_{BF}\text{-(C}_B\text{)(C}_{BF})_2$ ] groups,  $\Delta H_f^\circ$  values were derived from the measured values for the heats of formation of the ortho-fused PAHs listed in Table II.

In the calculation of entropies and heat capacities, the contributions of these two groups are assumed to be equivalent. That is, the group values for  $S_{\text{int}}^\circ$  and  $C_p^\circ$  for these two groups are the same, which is equivalent to the assumption that the intrinsic entropies and heat capacities of anthracene and phenanthrene are equal. Values of  $S_{\text{int}}^\circ$  for these groups were obtained by fitting calculated entropies to entropies derived from experimental data (see later).

Heat capacity values for the [ $C_{BF}\text{-(C}_B)_2\text{(C}_{BF})$ ] and [ $C_{BF}\text{-(C}_B\text{)(C}_{BF})_2$ ] groups were simply derived from the published values for naphthalene<sup>11</sup> by subtracting the contributions from the eight  $C_B\text{-(H)}$  groups.

Since the [ $C_{BF}\text{-(C}_{BF})_3$ ] group is similar to a graphitic carbon atom, and since little data are available for PAHs containing this group, values for this group were derived from graphite. Thus, convergence of calculated thermodynamic quantities to a "gaseous" graphite layer for very large highly condensed PAHs is assured. Since the heat of formation of graphite is defined as zero, and the heat of sublimation per carbon atom for large, fully conjugated PCACs have been measured to be  $1.45 \pm 0.10 \text{ kcal mol}^{-1}$ ,<sup>12,13</sup> the heat of formation for this group is set at  $1.45 \text{ kcal mol}^{-1}$ .

The value of  $S_{\text{int}}^\circ$  was derived in the following manner. Consider a very large layer of graphite in the bulk phase. The entropy per carbon atom is<sup>14</sup>  $1.36 \text{ cal mol}^{-1} \text{ K}^{-1}$ . If the bulk graphite is cleaved so that this layer becomes a surface layer, the entropy gain per carbon atom,<sup>15</sup>  $\Delta S_{\text{int}}^\circ(\text{bulk} \rightarrow$

<sup>§</sup> This work was performed for the United States Energy Research and Development Administration under Contract No. E(49-18)-2202.

<sup>†</sup> Present address: Department of Chemistry, West Virginia University, Morgantown, W.V. 26506.

<sup>‡</sup> Present address: Department of Chemistry, University of Southern California, Los Angeles, Calif. 90007.

TABLE I: Group Additivity Values

Group	$\Delta H_f^{\circ}{}_{298}$ , kcal mol <sup>-1</sup>	$S^{\circ}{}_{298}$ , cal mol <sup>-1</sup> K <sup>-1</sup>	$C_{p^{\circ}T}$ , cal mol <sup>-1</sup> K <sup>-1</sup>					
			300 K	400 K	500 K	600 K	800 K	1000 K
C <sub>B</sub> -(H)	3.30	11.53	3.24	4.44	5.46	6.30	7.54	8.41
C <sub>BF</sub> -(C <sub>B</sub> ) <sub>2</sub> (C <sub>BF</sub> )	4.80	-5.00	2.99	3.66	4.22	4.64	5.23	5.55
C <sub>BF</sub> -(C <sub>B</sub> )(C <sub>BF</sub> ) <sub>2</sub>	3.70	-5.00	2.99	3.66	4.22	4.64	5.23	5.55
C <sub>BF</sub> -(C <sub>BF</sub> ) <sub>3</sub>	1.45	1.82	2.08	2.85	3.50	4.03	4.75	5.14

TABLE II:  $S_{\text{int}}^{\circ}{}_{298}$ (gas) for PCAHs (cal mol<sup>-1</sup> K<sup>-1</sup>)

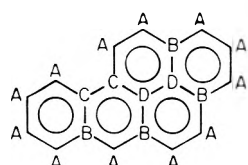
Compound	$S^{\circ}{}_{298}$ (solid) <sup>a</sup>	$\frac{\Delta H_{298}^{\circ}}{298}$ (sublim)/298	$R \ln P_v^b$	$R \ln \sigma^c$	$S_{\text{int}}^{\circ}{}_{298}$ (expt) <sup>d</sup>	$S_{\text{int}}^{\circ}{}_{298}$ (GA)	$\Delta$
Naphthalene					83.0 ± 1 <sup>a</sup>	82.2	-0.8
Phenanthrene	50.63	72.85 <sup>e</sup>	-29.57	1.38	95.3 ± 2	95.3	0.0
Anthracene	49.58	81.54 <sup>e</sup>	-38.71	2.75	95.2 ± 3	95.3	-0.1
Pyrene	53.75	81.00 <sup>f</sup>	-37.02	2.75	100.5 ± 3	98.9	-1.6
					98.1 ± 1 <sup>g</sup>	98.9	+0.8
Triphenylene	60.89	98.68 <sup>e</sup>	-50.5	3.56	108.6 ± 3	108.4	-0.2

<sup>a</sup> Reference 11. <sup>b</sup>  $P_v$  = vapor pressure at 298 K in units of atmospheres, see Table III. <sup>c</sup>  $\sigma$  = symmetry number. <sup>d</sup>  $S^{\circ}{}_{298}$ (gas) =  $S^{\circ}{}_{298}$ (solid) +  $\Delta H_{298}^{\circ}$ (sublim) +  $R \ln P_v$ . <sup>e</sup> From ref 18. <sup>f</sup> Reference 17. <sup>g</sup> From molecular properties (see text).

TABLE III: Comparison of Extrapolated Vapor Pressures (Torr) at 298.15 K<sup>a</sup>

Compound	A <sub>1</sub>	A <sub>2</sub>	B	C	D	Chosen value
Phenanthrene	1.3 × 10 <sup>-4</sup>	b	7.6 × 10 <sup>-4</sup>	1.7 × 10 <sup>-4</sup>		2.6 × 10 <sup>-4</sup>
Anthracene	2.3 × 10 <sup>-6</sup>	1.1 × 10 <sup>-7</sup>	( $\frac{2.8}{2.2}$ ) × 10 <sup>-5</sup>	6.2 × 10 <sup>-6</sup>		2.6 × 10 <sup>-6</sup>
Pyrene	5.1 × 10 <sup>-6</sup>	2.5 × 10 <sup>-6</sup>	2.2 × 10 <sup>-5</sup>	6.6 × 10 <sup>-6</sup>	4.5 × 10 <sup>-6</sup>	6.1 × 10 <sup>-6</sup>
Triphenylene		1.7 × 10 <sup>-8</sup>	2.8 × 10 <sup>-9</sup>			7.0 × 10 <sup>-9</sup>

<sup>a</sup> Sources A<sub>1</sub>. H. Hoyer and W. Peperle, *Z. Elektrochem.*, 62, 61 (1958); from Figure 4 in this reference. A<sub>2</sub>. From Table 1a in above ref. The reasons for the discrepancies between this and source A<sub>1</sub>, above are not known. B. Reference 12a,b. C. R. S. Bradley and T. G. Cleasby, *J. Chem. Soc.*, 1680 (1953). D. Reference 13. <sup>b</sup> An apparent typographical error in Table 1a of this reference made it impossible to extract a vapor pressure for this compound.



A = [C<sub>B</sub>-(H)]  
 B = [C<sub>BF</sub>-(C<sub>B</sub>)<sub>2</sub>(C<sub>BF</sub>)]  
 C = [C<sub>BF</sub>-(C<sub>B</sub>)(C<sub>BF</sub>)<sub>2</sub>]  
 D = [C<sub>BF</sub>-(C<sub>BF</sub>)<sub>3</sub>]

Figure 1. Benzo[a]pyrene consists of 12 [C<sub>B</sub>-(H)], 4 [C<sub>BF</sub>-(C<sub>B</sub>)<sub>2</sub>(C<sub>BF</sub>)], 2 [C<sub>BF</sub>-(C<sub>B</sub>)(C<sub>BF</sub>)<sub>2</sub>], and 2 [C<sub>BF</sub>-(C<sub>BF</sub>)<sub>3</sub>] groups.

surface) (identical with the graphite basal plane surface entropy), is 0.23 cal mol<sup>-1</sup> K<sup>-1</sup>. This value was derived by Abrahamson<sup>17</sup> from a careful analysis of the surface properties of graphite. Its usage, in the present context, assumes that all of the surface entropy is deposited only in the layer at the surface. The sum of the change in entropy per carbon in the surface layer upon evaporation of this layer,  $\Delta S^{\circ}{}_{298}$ (surface → gas), and the surface and bulk entropy (1.59 cal mol<sup>-1</sup> K<sup>-1</sup>), yields the entropy per carbon atom in a graphitic layer in the gas phase [C<sub>BF</sub>-(C<sub>BF</sub>)<sub>3</sub>]. Since no experimental value for  $\Delta S^{\circ}{}_{298}$ (surface → gas) is available, its value must be estimated. If the assumption is made that cleaving a graphite crystal just below the surface plane to form a gaseous layer generates as much entropy as a cleavage deeper within the crystal, then  $\Delta S^{\circ}{}_{298}$ (surface → gas) =  $\Delta S^{\circ}{}_{298}$ (bulk → surface) = 0.23 cal mol<sup>-1</sup> K<sup>-1</sup>, and  $S^{\circ}{}_{298}$ [C<sub>BF</sub>-(C<sub>BF</sub>)<sub>3</sub>] = 1.82 cal mol<sup>-1</sup> K<sup>-1</sup>. We choose this assumption in view of the relatively small interplanar interactions (1.45 kcal mol<sup>-1</sup> per carbon atom).

Since the surface heat capacity has been calculated as<sup>17</sup> <0.02 cal mol<sup>-1</sup> K<sup>-1</sup>,  $C_{p^{\circ}T}$ [C<sub>BF</sub>-(C<sub>BF</sub>)<sub>3</sub>] is taken to be equal

to published<sup>14</sup> values for  $C_{p^{\circ}T}$ (graphite).

Table II lists  $S_{\text{int}}^{\circ}{}_{298}$  values for PCAHs derived from literature sources. Calculations with the "third-law" method require accurate values for the entropy of the solid, heat of sublimation, and vapor pressure, all at 298 K. The choice of the best value for the vapor pressure at 298 K was based on the different experimental values listed in Table III and was taken to be the geometric mean of all values.

From published vibrational frequencies<sup>16</sup> and assumed geometry (C-C bond distance of 1.4 Å, and C-H distance of 1.08 Å), we have derived  $S_{\text{int}}^{\circ}{}_{298}$  for pyrene. This value, given in Table III, is 1.32 cal mol<sup>-1</sup> K<sup>-1</sup> higher than that calculated by others<sup>17</sup> on the basis of equivalent data. We are uncertain of the cause of this discrepancy.

The agreement between predicted and measured entropies (Table II) falls within the uncertainties of the measurements. Entropies for higher PCAHs could not be calculated because of a lack of reliable experimental data. We find that the predictions of  $C_{p^{\circ}T}$  by this GA method for pyrene agree with  $C_{p^{\circ}T}$  values based on the vibrational assignment of Bree et al.<sup>16</sup> to within 0.4 cal mol<sup>-1</sup> K<sup>-1</sup> over the range 300–1000 K.

This GA method is expected to apply directly only to PCAHs containing six-member rings, since groups were derived from such compounds. When nonhexagonal aromatic rings are present (such as in fluorene and biphenylene), additional "strain" is introduced into the molecule, resulting in an increase in  $\Delta H_f^{\circ}{}_{298}$  and a lowering of  $S_{\text{int}}^{\circ}{}_{298}$  and  $C_{p^{\circ}T}$ . Because of the general lack of reliable data, and the many different varieties of such strain, these structures have not been incorporated into the present GA technique.

One additional point concerning the applicability of these groups to PCAHs needs to be clarified. Somayajulu

TABLE IV: Comparison of Calculated<sup>a</sup> and Experimental  $\Delta H_f^\circ_{298}$  (kcal mol<sup>-1</sup>)

Compound	$\Delta H_f^\circ(\text{expt})^b$	$\Delta H_f^\circ_{298}(\text{calcd}) - \Delta H_f^\circ_{298}(\text{expt})$			Expt precision
		GA <sup>c</sup>	Laidler-type bond additivity <sup>d</sup>	Resonance theory <sup>e</sup>	
Benzene	19.8	0.0	0.0	+1.6	±0.13
Naphthalene	35.8	+0.2	0.7	-1.0	±0.25
Anthracene	54.4	-2.2	-1.1	-2.6	±1.1
Phenanthrene	50.0	+0.5	+0.4	-0.5	±1.1
Tetracene	67.8	+0.7	+2.4	+2.4	±1.1
Benz[a]anthracene	66.0	+0.2	+0.7	-1.5	±1.0
Chrysene	62.8	+1.2	+0.5	+1.2	±1.2
Triphenylene	61.9	-0.1	-2.0	+2.2	±1.1
Pyrene	51.6	+3.6	+5.0	+1.8	±0.4
Perylene	73.7	-6.7	-7.0	-3.0	±1.1
Benz[c]phenanthrene	69.6	-4.2	-6.3	-10.7	±1.2
Average		1.8[1.5] <sup>f</sup>	2.4[2.0] <sup>f</sup>	2.6[1.8] <sup>f</sup>	±0.9

<sup>a</sup> All three schemes use four parameters. <sup>b</sup> Experimental values used are the same as those used in ref 2, except for the application of the most recent measurement of the heat of sublimation of pyrene (ref 17). <sup>c</sup> Group values as given in Table I. <sup>d</sup> Bond additivity values as given in ref 20. <sup>e</sup> Calculated in ref 2. <sup>f</sup> These average values exclude benz[c]phenanthrene because of its unique 1,5 H,H repulsion.

TABLE V: Calculated<sup>a</sup>  $\Delta H_f^\circ_{298}$  (kcal mol<sup>-1</sup>) for Large PCAHs

	Group additivity	Bond additivity <sup>b</sup>	Resonance theory <sup>c</sup>	Triatomic additivity <sup>d</sup>
Coronene	77.1	80.2	72.6	81.3
Ovalene	99.1	103.8	98.2	115.1
Circumanthrene	121.1	127.3	119.0 <sup>e</sup>	147.5
Anthanthrene	74.2	76.8	76.1	74.0
Pentacene	84.6	89.0	86.8	93.9
Benz[a]pyrene	69.1	70.0	69.7	73.2
Benz[e]pyrene	67.0	66.7	67.9	70.9
Dibenz[a,c]anthracene	78.0	76.6	78.7	81.1
Dibenz[a,h]anthracene	80.2	80.0	77.8	82.5
Dibenz[a,j]anthracene	80.2	80.0	77.8	82.5
Benzo[1,12]perylene	72.2	73.4	70.4	77.4
Dibenzo[a,l]pyrene	85.2	86.3	91.4	95.0
Dibenzo[a,h]pyrene	83.2	83.4	88.1	89.8
Dibenzo[a,c]pyrene	81.0	80.0	84.7	90.5
Dibenzo[a,i]pyrene	83.2	83.4	85.9	89.8
Quaterylene	129.0	127.0	142.2	160.4

<sup>a</sup> The first three methods are all effectively five-parameter methods, since they use a 1,5 H,H repulsion term derived from benz[c]phenanthrene in the dibenzo[a,l]pyrene calculation. The triatomic additivity method uses nine parameters. <sup>b</sup> Uses bond additivity values given by ref 20, p 587. <sup>c</sup> Based on the five-parameter technique given in ref 2, using resonance energy parameters given in ref 21, except where noted. <sup>d</sup> Uses eight parameters given in ref 3. <sup>e</sup> Resonance energy contribution calculated to be 82.7 kcal mol<sup>-1</sup>, using the method of ref 21b normalized for use in calculations described in ref 2.

and Zwolinski<sup>3</sup> have derived a formula, based on the arguments of Nelander and Sunner,<sup>18</sup> which point out that  $\Delta E$ , not  $\Delta H$ , should be used in discussing ring strain, for applying acyclic groups to PCACs. They add  $1/6\nu RT$  to  $\Delta H_f^\circ_{298}$  to correct for this effect, where  $\nu = 6 + n - 2m$ , for PCACs of formula  $C_nH_m$ .

For PCAHs containing six-membered rings,  $\nu$  is generally equal to the number of  $[C_{BF}-(C_{BF})_3]$  groups and is thereby intrinsically incorporated into this group value. For molecules where this equality is not perfect, errors will be, generally, <0.2 kcal mol<sup>-1</sup> in the calculated  $\Delta H_f^\circ_{298}$ .

## Results and Discussion

Differences between measured  $\Delta H_f^\circ_{298}$  and values calculated by our scheme and by three other schemes are given in Table IV.

A four-parameter Laidler type of bond additivity scheme<sup>19</sup> using values suggested by Cox and Pilcher<sup>4</sup> gives less accurate heats of formation than the present GA scheme. The superior predictive ability of the proposed four-parameter GA scheme results from fitting its group values to a larger data base; otherwise, of course, they would be equivalent.<sup>4</sup>

The GA approach yields generally very accurate values for all ortho-fused systems. The errors in pyrene and

perylene are more substantial, and all these methods predict pyrene to be less stable and perylene to be more stable than observed. Such errors may arise from the imperfect accounting for resonance energy by these schemes. We expect relative errors of the present GA scheme for larger peri-fused PCAHs to be smaller because of its forced convergence to graphite.

It is interesting to compute  $\Delta H_f^\circ_{298}$  for perylene assuming that the two nonaromatic bonds connecting the naphthyl moieties are of the biphenyl type. Using groups derived from biphenyl-type compounds by Benson et al.,<sup>7</sup>  $\Delta H_f^\circ_{298}$  is overestimated by 5.0 kcal mol<sup>-1</sup>; this assumption leads to an underestimate of perylene stability.

A different approach to  $\Delta H_f^\circ_{298}$  calculation has been to sum atom additivity terms, hydrogen atom repulsion terms, and calculated resonance energy. The most accurate such scheme has been reported by Herndon,<sup>2</sup> who used a startlingly simple extension of resonance theory,<sup>21</sup> in which resonance energies are related to the number of stable Kekule structures. In Table IV, this scheme, while it has been shown to describe resonance energies as well as the best current quantum mechanical calculations, is actually less accurate than our more naive method. While Herndon's scheme yields somewhat better values for pyrene and perylene (even though the errors are still in

TABLE VI: Comparison of Predicted<sup>a</sup> and Experimental  $\Delta H_f^\circ$  (kcal mol<sup>-1</sup>) for Substituted Naphthalenes

Naphthalene substituent	$\Delta H_f^\circ$ (expt) <sup>a</sup>	$\Delta H_f^\circ$ (GA) - $\Delta H_f^\circ$ (expt)	Stated expt uncertainty	Ref
1-CH <sub>3</sub>	27.2	+0.8	±0.5	b,c
2-CH <sub>3</sub>	26.4	+1.6	±0.6	b,c
1-NH <sub>2</sub>	37.7	-0.7	±1.7	b
2-NH <sub>2</sub>	35.5	+1.5	±1.3	b
1-OH	-7.14	+1.0	±0.26	d
2-OH	-7.18	+1.1	±0.27	d
1-Cl	28.6	+0.3	±2.3	b
2-Cl	32.8	-3.9	±2.4	b
1-I	55.9	+0.8	±2.1	b
2-I	56.2	+0.5	±2.2	b
A <sub>v</sub> ,dev		±0.9	±1.2	

<sup>a</sup> Derived using substituent groups developed for substituted benzenes and biphenyls in ref 7, along with GA values in Table I. <sup>b</sup> See ref 13. <sup>c</sup> R. Sabbah, R. Chastel, and M. Lafitte, *Thermochem. Acta*, **10**, 353 (1974). <sup>d</sup> M. Colomina, M. V. Roux, and C. Turrión, *J. Chem. Thermodyn.*, **6**, 571 (1974).

the same direction as for the group and bond additivity schemes), it is only at the expense of a considerably poorer fit to ortho-condensed systems. Therefore, while we do not question the general correctness of this approach, based on agreement with available experimental evidence we prefer the GA approach. Group additivity is easier to use, especially for molecules with a very large number of Kekule structures, and it more naturally fits into existing, highly developed GA schemes.<sup>9</sup>

It is instructive to compare  $\Delta H_f^\circ$  values predicted by different calculational schemes for PCAHs whose heats of formation have not been experimentally measured. Table V gives such a comparison which also includes values derived from a recent triatomic additivity method<sup>3</sup> using eight parameters to describe the PCAHs (additional parameters were derived for less common interactions). Predicted  $\Delta H_f^\circ$  values are generally somewhat higher than for the three previously mentioned schemes. The lack of convergence to graphite for large PCAHs is a defect of this scheme.

The GA theory results differ from bond additivity, resonance theory, and triatomic additivity by an average of 2.1, 2.9, and 8.3 kcal mol<sup>-1</sup> per compound, respectively. The most striking differences are for quaterrylene, a molecule that, like perylene, contains rings for which only exo-bond structures may be written.

The GA method is easily extended to substituted PCAHs by using the appropriate groups developed for substituted benzenes. Table VI compares predicted  $\Delta H_f^\circ$  with measured values for substituted naphthalenes. The resulting average deviation of 1.2 kcal mol<sup>-1</sup> is less than the average experimental uncertainty of 1.4 kcal mol<sup>-1</sup>. There is no substantial difference in measured  $\Delta H_f^\circ$  for

$\alpha$  and  $\beta$  substitution, except, perhaps, in the case of Cl substitution.

The question of the magnitude of substituent interactions has few quantitative answers. However, in applying known and assumed interaction heats to the present GA method, it must be recognized that a C<sub>BF</sub>-(C<sub>B</sub>)(C<sub>BF</sub>)<sub>2</sub>  $\Delta H_f^\circ$  group inherently contains half of a 1,5 H,H repulsion term. Thus, the additive interaction term for the 1,5 H,H repulsion in benz[c]phenanthrene is only 4.2 kcal mol<sup>-1</sup> (Table II). The actual interaction heat is predicted to be higher than this value by a 1,5 H,H repulsion heat term (given as 2.4 kcal mol<sup>-1</sup> by Herndon<sup>2</sup>) owing to the two C<sub>BF</sub>-(C<sub>B</sub>)(C<sub>BF</sub>)<sub>2</sub> groups used in the calculation for  $\Delta H_f^\circ$ . Roughly equal interaction terms for 1,5 CH<sub>3</sub>,H and 1,5 CH<sub>3</sub>,CH<sub>3</sub> repulsion terms of 12 ± 2 kcal mol<sup>-1</sup> can be derived from measured  $\Delta H_f^\circ$  for several substituted three- and four-ring ortho-condensed PCAHs.<sup>20</sup>

## References and Notes

- (1)  $S_m^\circ = S^\circ_{298} + R \ln (\sigma/n)$  where  $\sigma$  is the symmetry number and  $n$  is the number of optical isomers.
- (2) W. C. Herndon, *Thermochem. Acta*, **8**, 225 (1974).
- (3) G. R. Somayajulu and B. J. Zwolinski, *J. Chem. Soc., Faraday Trans. 2*, **70**, 1889 (1974).
- (4) J. D. Cox and G. Pilcher, "Thermochemistry of Organic and Organometallic Compounds", Academic Press, New York, N.Y., 1970, pp 587-588.
- (5) R. M. Joshi, *J. Macromol. Sci. Chem.*, **A5**, 687 (1971).
- (6) S. W. Benson and J. H. Buss, *J. Chem. Phys.*, **29**, 546 (1958).
- (7) S. W. Benson, F. R. Cruickshank, D. M. Golden, G. R. Haugen, H. E. O'Neal, A. S. Rodgers, R. Shaw, and R. Walsh, *Chem. Rev.*, **69**, 279 (1969).
- (8) A group consists of a polyvalent atom with its covalently bonded neighbors. For example, ethane consists of two C-(C)(H)<sub>3</sub> groups.
- (9) S. W. Benson, "Thermochemical Kinetics", Wiley, New York, N.Y., 1968.
- (10) A larger number of groups, such as C<sub>B</sub>-(C<sub>BF</sub>)(H), may be logically distinguished. We find that such additional groups do not substantially increase predictive accuracy.
- (11) A. Bree, R. A. Kydd, T. N. Misra, and V. V. B. Vilkes, *Spectrochim. Acta, Sect. A*, **27**, 2315 (1971).
- (12) L. Malaspina, G. Bardi, and R. Gigi, *J. Chem. Thermodyn.*, **6**, 1052 (1974).
- (13) D. R. Stull, E. F. Westrum, Jr., and G. C. Sinke, "The Chemical Thermodynamics of Organic Compounds", Wiley, New York, N.Y., 1969.
- (14) (a) H. Inokuchi, S. Shiba, T. Handa, and H. Akamata, *Bull. Chem. Soc. Jpn.*, **25**, 299 (1952); (b) N. Wakayama and H. Inokuchi, *ibid.*, **40**, 2267 (1967).
- (15) We have chosen this value over the published value of 1.51 kcal mol<sup>-1</sup> per carbon atom<sup>16</sup> since this latter value was based on a set of measurements of heats of sublimation that were often slightly higher than those reported by other workers. See, for example, E. Morawetz, *J. Chem. Thermodyn.*, **4**, 461 (1972); J. J. Murray, R. F. Pottier, and C. Pupp, *Can. J. Chem.*, **55**, 757 (1974).
- (16) JANAF Thermochemical Tables, *Natl. Stand. Ref. Data Ser., Natl. Bur. Stand.*, **No. 37** (1971).
- (17) J. Abrahamson, *Carbon*, **11**, 337 (1973).
- (18) B. Nelander and S. Sunner, *J. Chem. Phys.*, **44**, 2476 (1966).
- (19) K. J. Laidler, *Can. J. Chem.*, **34**, 626 (1956).
- (20) J. C. Cox and G. Pilcher, "Thermochemistry of Organic and Organometallic Compounds", Academic Press, New York, N.Y., 1970.
- (21) (a) W. C. Herndon and M. L. Ellzey, Jr., *J. Am. Chem. Soc.*, **97**, 6631 (1975); (b) R. Swindorne-Sheldrake, W. C. Herndon, and I. Gutman, *Tetrahedron Lett.*, **10**, 755 (1975).

# Phase Relationships and Thermodynamic Properties of Transition Metal Borides. 1. The Molybdenum–Boron System and Elemental Boron<sup>†</sup>

Edmund Storms\* and Barbara Mueller

Los Alamos Scientific Laboratory of the University of California, Los Alamos, New Mexico 87544 (Received June 18, 1976; Revised Manuscript Received November 30, 1976)

Publication costs assisted by the U.S. Energy Research and Development Administration

The chemical activity of boron has been measured for compositions throughout the Mo–B system between 1800 and 2200 K using a mass spectrometer. A complete thermodynamic analysis is given. Based on this data and previously reported work, the Mo–B phase diagram has been refined. A value of  $137.4 \pm 0.2$  kcal/mol ( $574.9 \pm 0.8$  kJ/mol) at 298.15 K was determined for the second law enthalpy of vaporization of elemental boron. A photon counting pyrometer is described which permits temperatures near 2000 K to be determined with a precision of  $\pm 0.2$  K. By using this instrument, second law enthalpies of vaporization can be measured with an accuracy as good as that obtained from the third law method.

## I. Introduction

The molybdenum borides belong to a series of compounds which have properties of possible usefulness in thermionic energy conversion and magnetohydrodynamic generators (MHD). This paper reports the first of a series of studies which will present a coherent picture of the phase relationships and thermodynamic properties of these materials, and which will relate the results to a bonding model from which other properties can be predicted.

A mass spectrometer was used to measure the chemical activity of boron throughout the boride system. This information, in conjunction with previous studies, was used to refine the phase diagram between 1700 K and the melting points, and to calculate the free energy of the phases.

A photon counting pyrometer has permitted the second law enthalpies to be obtained with accuracy exceeding that obtained using other techniques to measure the temperature. Indeed, the second law method can now produce an enthalpy value which is at least as accurate as that derived from the third law method. Vaporization of elemental boron was studied using this instrument and a new value for the enthalpy of vaporization is presented.

The phase relationship in the Mo–B system has been studied most recently and completely by Rudy and Windisch.<sup>1</sup> Kiessling<sup>2</sup> has made the structure determinations. They found the system to consist of tetragonal (C16) Mo<sub>2</sub>B; MoB having two crystal forms, tetragonal (Bg) and orthorhombic (CrB type); "MoB<sub>2</sub>" with a simple hexagonal (C32) structure; "Mo<sub>2</sub>B<sub>5</sub>" which is rhombohedral (D8<sub>h</sub>); and a compound near MoB<sub>12</sub> of unknown structure. Previous assertions of a Mo<sub>3</sub>B<sub>2</sub> phase<sup>3,4</sup> were apparently based on impure material. We were able to confirm the work reported in ref 1 in many respects except as to the positions of the phase boundaries of the "MoB<sub>2</sub>" and "Mo<sub>2</sub>B<sub>5</sub>" phases. Indeed, our work suggests that the assigned crystal structures, from which the stoichiometry is implied, may not be correct. However, we will use the designations adopted by previous workers to avoid confusion.

There are very little data concerning the vaporization and thermodynamic properties of this system. Gilles and Pollock<sup>5</sup> measured pressures over various compositions using the Langmuir technique. Composition gradients

produced by the preferential loss of boron were a serious problem in their work. Baehren and Vollath<sup>6</sup> studied the reaction of Mo with BN to give Mo<sub>2</sub>B and nitrogen between 1358 and 1448 K from which the boron activity can be derived.

Mezaki et al.<sup>7</sup> have reported heat capacity values from 414 to 876 K for Mo<sub>2</sub>B and from  $\sim 450$  to  $\sim 1100$  K for MoB and MoB<sub>2</sub>. They also estimated the entropy for these phases at 298 K. However, the resulting thermal functions are too imprecise to permit an extrapolation to other temperatures.

The accepted value for the enthalpy of vaporization of elemental boron ( $\Delta H^\circ_{298}$ ) is  $133.8 \pm 3$  kcal/mol (CODATA, 1975). This is based on absolute vapor pressure measurements summarized in Table I and mass spectrometer measurements by Askishin et al.<sup>13</sup> (131.7 kcal/mol, third law) and by Schissel and Trulson<sup>14</sup> (132.8 kcal/mol, second law). The large uncertainty in the accepted value made a new study necessary.

## II. Experimental Section

A 60° sector, single focusing mass spectrometer was combined with a Knudsen effusion cell to measure the boron pressures over the boride compositions relative to pure boron. This method gave direct values for the chemical activity of boron. All measurements were made using tungsten effusion cells having either a  $6.2 \times 10^{-3}$  or a  $3.8 \times 10^{-2}$  cm<sup>2</sup> orifice. The cells were presaturated with boron before they were used. Consequently, the inner surface was tungsten boride.

Temperatures were measured at a black body hole through the side of the cell at the level of the sample surface. Temperature gradients were eliminated by suitably altering the power supplied to three independent, concentric tungsten filaments which supplied the electron bombardment current. Details of the oven and cell design can be found in ref 16.

*Temperature Measurement.* Temperatures (1968 IPTS) were measured using either a Pyro microoptical pyrometer or a photon counting pyrometer. Although the latter technique, proposed by Treiman,<sup>17</sup> will be described in detail elsewhere, some features of the design will be given here.

A Pyro microoptical pyrometer (The Pyrometer Instrument Co., Inc., Bergenfield, N.J.) was modified as shown in Figure 1. Light from the black body hole was focused onto a mirror containing a 0.010-cm hole using the

<sup>†</sup> Work completed under the auspices of the U.S. Energy Research and Development Administration, Division of Physical Research.

TABLE I: Third Law Enthalpy of Vaporization for Boron at 298 K, Revised Using JANAF<sup>15</sup> Functions

Ref	Reaction	Method	Value, kcal/mol
8	$B_s = B_g$	Langmuir	$136.4 \pm 0.3$
9	$B_s = B_g$	Knudsen, weight loss $ZrB_2$ cell	$138.1 \pm 0.3$
10	$B_s = B_g$	Torsion effusion	$136.1 \pm 0.3$
11	$B_4C = B_g + C_s$	Knudsen collection	$135.7 \pm 0.6$
12	$B_4C = B_g + C_s$	Torsion effusion	$136.4 \pm 1.3$
		Av	$136.5 \pm 0.5; 571.1 \pm 2.1$ kJ/mol

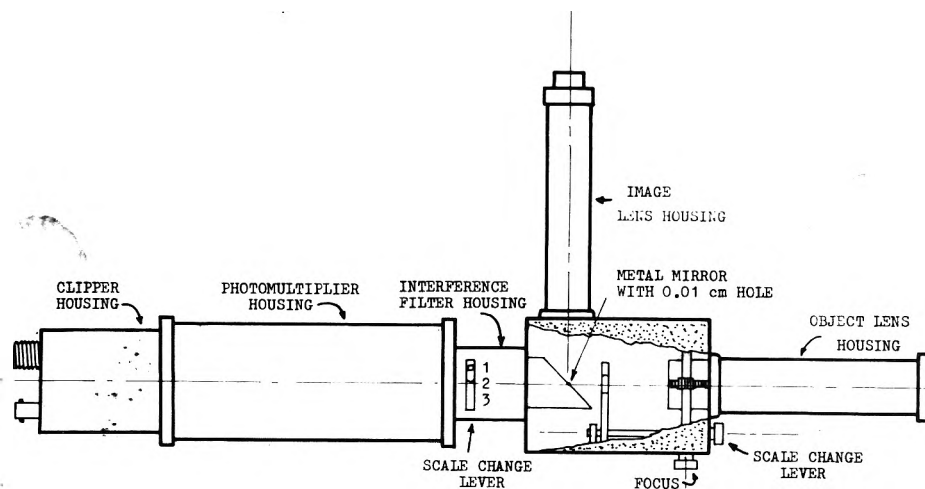


Figure 1. Top view of the photon counting pyrometer.

objective lens system. By viewing the mirror through the image lens system, the black body hole was focused and the hole in the mirror was placed on the image where the temperature was to be measured. Light which passed through the hole was attenuated by a choice of neutral density filters and by an interference filter having a transmission band centering at  $0.502 \times 10^{-6}$  m. The EMI 9502S photomultiplier was cooled to reduce background. Pulses from the photomultiplier were amplified, clipped, reamplified, and fed to a Hewlett-Packard 5345A counter.

Because the pulse width from the photomultiplier is approximately  $72 \times 10^{-9}$  s, dead-time corrections are necessary at the upper counting rates which approached  $10^6$  counts/s. This correction as well as attenuation factors for the filters were determined as follows: The pyrometer was focused onto an object at some temperature which gave a suitable count rate ( $R_1$ ) in the absence of a filter. A new count rate ( $R_2$ ) was measured with a filter in position. The attenuation factor ( $A$ ) and the dead-time ( $\gamma$ ) can be obtained from a series of such measurements by using the equation

$$R_1/R_2 = A - R_1\gamma(A - 1)$$

Attenuation factors for the other filters were found in a similar manner by using the ratio  $R_2/R_3$ ,  $R_3/R_4$ , etc. The corrected count rate ( $R_c$ ) was calculated from the measured count rate ( $R_m$ ) using the equation

$$R_c = (A_2, A_3, \text{etc})R_m/(1 - \gamma R_m)$$

where the attenuation factors for all lower scales are multiplied. Calibration of the pyrometer requires knowledge of the count rate ( $R_s$ ) at a known temperature ( $T_s$ ) (the gold point is used), the wavelength of the transmission maximum in the interference filter ( $\lambda$ ), and Planck's second radiation constant ( $C_2$ ). Planck's law relates the count rate,  $R_c$ , and the unknown temperature,  $T_m$ , through the equation

$$T_m = 1/((\ln R_s - \ln R_c)\gamma/C_2 + 1/T_s)$$

where  $C_2$  is taken as 0.014388 mK and  $1/T$  (the gold point)

is  $7.4762 \times 10^{-4} \text{ K}^{-1}$ . A further correction is imposed on  $T_m$  for the quartz window. Because this device uses the very basis for extrapolating the thermodynamic temperature scale above the gold point, the absolute accuracy is, in principle, as good as can be obtained. The precision, based on experience, is better than  $\pm 0.2$  K at 2000 K. A periodic comparison to a NBS calibrated optical pyrometer failed to show any difference which was outside the precision of the optical pyrometer ( $\pm 2^\circ$ ).

Second law enthalpies determined using this device are insensitive to all the calibration factors except the dead-time correction. This is because the relationship between the photon emission rate and temperature, and the relationship between ion current and temperature have a similar mathematical form in this application. As a result, the reproducibility in the enthalpy appears to be better than  $\pm 0.2$  kcal/mol ( $\pm 0.8$  kJ/mol). It is reassuring that the second law enthalpies obtained using a NBS calibrated optical pyrometer do not differ significantly from those obtained from the photon counting technique, although the former values show a much greater scatter.

Larger errors were encountered in the boride study because of the limited temperature range available for measurement (sample M) and possible variation in composition caused by the preferential vaporization of boron.

*Material Preparation and Characterization.* The borides were prepared by arc-melting together boron and molybdenum. Most of the samples were then annealed as the arc-melted button under vacuum to produce a homogeneous material. Samples were studied in the spectrometer as 20–60 mesh granulations.

Analysis for boron and molybdenum was made on the starting material. The sample was decomposed by sodium carbonate fusion and the components were separated using Dowex 1 resin. Mo was determined gravimetrically using  $\alpha$ -benzoin oxime and the boron content was obtained from the titration of mannitolboric acid. A few samples were analyzed for oxygen, by Pt fusion, and for carbon, by combustion in oxygen, after the study. Because the carbon

TABLE II: Summary of Minor Constituents in Certain Boride Samples

	Carbon, wt %	Oxygen, wt %
MoB <sub>2.56</sub> (A)	0.098	
MoB <sub>1.39</sub> (H)	0.058	
MoB <sub>1.01</sub> (J)	0.025	0.053
Boron <sup>a</sup>	0.20	

<sup>a</sup> Spectrochemical analysis found the following in ppm; Al, 200; Si, 500; Ca, 100; Ti, 400; Mn, 200; and Fe, 200.

originated in the boron, all of the borides had a carbon content which was proportional to the boron content. The results are listed in Table II. X-ray powder patterns, obtained using Cu K<sub>α</sub> radiation and a 114.6-mm diameter Debye-Scherrer camera, were used for phase identification.

**Vaporization Measurements and Data Treatment.** The <sup>11</sup>B vapor was ionized with 20-eV electrons. The resulting ion current (*I*) was combined with the measured temperature to give a linear least-squares relationship between log *IT* and 1/*T*. The boron activity was obtained by comparing the ion current from pure boron to that from the boride in consecutive measurements using the same Knudsen cell. Further details about the technique can be found in ref 19.

Each composition was studied more than once. The resulting second law enthalpies ( $\Delta\bar{H}_B$ ) and the interpolated log  $\alpha_B$  values at 2000 K were each averaged and combined to give an equation of the form  $\log \alpha_B = (\Delta H_B^\circ - \Delta\bar{H}_B)/RT + \Delta S_B$  for each composition. These data are listed in Table III.

Thus,  $\Delta\bar{H}_B$  and log  $\alpha_B$  were measured independently. If all of the error is assumed to be in the temperature measurement, typically the optical pyrometer gave a standard deviation of the points from the least-squares line of  $\pm 3$  K while the photon pyrometer gave a value of  $\pm 0.2$  K.

### III. Experimental Data

**Vaporization.** To provide a basis for the activity calculations, elemental boron was studied between approximately 1750 and 2050 K. Over this temperature range the vaporization enthalpy of boron was found to be  $135.9 \pm 0.2$  kcal/mol ( $568.6 \pm 0.8$  kJ/mol) and this value was used for all activity calculations. The data on which this value is based are listed in Table IV.

All of the borides evolved a large quantity of boron between 1000 and 1200 K when they were first heated after having been exposed to air. The amount evolved appeared to be greater the higher the boron content and this vapor was observed even if air exposure was less than 1 min. Exposure to water vapor produced the greatest effect. Only part of the boron ion signal was removed when the shutter between the ionization region and the oven was closed indicating that part of the boron containing gas could diffuse around the barrier. In addition, significant shutterable signals were observed at *m/e* values of 12, 27, and 70 indicating the presence of BH, BO, and B<sub>2</sub>O<sub>3</sub>.

Elemental boron continued to show the presence of BH and BO after the initial large burst had subsided. Under this condition, the second law enthalpy was influenced by the energy of the electrons used to ionize the vapor. Above approximately 25 eV the enthalpy increased as the electron energy increased. An enthalpy of 148 kcal/mol was obtained using 50-eV electrons. This effect appeared to be most pronounced when the vacuum in the oven region was the poorest ( $10^{-6}$  Torr). Below 25 eV the enthalpy appeared to be independent of electron energy. An energy of 20 eV was used for all measurements.

Boron which had been repeatedly exposed to air and vaporized showed a higher second law enthalpy, even at low electron energies. This we attribute to an increasingly thick coat of WB<sub>12</sub> on the boron caused by an exchange reaction between BO<sub>g</sub> and WO<sub>g</sub>.

The boride samples gave a reproducible second law enthalpy provided the vaporization rate from the cell was kept below a critical value. Once the temperature was increased so that the critical loss rate from the sample was exceeded, the boron signal began to fall and all subsequent measurements fell on a new line at lower boron pressures. On the other hand, when sample E (MoB<sub>1.86</sub>) was studied as the arc-melted button, without a previous anneal, the boron signal declined steadily at 1800 K and eventually reached a steady value after about 2.5 h. The signal dropped to about 1/3 of its initial value and the sample reached an activity characteristic of "MoB<sub>2</sub>" + "Mo<sub>2</sub>B<sub>5</sub>". Before the measurement the sample contained essentially pure "MoB<sub>2</sub>", but afterward nearly equal quantities of "MoB<sub>2</sub>" and "Mo<sub>2</sub>B<sub>5</sub>" were present. This sample also slowly converted to "MoB<sub>2</sub>" + "Mo<sub>2</sub>B<sub>5</sub>" while being stored at room temperature. Sample F also was pure "MoB<sub>2</sub>" after arc-melting but contained small amounts of MoB and "Mo<sub>2</sub>B<sub>5</sub>" after the activity measurements.

Samples I and J were pure  $\beta$ -MoB after arc-melting but were converted to  $\alpha$ -MoB + Mo<sub>2</sub>B by an anneal before the activity measurements.

**Lattice Parameter of "MoB<sub>2</sub>".** Lattice parameter values for "MoB<sub>2</sub>" are summarized in Table V. Samples in the region of MoB<sub>1.6</sub> which were cooled slowly contained three phases and the lattice parameter of "MoB<sub>2</sub>" appeared to be independent of composition. According to the phase diagram, a fixed composition at MoB<sub>1.62</sub> is retained under these conditions. Average lattice parameters of *a* = 3.040 Å and *c* = 3.061 Å were calculated for this composition. However, higher compositions of boron can be retained if a rapid quench is used. Increased retained boron causes no change in the "a" parameter but the "c" parameter is increased.

### IV. Discussion

**Elemental Boron.** Boron apparently reacts with absorbed or gaseous water at high temperatures to vaporize BH and BO. Measurements of the boron vapor pressure by mass spectrometry or by an absolute technique made under those conditions which produce BH and BO would give pressure values that are too high and, consequently, would give a third law enthalpy which is too low. We propose that this has caused a slight downward bias in previously reported, third law enthalpies. Thus, the correct value should be somewhat higher than the average of the values listed in Table I. The very low values obtained from mass spectrometric studies mentioned in the Introduction have been ignored.

In addition to the error introduced by additional boron containing species, there is the possibility that the vapor transport of tungsten to the boron surface would add an additional error to the second law value.

After minimizing these effects, we observe a second law enthalpy of vaporization for boron between 1800 and 2100 K of  $135.9 \pm 0.2$  kcal/mol based on the data listed in Table IV. Using the JANAF<sup>15</sup> thermal functions, this is equivalent to 137.4 kcal/mol ( $574.9 \pm 0.8$  kJ/mol) at 298.15 K.

**Thermodynamic Values for the Borides.** The only region which permits a comparison to other work is where Mo + Mo<sub>2</sub>B are in equilibrium. Baehren and Vollath<sup>6</sup> studied the equilibrium  $2\text{BN} + 4\text{Mo} = 2\text{Mo}_2\text{B} + \text{N}_2$ . We have converted their reported N<sub>2</sub> pressures to boron ac-

TABLE III: Summary of Boron Activity Measurements

No. of points	Apparent $\Delta\bar{H}_B$ , kcal/mol	Pyrometer	$-\log a_B$ 2000 K	No. of points	Apparent $\Delta\bar{H}_B$ , kcal/mol	Pyrometer	$-\log a_B$ 2000 K
A. $\text{MoB}_{2.56} \text{Mo}_2\text{B}_5 \gg \text{MoB}_{12}$							
9	141.15	Photon	0.026	8	141.04	Optical	0.000
6	139.99	Optical		13	140.37	Optical	0.068
$\log a_B = -1027/T + 0.483$							
B. $\text{MoB}_{2.16} \text{Mo}_2\text{B}_5 \gg \text{MoB}_{12}$							
11	144.25	Photon	0.040	9	139.55	Optical	
15	142.53	Photon	0.000	6	140.82	Optical	
$\log a_B = -1288/T + 0.624$							
C. $\text{MoB}_{2.15} \text{Mo}_2\text{B}_5$							
11	141.67	Photon	0.172	10	141.91	Optical	0.130
$\log a_B = -1288/T + 0.493$							
D. $\text{MoB}_{2.00} \text{Mo}_2\text{B}_5 \gg \text{MoB}_2$							
10	157.26	Photon	0.508	14	157.67	Optical	0.559
13	157.82	Photon	0.527	9	159.54	Optical	0.550
$\log a_B = -4845/T + 1.887$							
E. $\text{MoB}_{1.84} \text{MoB}_2 = \text{Mo}_2\text{B}_5$							
12	156.84	Photon	0.435	10	155.55	Optical	0.558
10	159.19	Optical	0.458	6	157.15	Optical	
$\log a_B = -4651/T + 1.842$							
F. $\text{MoB}_{1.62}$ Annealed, $\text{MoB}_2 > \text{MoB} \gg \text{Mo}_2\text{B}_5$							
12	151.66	Photon	0.584	12	151.06	Photon	0.570
$\log a_B = -3379/T + 1.113$							
G. $\text{MoB}_{1.55}$ Annealed, $\text{MoB}_2 \gg \text{MoB} = \text{Mo}_2\text{B}_5$							
12	139.87	Photon	0.710	11	142.60	Optical	0.710
14	139.83	Photon	0.760				
$\log a_B = -1065/T - 0.194$							
H. $\text{MoB}_{1.39}$ Annealed, $\text{MoB}_2 > \text{MoB} > \text{Mo}_2\text{B}_5$							
12	140.21	Photon	0.840	15	140.60	Photon	0.834
10	144.49	Photon	0.840	12	139.48	Optical	0.804
6	140.15	Photon		14	141.15	Optical	0.836
$\log a_B = -1117/T - 0.271$							
I. $\text{MoB}_{1.06}$ Annealed, $\alpha\text{-MoB} > \text{MoB}_2$							
17	140.49	Photon	0.797	5	136.31	Optical	0.751
9	139.05	Photon	0.666				
$\log a_B = -595/T - 0.441$							
J. $\text{MoB}_{1.01} \alpha\text{-MoB} > \text{MoB}_2$							
11	136.28	Photon	0.736	8	136.56	Optical	0.800
6	137.60	Optical		8	135.10	Optical	
11	134.11	Optical	0.835				
$\log a_B = -7/T - 0.787$							
K. $\text{MoB}_{0.790} \text{Mo}_2\text{B} = \alpha\text{-MoB}$							
21	138.84	Photon	2.22	10	164.34	Optical	2.46
12	142.85	Photon	2.08	5	156.07	Optical	
9	167.94	Optical	2.52	9	162.34	Optical	
$\log a_B = -4262/T - 0.189$							
L. $\text{MoB}_{0.49} \text{Mo}_2\text{B} \gg \text{Mo}$							
14	160.23	Photon	2.58	13	155.90	Optical	2.49
$\log a_B = -4845/T - 0.117$							
M. $\text{MoB}_{0.37} \text{Mo}_2\text{B} = \text{Mo}$							
6	158.14	Optical	2.93	9	176.88	Optical	2.97
$\log a_B = -6906/T + 0.503$							

tivities using the free energy for BN as compiled by JANAF.<sup>15</sup> Their results are compared to the results from our measurement of sample M in Figure 2. By combining both data sets, the equation  $\log a_B = -7240/T + 0.673$  is obtained and plotted in Figure 2. All subsequent calculations will be based on this equation. Also shown on the figure is the activity resulting from the Langmuir measurements of Gilles and Pollock.<sup>5</sup> Other compositions studied by Gilles and Pollock<sup>5</sup> gave pressures which are in substantial disagreement with our work, owing, we believe, to a large preferential loss of boron from this system, and the resulting concentration gradients in their samples.

The molybdenum activity for the various two phase regions was determined from a Gibbs-Duhem integration of the boron activities shown in Figures 3 and 4. Table VI lists the relevant data. Equations listed in Table VII were obtained by combining the resulting Mo activities at the two temperatures shown in Table VI.

*Phase Diagram.* The results of our X-ray examination, the variation of activity with composition shown in Figures 3 and 4, and the extensive studies of Rudy and Windisch<sup>1</sup> were all combined to produce the phase diagram shown in Figure 5. Also shown in this figure is the temperature range of each activity measurement. Each phase will now be discussed separately.

TABLE IV: Summary of the Measured Second Law Enthalpy of Vaporization for Boron

Enthalpy, kcal/mol	Error <sup>a</sup>	Error K <sup>b</sup>	No. of points	Temp range, K
136.69	0.04	0.1	13	1857-2088
135.19	0.14	0.5	12	1765-2096
135.75	0.08	0.3	7	
135.88	0.12	0.4	6	
136.03	0.11	0.4	14	1721-2118
135.31	0.07	0.3	11	1586-2055
136.28	0.11	0.4	9	
136.12	0.18	0.5	10	1752-2005
136.00	0.19	0.5	7	
136.14	0.25	0.6	6	
136.02	0.27	0.5	9	
135.14	0.09	0.3	19	1752-2012
136.03	0.17	0.5	13	1769-1977
Av				
135.89	0.14 <sup>c</sup>	at 1900		

<sup>a</sup> Standard deviation in the enthalpy based on least-squares treatment. <sup>b</sup> Standard deviation of a point from the least-squares line assuming all of the error in the temperature value. <sup>c</sup> Standard deviation of each enthalpy from the average. Each entry resulted from separate boron loading. The measurements were interspersed between the various Mo-B samples.

TABLE V: Summary of Lattice Parameter Values (Å) for "MoB<sub>2</sub>"

B/Mo	Arc-melted	After mass spectrometer study
1.84 E	a 3.040 ± 0.001	3.040 ± 0.001
	c 3.072	3.060
1.62 F	a 3.040	3.040
	c 3.061	3.061
1.55 G	a	3.039
	c	3.062
1.48	a 3.038	3.039
	c 3.062	3.060

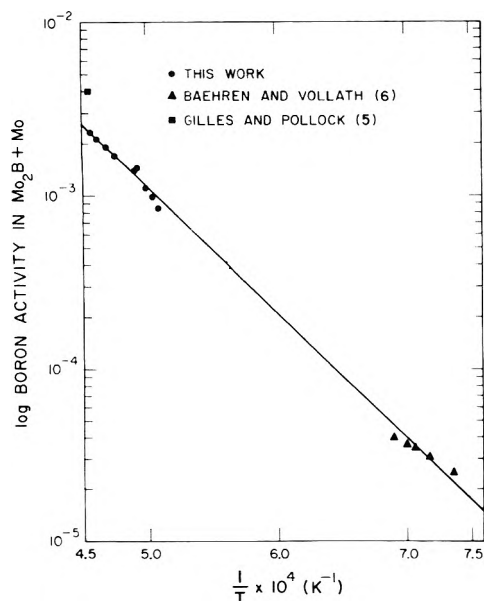


Figure 2. Comparison between the various measurements of boron activity in Mo<sub>2</sub>B + Mo.

**Mo<sub>2</sub>B.** Based on the measured boron activity, sample L (MoB<sub>0.49</sub>) was single phase over the temperature range of measurement. However, the X-ray powder pattern showed lines attributable to Mo metal. Thus, Mo<sub>2</sub>B appears to be a line compound at low temperatures with a slight widening on the low boron side as the temperature is increased.

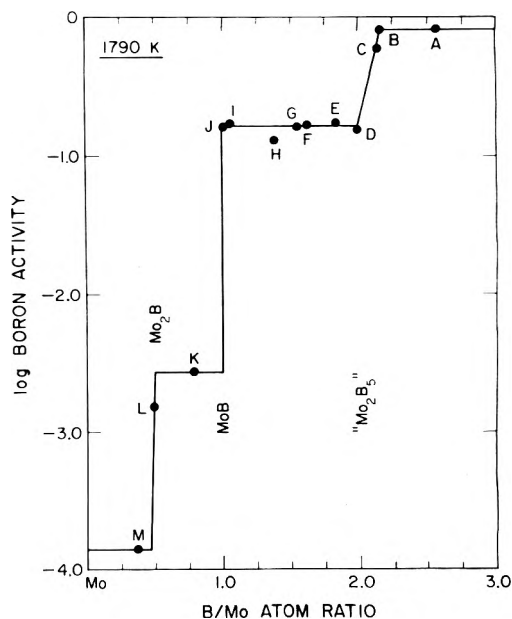


Figure 3. Log boron activity as a function of B/Mo atom ratio at 1790 K.

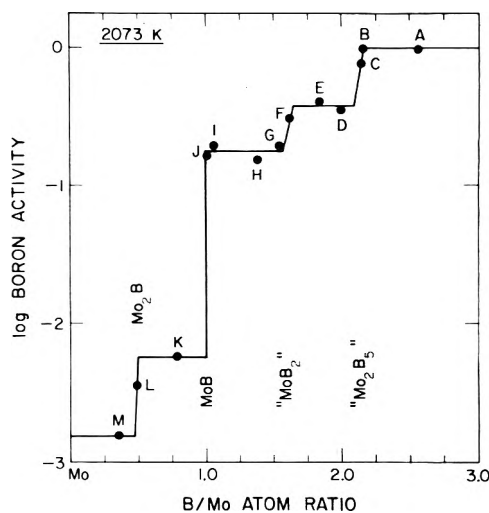


Figure 4. Log boron activity as a function of B/Mc atom ratio at 2073 K.

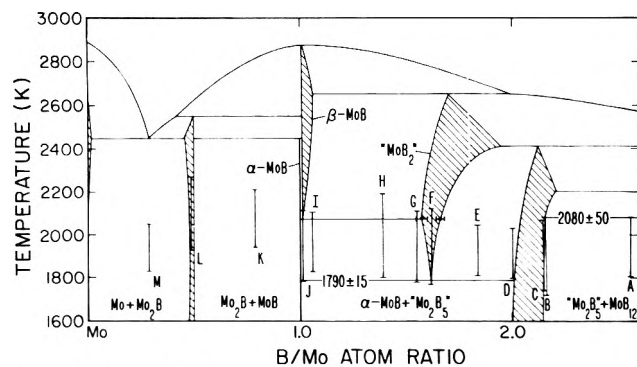


Figure 5. Phase diagram of the Mo-B system.

**MoB.** Sample J restricts the high boron boundary of  $\alpha$ -MoB to values below MoB<sub>1.01</sub>. The position of the low boron boundary is uncertain and has been drawn to indicate a line compound. According to Rudy and Windisch,<sup>1</sup> the  $\beta$  form widens on the high boron side.

**"MoB<sub>2</sub>".** The composition of "MoB<sub>2</sub>" lies significantly below the perfect lattice composition assigned to this compound. The maximum in the lower boundary falls between MoB<sub>1.55</sub> and MoB<sub>1.60</sub> at 2073 K (Figure 4) and the

TABLE VI: Mo and B Activities and Free Energies of Formation for Various Phase Boundary Compositions at 1790 and 2073 K

Phase designation	Lower phase boundary				Upper phase boundary			
	B/Mo	Boron activity	Molybdenum activity	$-\Delta G_f^a$ , kcal/mol	B/Mo	Boron activity	Molybdenum activity	$-\Delta G_f^a$ , kcal/mol
$T = 1790$ K								
Mo <sub>2</sub> B	0.48	4.25E-04	1.00E 00	13.26	0.50	2.69E-03	4.05E-01	13.74
$\alpha$ -MoB	1.00	2.69E-03	4.05E-01	24.27	1.00	1.60E-01	6.81E-03	24.27
"MoB <sub>2</sub> "	1.26	1.60E-01	6.81E-03	28.31	1.62	1.60E-01	6.81E-03	28.31
"Mo <sub>2</sub> B <sub>5</sub> "	2.00	1.60E-01	6.81E-03	30.79	2.16	8.10E-01	2.33E-04	31.37
MoB <sub>1,2</sub>	12.00	8.10E-01	2.33E-04	38.74	12.00	1.00E 00	1.86E-05	38.74
$T = 2073$ K								
Mo <sub>2</sub> B	0.48	1.52E-03	1.00E 00	12.83	0.50	5.69E-03	5.24E-01	13.31
$\alpha$ -MoB	1.00	5.69E-03	5.24E-01	23.96	1.00	1.78E-01	1.67E-02	23.96
"MoB <sub>2</sub> "	1.58	1.78E-01	1.67E-02	28.08	1.66	3.70E-01	5.12E-03	28.53
"Mo <sub>2</sub> B <sub>5</sub> "	2.10	3.70E-01	5.12E-03	30.33	2.16	1.00E-00	6.16E-04	30.46
MoB <sub>1,2</sub>	12.00	1.00E 00	6.16E-04	30.46	12.00	1.00E-00	6.16E-04	30.46

<sup>a</sup> Based on 1 g atom of molybdenum for a composition at the phase boundary.

TABLE VII: Equations Describing the Mo Activity Vs. Temperature in the Various Two Phase Regions of the MoB System

Phases in equilibrium	$\log a_{\text{Mo}} = A/T + B(1790-2073 \text{ K})$	
	A	B
Mo <sub>2</sub> B + MoB	-1467	+0.427
MoB + "MoB <sub>2</sub> "	-5108	+0.687
"Mo <sub>2</sub> B <sub>5</sub> " + "MoB <sub>2</sub> "	+1624	-3.074
MoB <sub>1,2</sub> + "Mo <sub>2</sub> B <sub>5</sub> "	-5460	-0.547
B + MoB <sub>1,2</sub>	-19854	+6.397

maximum in the upper boundary is between MoB<sub>1,9</sub> and MoB<sub>2,0</sub> at the peritectic temperature. The latter conclusion is based on the observation in ref 1 that MoB<sub>1,94</sub> quenched from the melt contained only "MoB<sub>2</sub>" and our observation that MoB<sub>2,00</sub> treated in a similar manner contained a mixture of "MoB<sub>2</sub>" and "Mo<sub>2</sub>B<sub>5</sub>". The decomposition temperature of "MoB<sub>2</sub>" was found to be  $1790 \pm 15$  K, by determining the temperature at which calculated boron activities of samples D, E, F, G, H, I, and J have a minimum deviation from the same activity value (Figure 3). Rudy and Windisch<sup>1</sup> report  $1793 \pm 50$  K for this temperature based on thermal arrest measurements.

"Mo<sub>2</sub>B<sub>5</sub>". Like "MoB<sub>2</sub>", the composition of this phase lies significantly lower than that based on its perfect lattice composition. Samples B, C, and D place the single phase region between MoB<sub>2,00</sub> and MoB<sub>2,16</sub> between 1800 and 2100 K. Both phase boundaries shift to an increased stoichiometry as the temperature is increased but the magnitude is uncertain. The data presented by Rudy and Windisch<sup>1</sup> do not conflict with this conclusion.

MoB<sub>1,2</sub>. The temperature at which the MoB<sub>1,2</sub> phase decomposes was found to be  $2080 \pm 50$  K, obtained by averaging the temperatures at which the boron activity in samples A and B equals unity. Rudy and Windisch<sup>1</sup> report  $\sim 2073$  K.

**Structure.** Boride structures are strongly influenced by covalently bonded chains or networks between the boron atoms. Indeed, these networks are believed to be the dominant factor in holding the lattices of the higher borides together. Consequently, it is surprising to find that "MoB<sub>2</sub>" and "Mo<sub>2</sub>B<sub>5</sub>" can contain such a high concentration of boron vacancies. On the other hand, a more consistent picture of boride chemistry would result if the structures previously proposed for both "MoB<sub>2</sub>" and "Mo<sub>2</sub>B<sub>5</sub>" are wrong, if the correct structures have respective stoichiometries of Mo<sub>2</sub>B<sub>3</sub> and MoB<sub>2</sub>, and if the observed variation in composition is owing to the presence of vacancies in the metal sublattice. However, the lattice

expands as the atom ratio increases, a very unusual behavior if the metal vacancy content is increasing. These possibilities are worth exploring in future studies.

## V. Summary

The present measurements have refined the phase diagram of the Mo-B system and have produced thermochemical data for compositions above Mo<sub>2</sub>B for the first time.

With a few exceptions the phase relationships reported by Rudy and Windisch<sup>1</sup> have been confirmed. Our work places the "MoB<sub>2</sub>" and "Mo<sub>2</sub>B<sub>5</sub>" phases at such a low stoichiometry compared to the proposed lattice composition that there is doubt that the correct structures have been reported for these phases.

Values for the partial enthalpies of vaporization, and partial and total free energies of formation have been determined throughout the composition range of the system. The results indicate that the borides of molybdenum appear to be at least twice as stable as the molybdenum carbides.

The enthalpy of vaporization of pure boron has been redetermined using a photon counting pyrometer by the second law technique. We propose a value of  $137.4 \pm 0.2$  kcal/mol ( $574.9 \pm 0.8$  kJ/mol) at 298.15 K.

A photon counting pyrometer is described which permits second law enthalpies to be determined with an accuracy equal to that obtained from third law methods.

**Acknowledgment.** Ms. M. Pretzel prepared the X-ray films. J. E. Troxel, A. D. Hues, A. L. Henicksman, B. H. Baca, and L. A. Pulliam (CMB-1) analyzed the samples. S. R. Skaggs aided the X-ray analysis and R. G. Behrens gave editorial advice. J. Farr, by his continued interest, facilitated this work.

## References and Notes

- (1) E. Rudy and St. Windisch, AFML-TR-65-2, Part I, Vol. III (1965).
- (2) R. Kießling, *Acta Chem. Scand.* **1**, 893 (1947).
- (3) R. Steinitz, L. Binder, and D. Moskowitz, *J. Metals*, **4**, 983 (1952).
- (4) P. W. Gilles and B. D. Pollock, *J. Metals*, **5**, 1537 (1953).
- (5) P. W. Gilles and B. D. Pollock, AECU-2894 (1962).
- (6) Von F. D. Baehren and D. Vollath, *Planseeber. Pulvermetall.*, **17**, 180 (1969).
- (7) R. Mezaki, E. W. Tilleux, D. W. Barnes, and J. L. Margrave, Proceedings of the International Symposium on the Thermodynamics of Nuclear Materials, Paper S-M26/48, Vienna, 1962, pp 775-788.
- (8) R. G. Paule and J. L. Margrave, *J. Phys. Chem.*, **67**, 1368 (1963).
- (9) A. W. Searcy and C. E. Myers, *J. Phys. Chem.*, **61**, 957 (1957).
- (10) D. L. Hildenbrand, "QLR-64-10", Philco Corp., Calif.
- (11) H. E. Robson and P. W. Gilles, *J. Phys. Chem.*, **68**, 983 (1964).
- (12) D. L. Hildenbrand and W. F. Hall, *J. Phys. Chem.*, **68**, 989 (1964).
- (13) P. A. Akishin, D. O. Hikitin, and L. N. Gorokhov, *Proc. Acad. Sci., USSR*, **129**, 1075 (1959).
- (14) P. O. Schissel and O. C. Trulson, *J. Phys. Chem.*, **66**, 1492 (1962).

- (15) "JANAF Thermochemical Data", Dow Chemical Co., Midland, Mich, 1964.  
 (16) E. K. Storms, *High Temp. Sci.*, **1**, 456 (1969).  
 (17) L. H. Treiman, *Temp. Its Meas. Control Sci. Ind., Proc. Symp. Temp.*

- 1961, **3**, 523 (1962).  
 (18) J. K. Hulm and B. T. Matthias, *Phys. Rev.*, **82**, 273 (1951).  
 (19) E. K. Storms, B. Calkin, and A. Yench, *High Temp. Sci.*, **1**, 430 (1969).

## Internal Pressures and Solubility Parameters for Carbon Disulfide, Benzene, and Cyclohexane

J. A. R. Renuncio,<sup>†</sup> G. J. F. Breedveld,\* and J. M. Prausnitz

Chemical Engineering Department, University of California, Berkeley, California 94720 (Received March 29, 1976)

Publication costs assisted by the National Science Foundation

Densities of carbon disulfide, benzene, and cyclohexane were measured in the region 23–65 °C at pressures to 1 kbar. The data were used to calculate internal pressures and these were compared with solubility parameters obtained from liquid molar volumes at saturation and isothermal energies of vaporization to the ideal-gas state. Along the saturation line, the square root of the internal pressure is somewhat larger than the solubility parameter (square root of cohesive energy density). For benzene and cyclohexane the internal pressure decreases with temperature while the reverse holds true for carbon disulfide. As the external pressure rises, the internal pressures of benzene and cyclohexane generally increase while that of carbon disulfide tends to decrease. The new data also suggest that the previously reported internal pressures for carbon disulfide are too low. The new data show that the ratio of internal pressure to cohesive energy density is slightly larger than unity for all three liquids.

The role of internal pressure in liquid-solution thermodynamics was recognized many years ago by Hildebrand<sup>1</sup> following earlier work by van Laar.<sup>2</sup> The use of this fundamental property has for a long time been limited to descriptive or qualitative purposes. As noted by Barton,<sup>3</sup> it is only recently that its usefulness has been explored for quantitative study of intermolecular forces. Since the early attempts to calculate this property by the van der Waals equation (as suggested by van Laar) yielded only qualitative results, Hildebrand and Scatchard<sup>2</sup> proposed the concept of cohesive energy density which is the energy of isothermal vaporization from the liquid to the ideal-gas state, not per mole but per unit volume of fluid. The large advantage of the cohesive energy density is that it can be calculated easily for liquids at normal conditions using readily available data. The square root of the cohesive energy density is the well-known solubility parameter  $\delta$ . This property is extensively discussed in a review presented by Barton.<sup>3</sup>

In our work we present some new data on the internal pressures of three common fluids and we discuss the relation between these data and the solubility parameter.

The quantitative relation between solubility parameter and internal pressure  $P_i$  has not been completely resolved. The formal definitions of these quantities are

$$\delta = [\Delta U/V]^{1/2} \quad (1)$$

$$P_i = \left( \frac{\partial U}{\partial V} \right)_T = \left[ T \left( \frac{\partial P}{\partial T} \right)_V - P \right] \quad (2)$$

where  $V$  is the molar volume of the liquid and  $\Delta U$  is the molar energy of complete vaporization as indicated above.  $P_i$  is clearly the isothermal volume derivative of the internal energy and a detailed knowledge of  $U$  as a function

of volume would be required to relate  $P_i$  to  $\delta^2$ , the latter being an integral quantity and a commonly used measure of molecular cohesion in the liquid state.

To relate the two quantities, Hildebrand<sup>1</sup> proposed the empirical equation

$$P_i = n \frac{\Delta U}{V} = n \delta^2 \quad (3)$$

where  $n$  is a constant. Equation 3 was suggested by van der Waals' equation where  $n$  is exactly equal to unity; data by Hildebrand and co-workers<sup>1</sup> indicated that  $n$  is a little larger than unity (within about 10%) for typical nonpolar liquids. For benzene and *n*-heptane Hildebrand found, respectively,  $n = 1.05$  and  $1.09$ . Carbon disulfide gave a surprisingly low value (0.89) which indicated either that there was something qualitatively "different" about carbon disulfide in the liquid state or else that the experimental data for carbon disulfide were not reliable.

### Experimental Section

We have measured the volumes of benzene, cyclohexane, and carbon disulfide as a function of temperature and pressure, using a high-pressure bellows dilatometer described elsewhere.<sup>4,5</sup> Measurements extend to 1000 bars and cover the temperature region 23–65 °C. Volumes are measured relative to those at the same temperature at atmospheric pressure. Pressures were measured with a precision Heise gauge with an accuracy of about  $\pm 1$  bar. The high-pressure dilatometer was in a constant-temperature bath controlled to  $\pm 0.01$  °C by a Hallikainen proportional controller. Temperatures were measured with calibrated thermometers with an accuracy of  $\pm 0.05$  °C. The overall uncertainty in the volumetric measurements is estimated to be  $\pm 0.04\%$ .

The liquids were of spectroquality; benzene and cyclohexane were obtained from Matheson Coleman and Bell (Norwood, Ohio) and carbon disulfide was obtained from

<sup>†</sup> Current address: Dpto. de Quimica Fisica, Facultad de Quimicas, Ciudad Universitaria, Madrid-3, Spain.

TABLE I: Constants in the Tait Equation of State<sup>a</sup>

Constant	Carbon disulfide		Benzene	Cyclohexane
	This work	Bridgman		
$B_1$	-0.303 21	0.310 81	1.692 0	1.018 62
$B_2$	$0.986 87 \times 10^{-2}$	$0.361 21 \times 10^{-2}$	$-0.831 40 \times 10^{-2}$	$0.610 96 \times 10^{-3}$
$B_3$	$-0.322 59 \times 10^{-4}$	$-0.110 54 \times 10^{-4}$	$0.416 86 \times 10^{-4}$	$-0.110 10 \times 10^{-6}$
$B_4$	$0.386 63 \times 10^{-7}$	$0.147 83 \times 10^{-7}$	$-0.119 73 \times 10^{-6}$	$0.379 34 \times 10^{-8}$
$B_5$	0	0	$0.173 54 \times 10^{-9}$	0
$B_6$	0	0	$-0.103 24 \times 10^{-12}$	0
$C$	0.143 57	0.107 69	$0.978 18 \times 10^{-1}$	$0.925 98 \times 10^{-1}$
$D_1$	$0.892 69 \times 10^4$	$0.122 92 \times 10^5$	$0.108 70 \times 10^5$	$0.935 28 \times 10^4$
$D_2$	$0.537 27 \times 10^{-2}$	$0.783 92 \times 10^{-2}$	$0.801 30 \times 10^{-2}$	$0.815 70 \times 10^{-2}$

<sup>a</sup> Volumes in cm<sup>3</sup>/g, pressures in bars, temperatures in K.

Mallinckrodt Chemical Works (St. Louis, Mo.).

## Results

Detailed experimental results are available as supplementary material (see paragraph at end of text). We report here only a summary. The data were represented by a particular form<sup>4</sup> of the Tait equation

$$V/V_0 = 1 - C \ln(1 + P/F) \quad (4)$$

where  $V$  is the volume of the liquid at pressure  $P$  and temperature  $T$  and  $V_0$  is the volume at  $P = 1$  bar and temperature  $T$ . Units are cm<sup>3</sup>/g, bars, and kelvin. The constant  $C$  is independent of temperature but the constant  $F$  depends on  $T$  according to

$$F = D_1 \exp(-D_2 T) \quad (5)$$

where  $D_1$  and  $D_2$  are constants.

For carbon disulfide and cyclohexane the volume  $V_0$  was expressed as a function of temperature by

$$V_0 = B_1 + B_2 T + B_3 T^2 + B_4 T^3 \quad (6)$$

while for benzene, the equation used has the form

$$V_0 = [B_1 + B_2 T + B_3 T^2 + B_4 T^3 + B_5 T^4 + B_6 T^5]^{-1} \quad (7)$$

To obtain the empirical  $B$  constants for carbon disulfide, we used data from the literature.<sup>6-10</sup> For cyclohexane the constants are given by Nelson<sup>11</sup> and for benzene by Ambrose and Lawrenson.<sup>12</sup> All empirical coefficients are given in Table I.

Internal pressures were calculated from the Tait equation using standard thermodynamics. Solubility parameters were calculated for the saturated liquids as discussed by Hildebrand and Scott<sup>1</sup> using vapor-pressure data, molar liquid volumes along the saturation curve, and (small) corrections for gas-phase imperfections.

We also calculated internal pressures using Bridgman's<sup>13</sup> carbon disulfide data for pressures to 980 bars using his  $B$  constants. However, Bridgman's volumetric data for this region are extremely limited and, therefore, internal pressures calculated from these data are not highly reliable.

Figure 1 shows internal pressures for carbon disulfide as a function of temperature. We compare our results with those based on Bridgman's data and note that our internal pressures are 4-9% larger than those based on his measurements. Further, we call attention to the importance at high pressures of the second term in the definition of the  $P_i$  (eq 2). In the literature one often finds a definition of the internal pressure which neglects  $P$ . At low pressures, where  $P \ll T(\partial P/\partial T)_V$ , the second term can be neglected without significant error but at high pressures one must be sure to include it.

Figure 2 shows internal pressures and solubility parameters as a function of temperature for carbon disulfide,

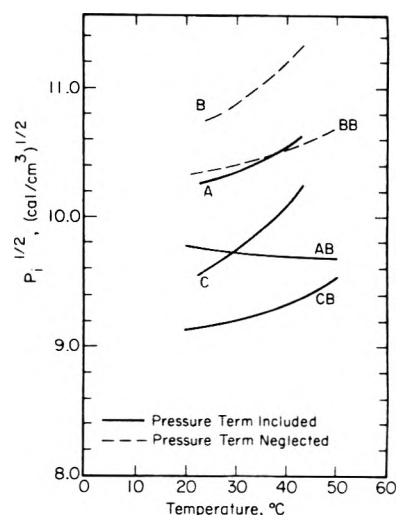


Figure 1. Square root of internal pressure  $P_i$  for carbon disulfide: (A) this work, zero pressure; (B) this work, 1000 bars, pressure term in  $P_i$  neglected; (C) this work, 1000 bars; AB, BB, CB same as A, B, C, respectively, but using Bridgman's<sup>13</sup> data, maximum pressure 980 bars.

benzene, and cyclohexane. Lines A, B, and C give internal pressures calculated as indicated in the figure caption; lines D give solubility parameters.

Finally, Figure 3 presents internal pressures for carbon disulfide, cyclohexane, and benzene as a function of volume at constant temperature. (Note the special volume scale for cyclohexane.)

Curves A, B, and C for benzene and cyclohexane change inconsistently with increasing temperature, in contrast with the behavior of the curves for carbon disulfide, which show no anomalies. Since the pressure-temperature data for carbon disulfide are much farther below the freezing line than the data for benzene and cyclohexane, we excluded for the latter two substances a number of data points which are near the freezing lines, to eliminate prefreezing effects, if any. This exclusion produces a change of the constants in eq 4 and 5 but no improvement in the shape of the curves. Gibson and Loeffler,<sup>14</sup> using Gibson and Kincaid's<sup>14</sup> equations for benzene, obtain curves without the erratic characteristics of the ones shown in this work, although the differences in  $P_i^{1/2}$  only vary from -2 to +4%. Their equation is similar to our eq 4 but

$$F = D_1 - D_2(T - 298.15) + D_3(T - 298.15)^2 \quad (8)$$

Our eq 4 and 5, fitted to their data, result in the same erratic curves as those shown in Figure 3. The combination of eq 4 and their eq 8 fitted to our data, however, results in properly shaped curves with  $P_i^{1/2}$  differing between -1.7 and +0.9% from our original values. The calculated volumes differ from -0.03 to +0.03%. The use of eq 4 and 8 with our data for cyclohexane slightly accentuates the

TABLE II: Empirical Constant  $n$  in Eq 3

Temp, °C	Carbon disulfide			Benzene		Cyclohexane	
	20	25	35	25	35	25	35
$P_i$ from this work	1.04 <sup>a</sup>	1.06 <sup>a</sup>	1.12 <sup>a</sup>	1.06 <sup>c</sup>	1.06 <sup>c</sup>	1.14 <sup>e</sup>	1.15 <sup>e</sup>
$P_i$ from earlier work	0.88 <sup>b</sup>	0.88 <sup>b</sup>	0.91 <sup>b</sup>	1.06 <sup>d</sup>	1.07 <sup>d</sup>	1.15 <sup>f</sup>	1.16 <sup>f</sup>

<sup>a</sup>  $\Delta U$  from ref 1 and 18. <sup>b</sup>  $\Delta U$  from a;  $P_i$  from ref 16 and 17. <sup>c</sup>  $\Delta U$  from ref 1 and 12. <sup>d</sup>  $\Delta U$  from c;  $P_i$  from ref 16, 17, and 19. <sup>e</sup>  $\Delta U$  from ref 17 and 21. <sup>f</sup>  $\Delta U$  from e;  $P_i$  from ref 21.

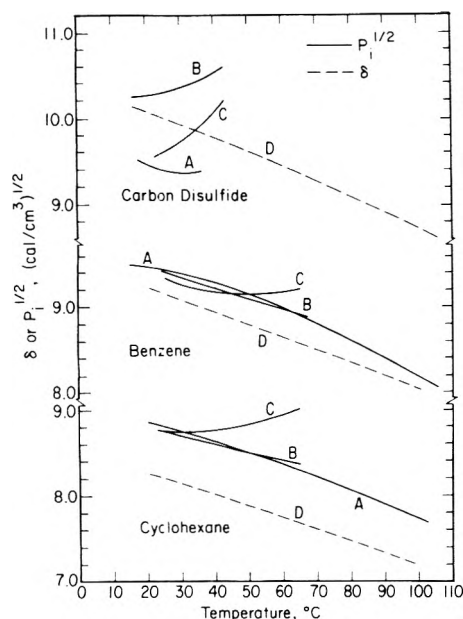


**Figure 2.** Solubility parameter  $\delta$  and internal pressure  $P_i$ . Carbon disulfide: (A)  $P_i^{1/2}$ , Westwater et al.,<sup>16</sup> Allen et al.,<sup>17</sup> maximum 24 bars; (B)  $P_i^{1/2}$  this work, saturation curve,<sup>18</sup> maximum 1.1 bar; (C)  $P_i^{1/2}$ , this work, 1000 bars; (D)  $\delta$ , calculated from energies of vaporization, Hildebrand and Scott,<sup>7</sup> and O'Brien and Alford,<sup>18</sup> maximum 5 bars. Benzene: (A)  $P_i^{1/2}$ , Westwater et al.,<sup>16</sup> Allen et al.,<sup>17</sup> Rowlinson,<sup>19</sup> maximum 24 bars; (B)  $P_i^{1/2}$  this work, saturation curve,<sup>12</sup> maximum 1.8 bars; (C)  $P_i^{1/2}$ , this work, 700–1000 bars, (smoothed); (D)  $\delta$ , calculated from energies of vaporization, Hildebrand and Scott,<sup>1</sup> Ambrose and Lawrenson,<sup>12</sup> maximum 1.8 bars. Cyclohexane: (A)  $P_i^{1/2}$ , Allen et al.,<sup>17</sup> Bianchi et al.,<sup>20</sup> Bagley et al.,<sup>21</sup> maximum 30 bars; (B)  $P_i^{1/2}$ , this work, saturation curve,<sup>22</sup> maximum 0.97 bar; (C)  $P_i^{1/2}$ , this work, 300–1000 bars (smoothed); (D)  $\delta$  calculated from energies of vaporization, Allen et al.,<sup>17</sup> Bagley et al.,<sup>21</sup> maximum 1.6 bars.

erratic behavior of the curves. Possibly another equation of state or somewhat greater experimental accuracy are required to remove the apparent unusual behavior.

Calculated internal pressures appear to be sensitive to the experimental accuracy and to the equations of state used for representation of the data. This may partly be due to the fact that  $P_i^{1/2}$  is closely related to  $(\partial P/\partial T)_V = -(\partial V/\partial T)_P/(\partial V/\partial P)_T$ . Therefore one cannot expect highly reliable results if data in the particular pressure–temperature range are scarce. This is the case with Bridgman's<sup>13</sup> data for carbon disulfide and also with Reamer and Sage's<sup>15</sup> data for cyclohexane. With the latter we obtain proper curves with our and also with Gibson and Kincaid's equations of state, with  $P_i^{1/2}$  values differing between –6 and 9% from ours. The former also do not agree with those reported by Westwater et al.<sup>16</sup> and by Allen et al.<sup>17</sup>

The results shown in Figures 1–3 suggest, once again, that while internal pressure and cohesive energy density are of comparable magnitude, there is no simple quantitative relation between internal pressure and solubility parameter. Along the saturation line the square root of the internal pressure is somewhat larger than the solubility parameter. For benzene and cyclohexane the internal pressure decreases with temperature while the reverse is observed for carbon disulfide. At pressures in excess of

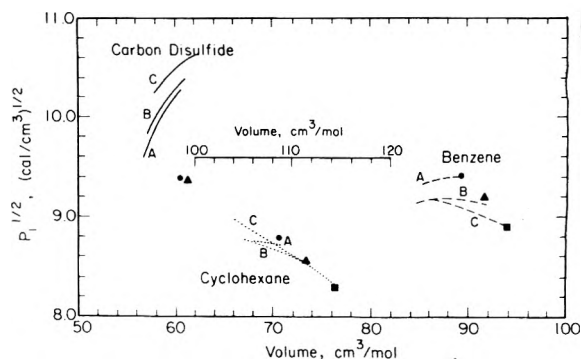


**Figure 3.** Effect of volume on internal pressure at constant temperature. Carbon disulfide: (—) this work, (A) 25 °C, maximum 1000 bars; (B) 33.9 °C, maximum 1000 bar; (C) 43.3 °C, maximum 1000 bars; (●) 25 °C, (▲) 33.9 °C, maximum 25 bars, Westwater et al.,<sup>16</sup> Allen et al.<sup>17</sup> Cyclohexane: (.....) this work, (A) 25 °C, maximum 300 bars; (B) 45 °C, maximum 700 bars; (C) 65 °C, maximum 1000 bars; (●) 25 °C, (▲) 45 °C, (■) 65 °C, maximum 30 bars, Allen et al.,<sup>17</sup> Bianchi et al.,<sup>20</sup> Bagley et al.<sup>21</sup> Benzene: (----) this work (A) 25 °C, maximum 700 bars; (B) 45 °C, maximum 1000 bars; (C) 65 °C, maximum 1000 bars; (●) 25 °C, (▲) 45 °C, (■) 65 °C, maximum 25 bars, Westwater et al.,<sup>16</sup> Allen et al.,<sup>17</sup> Bagley et al.<sup>20</sup>

the saturation pressure, the internal pressure of benzene and cyclohexane generally increase with pressure while that of carbon disulfide tends to decrease. The new experimental data for carbon disulfide are appreciably different from those reported previously.<sup>16,17</sup> When new data are used, the empirical constant  $n$  (eq 3) is slightly larger than unity, as shown in Table II, consistent with results obtained for other nonpolar fluids. Table II also shows the constant  $n$  for benzene and for cyclohexane; for these fluids results obtained in this work are in good agreement with those obtained earlier.<sup>1,4,17,20</sup> It appears, therefore, that along the saturation curve, the relation between  $\delta$  and  $P_i^{1/2}$  does not exhibit any anomalies relative to those for benzene and cyclohexane.

Finally, the results presented here indicate that the approximate relation given by Hildebrand and Scott<sup>1</sup>

$$\delta \approx \left[ T \left( \frac{\partial P}{\partial T} \right)_V \right]^{1/2} = (T\alpha/\beta)^{1/2} \quad (9)$$

is indeed only a rough approximation, especially if the coefficient of thermal expansion  $\alpha$  and the compressibility  $\beta$  are measured at pressures appreciably higher than the saturation pressure of the fluid. The approximations inherent in eq 9 are fully discussed by Hildebrand and Scott.<sup>1</sup>

**Acknowledgment.** The authors are grateful to the National Science Foundation for financial support, to the Computer Center, University of California (Berkeley) for the use of its facilities, and to a grant from the Commission of Educational Exchange between the United States and Spain awarded to J.A.R.R. We are grateful to J. H. Hildebrand for his sustaining interest in this work.

**Supplementary Material Available:** Tables containing all experimental volumetric data (6 pages). Ordering

information is available on any current masthead page.

## References and Notes

- (1) J. H. Hildebrand and R. L. Scott, "The Solubility of Non Electrolytes", 3d ed, Dover Publications, New York, N.Y., 1964, Chapters V, XXIII and Appendix I.
- (2) J. M. Prausnitz, "Molecular Thermodynamics of Fluid Phase Equilibria", Prentice-Hall, Englewood Cliffs, N.J., 1969, Chapter 7.
- (3) A. F. M. Barton, *J. Chem. Educ.*, **48**, 156 (1971); *Chem. Rev.*, **75**, 731 (1975).
- (4) S. Beret and J. M. Prausnitz, *Macromolecules*, **8**, 536 (1975).
- (5) J. A. R. Renuncio and J. M. Prausnitz, *Macromolecules*, in press.
- (6) D. Tyrer, *J. Chem. Soc.*, **103**, 1675 (1913).
- (7) J. Timmermans, "Physico Chemical Constants of Pure Organic Compounds", Vol. 1, Elsevier, New York, N.Y., 1950, p 612.
- (8) "Kirk-Othmer Encyclopedia of Chemical Technology", 2d ed, Vol. 4, Interscience, New York, N.Y., 1964, p 371.
- (9) "Ullmann's Encyklopadie der Technischen Chemie", 3d ed, Vol. 15, Urband and Schwarzenberg, Munich, 1964, p 534.
- (10) "Nouveau Traite de Chimie Minerale", Vol. VIII(1), Masson et Cie, Paris, France, 1968, p 805.
- (11) T. P. Nelson, Doctoral Dissertation, Washington University, St. Louis, Mo., June 1971.
- (12) D. Ambrose and I. J. Lawrenson, *Process Technol. Int.*, **17**, 968 (1972).
- (13) P. W. Bridgman, *Proc. Am. Acad. Arts. Sci.*, **49**, 3 (1913).
- (14) R. E. Gibson and J. F. Kincaid, *J. Am. Chem. Soc.*, **60**, 511 (1938); R. E. Gibson and O. H. Loeffler, *ibid.*, **61**, 2515 (1939).
- (15) H. H. Reamer and B. H. Sage, *Ind. Eng. Chem. Data Ser.*, **2**, 9 (1957).
- (16) W. Westwater, H. W. Frantz, and J. H. Hildebrand, *Phys. Rev.*, **31**, 135 (1928).
- (17) G. Allen, G. Gee, and G. J. Wilson, *Polymer*, **1**, 456 (1960).
- (18) L. J. O'Brien and W. J. Alford, *Ind. Eng. Data Ser.*, **43**, 506 (1951).
- (19) J. S. Rowlinson, "Liquids and Liquid Mixtures", 2d ed, Butterworths, London, 1969, Chapter 2.
- (20) U. Bianchi, G. Agabio, and A. Turturro, *J. Phys. Chem.*, **69**, 4392 (1965).
- (21) E. B. Bagley, T. P. Nelson, J. W. Barlow, and S. A. Chen, *Ind. Eng. Chem., Fundam.*, **9**, 93 (1970).
- (22) Vapor pressure data from T. Boubik, V. Fried, and E. Hala, "The Vapour Pressures of Pure Substances", Elsevier, Amsterdam, 1973. Saturated density data from Landolt Bornstein "Physikalisch-Chemische Tabellen", Dritter Erg. Bd. (I), Julius Springer, Berlin, 1935.

## Coadsorption of *n*-Alkyl Alcohols and Hydrogen Sulfide at the Aqueous Solution Interface<sup>†</sup>

Graeme G. Strathdee\* and Russell M. Given

Whiteshell Nuclear Research Establishment, Atomic Energy of Canada Limited, Pinawa, Manitoba ROE 1LO, Canada (Received July 21, 1976)

Publication costs assisted by Atomic Energy of Canada Limited

Adsorption of H<sub>2</sub>S at the gas-liquid interface of aqueous solutions of three normal alcohols was found to decrease with increased surface coverage of the *n*-alkyl alcohols. The free energy of adsorption of H<sub>2</sub>S calculated at its zero-coverage limit increased with the carbon number at a fixed surface excess of the *n*-alkyl alcohol in the sequence *n*-propyl < *n*-butyl < *n*-pentyl. Similarly, adsorption of these normal alcohols at the aqueous interface was reduced by high pressure of H<sub>2</sub>S, that is, the free energy of adsorption of each *n*-alkyl alcohol at zero coverage increased with the surface excess of H<sub>2</sub>S. Since adsorption of neither H<sub>2</sub>S nor *n*-alkyl alcohols is enhanced in these three-component systems, repulsive interactions between adsorbates must be dominant. A model based on kinetic theory is employed to explain these observations.

### Introduction

This work extends our previous study of the adsorption of hydrogen sulfide at the aqueous solution interface<sup>1</sup> to three-component mixtures. The H<sub>2</sub>S-H<sub>2</sub>O interface is important to us because it occurs within the Girdler-sulfide (GS) process for the production of heavy water. We found previously that H<sub>2</sub>S was more highly adsorbed at the gas-liquid interface than other low molecular weight surfactants such as CO<sub>2</sub>, N<sub>2</sub>O, or propane, all of which have been examined by Massoudi and King.<sup>2</sup> This difference in properties suggested that H<sub>2</sub>S might have a greater effect on other coadsorbed molecules than these related gases.

The coadsorption of *n*-propyl, *n*-butyl, or *n*-pentyl alcohol with H<sub>2</sub>S was studied to determine how the carbon number *n* of the alkyl group affected the free energy of adsorption of H<sub>2</sub>S. Since the free energies of adsorption of the lower homologues of this series of surfactants obey Traube's rule ( $\Delta G^\circ$  per methylene group is about -2.7 kJ/mol<sup>3</sup>), we expected that for a given surface coverage of *n*-alkyl alcohol, (i) adsorption of H<sub>2</sub>S would decrease with greater *n* if there was a net repulsive interaction with H<sub>2</sub>S, or (ii) adsorption of H<sub>2</sub>S would increase with *n* if there

was net attraction between the adsorbates. From the analogous work of Massoudi and King,<sup>4</sup> in which they studied adsorption of low molecular weight gases in the presence of the soluble tetra-*n*-butylammonium halide surfactants, we expected alternative (i) to hold.

It was also important to us to establish if H<sub>2</sub>S either enhanced or inhibited the coadsorption of *n*-alkyl alcohols at partial pressures of H<sub>2</sub>S close to its saturation pressure  $P_s$ . The cold towers of the H<sub>2</sub>S-H<sub>2</sub>O process operate at pressures near 2.0 MPa (0.9 $P_s$ ) and at a temperature close to 30 °C. Under those conditions, about three monolayers of H<sub>2</sub>S are adsorbed on the aqueous interface.<sup>1</sup> Some chemical process instabilities have been related to the presence of trace quantities of organic surfactants in the H<sub>2</sub>S-H<sub>2</sub>O dispersion on the sieve trays of these gas-liquid contactors. For that reason, we desired to know if adsorption of surface active solutes of the type likely to stabilize the H<sub>2</sub>S-H<sub>2</sub>O froth or to inhibit bubble coalescence<sup>5</sup> was reduced in the presence of high pressure H<sub>2</sub>S compared to adsorption in air.

### Experimental Section

Surface tensions of three-component H<sub>2</sub>S-*n*-alkyl alcohol-H<sub>2</sub>O mixtures were measured by the pendant drop technique as previously described.<sup>1</sup> Droplets were formed

<sup>†</sup> Issued as AECL 5653.

and contained at high pressure in either a modified 1-cm path length optical cell (Aminco) or a chamber of approximately 73 cm<sup>3</sup> total volume. In each case, extra solution was added to ensure that the vapor space of the cell was saturated with *n*-alkyl alcohol. Each surface tension presented below was the mean of two or more measurements which generally agreed to within 0.2 mN/m. Droplets were photographed upon suspension for 300 s, although no detectable change in surface tension was found after about 15 s. The surfaces of these solutions equilibrated rapidly and no significant aging effects were encountered.

The densities of the *n*-alkyl alcohol aqueous solutions differed slightly from that of pure water at 30 °C,<sup>6,8</sup> and we measured them pycnometrically. To calculate the surface tension of three-component mixtures using

$$\sigma = g(\rho_1 - \rho_2)d_e^2/H \quad (1)$$

we assumed that the density was independent of H<sub>2</sub>S pressure. Murphy and Gaines<sup>9</sup> have shown that the density of water is not significantly changed upon saturation with H<sub>2</sub>S gas. In eq 1,  $\sigma$  is the surface tension in mN/m,  $g$  is the gravitational constant,  $\rho_2$  is the density of the aqueous solution,  $\rho_1$  is the density of the gas phase, and  $d_e$  is the maximum diameter of the liquid drop. The term,  $1/H$ , was obtained from the measured shape factor  $S = d_s/d_e$ , where  $d_s$  is the diameter of the drop at the plane normal to the axis of symmetry at dimension  $d_e$  from the drop tip, using the correlations reported by Misak.<sup>10</sup>

The *n*-alkyl alcohols were reagent grade chemicals and were fractionated prior to use. Water was triply distilled and always had a surface tension of 71.5 ± 0.2 mN/m at 30 °C. Hydrogen sulfide was CP grade. The last one-third of the contents of each lecture bottle was rejected to avoid transfer of traces of thiols.

## Results

Surface tension data for three three-component systems are presented in Figure 1. In each case, *n*-alkyl alcohol solution surface tensions were first measured in air to ensure that those values were reproducible and invariant with time. Fresh droplets were employed for each measurement. The data points plotted in Figure 1A–C were the mean of at least two determinations which agreed to within 0.2 mN/m. Surface tensions were always recorded after raising the H<sub>2</sub>S pressure to the desired value.

For each *n*-alkyl alcohol solution, the surface tension decreased linearly with increased H<sub>2</sub>S pressure up to about 1.5 MPa. The more rapid falloff observed for  $\sigma$  above that point resembled the curve for the two-component H<sub>2</sub>S–H<sub>2</sub>O system shown as the upper line in panel 1B and the dashed lines in panels 1A and 1C. The departure from linearity in the H<sub>2</sub>S–H<sub>2</sub>O system was due to multilayer condensation of H<sub>2</sub>S on the surface.<sup>1</sup> Note that as the molecular weight of the *n*-alkyl alcohol increased, the slope  $\partial\sigma/\partial P$  of the linear portion became smaller for a given *n*-alkyl alcohol initial surface pressure  $\pi = \sigma_0 - \sigma$ . This caused a crossover of the  $\sigma$  against  $P$  plot for the H<sub>2</sub>S–C<sub>5</sub>H<sub>11</sub>OH–H<sub>2</sub>O system, Figure 1C, which was absent in 1A and 1B.

It was desirable to collect data at concentrations where the bulk solutions were essentially ideal. For this reason, we chose to study the change in free energy of adsorption of H<sub>2</sub>S in solutions of *n*-alkyl alcohols for which  $\pi$  was less than 10 mN/m. Within that range, plots of  $\sigma$  against  $x$  (mole fraction) are linear for the lower members of the homologous series of alcohols.<sup>3,11</sup> Also, the activity coefficients,  $\gamma^*$ , normalized according to the unsymmetrical convention<sup>12</sup> (the infinitely dilute solution is the standard

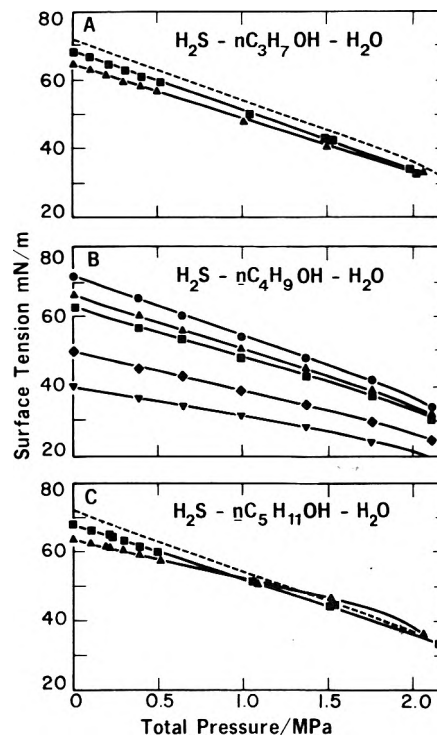


**Figure 1.** The effect of H<sub>2</sub>S pressure on the surface tension of aqueous *n*-alkyl alcohol solutions. The filled circles in panel 1B and the dashed lines in panels 1A and 1C are for H<sub>2</sub>S–H<sub>2</sub>O without *n*-alkyl alcohol. The other curves with decreasing surface tension intercepts in each panel correspond to the solutions of increasing *n*-alkyl alcohol concentration listed in Table I.

state) are close to unity under these conditions.<sup>13,14</sup>

Experiments were done at 30 °C to make accessible the full range of pressure up to the liquefaction point of H<sub>2</sub>S. Below 29.45 °C the solid H<sub>2</sub>S hydrate forms.<sup>1</sup>

**Free Energy of Adsorption of H<sub>2</sub>S.** The free energy of adsorption of H<sub>2</sub>S, component 2,<sup>15</sup> from the solution to the interface was calculated from the limiting slope  $m_2 = \lim_{a_2 \rightarrow 0} (\partial\pi/\partial a_2)$  by means of

$$\Delta G_i^\circ = -RT \ln (m_i/\pi^\circ) \quad (2)$$

where  $R$  is the gas constant,  $T$  is the absolute temperature, and  $\pi^\circ$  is the standard state surface pressure taken to be 0.338 mN/m.<sup>16,17</sup> Ross and Chen<sup>17</sup> have presented a derivation of eq 2. Solute activities  $a_i$  rather than mole fraction concentrations  $x_i$  have been employed in this work since activity coefficients  $\gamma_i^*$  are available for the two-component solutions<sup>13,14,18</sup> and  $a_i = \gamma_i^*x_i$ . For H<sub>2</sub>S, the slope  $m_2$  is given by

$$m_2 = \lim_{P \rightarrow 0} \left( \frac{\partial\pi}{\partial P} \right) \lim_{a_2 \rightarrow 0} \left( \frac{\partial P}{\partial a_2} \right) = \lim_{a_2 \rightarrow 0} \left( \frac{\partial\pi}{\partial a_2} \right) \quad (3)$$

The first term of the product is the slope of the best straight line fitted to each set of data presented in Figure 1. The second term is the Henry's law constant,  $H_{2,1}$  expressed on the activity scale for dissolution of H<sub>2</sub>S in water and is 64.8 MPa at 30 °C.<sup>18</sup> Our values for the free energy of adsorption of H<sub>2</sub>S at its zero-coverage limit,  $\Delta G_2^\circ$ , are summarized in Table I and Figure 2 as a function of the surface excess of *n*-alkyl alcohol measured in the absence of H<sub>2</sub>S,  $\Gamma_3$ .<sup>1</sup>

The surface excess of each *n*-alkyl alcohol without H<sub>2</sub>S present was obtained from the slope of a tangent to a plot of surface tension against  $\ln a_3$  by use of Gibbs' equation and adoption of Gibbs' convention<sup>19</sup> that the surface excess of water  $\Gamma_1 = 0$ :

$$\Gamma_i^1 = -d\sigma/kT \, d \ln a_i \quad (4)$$

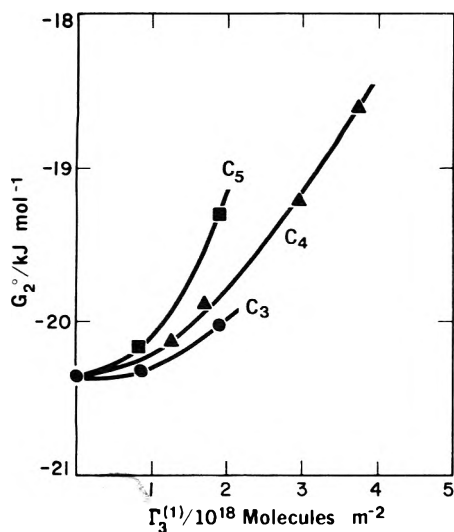


Figure 2. The dependence of the free energy of adsorption of  $H_2S$  at its zero-coverage limit on the surface excess of *n*-propyl, *n*-butyl, and *n*-pentyl alcohol.

TABLE I: Free Energies of Adsorption of  $H_2S$  at the Interface of Aqueous *n*-Alkyl Alcohol Solutions

Alkyl alcohol	$10^4 x_3$ , mole fraction	$10^{-18} \Gamma_3^{(1)}$ , mole-cules/ $m^2$	$-10^9 \lim_{(P_2 \rightarrow 0)} \partial\sigma/\partial P_2$ , mN $m^{-1}$	$-\lim_{(a_3 \rightarrow 0)} (\partial\sigma/\partial a_3)$ , mN $m^{-1}$	$\Delta G_2^\circ \pm 0.1$ , <sup>a</sup> kJ $mol^{-1}$
<i>n</i> Propyl	0	0	16.9	1095	-20.4
	8.7	0.84	16.6	1076	-20.3
	18.7	1.90	14.7	955	-20.0
<i>n</i> -Butyl	4.3	1.27	15.4	998	-20.1
	7.2	1.69	14.0	907	-19.9
	29.8	2.95	10.7	693	-19.2
	60.5	3.76	8.4	544	-18.6
<i>n</i> -Pentyl	1.1	0.83	15.7	1015	-20.2
	2.4	1.89	11.1	720	-19.3

<sup>a</sup> These free energies may be converted to values for adsorption from the gas phase to the interface with respect to the Kemball-Rideal standard state of 0.0608 mN/m<sup>20</sup> by addition of +11.95 kJ/mol.

Our experimental data at 30 °C agreed with the data of Clint et al.<sup>3</sup> in the low concentration region.

For each set of experimental data shown in Figure 1 values of  $\lim_{(P \rightarrow 0)} \partial\sigma/\partial P$  are reported in column 4 of Table I. The error was less than 2% which corresponds to an error in  $\Delta G_2^\circ$  of  $\pm 0.1$  kJ/mol.

To employ eq 3, we have also assumed that the Henry's law constant  $H_{2,1}$  for  $H_2S$  is independent of *n*-alkyl alcohol concentration below  $10^{-3}$  mole fraction. There is a limited amount of data for other systems which support this. McLauchlan found that the reduction in the solubility of  $H_2S$  in water by low concentrations of added ethanol was insignificant within our range of solute concentrations.<sup>21</sup> Also, Sada et al. have reported that the Henry's law constant for the related gas  $N_2O$  decreased only 0.25% in aqueous solutions that contained  $10^{-3}$  mole fraction of methyl, ethyl, or propyl alcohols.<sup>23</sup> We therefore assumed that  $H_2S$  solubility is essentially unchanged in the aqueous solutions which we used and that the solvent activity is that of pure water.

Figure 2 illustrates that the free energy of adsorption of  $H_2S$  increases with the surface coverage of each *n*-alkyl alcohol. This result is consistent with the finding of Clint et al.<sup>3</sup> who have reported that the lower molecular weight

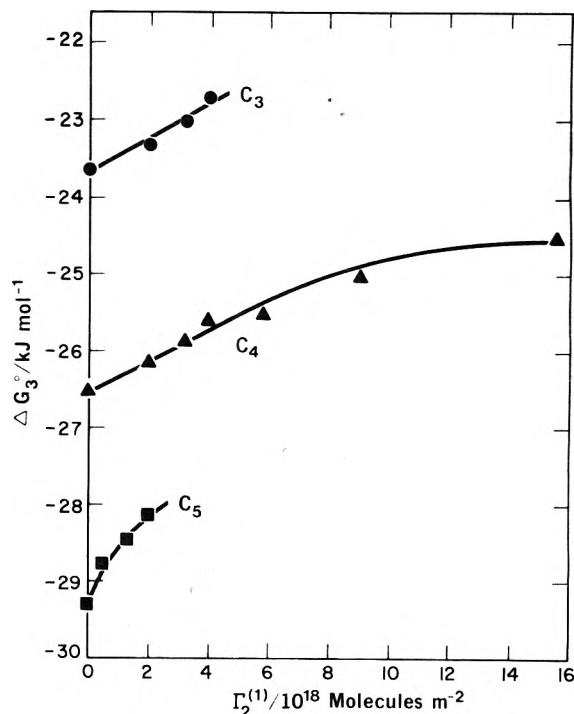


Figure 3. The dependence of the free energy of adsorption of *n*-propyl, *n*-butyl, and *n*-pentyl alcohol, at their respective zero-coverage limits, on the surface excess of  $H_2S$ .

TABLE II: Free Energies of Adsorption of *n*-Alkyl Alcohols at the Interface of Aqueous  $H_2S$  Solutions

Alkyl alcohol	$P_2$ , MPa	$10^3 a_2$ , mole fraction	$10^{-18} \Gamma_2^{(1)}$ , mole-cules/ $m^2$	$-\lim_{(a_3 \rightarrow 0)} (\partial\sigma/\partial a_3)$ , mN $m^{-1}$	$\Delta G_3^\circ \pm 0.1$ , kJ $mol^{-1}$
<i>n</i> -Propyl	0.0			4.0	-23.6
	0.39	6.0	2.0	3.5	-23.3
	0.65	10.0	3.2	3.1	-23.0
	0.99	15.0	4.0	2.8	-22.7
<i>n</i> -Butyl	0.0			12.7	-26.5
	0.39	6.0	2.0	10.9	-26.1
	0.65	10.0	3.2	9.8	-25.9
	0.99	15.0	4.0	8.8	-25.6
	1.37	20.0	5.8	8.5	-25.5
	1.77	25.0	9.0	7.0	-25.0
2.12	29.0	15.6	5.7	-24.5	
<i>n</i> -Pentyl	0.0			34.0	-29.0
	0.1	1.6	0.5	31.0	-28.8
	0.3	4.8	1.3	27.0	-28.4

*n*-alkyl alcohols conform to Traube's rule. At low values of surface coverage of an alcohol, e.g.,  $\Gamma_3^{(1)} = 1-2 \times 10^{18}$  molecules  $m^{-2}$ , the alkyl chains undoubtedly have exposed their maximum projected molecular area toward the water surface and that area increases slightly in the sequence of  $C_3$  to  $C_5$ . One might expect that coadsorption of  $H_2S$  would modify the hydrocarbon chain-water interaction, for example, by displacement of the chain from the surface. This effect should be greater the larger the area of alkyl chain on the surface, i.e., the increase of  $\Delta G_3^\circ$  at a fixed surface excess  $\Gamma_3^{(1)}$  should be the greatest with *n*-pentyl alcohol, as observed.

*Free Energy of Adsorption of n-Alkyl Alcohols.* The data presented in Figure 1 were employed to construct plots of  $\sigma$  against  $a_3$  at several partial pressures of  $H_2S$ . The slopes of these curves at infinite dilution of alcohol yielded  $\lim_{(a_3 \rightarrow 0)} \partial\sigma/\partial a_3$  and, from those data, the free energies of adsorption of the three *n*-alkyl alcohols at the zero-coverage limit were calculated using eq 2. These

results are reported in Figure 3 and Table II as a function of the surface excess of H<sub>2</sub>S at  $a_3 = 0$ .<sup>1</sup>

Our values of  $\Delta G_3^\circ$  at  $a_2 = 0$  were within 0.2 kJ/mol of those obtained by Clint et al.<sup>3</sup> For each alcohol,  $\Delta G_3^\circ$  increased with H<sub>2</sub>S coverage, although the effect was greatest for *n*-pentyl alcohol. Equation 2 could not be applied reliably to data collected at high H<sub>2</sub>S pressure because of lack of information on the variation of *n*-alkyl alcohol activity coefficients  $\gamma_3^*$  in concentrated H<sub>2</sub>S solutions at pressures up to 2.12 MPa, and the points above about  $5 \times 10^{18}$  molecules m<sup>-2</sup> are of uncertain value for this reason.

These data suggest that there is no marked dependence of the relative desorption of the C<sub>3</sub> to C<sub>5</sub> normal alcohols with increased H<sub>2</sub>S gas pressure, i.e., of  $\partial \Delta G_3^\circ / \partial \Gamma_2^{(1)}$ , on the absolute magnitude of  $\Delta G_3^\circ$ . We had expected that the slope might decrease as  $\Delta G_3^\circ$  (or carbon number) increased, because reduction of the *n*-alkyl alcohol-water interaction by coadsorbed H<sub>2</sub>S presumably would become more difficult. In this regard, Massoudi and King have reported that the surface excess of the surfactant tetra-*n*-butylammonium bromide did not vary with the partial pressure of *n*-butane.<sup>4</sup> The free energy of adsorption of that solute calculated from their data was only -27.7 kJ/mol. Thus, the difference between free energies of adsorption of species at the aqueous interface does not seem to reflect the interaction between the adsorbates.

## Discussion

*Adsorption from Multicomponent Solutions.* The surface tension of multicomponent solutions may in principle be accurately calculated from physical and molecular properties of the pure components. Theories of adsorption for these systems have adopted a variety of approaches which include the statistical mechanics of Guggenheim,<sup>24</sup> Prigogine,<sup>25</sup> and Eckert and Prausnitz,<sup>26</sup> the classical thermodynamic methods reviewed by Eriksson,<sup>27</sup> and a number of semiempirical methods which incorporate the adsorption isotherms of Freundlich, Langmuir, or Szyszkowski. In general, the best agreement between calculation and experiment is obtained for regular solutions of nonpolar molecules, that is, for systems in which the surface tensions of the pure components are similar and the extent of adsorption of each at the interface is comparable. Getzen has described a calculation procedure which is useful for systems which exhibit nonideal behavior within the surface region, and has determined surface activity coefficients from bulk-to-surface adsorption constants and partial molal cross-sectional areas.<sup>28</sup> Because of the nature of our system, we have selected a simple kinetic theory approach to analyze our results.

The H<sub>2</sub>S-*n*-alkyl alcohol-water solutions possess distinctive characteristics: H<sub>2</sub>S, a volatile surfactant, readily condenses to yield multilayers at partial pressures above about 0.5P<sub>s</sub>; *n*-alkyl alcohols, readily soluble in water, are moderately adsorbed at the aqueous interface. To understand the dependence of the free energy of adsorption of H<sub>2</sub>S or *n*-alkyl alcohols on the extent of surface coverage by a coadsorbent, we have adopted and modified a rather simple approach for mixed surfactant systems which was developed by Butler.<sup>29</sup> The equations which we have derived for our three-component system illustrate that the changes in  $\Delta G_i^\circ$  are due to variation in one or all of the following: bulk-to-surface adsorption constants, surface activity coefficients and partial molal areas, and the concentration of a second surfactant.

*Dependence of the Free Energy of Adsorption of H<sub>2</sub>S on the Activity of *n*-Butyl Alcohol.* Assume that (i) the rate of adsorption of H<sub>2</sub>S,  $R_2$ , is proportional to the product

of its activity in solution and the fraction of unoccupied surface:

$$R_2 = k_2 a_2 (1 - \gamma_2^s A_2 \Gamma_2^{(1)}) = k_2 a_2 (1 - \gamma_2^s \theta_2) \quad (5)$$

where  $\gamma_2^s$  is the surface activity coefficient of H<sub>2</sub>S,  $A_2$  is its partial molal area, and  $\theta_2$  is the fraction of the aqueous solution surface covered by H<sub>2</sub>S; and (ii) that the rate of desorption of H<sub>2</sub>S,  $R_{-2}$ , varies with its surface fraction  $\theta_2$ :

$$R_{-2} = k_{-2} \gamma_2^s A_2 \Gamma_2^{(1)} = k_{-2} \gamma_2^s \theta_2 \quad (6)$$

The rate constants,  $k_2$  and  $k_{-2}$ , have dimensions of reciprocal time and the ratio  $k_2/k_{-2}$  defines a bulk-to-surface adsorption constant  $K_2$ . Similar expressions are obtained for the *n*-alkyl alcohols by replacing the subscript 2 with 3.

At equilibrium,  $R_2 = R_{-2}$  so that for a three-component system where  $\theta_{\text{free}} + \theta_2 + \theta_3 = 1$  and  $\theta_{\text{free}}$  is the unoccupied surface fraction, we may write for component 2:

$$k_{-2} \gamma_2^s A_2 \Gamma_2^{(1)} = k_2 a_2 [1 - \gamma_2^s A_2 \Gamma_2^{(1)} - \gamma_3^s A_3 \Gamma_3^{(1)}] \quad (7)$$

and for component 3:

$$k_{-3} \gamma_3^s A_3 \Gamma_3^{(1)} = k_3 a_3 [1 - \gamma_2^s A_2 \Gamma_2^{(1)} - \gamma_3^s A_3 \Gamma_3^{(1)}] \quad (8)$$

From (7) and (8) we obtain:

$$\Gamma_3^{(1)} = (k_3 k_{-2} \gamma_2^s A_2 a_3 / k_2 k_{-3} \gamma_3^s A_3 a_2) \Gamma_2^{(1)} \quad (9)$$

Substitution of (9) into (7) yields  $\Gamma_2^{(1)}$  as a function of  $a_2$  and  $a_3$ :

$$\Gamma_2^{(1)} = k_2 a_2 / (k_{-2} \gamma_2^s A_2 + k_2 \gamma_2^s A_2 a_2 + k_{-2} k_3 \gamma_2^s A_2 a_3 / k_{-3}) \quad (10)$$

Introduction of (10) into Gibbs' eq 4 above, followed by integration, yields the surface pressure  $\pi = \sigma_0 - \sigma$ , where  $\sigma_0$  = surface tension of an H<sub>2</sub>S-free aqueous *n*-alkyl alcohol solution of activity  $a_3$ :

$$\pi = \frac{RT}{c_2} \ln \left( 1 + \frac{c_2 a_2}{c_1} \right) \quad (11)$$

in which  $c_1 = \gamma_2^s A_2 (1 + K_3 a_3) / K_2$  and  $c_2 = \gamma_2^s A_2$ . For small  $a_2$ ,  $\ln(1 + c_2 a_2 / c_1) = c_2 a_2 / c_1$ . Experimentally we find that  $\pi = m_2 a_2$  (cf. eq 3), therefore

$$\frac{RT}{m_2} = \frac{\gamma_2^s A_2}{K_2} + \left( \frac{K_3 \gamma_2^s A_2}{K_2} \right) a_3 \quad (12)$$

From eq 2,  $m_2 = \pi^\circ \exp(\Delta G_2^\circ / RT)$ . Note that eq 12 predicts that in general for any case of coadsorption, the free energy of adsorption of one component should be dependent on the concentration of other surface-active species.

The effect of H<sub>2</sub>S on the adsorption of *n*-alkyl alcohols is given similarly by

$$\frac{RT}{m_3} = \frac{\gamma_3^s A_3}{K_3} + \left( \frac{K_2 \gamma_3^s A_3}{K_3} \right) a_2 \quad (13)$$

The validity of eq 12 and 13 was tested by using data from columns 2 and 5 of both Tables I and II. Plots of  $RT/m_2$  against  $a_3$  and  $RT/m_3$  against  $a_2$  are shown in Figures 4 and 5, respectively. In each case the data fall on approximately straight lines as predicted. Note that monolayer coverage by H<sub>2</sub>S in Figure 5 is exceeded at an activity of 0.018. Monolayer coverage by *n*-alkyl alcohols is not reached at any of the concentrations used. Equation 5 does not hold, if  $\theta_2 + \theta_3 > 1$ , but this occurs only in the three highest H<sub>2</sub>S pressure cases with aqueous *n*-butyl alcohol. We now derive numerical values for the parameters of this model for coadsorption.

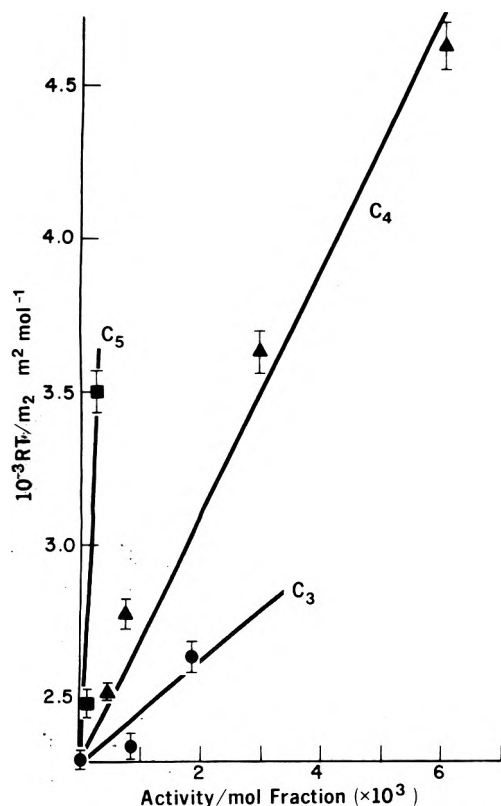


Figure 4. Test of eq 12 with data from Table I.  $C_n$  is the carbon number of the  $n$ -alkyl alcohol.

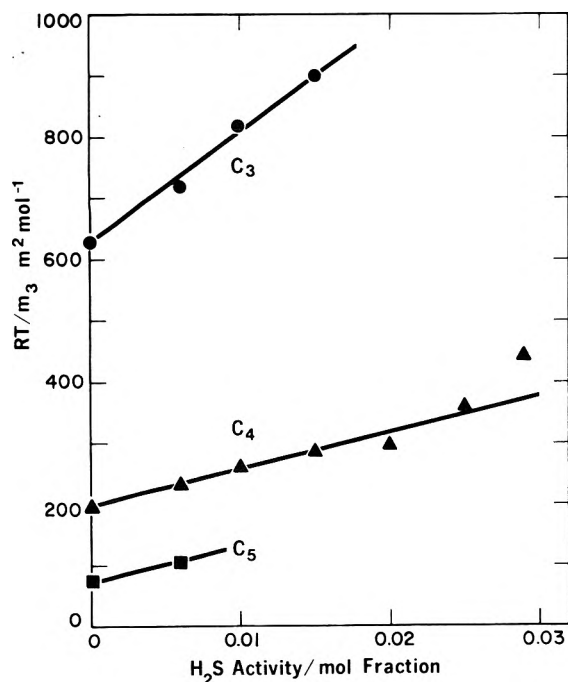


Figure 5. Test of eq 13 with data from Table II.  $C_n$  is the carbon number of the  $n$ -alkyl alcohol.

**Adsorption and Surface Activity Coefficients.** We have selected as the standard reference state the adsorption of each surfactant at zero coverage of the other. Each adsorption constant,  $K_2$  for  $H_2S$  and  $K_3$  for the  $n$ -alkyl alcohols, is therefore equivalent to that for each two-component system. To account for nonideal interaction between coadsorbed molecules, we have considered that the surface activity coefficient for species  $i$  varies from 1 at zero-coverage of that adsorbate to the value which allows the standard state constant  $K_i$  to be retained upon

TABLE III: Adsorption and Surface Activity Coefficients and Molar Areas for the  $H_2S$ - $n$ -Alkyl Alcohol- $H_2O$  System

Surfactants	Parameter				
	$K_2$	$K_3$	$A_3$ , ( $\times 10^5$ ), $m^2$ $mol^{-1}$	$\gamma_2^s$	$\gamma_3^s$
$H_2S$ + $n$ -propyl alcohol	395	2 290 2 380 <sup>a</sup>	14.4	0.031	0.073
$H_2S$ + $n$ -butyl alcohol	395	8 320 7 990 <sup>a</sup>	16.5	0.021	0.077
$H_2S$ + $n$ -pentyl alcohol	395	24 800 25 600 <sup>a</sup>	18.4	0.081	0.19

<sup>a</sup> Calculated from adsorption data in ref 3.

coadsorption of  $H_2S$  and an  $n$ -alkyl alcohol. The coefficients have been evaluated in the following way.

The bulk-to-surface adsorption constant  $K_2$  was calculated at  $a_3 = 0$  from the intercept of Figure 4, assuming  $\gamma_2^s = 1$ . The molar area of  $H_2S$ ,  $A_2$ , was obtained using the general expression  $A_i = N_A^{1/3}(\bar{V}_i^0)^{2/3}$  in which  $N_A$  is Avogadro's number of the solute. For  $H_2S$ ,  $\bar{V}_2^0 = 35.1 \times 10^{-6} m^3/mol$  reported by Murphy and Gaines<sup>9</sup> and this gave  $A_2 = 9.1 \times 10^5 m^2 mol^{-1}$ . The intercept at  $a_3 = 0$  for each set of  $n$ -alkyl alcohol data in Figure 4 was taken to be the value for the two-component  $H_2S$ - $H_2O$  system,  $K_2 = 395$ . This dimensionless constant is related to the experimental slopes  $m_2$  given in column 5 of Table I by  $K_2 = A_2 m_2 / RT$ .

The adsorption constants  $K_3$  for the  $n$ -alkyl alcohols were obtained in a similar way using eq 13 and the intercepts at  $a_2 = 0$  taken from Figure 5. These results, together with the molar areas of the  $n$ -alkyl alcohols calculated from the partial molal volumes  $\bar{V}_3^0$  reported by Friedman and Scheraga,<sup>7</sup> are presented in Table III.

A surface activity coefficient was derived from the slope  $\Sigma$  of each line in Figures 4 and 5. For  $H_2S$ , the plots of  $RT/m_2$  against  $a_3$  gave  $\gamma_2^s = K_2 \Sigma / K_3 A_2$  in which  $K_2$  and  $K_3$  are the standard state adsorption constants discussed above. Similarly for the  $n$ -alkyl alcohols, the plots of  $RT/m_3$  against  $a_2$  gave  $\gamma_3^s = K_3 \Sigma / K_2 A_3$ . These results are also summarized in Table III.

The significance of these surface activity coefficients is that all of the nonideality of the interaction between  $H_2S$  and the  $n$ -alkyl alcohols, as defined by the deviation from the adsorption characteristics of the separate two-component systems, is included in  $\gamma_2^s$  and  $\gamma_3^s$  for each three-component case. These factors are essentially parameters required to fit the present coadsorption model to our data and they reflect the result stated in Figures 2 and 3, namely, that the free energies of adsorption of each surfactant increase with increased coadsorption of the second species.

**The Nature of  $H_2S$ - $n$ -Alkyl Alcohols Interactions.** Our reported values of  $\Delta G_i^0$  at the zero-coverage limit in two-component systems provide a measure of vertical interactions between the adsorbate and the bulk solvent. In those experiments in which the aqueous interface is covered by a considerable fraction of a third species, our experimental data reflect not only vertical interactions between the condensed and bulk phases but also significant lateral adsorbate-adsorbate effects. The increase to more positive values of the free energies of adsorption of both  $H_2S$  or the  $n$ -alkyl alcohols was a measure of the net reduction in the total free energy of adsorption compared to that for the two-component system. This suggests that repulsive interactions may dominate in cases of coadsorption of  $H_2S$  and the  $n$ -alkyl alcohols. Our experiments

do not allow us to assess if this arises because of a change in enthalpy or entropy of adsorption.

**Utility of Coadsorption Model.** The analysis given above has attached physical meaning to the slopes and intercepts of the curves shown in Figures 4 and 5 relating experimental slopes  $m_i = d\sigma/da_i$  to the activities of coadsorbates. Because those curves closely represent our experimental data, it follows that by employing the parameters,  $K_i$ ,  $\gamma_i^s$ , and  $A_i$ , we may accurately calculate the variation in surface tension of H<sub>2</sub>S-*n*-alkyl alcohol-H<sub>2</sub>O solutions with the concentration of each solute. For example the change in surface tension with H<sub>2</sub>S activity  $a_2$  at constant *n*-alkyl alcohol activity  $a_3$  is given by this version of eq 12:

$$\sigma_0 - \sigma = m_2 a_2 = \frac{RTK_2 a_2}{A_2(1 + K_3 \gamma_3^s a_3)} \quad (14)$$

The analogous expression for the dependence of  $\sigma$  on  $a_3$  at constant  $a_2$  is obtained by exchanging the subscripts 2 and 3 in (14).

This model has general applicability to multiadsorbate systems. However, its use is limited to those cases for which the surface activity coefficients  $\gamma_i^s$  are known. These can be obtained only from experimental studies on the multicomponent system. Since binary mixture adsorption properties are insufficient, unless of course the adsorbates behave ideally according to the criteria discussed above, the utility of this approach is limited to the interpolation of the surface tension of mixtures from a comprehensive set of data.

It is worthwhile to consider the experimental results for a related system. Massoudi and King<sup>4</sup> have observed an exception to this prediction since they found that the adsorption of tetra-*n*-butylammonium bromide (TBAB) was unaffected upon pressurization of aqueous solutions with CO<sub>2</sub>, N<sub>2</sub>O, and hydrocarbon gases. Now eq 14 states that in any mixture of two surface active solutes, regardless of the degree of nonideality, a decrease of the ternary solution surface tension as a function of the concentration of one surfactant should also depend on the concentration of the other surfactant. In terms of our model, this result leads one to conclude that the ratio  $K_2 \gamma_3^s A_3 / K_3$  taken from the slope of eq 13 must be small or equal to zero where the subscript 2 refers to the gaseous surfactant and 3 to TBAB. This condition can be encountered when  $K_3 \gg K_2$ , but because  $\Delta G_3^\circ$  (TBAB) was only  $-27.7$  kJ mol<sup>-1</sup>, that criterion does not appear to be met. An alternative explanation for the dependence of the surface properties of that system on surfactant concentrations may be in the nonideality of the bulk phase rather than the interfacial region.

## Conclusions

The free energy of adsorption of each of the coadsorbates H<sub>2</sub>S and *n*-alkyl alcohols was found to increase to more positive values as the surface coverage of the second surfactant was raised.

A coadsorption model based on simple kinetic theory can account for the dependence of the free energy of adsorption of one species on the activity of the other.

The relative desorption of, e.g., H<sub>2</sub>S as a function of the surface excess of an *n*-alkyl alcohol suggested that this characteristic of coadsorption for this system was determined by repulsive lateral interactions between the adsorbates at the aqueous interface.

**Acknowledgment.** The authors wish to acknowledge the helpful discussions and reviews of this work provided by Drs. K. A. Burrill and N. H. Sagert and M. Tomlinson.

## Appendix I. List of Symbols

$a_i$	activity of component <i>i</i> , mole fraction
$d_e$	maximum diameter of pendant drop, m
$g$	gravitational constant, Nm <sup>2</sup> /kg <sup>2</sup>
$k$	Boltzmann constant, J-S
$k_{\pm 2}$	specific rate of adsorption (+) or desorption (-) of H <sub>2</sub> S, component 2, s <sup>-1</sup>
$m_i$	lim ( $a_i \rightarrow 0$ ) $d\sigma/da_i$ , mN m <sup>-1</sup>
$A_i$	molar area of component <i>i</i> , m <sup>2</sup> mol <sup>-1</sup>
$C_n$	carbon number of normal alkyl chain
$\Delta G_i^\circ$	free energy of adsorption of surfactant <i>i</i> , kJ mol <sup>-1</sup>
$H^{-1}$	shape factor <sup>10</sup>
$H_{2,1}$	Henry's law constant for H <sub>2</sub> S in H <sub>2</sub> O, MPa
$K_i$	bulk-to-surface adsorption coefficient for component <i>i</i>
$N_A$	Avogadro's number
$P$	pressure, Pa
$P_s$	saturation vapor pressure, Pa
$R$	gas constant, J K <sup>-1</sup> mol <sup>-1</sup>
$R_{\pm 2}$	rate of adsorption (+) or desorption (-) of component 2, s <sup>-1</sup>
$T$	absolute temperature, K
$\gamma_i^s$	surface activity coefficient of component <i>i</i>
$\pi$	surface pressure = $\sigma_0 - \sigma$ , mN m <sup>-1</sup>
$\pi^\circ$	standard state surface pressure = 0.338 mN m <sup>-1</sup>
$\rho_i$	density of phase <i>i</i> , kg·m <sup>-3</sup>
$\sigma$	surface tension, mN m <sup>-1</sup>
$\sigma_0$	surface tension of pure solvent or a two-component mixture of specified composition, mN m <sup>-1</sup>
$\Gamma_i^{(1)}$	surface excess of component <i>i</i> , molecules m <sup>-2</sup>
$\theta_i$	surface fractional coverage by component <i>i</i>

## References and Notes

- G. G. Strathdee and R. M. Given, *J. Phys. Chem.*, **80**, 1714 (1976).
- R. Massoudi and A. D. King, Jr., *J. Phys. Chem.*, **78**, 2262 (1974).
- J. H. Clint, J. M. Corkill, J. F. Goodman, and J. R. Tate, *J. Colloid Interface Sci.*, **28**, 522 (1968).
- R. Massoudi and A. D. King, Jr., *J. Phys. Chem.*, **79**, 1670 (1975).
- N. H. Sagert and M. J. Quinn, *Can. J. Chem. Eng.*, **54**, 392 (1976).
- F. Franks and H. T. Smith, *J. Chem. Eng. Data*, **13**, 539 (1968).
- M. E. Friedman and H. A. Scheraga, *J. Phys. Chem.*, **69**, 3795 (1965).
- S. Terasawa, H. Itsuki, and S. Arakawa, *J. Phys. Chem.*, **79**, 2345 (1975).
- J. A. Murphy and G. L. Gaines, Jr., *J. Chem. Eng. Data*, **19**, 359 (1974).
- M. D. Misak, *J. Colloid Interface Sci.*, **27**, 141 (1968).
- N. H. Sagert, M. J. Quinn, S. C. Cribbs, and E. L. J. Rosinger, Society of Chemical Industry Symposium on Foams, Academic Press, London, 1976, in press.
- J. M. Prausnitz, "Molecular Thermodynamics of Fluid Phase Equilibria", Prentice-Hall, Englewood Cliffs, N.J., 1969, p 418.
- T. J. Webb and C. H. Lindsley, *J. Am. Chem. Soc.*, **56**, 874 (1934).
- W. D. Harkins and R. W. Wampler, *J. Am. Chem. Soc.*, **53**, 850 (1961).
- Notation convention: Subscripts 1, 2, and 3 refer to H<sub>2</sub>O, H<sub>2</sub>S, and 1-alkanol respectively.
- J. H. DeBoer, "The Dynamical Character of Adsorption", Oxford University Press, London, 1953, p 115.
- S. Ross and E. S. Chen, "Chemistry and Physics of Interfaces", American Chemical Society, Washington, D.C., 1966, p 44.
- L. G. Walker and H. J. Neuberger, private communication. Activity coefficients for aqueous H<sub>2</sub>S will be reported in the revised GS Process Handbook. To be published by Atomic Energy of Canada Limited.
- A. W. Adamson, "Physical Chemistry of Surfaces", Interscience, New York, N.Y., 1967, p 80.
- C. Kemball and E. K. Rideal, *Proc. R. Soc. London, Ser. A*, **187**, 53 (1946).
- W. H. McLauchlan, *Z. Phys. Chem.*, **44**, 600 (1903).
- E. Sada, N. Ando, and S. Kito, *J. Appl. Chem. Biotechnol.*, **22**, 1185 (1972).
- E. Sada, S. Kito, and Y. Ito, *Ind. Eng. Chem. Fundam.*, **14**, 232 (1975).
- E. A. Guggenheim, "Mixtures", Oxford University Press, London, 1952, Chapter 9.
- A. Englert-Chwoles and I. Prigogine, *J. Chim. Phys.*, **55**, 16 (1958).
- C. A. Eckert and J. M. Prausnitz, *AIChE. J.*, **10**, 677 (1964).
- J. C. Eriksson, *Adv. Chem. Phys.*, **6**, 145 (1964).
- F. W. Getzen, *J. Colloid Interface Sci.*, **37**, 668 (1971).
- J. A. V. Butler and C. Ockrent, *J. Phys. Chem.*, **34**, 2841 (1930).
- C. Vidal-Madjar, G. Culochon, and B. L. Karger, *J. Phys. Chem.*, **80**, 394 (1976).

# Chemical and Spectroscopic Properties of Copper Containing Zeolites

J. Texter,<sup>1</sup> D. H. Strome, R. G. Herman, and K. Klier\*

Center for Surface and Coatings Research and Department of Chemistry, Lehigh University, Bethlehem, Pennsylvania 18015 (Received August 2, 1976)

Publication costs assisted by the Petroleum Research Fund

Optical absorption and emission spectra have been used to study the reduction of Cu(II) and Cu(I) exchanged zeolites by hydrogen. The emission of Cu(I) was identified as a spin-forbidden transition  ${}^1A_1 ({}^1S_0) \leftarrow {}^3E ({}^3D_3)$ . Additional intermediates were found spectroscopically, possibly involving copper hydride and isolated copper atoms. The final product is metallic copper in various states of agglomeration, characterized by an absorption edge at  $17\,000\text{ cm}^{-1}$ .

## Introduction

Cuprous Y and X type zeolites have received wide attention over the past several years following the finding that the Cu(I) centers serve to catalyze electrocyclization reactions of hydrocarbons<sup>2</sup> and the oxidation of CO.<sup>3</sup> The preparation of cuprous zeolites can be achieved by the activated reduction of cupric zeolites with H<sub>2</sub>, CO, NH<sub>3</sub>, and several hydrocarbons, as well as by the direct method of ion exchange in liquid ammonia solutions of cuprous iodide.<sup>4</sup> The chemical and physical properties of Cu(I) zeolites are rich in their diversity and include, in addition to catalytic activity, the physical adsorption and chemisorption of small molecules, photoluminescence and cathodoluminescence, and nucleation of metallic clusters and crystallites following activated treatments with H<sub>2</sub>. These phenomena have so far been quantitatively investigated by gas adsorption,<sup>3,5-10</sup> X-ray powder diffraction,<sup>9,11</sup> infrared,<sup>9,10,12,13</sup> ESR,<sup>9,14,15</sup> and photoluminescence<sup>10,15</sup> techniques. The various oxidation states of copper are known to have quite distinct absorption properties over the  $5000\text{--}50\,000\text{-cm}^{-1}$  range.<sup>16</sup> However, there has been a paucity of optical absorption data for copper zeolite systems; such data have been restricted to cursory characterizations of color, with the exception of reports of Cu(II)Y<sup>10,17,18</sup> and Cu(II)A<sup>19</sup> electronic spectra assigned to d-d transitions in the  $10\,000\text{--}33\,000\text{-cm}^{-1}$  interval.<sup>20</sup>

We report herein on the optical spectra of Cu(II), Cu(I), and Cu(0) species in sodium Y and A type zeolites where the copper zeolites were prepared by aqueous ion exchange with cupric ions and by ion exchange in liquid ammonia solutions of cuprous iodide. Diffuse reflectance and luminescence spectra permitted the identification of monodispersed Cu(II), Cu(I), and Cu(0) centers, which resulted from dehydration and deammoniation of the ion-exchange products and by activated H<sub>2</sub> and D<sub>2</sub> reduction, as well as gas adsorption complexes with H<sub>2</sub>, CO, O<sub>2</sub>, and H<sub>2</sub>S, and the development of interband transitions of metallic copper clusters. The UV absorption and visible emission spectra of the Cu(I) centers were interpreted in terms of C<sub>3v</sub> crystal field, charge density electron repulsion, and Jahn-Teller effects simultaneously affecting the  $(3d^{10}) {}^1S_0 \rightarrow (3d^9 4s^1) {}^1D_1$  absorption and the  $(3d^9 4s^1) {}^3D_3 \rightarrow {}^1S_0$  emission.

## Experimental Section

**Sample Preparation.** Copper Y and A type zeolites were prepared by ion exchange in aqueous Cu(NO<sub>3</sub>)<sub>2</sub> solutions and in liquid ammonia solutions of cuprous iodide. Cu<sub>14</sub>Na<sub>28</sub>Y (CuY2)<sup>21</sup> was prepared by stirring a slurry of 50 g of NaY (Linde SK-40) in 1 L of 0.05 M Cu(NO<sub>3</sub>)<sub>2</sub> at 25 °C for 4 h. Cu<sub>1</sub>Na<sub>10</sub>A (CuA2) was prepared by stirring

a slurry of 10 g of NaA (Linde 4A) in 2 L of 1.5 mM Cu(NO<sub>3</sub>)<sub>2</sub> at 25 °C for 6 h. These cupric exchanged samples were repeatedly washed and air dried before further use. Cu<sub>16</sub>Na<sub>40</sub>Y (CuY1) and Cu<sub>7</sub>Na<sub>11</sub>A (CuA1) samples were prepared by ion exchange in nearly saturated liquid ammonia solutions of cuprous iodide, according to a procedure described elsewhere.<sup>4,22</sup> These cuprous exchanged samples were dried in a nitrogen stream at 25 °C and stored under nitrogen or in vacuo until further use. Analyses of the dried products showed that no iodide ion was held in the zeolites. Dehydration and deammoniation was carried out by heating in vacuo using a stepped program at temperatures up to 450 °C. Reductions in research grade hydrogen and deuterium were carried out at various elevated temperatures and at pressures close to atmospheric. Gas adsorptions of H<sub>2</sub>S, CO, and O<sub>2</sub> were carried out at room temperature and atmospheric pressure.

**X-Ray Diffraction.** Powder patterns were recorded on a Siemens diffractometer using Cu K $\alpha$  radiation. Retention of crystallinity in all samples was confirmed.

**Spectroscopy.** Diffuse reflectance spectra (DRS) were recorded on a Cary 14R spectrophotometer with digital output; the data were processed according to Schuster-Kubelka-Munk theory as has been previously described.<sup>23</sup> Dispersed illumination (mode 1) was used in the near-infrared (near IR; 2.17–0.7  $\mu\text{m}$ ), visible (0.7–0.36  $\mu\text{m}$ ), and UV (0.36–0.2  $\mu\text{m}$ ) regions, and undispersed illumination (mode 2) was also used in the visible and UV regions so that absorption spectra could be obtained for the luminescent samples. Emission and excitation spectra were recorded using a Spex No. 1702 monochromator with an RCA No. 8852 photomultiplier to measure the emission and a Bausch and Lomb double grating monochromator, with 150-W Xe and 45-W D<sub>2</sub> lamps used for excitation. Lifetime measurements at 25 °C were made by using a pulsed N<sub>2</sub> laser<sup>24</sup> for excitation and a Tektronix 564 oscilloscope to follow the time decay of the amplified photomultiplier output at 540 nm.

## Results

**Dehydration and Deammoniation.** The dehydration in vacuo of the cupric (CuY2 and CuA2) exchanged sieves was monitored in the near IR by the reduction of absorption intensity due to the  $\nu_3 + \delta$  ( $5100\text{ cm}^{-1}$ ) and  $2\nu$  ( $6800\text{ cm}^{-1}$ ) combination-overtone vibrational bands of water.<sup>25</sup> The sensitivity of the DRS technique utilized here for probing the  $\nu_3 + \delta$  and  $2\nu$  absorptions of molecular water is better than 1 H<sub>2</sub>O/80 A type unit cells<sup>26</sup> or 1 H<sub>2</sub>O/10 Y type unit cells. The deammoniation of the cuprous (CuY1 and CuA1) exchanged samples was similarly monitored in terms of the  $\nu_3 + \nu_4$  ( $5000\text{ cm}^{-1}$ ) and  $3\nu_1$  ( $9700\text{ cm}^{-1}$ ) vi-

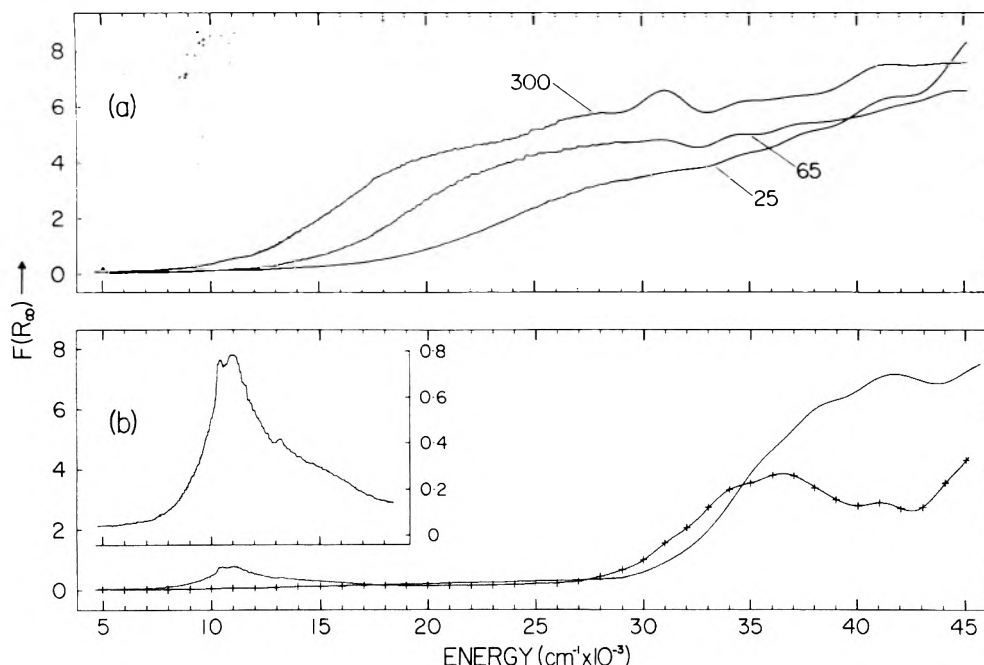


**Figure 1.** Optical spectra of degassed CuA (a) and CuY (b) zeolites. (a) Mode 1 spectra of the CuAl sample which illustrate the effects of increasing deammoniation temperature on the movement of the absorption edge to  $15\,500\text{ cm}^{-1}$  (at  $300\text{ }^{\circ}\text{C}$ ) upon complete deammoniation. (b) The solid line spectrum (mode 1) exhibiting a  $10\,000\text{--}17\,000\text{ cm}^{-1}$  absorption band is that of the CuY2 sample after dehydration in vacuo at  $415\text{ }^{\circ}\text{C}$  for 3 h; (+ + +) spectrum of the CuY1 sample after deammoniation in vacuo at  $450\text{ }^{\circ}\text{C}$  for 15 h; the near IR and visible components were recorded in mode 1, while the UV component was recorded in mode 2 so that the UV excited luminescence of Cu(I) would not be detected.

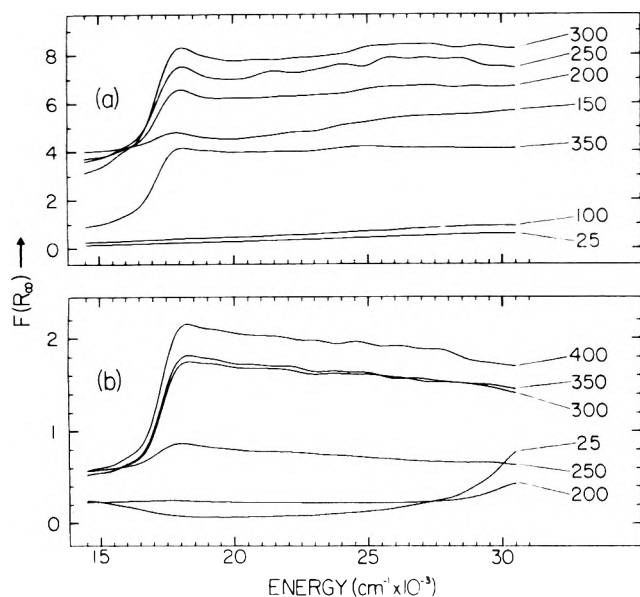


**Figure 2.** Visible (mode 1) spectra of liquid ammonia Cu(I) exchanged (a, CuY1) and aqueous Cu(II) exchanged (b, CuY2) copper Y zeolites illustrating the nucleation of copper as a function of reduction temperature. (a) Spectra of the CuY1 sample after reduction in hydrogen (740 Torr) for 12 h at the indicated temperatures ( $^{\circ}\text{C}$ ). (b) Spectra of the CuY2 sample after reduction in hydrogen (740 Torr) for 12 h at the indicated temperatures. The  $25\text{ }^{\circ}\text{C}$  spectra are those of the respective degassed samples.

brational bands of molecular ammonia. Optical spectra of the completely degassed CuA1 and CuY samples are compared in Figure 1. The CuY2 sample exhibits absorption bands, characteristic of the  $e \rightarrow e$  and  $e \rightarrow a_1$  ( $10\,000\text{--}17\,000\text{ cm}^{-1}$ ) transitions of the Cu(II) ( $3d^9$ ) ion in the trigonal ( $C_{3v}$ ) site. The CuA2 spectrum is identical with that of CuY2. The intense UV absorption component is attributed to charge transfer excitation. The spectra of the CuA1 and CuY1 samples are different. The CuA1 sample exhibits a broad absorption edge at  $15\,500\text{ cm}^{-1}$ , while the CuY1 sample exhibits a multiplet structure

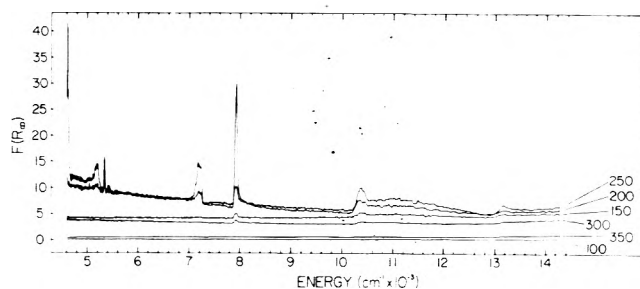


**Figure 3.** Near IR (mode 1) spectra of the CuY1 sample after reduction in  $\text{H}_2$  (740 Torr) for 12 h at the indicated temperature ( $^{\circ}\text{C}$ ). The integrated peak intensities grow in the same proportion, within experimental error, on going from 200 to  $250\text{ }^{\circ}\text{C}$ . The complete envelope of the  $4617\text{ cm}^{-1}$  band could not be obtained due to the low power density of the tungsten source at wavelength greater than  $2.17\text{ }\mu\text{m}$ .

( $31\,000\text{--}44\,000\text{ cm}^{-1}$ ) assigned to the  $(3d^{10})\ ^1S_0 \rightarrow (3d^9\ 4s^1)\ ^1D_2$  configurational transition of Cu(I). The CuY1 sample displays a luminescent emission at  $540\text{ nm}$ .

**Reductions in Hydrogen and Deuterium.** To investigate the effects of  $\text{H}_2$  reduction on cuprous exchanged zeolites, a CuY1 sample was treated in 760 Torr of  $\text{H}_2$  at  $205\text{ }^{\circ}\text{C}$  for 12 h. This treatment resulted in the appearance of the  $17\,000\text{ cm}^{-1}$  metallic copper absorption edge, an intense gray background continuum, and a series of eight absorption bands in the near IR superimposed upon the continuum. Reduction in deuterium gave rise to the same near IR absorption bands, showing that none of these bands originated from water of hydroxyl vibrations. The development of the metallic copper absorption edge for CuY1 is illustrated in Figure 2a. In Figure 3 the corresponding near IR spectra are depicted. These near IR peaks are tentatively assigned to the  $(3d^9\ 4s^2)\ ^2D$  and  $(3d^{10}\ 4p^1)\ ^2P$  configurational transitions<sup>16</sup> of atomically dispersed Cu(0). The growth and decay of the continuous background is apparent in both Figures 2a and 3.

Cupric Y zeolites could be first reduced to the cuprous state, as evidenced by a UV excited green luminescence, by treatment with  $\text{H}_2$  at elevated temperatures. Further reduction in  $\text{H}_2$  resulted in the nucleation of metallic

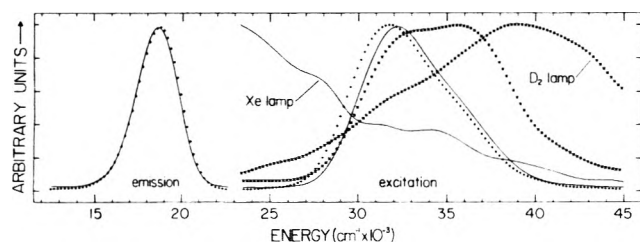


**Figure 4.** Emission and excitation spectra of Cu(I) centers in CuY1 and CuY2 samples. Also indicated are the Xe (150 W) and D<sub>2</sub> (45 W) lamp power density spectra (manufacturers' values) where the maximum indicated spectral irradiance values at 50 cm are 1.0 and 0.05  $\mu\text{W cm}^{-2} \text{nm}^{-1}$  for the Xe and D<sub>2</sub> sources, respectively. (+++) Data for the CuY1 sample using the Xe source. The other data illustrated are for the CuY2 sample reduced in H<sub>2</sub> (740 Torr) at 200 °C for 12 h. The continuous line curves are the emission and excitation spectra for the CuY2 sample obtained with Xe excitation and the (XXX) curve is the excitation spectrum of the CuY2 sample with D<sub>2</sub> excitation.

copper crystallites, as confirmed by X-ray powder diffraction measurements. In Figure 2b is illustrated the development of the absorption edge in CuY2, characteristic of metallic copper, as a function of the reducing temperature in 740 Torr of H<sub>2</sub>. Concurrent with the growth of the 17 000-cm<sup>-1</sup> absorption edge is the growth with increasing temperature of continuous background absorption, which extends through the near IR. Absorption peaks of low intensity were observed to appear and then disappear at 8000 and 10 500 cm<sup>-1</sup> as the reduction temperature was raised stepwise. The maximum Cu(I) content, as evidenced by a maximum in the UV excited 540-nm emission, occurred after treatment with H<sub>2</sub> at 250 °C. No bands in the near IR attributable to the production of H<sub>2</sub>O or hydroxyls were observed after the dehydration or the hydrogen reduction of the CuY2 sample. The corresponding nucleation of metallic copper in the CuA2 sample by reduction at 310 °C was also demonstrated by the appearance of the 17 000-cm<sup>-1</sup> absorption edge.

**Photoluminescence.** Emission and excitation spectra, taken at 25 °C, for CuY2 (reduced in H<sub>2</sub> at 200 °C) and CuY1 are illustrated in Figure 4. These complement the excitation curves reported by Maxwell and Drent<sup>15</sup> for this system at liquid nitrogen temperature. It is apparent that the excitation spectra depended critically upon the wavelength dependence of the source intensity. Excitation spectra for the CuY1 and CuY2 samples were also obtained by subtracting UV mode 1 spectra from UV mode 2 spectra, and were nearly identical with the UV mode 2 (absorption) spectra. The quantum efficiency of the luminescence was estimated to be of the order of unity since the integrated intensities of the excitation spectra obtained as a difference between mode 2 and mode 1 signals were nearly as great as the integrated intensities of the corresponding mode 2 spectra. A lifetime of approximately 100  $\mu\text{s}$  at 25 °C was measured for the Cu(I) luminescence. The emission remained unchanged in the presence of hydrogen at 25 °C.

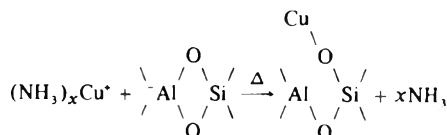
Admission of humid air to luminescing samples of CuY1 and CuY2 resulted in the rapid loss of the 540-nm emission intensity. Admission of CO and O<sub>2</sub> to CuY1 samples at ambient temperature and atmospheric pressure resulted in a partial quenching of the 540-nm emission, which was accompanied by an increase in the absorption coefficient in the 33 000–45 000-cm<sup>-1</sup> interval. Admission of H<sub>2</sub>S to CuY1 at room temperature and atmospheric pressure resulted in almost complete quenching of the emission and the development of an absorption maximum at about 40 000 cm<sup>-1</sup>. The H<sub>2</sub>S–Cu(I) complex was irreversibly formed, and upon stepwise heating in vacuo to 300 °C, a dark green product, believed to be CuSH<sup>+</sup>, resulted which

had an absorption maximum at 11 000 cm<sup>-1</sup>.

## Discussion

**Properties of the Copper Containing Type A Sieves.** While processes leading to the nucleation of metallic copper in cupric and cuprous exchanged Y sieves have closely resembling intermediates and products, a similar analogy does not hold for the A sieves. Similarities between CuA2 and CuY2 do exist and include the hydrogen reduction Cu(II) → Cu(I) without near IR evidence for the production of water or sieve hydroxylation, the occurrence of UV excited luminescence of the Cu(I) centers, and the formation (by further reduction) of metallic clusters as evidenced by X-ray diffraction and optical absorption at 17 000-cm<sup>-1</sup>. The CuA2 and CuY2 samples differ in that the luminescence of the A zeolite exhibited a lower quantum efficiency (<0.1) than that of the Y type. In comparing the cuprous exchanged samples, a significant difference arose at the outset of the ion exchange. While the CuY1 samples assumed a pale blue color when immersed in liquid ammonia (the solution of which is dark blue), CuA1 powder became yellow during the same exchange procedure. Upon the activated deammoniation of CuA1, an absorption edge developed and shifted to lower energies with increasing activation temperature; the deammoniated product was dark brown, but the X-ray diffraction pattern of the product indicated that no Cu<sub>2</sub>O was present.

These properties are similar to those of Cu<sub>2</sub>O,<sup>27</sup> which has an absorption edge of 15 900 cm<sup>-1</sup>. On this basis, and the absorption edge observed at 15 500 cm<sup>-1</sup> with CuA1, it is suggested that a zeolitic analogue of Cu<sub>2</sub>O may be formed according to the following reaction:



where the electron transfer along the Cu–O bond would appear at energies within 500 cm<sup>-1</sup> of those of the band-to-band transition in Cu<sub>2</sub>O. This interpretation is consistent with the greater lability of NaA, compared with NaX and NaY. Because of the ion-skeletal reaction depicted above, the Cu(I) ions in type A sieves (exchanged in liquid ammonia) are not luminescent centers as photoluminescence is quenched by electron exchange and charge transfer.

The type Y zeolites are substantially more stable and inert matrices for the Cu(I) ions, however, and the dissipation of excitation is almost entirely by light emission.

**Optical Properties of Cu(I).** The UV mode 2 absorption spectra of Cu(I) in CuY1 (cf. Figure 1b) and CuY2 are nearly identical except for minor differences in intensity and slight shifts in band maxima positions. The spectra, e.g., that of CuY1 in Figure 1b, indicate the existence of five shoulders and peaks, occurring at 31 070, 33 820, 36 350, 40 900, and 44 160 cm<sup>-1</sup>. This multiplet is assigned to the (3d<sup>10</sup>) <sup>1</sup>S<sub>0</sub> → (3d<sup>9</sup> 4s<sup>1</sup>) <sup>1</sup>D<sub>2</sub> configurational transition,<sup>16,28</sup> where the excited state <sup>1</sup>D<sub>2</sub> is split by the C<sub>3v</sub> crystal field and Jahn–Teller distortions, as schematically represented in Figure 5. In the absence of low temperature spectra, the magnitude of the separation of crystal field and Jahn–Teller energies cannot be determined, and therefore it is not possible to assign the individual components of the observed multiplets to the specific theoretical states labeled by the irreducible representations of the C<sub>3v</sub> group. However, that the multiplet states belong to a singlet configuration 3d<sup>9</sup> 4s<sup>1</sup> is supported by a comparison of the energies of the 3d<sup>9</sup> 4s<sup>1</sup> singlet and triplet states in the free

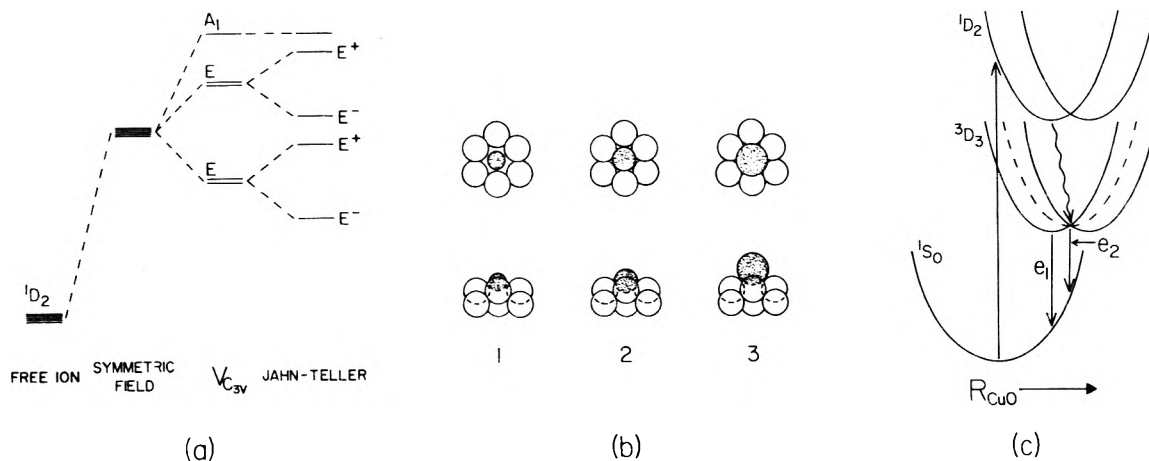


**Figure 5.** (a) Schematic energy level diagram for the  $(3d^9 4s^1) {}^1D_2$  excited state of Cu(I). The totally symmetric component of the zeolitic field raises the center of weight of the  ${}^1D_2$  term above that of the free ion. The  $C_{3v}$  field then splits the term:  ${}^1D_2 \rightarrow {}^1A_1 \oplus {}^1E \oplus {}^1E$ . Jahn-Teller distortions of the doubly degenerate states induce further splitting:  $E \rightarrow E^+ \oplus E^-$ .<sup>32</sup> (b) Close to scale representations of Cu(I) ions (shaded circles) sitting in hexagonal oxygen six-ring pockets of  $C_{3v}$  symmetry (sites I', II, and II') in Y zeolite, at three different hypothesized stages of electronic excitation. The lower drawings depict views in the plane of the six-rings, and the upper drawings are axial views. State 1 represents the unexcited equilibrium configuration. State 2 represents the substantial increase of the Cu(I) ionic radius immediately after electronic (vertical) excitation. The excited state  $(3d^9 4s^1)$  ionic radius, on the time scale of absorption, is constrained from reaching the equilibrium value due to charge density repulsion by the six-ring oxygens. State 3 represents the equilibrium excited state configuration. (c) Schematic potential energy diagram as a function of copper-oxygen distance where the ground state and the lowest lying Jahn-Teller split singlet and triplet excited states are depicted. Absorption occurs as a vertical transition (cf. state 2 of part b) and is followed by a relaxation of potential energy along the  ${}^1D_2$  ( $E^-$ ) potential well (cf. state 3 of part b). Energy is then transferred nonradiatively to the lowest lying triplet, after which a photon of energy  $e_1$  is emitted, and the cuprous ion returns to its equilibrium ground state configuration (cf. state 1 of part b). The dashed potential well and emission photon energy  $e_2$  illustrate how a lower emission energy might be observed if Jahn-Teller distortions are not significant.

ion with those in zeolites and alkali halides, and an entirely consistent picture ensues from the qualitative analysis which follows.

The  $(3d^9 4s^1) {}^1D_2$  term appears at  $26265 \text{ cm}^{-1}$  in the free ion,  $10995 \text{ cm}^{-1}$  below that of the corresponding Cu(II)Y term, and the free ion:  $(3d^9 4s^1) {}^3D_3$  term occurs at  $21929 \text{ cm}^{-1}$ , which is  $4329 \text{ cm}^{-1}$  above the Cu(I) emitting level. The first of these effects can be interpreted in terms of electron repulsion of the excited state by the zeolite lattice. Consider the model of Figure 5b where the Cu(I) center is placed in a  $C_{3v}$  environment; the ground state ionic radius of Cu(I) is of the order of  $0.96 \text{ \AA}$ . According to Slater's rules, the  $3d^9 4s^1$  excited state should exhibit an ionic radius in excess of  $1.59 \text{ \AA}$ . Such an expansion overlaps considerably with the neighboring lattice oxygens, and hence energy of the  ${}^1D_2$  state is increased by repulsion. This explanation is entirely consistent with the lattice repulsion of the  $4d^9 5s^1$  absorptions of  $\text{Ag}^+$  in  $\text{AgCl}$  ( $255 \text{ nm}$ ),  $\text{AgBr}$  ( $315 \text{ nm}$ ), and  $\text{AgI}$  ( $423 \text{ nm}$ ),<sup>29</sup> of  $\text{Cu}^+$  in  $\text{CuCl}$  ( $372 \text{ nm}$ ) and  $\text{CuBr}$  ( $395 \text{ nm}$ ),<sup>29</sup> and of  $\text{Cu}^+$  doped into  $\text{LiI}$  ( $245 \text{ nm}$ ),  $\text{NaI}$  ( $257 \text{ nm}$ ),  $\text{KI}$  ( $263 \text{ nm}$ ), and  $\text{RbI}$  ( $267 \text{ nm}$ ).<sup>30,31</sup> Thus, the higher the observed absorption energy (or lower the observed wavelength), the more constrained are the Cu(I) ions in the given crystal lattice. The energy of the emission from the triplet is less than that which would result from the free ion levels because the emission is into a highly vibrationally excited sublevel of the electronic ground state (cf. Figure 5). The Jahn-Teller effect, also indicated in Figure 5, goes counter to the repulsion and tends to increase the emission energy. The resulting observed emission frequency  $e_1$  is thus intermediate between that of the free ion and the frequency ( $e_2$ ) that would be observed if the Jahn-Teller effect did not operate.

The picture of electronic absorption and emission presented above may be used to explain the small differences observed between CuY1 and CuY2 (Xe excited) excitation and emission spectra (cf. Figure 4). Note that the excitation curve for CuY2 lies about  $1000 \text{ cm}^{-1}$  above that for CuY1. This result is consistent with the mode 2

UV absorption spectrum (not illustrated) for the CuY2 sample, where the low energy shoulder in the  $3d^9 4s^1$  absorption multiplet is shifted  $1000 \text{ cm}^{-1}$  to higher energy than that observed for CuY1 (cf. Figure 1b). The absorption and emission data indicate that the location of the Cu(I) centers in CuY1 and in reduced CuY2 is almost identical except for a slightly higher repulsion in CuY2 (cf. Figure 5).

**The CuH Continuum.** It is useful to consider Figure 6, where data from Figures 1-4 and other data are cast in a form suitable for mechanistic interpretation. The differential  $\text{H}_2$  uptake curve and background continuum absorption curve of Figure 6a demonstrate that in CuY1, the background absorption may be assigned as a property of the CuH intermediate. The band gap for this continuum, lying below  $4600 \text{ cm}^{-1}$ , has not been located. However, a satisfactory explanation of the observed continuum is obtained by considering that the theoretical ionization potential of the free hydride ion, obtained by a Hylleraas variational calculation (among the most accurate ab initio calculations available<sup>33</sup>), lies at  $5775 \text{ cm}^{-1}$  and that the ionization potential will be lowered by the dielectric field of the zeolite. The charge density delocalization effected by the bonding in CuH is reasonably expected to induce a further lowering of the ionization potential below that of the free hydride ion.

A similar but less intense absorption continuum of CuH was observed during the reduction of divalent copper in CuY2 (Figure 6b, dashed line). However, here the continuum appeared at higher temperatures than in CuY1 and only after Cu(I) ions have been formed (Figure 6b, X). This result suggests that the hydride is the product of oxidative addition of hydrogen to Cu(I), a reaction which cannot take place with the Cu(II) ions because of the very high third ionization potential of copper.

**Possible Evidence for Copper Atoms.** The sharp near IR transitions illustrated in Figure 3 belong to an intermediate whose temperature range of existence is marked by open squares in Figure 6a. We tentatively assign these transitions to those of atomically dispersed Cu(0) because

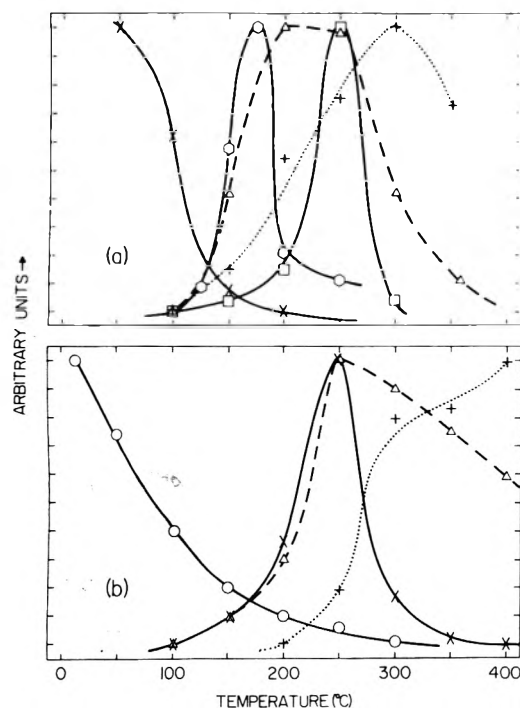


**Figure 6.** Comparison of linearly scaled properties of CuY1(a) and CuY2(b) samples as a function of reduction temperature in (740 Torr)  $H_2$ . (a) Properties of CuY1: (XXX) decrease of emission intensity at 540 nm with 313-nm excitation; ( $\Delta\Delta\Delta$ ) growth and decay of background continuum intensity at  $6000\text{ cm}^{-1}$ ; (+++) intensity of  $18\,000\text{-cm}^{-1}$  copper interband transition after subtraction of the background absorption; (OOO) differential uptake of  $H_2$  at 540 torr as measured in a volumetric apparatus; ( $\square\square\square$ ) growth and decay of the near IR absorption intensity of the peak at  $7929\text{ cm}^{-1}$  (cf. Figure 3). (b) Properties of CuY2: (OOO) decrease of Cu(II) absorption intensity at  $10\,990\text{ cm}^{-1}$ ; (XXX) growth and decay of background continuum intensity at  $6000\text{ cm}^{-1}$ ; (+++) intensity of  $18\,000\text{-cm}^{-1}$  copper cluster interband transition after subtraction of the background absorption. The linear scaling is such that each signal (e.g., emission or absorption corresponding to a particular species) is represented with the same maximum value. Absolute values, where available, are described in the text and in Figures 1-4.

(i) the narrow line width indicates that no phonons are involved in the transition, (ii) the number of lines (eight) corresponds to the number of states originating from the excited configurations ( $3d^9 4s^2$ )  $^2D_{5/2,3/2}$  and ( $3d^{10} 4p$ )  $^2P_{3/2,1/2}$  subject to spin-orbit coupling and a low symmetry crystal field, and (iii) the transitions are not of vibrational origin because substitution of hydrogen by deuterium does not change their wavelengths in the region where only hydrogen-containing oscillators could appear. The center of weight of the  $^2D$  and  $^2P$  states of the monoatomic copper held in the zeolite, if correctly assigned, is at  $8120\text{ cm}^{-1}$  above the ground state ( $^2S_{1/2}$ ), while it is at  $19\,029\text{ cm}^{-1}$  in free copper atoms.<sup>16</sup> The total shift could be caused by the zeolite dielectric field, requiring a local dielectric constant of 1.53 to reduce the energy of the transition.<sup>34</sup> Such a value compares favorably with the average static dielectric constant, less than 2, extrapolated from dielectric loss measurements in NaY zeolites.<sup>35</sup> However, there remains an uncertainty as to the edge of the ionization continuum which should be lowered from the ionization potential of copper atom ( $62\,370\text{ cm}^{-1}$ ) to  $27\,000\text{ cm}^{-1}$ , a frequency obscured by the copper metal continuum in the present system (Figure 2). Further confirmation of the atomic origin of the narrow band spectra observed here with copper should be sought with elements displaying analogous transition. For example, silver atoms in zeolites (dielectric constant 1.53) should exhibit eight lines centered at  $13\,400\text{ cm}^{-1}$  due to transitions from the  $^2S_{1/2}$  ground state

into the  $^2P_{1/2,3/2}$  and  $^2D_{5/2,3/2}$  excited states.

The spectrum in Figure 3 appeared only in trace amounts during the reduction of the cupric sieve CuY2. The reduction sequences in Figure 6b show that the maximum concentration of Cu(I) centers occurred in CuY2 at a temperature 200–250 °C higher than in CuY1, at which temperature the subsequently reduced copper atoms agglomerate so rapidly to metal clusters and particles that they cannot be isolated as metastable intermediates.

**Metallic Copper.** The development of the copper metal absorption edge at  $17\,000\text{ cm}^{-1}$  illustrated in Figure 2 is in good qualitative agreement with previous experimental measurements of copper metal specular reflectances<sup>36,37</sup> and K-band absorptions<sup>38</sup> as well as with band theory and cluster calculations.<sup>39-41</sup> The optical data for metallic copper over the range illustrated in Figure 2 are more refined than heretofore reported elsewhere, and are in agreement with the band structure density of states calculations of Burdick<sup>39</sup> with regard to the shape of the so called "d hump" at the absorption edge (due to interband d-d transitions).

It is seen in Figure 6 that the nucleation of clusters commenced at an early stage of reduction, and reached a maximum after most of the Cu(I) centers had been exterminated. The decrease in the metallic copper curve of Figure 6b is most probably due to an increase in the scattering coefficient of the copper zeolite due to a sufficiently high concentration of large ( $1\ \mu\text{m}$ ) copper particles. Comparison of visible absorption intensities and the high temperature limits of the curves in Figure 6 indicated that copper nucleation in CuY2 was still relatively incomplete at 400 °C.

**The Mechanism of Reduction and Agglomeration.** The most interesting result discussed above is that there are two spectroscopically identifiable intermediates in the reduction of the zeolite cuprous ions (such as in CuY1) to copper metal. Although the interpretation of the spectra of these intermediates is not definite, a mechanism of reduction may be proposed which contains more details than any considered previously. The first reaction sequence involves the formation of a copper hydride, either by oxidative addition (1) or by heteropolar splitting (2) of hydrogen. The copper atom formation is accomplished



by the decomposition of the hydrides (3, 4) followed by



the formation of clusters and metallic phase (5). Here reaction (4b) cannot be an extensive one because no evolution of hydrogen was observed during the formation of the intermediate identified as atomic copper. It should be remarked here that metallic copper exhibits no strong chemisorption of hydrogen.<sup>42</sup>

The protons produced by reactions 2, 3, and 4a are usually considered to react further with skeletal oxygens to form OH groups or water. We have made a search in the near IR and found neither OH nor  $H_2O$  present within instrumental sensitivities. From previously collected data,<sup>43</sup> the sensitivity of this method is predicted to be able to detect 0.01 water molecule per copper in Y zeolite. Conservative estimates of the near IR sensitivity for OH groups, based on a comparison of H Y zeolite spectra in the near IR with the instrument sensitivity,<sup>44</sup> have yielded

detectable concentrations of 0.1 hydroxyls per copper atom. It is therefore concluded that the production of OH groups of the type reported by Herman et al.<sup>9</sup> represents only a small fraction of the reduction mechanism, less than 10% by our estimates. It seems, therefore, that the protons are either attached to the zeolite by electrostatic forces or form heterogeneous OH groups with extremely broad vibrational bands, not detectable by refined near IR techniques.

### Conclusions

The present spectrochemical study of the reduction of copper containing zeolites showed that the Cu(II) molecular sieves CuY2 and CuA2 begin to be reduced at substantially higher temperatures than the Cu(I) zeolites CuY1 and CuA1. The low reduction temperature of CuY1 sieve permitted spectroscopically well-defined intermediates to be detected, one of which is possibly a copper atom with sharp line spectra displayed in the near infrared. By analogy, atomic spectra of other elements in zeolite matrices should be observable in the near-infrared and visible regions, e.g., the  $^2S_{1/2} \rightarrow ^2P_{1/2,3/2}$  and  $^2S_{1/2} \rightarrow ^2D_{5/2,3/2}$  transitions of silver atoms should be centered at 13 400  $\text{cm}^{-1}$ , and the  $^2S_{1/2} \rightarrow ^2P_{1/2,3/2}$  transitions of gold should appear around 17 000  $\text{cm}^{-1}$ . Temperatures above 250–300 °C cause agglomeration of copper outside the zeolite cavities, and are also expected to destroy intracavitary atomic dispersions of most metals.

**Acknowledgment.** The authors wish to thank Dr. R. B. Schoonheydt for his instructions in the preparation of CuA2 samples and Dr. R. P. Messmer for discussions on metallic clusters. Acknowledgment is made to the Donors of the Petroleum Research Fund, administered by the American Chemical Society, for partial support of this research. This work was in part supported by a grant from the Chevron Research Corp., and J.T. thanks Lehigh University for the grant of a Buch Fellowship.

### References and Notes

- (1) Present address: Physiology Department, University of California at Irvine, Irvine, Calif. 92664.
- (2) H. K. Reimlinger, E. H. DeRuiter, and U. K. Kruerke, U.S. Patent No. 3 444 253, May 13, 1969.
- (3) T. Kubo, H. Tominaga, and T. Kunugi, *Bull. Chem. Soc. Jpn.*, **46**, 3549 (1973).
- (4) U. K. Kruerke, U.S. Patent No. 3 497 462, Feb 24, 1970.
- (5) C. M. Naccache and Y. Ben Taarit, *J. Catal.*, **22**, 171 (1971).
- (6) J. Turkevich, Y. Ono, and J. Soria, *J. Catal.*, **25**, 44 (1972).
- (7) A. Egerton and F. S. Stone, *J. Chem. Soc., Faraday Trans. 1*, **69**, 22 (1973).
- (8) Y. Y. Huang, *J. Catal.*, **30**, 187 (1973).
- (9) R. G. Herman, J. H. Lunsford, H. Beyer, P. A. Jacobs, and J. B. Uytterhoeven, *J. Phys. Chem.*, **79**, 2388 (1975).
- (10) P. A. Jacobs, W. de Wilde, R. A. Schoonheydt, J. B. Uytterhoeven, and H. Beyer, *J. Chem. Soc., Faraday Trans. 1*, **72**, 1221 (1976).
- (11) W. G. Reman, A. U. Ali, and G. C. A. Schuit, *J. Catal.*, **20**, 374 (1971).
- (12) Y. Y. Huang, *J. Am. Chem. Soc.*, **95**, 6636 (1973).
- (13) D. R. Flentge, J. H. Lunsford, P. A. Jacobs, and J. B. Uytterhoeven, *J. Phys. Chem.*, **79**, 354 (1975).
- (14) C. C. Chao and J. H. Lunsford, *J. Phys. Chem.*, **76**, 1546 (1972).
- (15) I. E. Maxwell and E. Drent, *J. Catal.*, **41**, 412 (1976).
- (16) C. E. Moore, "Atomic Energy Levels", Vol. II, National Bureau of Standards (U.S.), Dec 1971.
- (17) I. D. Mikheikin, V. A. Shvets, and V. B. Kazanskii, *Kinet. Catal.*, **11**, 609 (1970).
- (18) A. V. Kiselev, N. M. Kuz'menko, and V. I. Lygin, *Russ. J. Phys. Chem.*, **47**, 88 (1973).
- (19) R. A. Schoonheydt, private communication.
- (20) R. Kellerman and K. Klier in "Surface and Defect Properties of Solids", Vol. 4, M. W. Roberts and J. M. Thomas, Ed., Billing & Sons Ltd., London, 1975, pp 1–33.
- (21) The copper and sodium subscripts indicate the number of the respective Cu(II) or Cu(I) and sodium ions per unit cell of Y or A type zeolite.
- (22) Further details about the apparatus and procedure are available from the authors on request.
- (23) K. Klier, *Catal. Rev.*, **1**, 207 (1967).
- (24) E. E. Bergmann, *Appl. Phys. Lett.*, **28**, 84 (1976).
- (25) G. Herzberg, "Infrared and Raman Spectra of Polyatomic Molecules", Van Nostrand, New York, N.Y., 1945.
- (26) K. Klier, J. Shen, and A. C. Zettlemoyer, Division of Petroleum Chemistry, American Chemical Society, Dallas, Texas, April 8–13, 1973; preprint volume, p 53.
- (27) P. W. Baumeister, *Phys. Rev.*, **121**, 359 (1961).
- (28) D. B. Chase and D. S. McClure, *J. Chem. Phys.*, **64**, 74 (1976).
- (29) F. Seitz, *Rev. Mod. Phys.*, **23**, 328 (1951).
- (30) S. A. Mack and W. J. van Sciver, *Phys. Status Solidi B*, **46**, 193 (1971).
- (31) R. L. Bateman and W. J. van Sciver, *Phys. Status Solidi B*, **46**, 779 (1971).
- (32) K. Klier, P. J. Hutta, and R. Kellerman, accepted by the 4th International Conference on Molecular Sieves, Chicago, April 1977.
- (33) C. L. Pekeris, *Phys. Rev.*, **112**, 1649 (1958).
- (34) C. Kittel, "Introduction to Solid State Physics", Wiley, New York, N.Y., 1971, Chapter 18.
- (35) R. A. Schoonheydt, W. de Wilde, and F. Velghe, *J. Phys. Chem.*, **80**, 511 (1976).
- (36) S. Roberts, *Phys. Rev.*, **118**, 1509 (1960).
- (37) D. Beaglehole, *Proc. Phys. Soc. (London)*, **85**, 1007 (1965).
- (38) W. W. Beeman and H. Friedman, *Phys. Rev.*, **56**, 392 (1939).
- (39) G. A. Burdick, *Phys. Rev.*, **129**, 138 (1963).
- (40) B. Segall, *Phys. Rev.*, **125**, 109 (1962).
- (41) R. P. Messmer, S. K. Knudson, K. H. Johnson, J. B. Diamond, and C. Y. Yang, *Phys. Rev. B*, **13**, 1396 (1976).
- (42) J. H. Sinfelt, *Adv. Catal.*, **23**, 91 (1973).
- (43) J. H. M. Shen, Ph.D. Dissertation, Lehigh University, 1974.
- (44) The H Y zeolite spectrum in near IR is a perfect analogue of the double-band spectra of Uytterhoeven et al.<sup>45</sup> observed in the IR region of 3600  $\text{cm}^{-1}$ . The H Y zeolite was prepared from an ammonium ion exchanged Y sieve by degassing stepwise under vacuum to 400 °C and gave rise to two OH bands, one at 7140  $\text{cm}^{-1}$  with  $F(R_{\omega}) = 0.027$  and another at 6940  $\text{cm}^{-1}$  with  $F(R_{\omega}) = 0.0028$ . Our detection limits are estimated to correspond to  $F(R_{\omega}) = 0.00026$ .
- (45) J. B. Uytterhoeven, L. G. Christner, and W. K. Hall, *J. Phys. Chem.*, **69**, 2117 (1965).

# Spectroscopic Characterization of the Pheophytin a Dication<sup>1</sup>

Walter Oettmeier,<sup>2</sup> Thomas R. Janson, Marlon C. Thurnauer, Lester L. Shipman, and Joseph J. Katz\*

Chemistry Division, Argonne National Laboratory, Argonne, Illinois 60439 (Received September 20, 1976)

Publication costs assisted by Argonne National Laboratory

The dication of pheophytin a has been studied by visible absorption, electron spin resonance, and proton magnetic resonance spectroscopy. Visible absorption spectroscopy was used to follow the conversion of chlorophyll a to pheophytin a dication by trifluoroacetic acid. Pheophytin a is half-converted to the dication by 85 equiv of trifluoroacetic acid in CCl<sub>4</sub> at 10<sup>-5</sup> M. No spectroscopic evidence for a pheophytin a monocation was found. In the dication, all protons experienced an initial downfield chemical shift, with those of the methine protons most pronounced. From the changes in the proton chemical shifts with increasing amounts of trifluoroacetic acid, it can be deduced that an additional protonated species is formed from the pheophytin a dication by hydrogen binding of a trifluoroacetic acid molecule to the C-9-keto carbonyl group. The zero field splitting parameters for the T<sub>1</sub> state of the protonated pheophytin a were determined by electron spin resonance spectroscopy to be 0.0288 ± 0.0009 and 0.0046 ± 0.0001 cm<sup>-1</sup> for D and E, respectively. The visible absorption spectrum of chlorophyll a and the pheophytin a dication are remarkably similar both with respect to peak positions and relative peak heights.

## I. Introduction

The characteristic color of chlorophyll a (Chl a) in neutral and basic solutions is lost upon slight acidification and the gray-brownish color of pheophytin a (Pheo a) is obtained. Pheo a is derived from Chl a by replacement of its central Mg<sup>2+</sup> by two protons (Figure 1). Strongly acidic solutions of Chl a have a color almost indistinguishable<sup>3</sup> from that of Chl a in organic solvents and the species responsible for this dark-green color is thought to be the dication of pheophytin a, i.e., H<sub>2</sub>Pheo a<sup>2+</sup> (Figure 1). H<sub>2</sub>Pheo a<sup>2+</sup> differs from Pheo a by two additional protons bonded to the pyrrole nitrogen atoms at the center of the macrocycle. A discrepancy exists in the literature on this subject as to the nature of the protonated species formed in acidic solution. Specifically, Delaporte and Laval-Martin<sup>4</sup> from potentiometric titration and visible absorption spectroscopy found evidence for a monocation in the system acetone/perchloric acid. On the other hand, Zanker et al.<sup>5</sup> from visible absorption spectroscopy found evidence for both a monocation of Pheo a (HPheo a<sup>+</sup>) with a pK = 1.6 and a dication of Pheo a<sup>2+</sup> (H<sub>2</sub>Pheo a<sup>2+</sup>) with a pK = 0.0 in the system acetone/water/hydrochloric acid.

To help clarify the nature of the protonated Pheo a species, we have examined the properties of Pheo a in acidic solution, and have characterized them by visible absorption, proton magnetic resonance (<sup>1</sup>H NMR), and electron spin resonance (ESR) studies. We have found that trifluoroacetic acid (TFA) has many advantages as the protonating acid and is particularly well suited for the spectroscopic techniques we have used.

## II. Experimental Section

Pheo a was prepared by acid treatment of Chl a<sup>6</sup> and dried on a vacuum line. Visible absorption spectra were recorded on a Cary 14 spectrometer equipped with a digitizer and interfaced to the Argonne Chemistry Division's central Sigma 5 computer. <sup>1</sup>H NMR spectra were recorded at 20 °C on a Varian HR-220 spectrometer operating in the Fourier transform mode. <sup>13</sup>C NMR spectra were obtained at 27 °C on a Bruker WP 60 spectrometer operating in the Fourier transform mode. ESR triplet spectra were recorded as previously described.<sup>7</sup>

## III. Visible Absorption Spectra

Visible absorption spectra for Chl a dissolved in TFA, Pheo a dissolved in TFA, Chl a-pyridine in CCl<sub>4</sub>,<sup>8</sup> and Pheo a in CCl<sub>4</sub>,<sup>8</sup> are compared in Figure 2. The action of TFA on Chl a or Pheo a yields the same end product for the spectrum of Chl a in TFA (λ<sub>max</sub> 660, 610, 575, and 528 nm) and Pheo a in TFA (λ<sub>max</sub> 659, 609, 573, and 526 nm) are almost indistinguishable (cf. Figure 2A and 2B). Chl a evidently loses its central magnesium very quickly on treatment with TFA and is protonated to form a cation; Pheo a is likewise protonated by TFA to form the same cation. Dissolution of Pheo a in TFA causes no chemical changes in the chlorin macrocycle. In the presence of water, hydrolysis at the propionic acid ester side chain may occur with formation of pheophorbide a; nothing happens to the carbomethoxy ester group even when substantial amounts of water are present, as judged from <sup>1</sup>H NMR spectra. The conditions under which the trifluoroacetic acid titrations were carried out do not yield any significant amounts of pheophorbide a, as shown by thin-layer chromatography. The spectrum of protonated Pheo a species formed from either Chl a or Pheo a dissolved in TFA is clearly different from Pheo a (cf. Figure 2A, 2B, and 2D).

To answer the question whether a mono- or dication of Pheo a is formed by the interaction of Pheo a and TFA (or Chl a and TFA) we carried out titration of 10<sup>-5</sup> M Chl a with TFA in CCl<sub>4</sub> as the solvent (Figure 3). Addition of 2 equiv of TFA almost completely converted Chl a to Pheo a as judged by the close similarity of the spectrum of the reaction product with the spectrum of Pheo a in CCl<sub>4</sub>. We assume that the displacement of Mg<sup>2+</sup> from Chl a to form Pheo a goes according to the reaction



Our visible absorption spectra show that over 90% of the Chl a molecules have been converted into Pheo a when 3 equiv of TFA have been added, and this places a lower bound of 6 × 10<sup>5</sup> M<sup>-1</sup> on the equilibrium constant for the conversion of Chl a into Pheo a. No further large changes in the visible absorption spectrum are observed until approximately 50 equiv of TFA have been added, and then a shoulder at 652 nm starts developing. The conversion

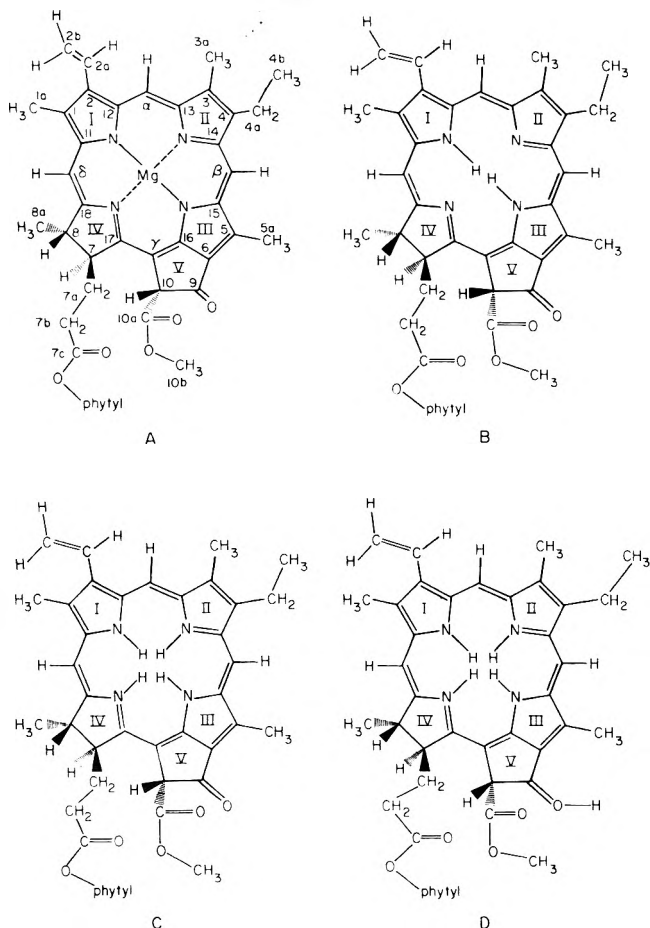


**Figure 1.** Chemical structure of (A) chlorophyll a (Chl a), (B) pheophytin a (Pheo a), (C) pheophytin a dication ( $H_2Pheo a^{2+}$ ), and (D) pheophytin a trication.

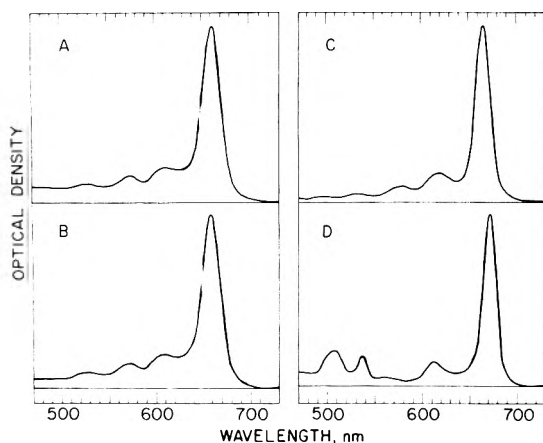


**Figure 2.** Visible absorption spectra of (A)  $10^{-5}$  M chlorophyll a added to trifluoroacetic acid, (B)  $10^{-5}$  M pheophytin a added to trifluoroacetic acid, (C)  $10^{-4}$  M chlorophyll a-pyridine in  $CCl_4$ , and (D)  $10^{-4}$  M pheophytin a in  $CCl_4$ .

from the 671-nm species (i.e., Pheo a) into the 652-nm species is completed by the addition of 500 equiv; further addition of TFA beyond 500 equiv results only in a small red shift of the major red absorption peak and subtle changes in the relative intensities of the peaks. In the conversion of Chl a to protonated Pheo a isosbestic points at 606 and 625 nm are observed and all but the 500-equiv

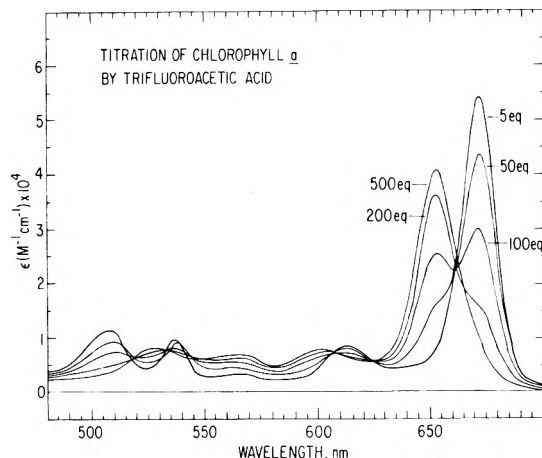


**Figure 3.** Visible absorption spectra corresponding to the addition of 5, 50, 100, 200, and 500 equiv of trifluoroacetic acid to a  $10^{-5}$  solution of chlorophyll a in  $CCl_4$ .

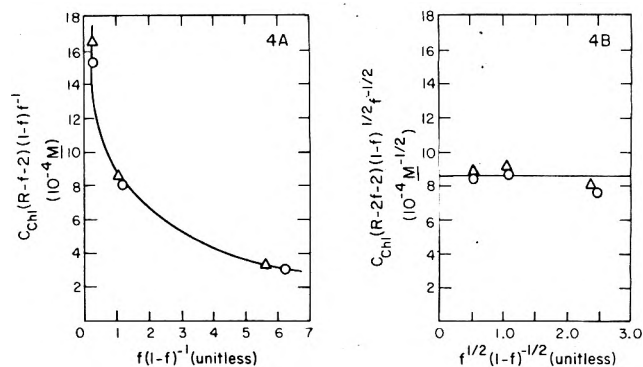


**Figure 4.** Equilibrium plot to determine if the protonated pheophytin a species formed through interaction with trifluoroacetic acid is (A) the monocation or (B) the dication. The circles correspond to points derived from the absorbance at 671 nm and the triangles correspond to points derived from the absorbance at 652 nm.

spectrum has an isosbestic point at 661 nm. We believe that the reason why the 500-equiv curve does not pass exactly through the isosbestic point is the result of a small additional red shift due to the binding of a third TFA molecule to the C-9 keto carbonyl. In neat TFA the main red peak is shifted all the way to 660 nm (Figure 2A).

By assuming that only Pheo a was formed when the TFA:Chl a ratio is 5:1 and at a ratio of 500:1 only a protonated species is present, it is possible to calculate the fraction,  $f$ , of the original Pheo a molecules protonated at each point in the titration. Because TFA is known to dimerize in nonpolar solvents<sup>9,10</sup> we assumed that the following two equilibria are also operative:



where  $n = 1$  for the formation of the Pheo a monocation and  $n = 2$  for the formation of the Pheo a dication. From eq 2 and 3, it can be shown that the equilibrium constant for monoprotonation is given by

$$C_{ChI}(R - f - 2)(1 - f)f^{-1} = [2f/KK_1^2(1 - f)] + K_1^{-1} \quad (4)$$

where  $C_{ChI}$  is the initial Chl concentration and  $R$  is the ratio of the added TFA concentration to the initial Chl concentration. Thus a plot of the left-hand side of eq 4 vs.  $f(1 - f)^{-1}$  should be a straight line with positive slope, if indeed the monocation is the species formed. Such a plot is shown in Figure 4A. It is obviously not a straight line and it has a negative slope. Alternatively, if the Pheo a

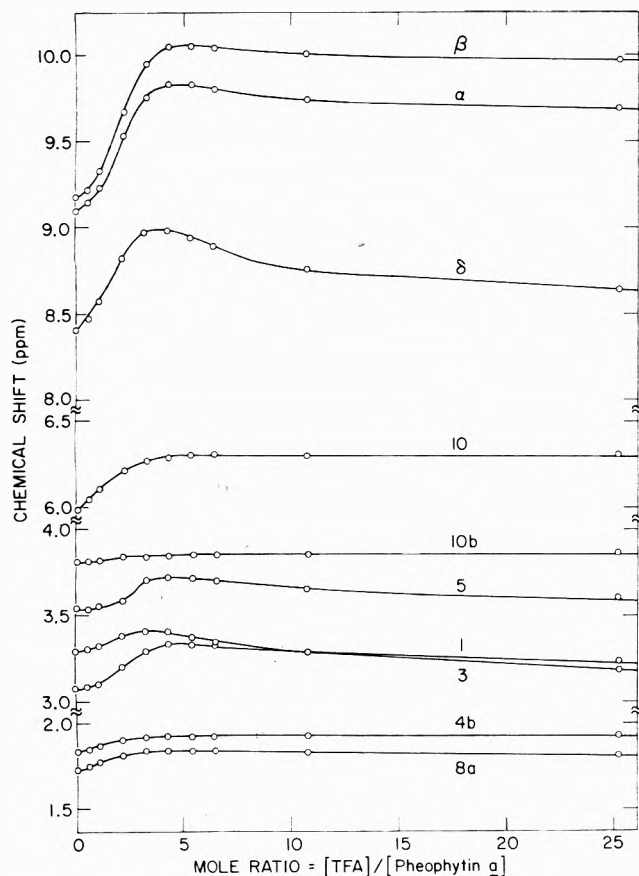


**Figure 5.**  $^1\text{H}$  NMR titration of  $2 \times 10^{-2}$  M pheophytin a in  $\text{CCl}_4$  with trifluoroacetic acid. The free induction decay was collected in 8192 channels. A  $90^\circ$  pulse was taken to be  $67 \mu\text{s}$  and 3 s relaxation interval was allowed between pulses. The processed free induction decay was the resultant of 300 pulses.

dication salt with TFA is the species being formed, then the following equation applies:

$$C_{\text{Chl}}(R - 2f - 2)(1 - f)^{1/2}f^{-1/2} = [2f^{1/2}/KK_2(1 - f)^{1/2}] + K_2^{-1/2} \quad (5)$$

Thus a plot of the left-hand side of eq 5 vs.  $f^{1/2}(1 - f)^{1/2}$  should be a straight line with slope of  $2K^{-1}K_2^{-1}$  and a y intercept  $K_2^{-1/2}$  for dication formation. We find that such a plot is nearly a horizontal straight line, i.e., the slope is small (Figure 4B). Setting the slope equal to zero, we obtain  $K_2^{-1/2} = (8.5 \pm 0.5) \times 10^4 \text{ M}$  and therefore  $K_2 = (1.4 \pm 0.2) \times 10^6 \text{ M}^{-2}$ . Thus, the spectral changes observed when  $10^{-5}$  M Chl a in  $\text{CCl}_4$  is titrated with TFA are consistent with the complete conversion of Chl a to Pheo a at just over 2 equiv, followed by the subsequent conversion of Pheo a to  $\text{H}_2\text{Pheo a}^{2+}$  with more TFA. One-half of the Pheo a is converted to  $\text{H}_2\text{Pheo a}^{2+}$  at the point where 85 equiv of TFA have been added.

#### IV. $^1\text{H}$ NMR Observations

A titration of Pheo a by TFA similar to that carried out by optical spectroscopy was performed by  $^1\text{H}$  NMR. A higher concentration of Pheo a was required because of the lower sensitivity of  $^1\text{H}$  NMR. TFA was added in small increments to a 0.02 M solution of Pheo a in  $\text{CCl}_4$  and the chemical shift changes of the various proton species in Pheo a are shown as a function of the TFA/Pheo a mole ratio in Figure 5. Several proton chemical shifts, notably those of the  $\alpha$ ,  $\beta$ , and  $\delta$  methine protons, experience large changes in chemical shift to lower field upon the addition of TFA, a shift which is consistent with that observed under similar circumstances for simple porphyrins.<sup>11</sup> A

**TABLE I.**  $^1\text{H}$  Chemical Shifts of Pheophytin a in Neat  $\text{CCl}_4$  and Trifluoroacetic Acid ( $\delta$ , ppm)<sup>a</sup>

Proton	Neat $\text{CCl}_4$	Neat TFA	$\Delta$
$\beta$	9.08	9.84	+0.76
$\alpha$	9.00	9.51	+0.51
$\delta$	8.36	8.44	+0.08
10	5.95	6.17	+0.22
10b	3.80	3.62	-0.18
5a	3.49	3.23	-0.26
1a	3.23	2.90	-0.33
3a	3.00	2.85	-0.15
N-H	-0.12; -2.15		

<sup>a</sup> Chemical shifts are downfield (+) from internal standard hexamethyldisiloxane (HMS). Other conditions as in Figure 5.

**TABLE II:**  $^{13}\text{C}$  Chemical Shifts of Cyclopentanone in  $\text{CCl}_4$  and Trifluoroacetic Acid ( $\delta$ , ppm)<sup>a</sup>

Solvent	C=O	$\alpha$ $\text{CH}_2$	$\beta$ $\text{CH}_2$
$\text{CCl}_4$	214.6	35.7	21.2
TFA	234.1	40.4	24.7
	$\Delta$ 19.5	$\Delta$ 4.7	$\Delta$ 3.5

<sup>a</sup> Chemical shifts are downfield from internal standard hexamethyldisiloxane (HMS). The repetition mode was 20 s and benzene- $d_6$  was used as internal lock.

maximum change is observed with the addition of ca. 4 equiv of TFA. The signals arising from the N-H protons ( $\delta = -0.12$  and  $-2.10$  ppm) are lost after addition of only small amounts of TFA, which is due to line broadening caused by rapid proton exchange. However, before the N-H signals completely vanish a small downfield shift was observed to occur, and this is contrary to what is generally observed in porphyrin diacids.<sup>11</sup> As judged from the steadily increasing downfield shifts of the protons during the early stages of the titration and from the immediate broadening of the N-H signal, no evidence can be adduced for an intermediate monocation.

With more than 4 equiv of TFA the proton chemical shifts either remain fairly constant or begin to move to high field. This is easily explained by a TFA solvent effect from the increasing concentration of TFA (see Table I for a comparison of the chemical shifts of some protons of Pheo a in neat  $\text{CCl}_4$  and neat TFA) and by changes in the  $\pi$  system of the macrocycle from protonation at the C-9 keto carbonyl group. Extrapolated values of the titration curve in Figure 5 coincide with chemical shifts in neat TFA. The change in slope of the chemical shifts is compatible with protonation at the C-9 keto carbonyl at high TFA concentrations. Further evidence on protonation at C-9 was sought by  $^{13}\text{C}$  NMR spectroscopy. Cyclopentanone was used as a model compound, and  $^{13}\text{C}$  NMR spectra were recorded on cyclopentanone in neat  $\text{CCl}_4$ , in neat TFA, and in  $\text{CCl}_4$  with various concentrations of TFA. As can be seen in Table II, the carbonyl carbon is by far the most strongly affected carbon atom in the molecule when interaction with TFA occurs, indicative of strong interaction with the oxygen of the C-9 keto function. Similarly, examination of the 2-carboethoxy derivative of cyclopentanone (basically the ring V of Pheo a) via  $^{13}\text{C}$  NMR indicates that the keto carbonyl is the preferential site of protonation. Approximate half-titration points for the reaction



were computed by finding the number of equivalents of TFA for which the chemical shifts changed by one-half of their maximum change during the course of the titration. Using the chemical shifts for the carbon atoms at the  $\alpha$ ,  $\beta$ ,  $\delta$ , 1a, 3a, 5a, and 10b positions, a value of  $1.8 \pm 0.3$  equiv

was computed for the half-titration point. A value of 1.8 is not consistent with  $n \geq 4$  (eq 6), because the half-titration point for the  $n \geq 4$  case *must* be greater than 2 equiv. For  $n = 2$ , then the equilibrium constant  $K_2 = 1.4 \times 10^6 \text{ M}^{-2}$ , determined from visible absorption spectroscopy, applies and a half-titration point of 1.04 is predicted. Because  $n \geq 4$  has been eliminated and a greater amount of TFA is required than for  $n = 2$ , we conclude that  $n = 3$  is the most likely value.

### V. Triplet Spectra

The ESR spectrum of the lowest triplet state ( $T_1$ ) of  $10^{-3} \text{ M}$  protonated Pheo a has been recorded at 5 K in two different solvent systems. In 50% TFA/50% glycerol v/v the zero field splitting parameters,  $D$  and  $E$ , are  $0.0288 \pm 0.0009$  and  $0.0046 \pm 0.0001 \text{ cm}^{-1}$ , respectively, and in neat TFA the corresponding  $D$  and  $E$  values are 0.0278 and  $0.0056 \text{ cm}^{-1}$ , respectively. These  $D$  and  $E$  values are to be compared with those previously reported for Chl a<sup>12-15</sup> and Pheo a.<sup>12,13</sup> The values reported for Chl a are both solvent and concentration dependent; reported values for  $D$  range from 0.0262 to  $0.0303 \text{ cm}^{-1}$  and values reported for  $E$  range from 0.0022 to  $0.0059 \text{ cm}^{-1}$ . The  $D$  values reported for Pheo a are  $0.0339^{12}$  and  $0.0341 \text{ cm}^{-1}$ <sup>13</sup> and the corresponding  $E$  value is  $0.0033 \text{ cm}^{-1}$ .<sup>12,13</sup> Thus, the zero field splitting parameters for the  $T_1$  state of protonated Pheo a are more similar to Chl a than to Pheo a.

### VI. Conclusions

Titration of  $10^{-5} \text{ M}$  Chl a with TFA in  $\text{CCl}_4$  solution shows that the Chl a is converted to Pheo a by the addition of just over 2 equiv of TFA. Further amounts of TFA (from 5 to 500 equiv) convert Pheo a to a single protonated species as indicated by the isosbestic point at 661 nm in the visible absorption spectra. This protonated species has its major absorption maximum at 652 nm. From the TFA dependence of the visible absorption spectrum it was possible to establish that the 652-nm absorbing species cannot be the monocation and that it is most likely the dication  $\text{H}_2\text{Pheo a}^{2+}$ . The equilibrium constant for the conversion of Pheo a to  $\text{H}_2\text{Pheo a}^{2+}$  was calculated to have the value  $1.4 \times 10^6 \text{ M}^{-2}$ .

A titration of  $2 \times 10^{-2} \text{ M}$  Pheo a with TFA in  $\text{CCl}_4$  followed by  $^1\text{H}$  NMR gives spectra that are not characteristic of a simple two-species equilibrium and there seem to be strong bulk solvent shifts of the various proton resonances as the solvent is varied from pure  $\text{CCl}_4$  to pure TFA. As judged by the approximate half-titration value of 1.8 equiv, the  $^1\text{H}$  NMR spectra can be interpreted to indicate the addition of three molecules of TFA to Pheo a. This conclusion is strongly supported by the results of a titration of cyclopentanone by TFA followed by  $^{13}\text{C}$  NMR. These results indicate a strong binding of TFA to the keto carbonyl group of cyclopentanone. Hence, the binding of the third molecule of TFA most probably takes place at the 9-keto carbonyl group in the cyclopentanone-like ring V of  $\text{Ph}_{20}\text{a}$ .

These conclusions from  $^1\text{H}$  NMR and  $^{13}\text{C}$  spectroscopy are consistent with the visible absorption spectra results for the titration at  $10^{-5} \text{ M}$  because when more than 500 equiv of TFA (i.e.,  $5 \times 10^{-3} \text{ M}$  TFA) have been added, a

red shift of the major absorption peak (from 652 to 660 nm in pure TFA) is observed. This red shift is consistent with the binding of an additional molecule of TFA to the ring V keto carbonyl, as it is known that binding of a metal ion at the ring V keto carbonyl brings about a red shift of the major absorption peak.<sup>8</sup>

Under our experimental conditions, which are quite different from those of Delaporte and Laval-Martin<sup>4</sup> and of Zanker et al.,<sup>5</sup> no monocation is observed in the Pheo a-TFA system. In an X-ray analysis of the dication of tetraphenylporphyrin, Fleischer and Stone<sup>16,17</sup> have shown that protonation destroys the planarity of the porphyrin aromatic system, and that the pyrrole rings are tilted alternatively up and down at  $28^\circ$  angles to the molecular plane. Such a conformational change may account for the instability of a Pheo a monocation. The energy barrier for the addition of the first proton to a pyrrole ring of the macrocycle may be greater than for the addition of the second. When the first proton is attached, the lone pair of the second nitrogen atom is exposed, as the pyrrole moiety gets tilted, and thus protonation of the second nitrogen atom is facilitated.<sup>16,17</sup> The optical spectra of  $\text{H}_2\text{Pheo a}^{2+}$  and Chl a show a close resemblance. Such a similarity is also observed on the triplet spectra of Chl a and protonated Pheo a species. The zero field splitting parameters,  $D$  and  $E$ , for the lowest triplet state ( $T_1$ ) of the Pheo a dication are 0.0288 and  $0.0046 \text{ cm}^{-1}$ , respectively. These values correspond much more closely to those of Chl a than of Pheo a. This may be taken as another indication that the addition of four protons to the four pyrrole rings of the chlorin macrocycle to form  $\text{H}_2\text{Pheo a}^{2+}$  results in an aromatic  $\pi$  system that has electronic properties almost indistinguishable from those produced by insertion of  $\text{Mg}^{2+}$  (to form Chl a) in the Pheo a macrocycle.

### References and Notes

- (1) This work was performed under the auspices of the Division of Physical Research, United States Energy Research and Development Administration.
- (2) Resident Research Associate, 1974-1976.
- (3) T. I. Strelkova and A. N. Sevchenko, *Izv. Akad. Nauk SSSR, Ser. Fiz.*, **29**, 1374 (1965); *Bull. Akad. Nauk SSSR, Ser. Fiz. (Engl. Trans.)*, **29**, 1381 (1965).
- (4) N. Delaporte and D. Laval-Martin, *Analysis*, **1**, 289 (1972).
- (5) V. Zanker, E. Rudolph, and F. Hindelang, *Z. Naturforsch. B*, **28**, 650 (1973).
- (6) W. A. Svec in "The Porphyrins", D. Dolphin, Ed., Academic Press, New York, N.Y., in press.
- (7) J. R. Norris, R. A. Uphaus, and J. J. Katz, *Chem. Phys. Lett.*, **31**, 157 (1975).
- (8) L. L. Shipman, T. M. Cotton, J. R. Norris, and J. J. Katz, *J. Am. Chem. Soc.*, **98**, 8222 (1976).
- (9) M. Kirszenbaum, J. Corset, and M. L. Josien, *J. Phys. Chem.*, **75**, 1327 (1971).
- (10) T. S. S. R. Murty and K. S. Pitzer, *J. Phys. Chem.*, **73**, 1426 (1969).
- (11) R. Bonnett, I. A. D. Gale, and C. F. Stephenson, *J. Chem. Soc. C*, 1168 (1967).
- (12) M. C. Thurnauer, J. J. Katz, and J. R. Norris, *Proc. Natl. Acad. Sci. USA*, **72**, 3270 (1975).
- (13) R. H. Clarke, R. E. Connors, T. J. Schaafsma, J. F. Kleibuker, and R. J. Platenkamp, *J. Am. Chem. Soc.*, **98**, 3474 (1976).
- (14) H. Levanon, and A. Scherz, *Chem. Phys. Lett.*, **31**, 119 (1975).
- (15) W. Hagele, F. Drissler, D. Schmid, and H. C. Wolf, paper presented at the Third International Seminar on Excitation Energy Transfer in Condensed Matter, Prague, Czechoslovakia, 1976.
- (16) E. B. Fleischer and A. L. Stone, *Chem. Commun.*, 332 (1967).
- (17) A. Stone and E. B. Fleischer, *J. Am. Chem. Soc.*, **90**, 2735 (1968).

# Vibrational Spectra and Force Constants of Heptasulfur Imide

Ralf Steudel

*Institut für Anorganische und Analytische Chemie, Technische Universität Berlin, Berlin-Charlottenburg, West Germany (Received August 20, 1976)*

*Publication costs assisted by Verband der Chemischen Industrie*

Raman, infrared, and far-infrared spectra of solid and dissolved  $S_7NH$ ,  $S_7ND$ ,  $S_7^{15}NH$ , and  $S_7^{15}ND$  have been recorded. All fundamental frequencies of heptasulfur imide have been observed and assigned in accordance with the molecular symmetry  $C_s$ . A normal-coordinate treatment was carried out using a modified Urey-Bradley force field with 16 independent force constants. Good agreement between observed and calculated frequencies was obtained and both Urey-Bradley and valence force constants are reported.

## Introduction

In recent years the vibrational spectra of certain sulfur rings such as  $S_6$ ,<sup>1</sup>  $S_8$ ,<sup>2</sup> and  $S_{12}$ <sup>3</sup> have been definitely assigned. These rings belong to the degenerate point groups  $D_{3d}$  and  $D_{4d}$ , respectively, and since there are no substituents the spectra consist of relatively few absorptions and Raman lines, respectively. It has been shown that the spectra can be understood by means of very simple Urey-Bradley force fields with six or seven independent force constants only. For these reasons sulfur rings are ideal molecules to study the dependence of certain fundamental vibrations on ring size and molecular symmetry as well as possible relationships between force constants and structural parameters.<sup>4,5</sup>

Oxidation of  $S_8$  with trifluoroperacetic acid yields  $S_8O^6$  whose molecules still contain eight-membered puckered rings but with  $C_s$  symmetry.<sup>7</sup> The oxygen is linked to one of the sulfur atoms by a double bond in an axial position. The vibrational spectra of  $S_8O$  have been investigated<sup>8</sup> and force constants have been calculated.<sup>9</sup> The results show that the lowering of ring symmetry in  $S_8O$  compared with  $S_8$  causes all bending and torsional modes degenerate in  $S_8$  to split into their components but without much change in average frequency and Raman intensity.<sup>9</sup>

Another possibility to lower the symmetry of the  $S_8$  ring is substitution of one sulfur atom by a heteroatom. The simplest compound of this type whose structure is known and which can be prepared in high purity is heptasulfur imide,  $S_7NH$ .  $S_7NH$  forms almost colorless crystals which can be prepared, for example, from  $S_8$  by treatment with  $NaN_3$  in tris(dimethylamino)phosphine oxide, subsequent hydrolysis in aqueous hydrochloric acid, and purification of the crude product by repeated recrystallization or column chromatography.<sup>10</sup> The molecular structure of  $S_7NH$  has been investigated several times<sup>11,12</sup> but only recently was it possible to determine the positions of all atoms including the hydrogen by x-ray diffraction on single crystals at  $-160^\circ C$ .<sup>13</sup> The molecules consist of crown-shaped  $S_7N$  rings containing almost planar groups  $S_2NH$ . The molecular and site symmetry is  $C_s$  and the centrosymmetric unit cell contains four molecules. The geometrical parameters are given in Table I; the numbering of atoms and bonds is shown in Figure 1.

The vibrational spectra of  $S_7NH$  were first investigated by Nelson<sup>14</sup> who recorded the Raman spectrum in the region  $40\text{--}3500\text{ cm}^{-1}$  and the infrared spectrum in the region  $200\text{--}4000\text{ cm}^{-1}$  using solid  $S_7NH$  and solutions in  $CS_2$ . However, Nelson did not observe all fundamental frequencies and made only a few assignments. Furthermore, some of the wavenumbers given in Tables 2 and 3 of Nelson's paper do not agree with the values which can

TABLE I: Bond Distances ( $r$ , Å), Valence Angles ( $\alpha$ ,  $\beta$ , deg), and Dihedral Angles ( $\tau$ , deg) of Heptasulfur Imide<sup>a</sup>

$r_1, r_2$	2.048	$\alpha_1$	107.2	$\tau_1, \tau_2$	93.5
$r_3, r_4$	2.062	$\alpha_2, \alpha_3$	106.8	$\tau_3, \tau_4$	99.4
$r_5, r_6$	2.049	$\alpha_4, \alpha_5$	108.3	$\tau_5, \tau_6$	94.8
$r_7, r_8$	1.676	$\alpha_6, \alpha_7$	110.1	$\tau_7, \tau_8$	96.5
$R_9$	0.91	$\alpha_8$	123.8	$\beta_1, \beta_2$	117.1

<sup>a</sup> The angle at atom  $i$  is termed  $\alpha_i$ , the two angles  $SNH$  are termed  $\beta_1$  and  $\beta_2$ , and the torsion angle at the bond  $\tau_i$  is called  $\tau_i$ .

be obtained from her Figures 2a and 2b.

To remove these discrepancies and to determine all fundamental frequencies of the heptasulfur imide molecule we recorded the Raman, infrared, and far-infrared spectra of  $S_7NH$ ,  $S_7ND$ ,  $S_7^{15}NH$ , and  $S_7^{15}ND$  in the solid state as well as in  $CS_2$  solutions and made a normal-coordinate analysis.

## Experimental Section

$S_7NH$  was prepared from  $S_8$  and  $NaN_3$ <sup>10</sup> since this method yields only traces of  $S_6(NH)_2$  and  $S_5(NH)_3$  which can be separated from  $S_7NH$  by chromatography only.<sup>15</sup> The crude product was extracted with boiling methanol from which on cooling  $S_8$  crystallizes first followed by  $S_7NH$  on evaporation. The samples used for spectroscopy were purified by repeated recrystallization from  $CH_3OH$  and  $CCl_4$  and in some cases by chromatography and showed melting points between  $109$  and  $113^\circ C$ . All samples were free of  $S_6(NH)_2$  as checked by thin-layer chromatography. Only traces of  $S_8$  were present in some cases but since all strong IR absorptions and Raman lines of  $S_8$  coincide with strong IR absorptions and Raman lines, respectively, of  $S_7NH$  no differences in the spectra of samples from different preparations were observed.

Since the hydrogen in  $S_7NH$  is fairly acidic ( $pK_a = 5^{16}$ )  $S_7ND$  was easily obtained by recrystallization of  $S_7NH$  from excess methanol- $d_1$  ( $\geq 99$  atom %  $CH_3OD$ ) or alternatively by very slow precipitation of 2 g of  $S_7NH$  dissolved in 120 ml of dry acetone with 50 ml of  $D_2O$  ( $\geq 99.7$  atom %  $D_2O$ ) and subsequent drying under high vacuum for several hours.

On standing in air  $S_7ND$  changes to  $S_7NH$  within 24 h. Therefore, due to the conventional sample preparation the IR spectra of  $S_7ND$  exhibited additional weak absorptions belonging to  $S_7NH$ .

$S_7^{15}NH$  was prepared from  $K^{15}NN_2$  (95 atom %  $^{15}N$  at one terminal atom of the azide anion) which first had to be converted into  $Na^{15}NN_2$  by ion exchange since  $KN_3$  does not react with  $S_8$  to give  $S_7NH$  in good yields. 1.6 g of  $Na^{15}NN_2$  was stirred with 1.7 g of  $S_8$  in 33 ml of

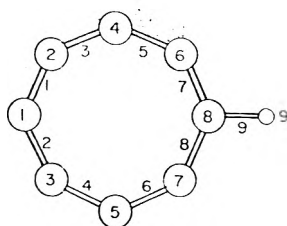


Figure 1. Numbering of atoms and bonds in heptasulfur imide.

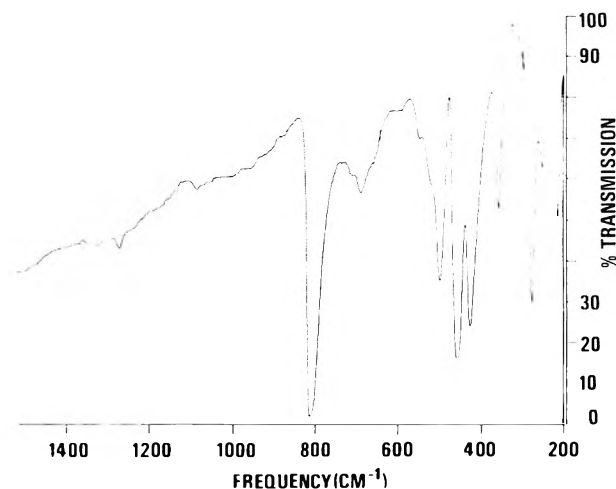


Figure 2. Infrared spectrum of solid  $S_7NH$  at 25 °C.

$[(CH_3)_2N]_3PO$ , the reaction bottle being placed in a nitrogen filled desiccator over  $CaCl_2$ . After hydrolysis in 40 ml of 10% hydrochloric acid and drying under high vacuum the crude product was extracted with 140 ml of hot methanol for 1 hr. After cooling and filtration the solvent was evaporated and the residue dissolved in  $CS_2$ . This solution was used for column chromatography on silica gel eluting with a mixture of equal volumes of  $CCl_4$  and  $n$ -hexane. The presence of  $S_7NH$  in the eluate was checked with alcoholic potassium hydroxide (turns violet with  $S_7NH$ ). After evaporation of the medium fraction and drying under high vacuum colorless crystals of a  $S_7^{14}NH/S_7^{15}NH$  mixture (1:1) were obtained (melting point 113 °C). In the following this mixture is denoted  $S_7^*NH$ . All chemicals used were of the highest commercially available quality.

The Raman spectra were recorded in the region 10–3500  $cm^{-1}$  using a Cary 82 spectrometer with triple monochromator and the 488.0-, 514.5-, and 647.1-nm lines of Ar and Kr lasers. Powdered samples as well as solutions in  $CS_2$  (freshly distilled from  $P_2O_{10}$ ) were investigated. With Ar laser excitation a rotating sample holder was used for solid samples. Polarization measurements were possible for the strongest Raman lines only since the solubility is not very high.

The infrared spectra in the region 200–4000  $cm^{-1}$  were recorded using two grating spectrometers (Beckman IR 12 and Perkin-Elmer 325). KBr, CsBr, and CsI disks were prepared with 5–35 mg of heptasulfur imide. Low temperature spectra were recorded using a device described earlier.<sup>17</sup> Solutions in  $CS_2$  were investigated in matched 0.1–1.0-mm cells of CsI. The region 50–400  $cm^{-1}$  was also investigated with a Polytec FIR 30 Fourier transform spectrometer using sample disks prepared from pure  $S_7NH$ .

#### Vibrational Spectra and Frequency Assignment

The observed infrared bands and Raman lines are listed in Tables II–IV and the spectra are shown in Figures 2–4. For a molecule of  $C_s$  symmetry consisting of 9 atoms, 21

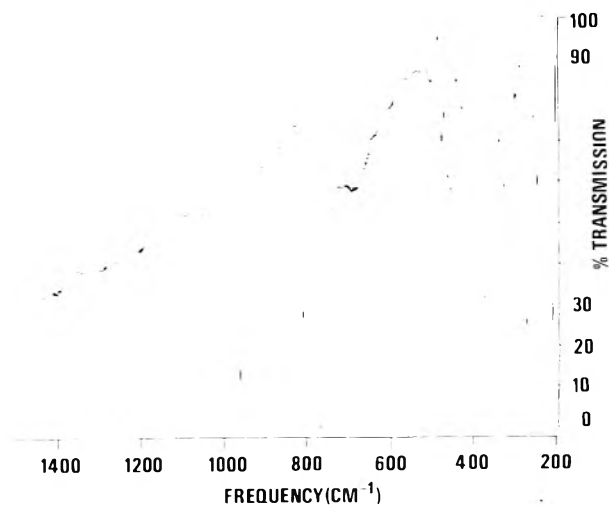


Figure 3. Infrared spectrum of solid  $S_7ND$  at 25 °C (containing approximately 10%  $S_7NH$ ).

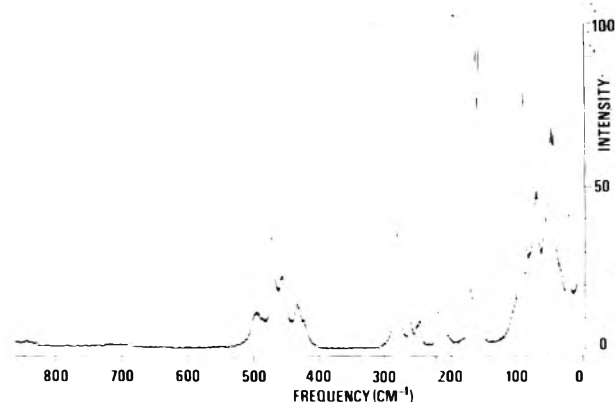


Figure 4. Raman spectrum of solid  $S_7NH$  at 25 °C (spectral bandwidth 1.5  $cm^{-1}$ ).

fundamental vibrations are to be expected, 12 of which belong to the species  $a'$  and 9 to  $a''$  and all of which are infrared and Raman active. There must be 9 stretching, 10 bending, and 2 torsion vibrations (cf.  $S_8O^9$ ). The NH stretching wavenumber of  $S_7NH$  at 3334  $cm^{-1}$  in  $CS_2$  shifts to 3270  $cm^{-1}$  in the solid due to weak intermolecular H...S hydrogen bonding.<sup>13</sup> In  $S_7ND$  it occurs at 2475  $cm^{-1}$  corresponding to a H/D ratio of 1.35.  $S_7^*NH$  shows  $\nu_{NH}$  at 3331  $cm^{-1}$  (in  $CS_2$ ) but no splitting was observed which, according to the mass difference between  $^{14}N$  and  $^{15}N$ , should amount to 7  $cm^{-1}$ .

The SN stretching wavenumbers can be expected in the region 600–1000  $cm^{-1}$  since the planar  $HNS_2$  group can be compared with the molecules  $OCl_2$  (673, 634<sup>18</sup>),  $H^{11}BCl_2$  (892, 740<sup>19</sup>), and  $HNCl_2$  (687, 666<sup>20</sup>) whose XCl stretching wavenumbers are given in parentheses. The antisymmetric SN vibration is of high IR intensity but does not show up in the Raman spectrum. It shifts on deuteration much more than on  $^{15}N$  substitution because of some coupling with  $\delta_{ND}(a'')$  in  $S_7ND$ . This mode occurs at 1288  $cm^{-1}$  in  $S_7NH$  and at 970  $cm^{-1}$  in  $S_7ND$ . The coupling also causes a substantial increase in IR intensity of  $\delta_{ND}$ . In  $HNCl_2$  the corresponding vibration occurs at 1295  $cm^{-1}$ .<sup>20</sup> The symmetric SN vibration of  $S_7NH$  does also not occur in the Raman spectrum and is of very low IR intensity at 25 °C but can be easily detected in IR spectra taken at -185 °C. The wavenumbers are listed in Table IV.

The six SS stretching wavenumbers ( $3a'$ ,  $3a''$ ) can be expected in the region 400–500  $cm^{-1}$  since there is a linear relationship between SS bond distances and average SS frequency<sup>5</sup> from which  $\nu_{SS} = 458 \text{ cm}^{-1}$  is obtained. Since

TABLE II: Vibrational Wavenumbers of S<sub>7</sub>NH (cm<sup>-1</sup>)<sup>a</sup>

Raman		Infrared		Assignment	
Solid	In CS <sub>2</sub>	Solid	In CS <sub>2</sub>		
21 m				} Lattice	
47 } vs					
50 } vs					
56 w,sh		52 vw			
71 s	obsc	63 w		a' τ	
91 vs	89 s	75 w		a'' τ	
105 w,sh		96 vw		91 + 21 or 63 + 52	
158 vs }		107 m		a' + a'' δ <sub>SSS</sub>	
162 vs }	160 vs,dp	168 m			
171 w	170 vw,sh			2·91	
215 vvs		212 s	204 s	a'' δ <sub>SSS</sub>	
220 vw,sh	212 vvs,p		211 m	a' δ <sub>SSS</sub>	
247 w				160 + 71	
251 vw	249 w	250 m	249 m	a' δ <sub>SSS</sub>	
261 w				160 + 91	
282 s	272 m,p	260 w		a'' δ <sub>SSN</sub>	
		276 s	272 m	a' δ <sub>SSN</sub>	
		295 w		212 + 91	
		356 m	358 w-m	a' δ <sub>SSN</sub>	
424 w,sh		427 s	424 s	a'' ν <sub>SS</sub>	
433 m	440 m			} + a' γ <sub>NH</sub>	
456 m	460 w	456 s	446 s		a' ν <sub>SS</sub>
			467 w,sh		a'' ν <sub>SS</sub>
473 s	478 m			a' ν <sub>SS</sub>	
496 m	487 m	500 m	494 m	a' ν <sub>SS</sub>	
		522 w,sh	517 w,sh	272 + 249	
		552 vw		500 + 52 or 500 + 63	
		660 vw,sh		500 + 160 or 456 + 212	
		694 w	680 w	a' ν <sub>SN</sub>	
		718 vw		456 + 261 or 2·356	
		740 vw		456 + 279	
		816 vvs	805.8 s	a'' ν <sub>SN</sub>	
		1274 vw	1288 m	a'' δ <sub>SNH</sub>	
3258 m-s		3270 m	3334 m	a' ν <sub>NH</sub>	

<sup>a</sup> v, very; s, strong; m, medium; w, weak; sh, shoulder; b, broad; p, polarized; dp, depolarized; obsc, obscured by CS<sub>2</sub>; ν, stretching; δ, bending; τ, torsion vibration.

the bond distances vary by only 0.014 Å, vibrational coupling only causes the ν<sub>SS</sub> to be spread over a certain region. The spectra of S<sub>7</sub>NH and S<sub>7</sub>ND show considerable differences in the 400–500-cm<sup>-1</sup> region. In the case of S<sub>7</sub>ND five frequencies of low or medium intensity are found in the IR and Raman spectra and can be assigned to the six SS stretching fundamentals assuming one incidental degeneracy at 463 cm<sup>-1</sup>. Since all the calculations show the SS stretching modes distributed in alternating order to the two symmetry species (a' > a'' ≈ a' > a'' > a' > a'') we assign the wavenumbers in the 420–480-cm<sup>-1</sup> region accordingly.

S<sub>7</sub>NH exhibits only three strong IR absorptions in the 400–500-cm<sup>-1</sup> region. These are absent not only in S<sub>7</sub>ND but also in the spectrum of (S<sub>7</sub>N)<sub>2</sub>S<sup>21</sup> in which two S<sub>7</sub>N rings are connected by a sulfur atom. The same holds for S<sub>7</sub>NCH<sub>3</sub>.<sup>22</sup> Therefore, we assume that the wavenumbers at 427, 456, and 498 cm<sup>-1</sup> in the spectra of S<sub>7</sub>NH are connected with the symmetric NH bending vibration (NH wagging). In S<sub>7</sub>ND this mode occurs as a broad structured absorption at 367 cm<sup>-1</sup>. In S<sub>7</sub>NH it must be coupled to some extent with the SS stretching modes and we assign the 500-cm<sup>-1</sup> frequency which occurs in the Raman spectrum at 496 cm<sup>-1</sup> and is polarized to the highest SS stretching mode which is intensified and shifted from 474 cm<sup>-1</sup> in S<sub>7</sub>ND by mixing with δ<sub>NH</sub>(a'). This assumption is supported by the normal-coordinate analysis (see below). The two remaining wavenumbers at 456 and 427 cm<sup>-1</sup> are assigned to δ<sub>NH</sub>(a') assuming a splitting caused by a slightly asymmetric double minimum potential (DMP) as has been observed for NH stretching frequencies previously.<sup>23</sup> The

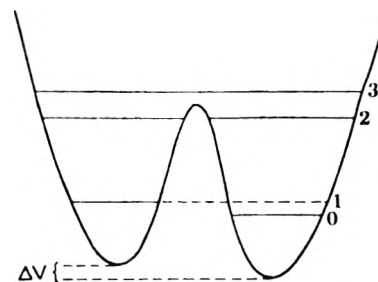


Figure 5. Assumed double minimum potential for the NH wagging mode of heptasulfur imide.

x-ray structure analysis of S<sub>7</sub>NH showed the hydrogen in an axial position with respect to the S<sub>7</sub>N ring but the angle between the NH bond and the plane formed by the neighboring atoms 6, 7, and 8 (see Figure 1) amounts to only 14° (in NH<sub>3</sub>, 56°). Since there must be another position for the hydrogen on the other side of that plane (equatorial position) differing in energy only slightly (due to the different long range SH interaction with atoms 4 and 5) the assumption of a DMP for the wagging vibration seems reasonable. The barrier between the axial and equatorial positions should be quite low causing the first vibrationally excited δ<sub>NH</sub> level to be located near the top of the barrier which results in a splitting of this level (see Figure 5). In this case the relative IR intensities of the transitions 0–2 and 0–3 can be of comparable magnitude.<sup>24,25</sup> On deuteration the levels 0 to 3 decrease in energy and the splitting of levels 2 and 3 becomes much smaller leading to one broad but structured absorption

TABLE III: Vibrational Wavenumbers of  $S_7ND$  ( $cm^{-1}$ )<sup>a</sup>

Raman solid	Infrared		Assignment
	Solid	In $CS_2$	
22 m			} Lattice
46 m			
49 m			
56 w,sh			
70 m			
91 s			
105 vw,sh			
157 } vs			
161 } vs			
171 w			
	211 vs	203 vs	$a'' \delta_{SSS}$
214 vs		210 m	$a' \delta_{SSS}$
221 w			160 + 70
247 w	247 m	248 s	$a' \delta_{SSS}$
252 w			160 + 91
262 w	262 w		$a'' \delta_{SSN}$
281 m	272 vs	270 s	$a' \delta_{SNS}$
	327 m	312 vs	$a' \delta_{SSN}$
	367 vs,b	368 vs	$a' \gamma_{ND}$
	426 w	427 m	$a'' \nu_{SS}$
439 w	435 vw		$a' \nu_{SS}$
	455 s	461 m	$a'' \nu_{SS}$
460 w,b	464 m	469 m	$a' + a'' \nu_{SS}$
472 s	475 m	478 m	$a' \nu_{SS}$
	501 w		$S_7NH$
		517 w	270 + 248
	658 w	655 w	461 + 204
	680 w-m	676 vw	$a' \nu_{SN}$
		697 w	427 + 270
709 vvw			
715 vvw			
721 vvw	723 w	713 w	455 + 272
729 vvw			
	776 vvs	774.5 vvs	$a'' \nu_{SN}$
	966 vs	970 vs	$a'' \delta_{SND}$
	1055 vw,b	1050 vw	970 + 91 or 776 + 272
2425 w	2433 s	2475 s	$a' \nu_{ND}$

<sup>a</sup> For abbreviations see Table II.

TABLE IV: SN Stretching Wavenumbers of Heptasulfur Imide ( $cm^{-1}$ )

Species	State	$S_7^{14}NH$	$S_7^{14}ND$	$S_7^{15}NH$	$S_7^{15}ND$
$a'$	Solid	694	680		
$a''$	In $CS_2$	805.8	774.5	787.0	762.0

band for  $\delta_{ND}(a')$ . This explanation for the strong IR absorptions of  $S_7NH$  in the region 400–500  $cm^{-1}$  is supported by the observation that these bands are observed in  $CS_2$  solution too but shifted to lower wavenumbers due to the cleavage of the weak hydrogen bonds in solid  $S_7NH$ . Furthermore,  $S_7NH$  reacts with tris(dimethylamino)-phosphorus oxide (TDPO) to form the solid adduct TDPO·2 $S_7NH$  in which according to a x-ray structure analysis the two NH groups are hydrogen bonded to the oxygen atom.<sup>26</sup> In this compound  $\delta_{NH}(a')$  occurs at 671  $cm^{-1}$  and  $\delta_{ND}(a')$  at 545  $cm^{-1}$  which in both cases corresponds to a shift from  $S_7NH(D)$  by a factor of 1.5 provided  $\delta_{NH}(a')$  is located near 450  $cm^{-1}$  in  $S_7NH$ .

The assignment of the 10 ring bending and torsional modes is more difficult. The highest frequency at 356  $cm^{-1}$  can be assigned to the symmetric SSN bending mode which according to the lower mass of nitrogen must be the highest ring bending mode.<sup>27</sup> No  $^{14}N/^{15}N$  splitting has been observed for this mode which due to the calculations should amount to 6  $cm^{-1}$ . In  $S_7ND$   $\delta_{SSN}(a')$  is repelled by  $\delta_{ND}(a')$  and therefore shifted to 327  $cm^{-1}$ .

The remaining nine modes can be expected between 300 and 60  $cm^{-1}$  since all corresponding vibrations of  $S_8$  and  $S_8O$  are found in this region. The two torsional modes degenerate in  $S_8$  (85  $cm^{-1}$ ) and split in  $S_8O$  (84, 67  $cm^{-1}$ )

TABLE V: Comparison of Bending and Torsional Modes of Eight-Membered Rings (Symmetry Species, Wavenumbers, Raman Intensities)

$S_8O$ ( $C_8$ )		$S_8$ ( $D_{4d}$ )		$S_7NH$ ( $C_8$ )	
$a'$	219 vs	$a_1$	216 s	$a'$	215 vvs
$a'$	250 vw	$b_2$	243 w	$a'$	282 s
$a'$	190 w		$e_1$	$e_1$	184 w
$a''$	197 w				
$a'$	67 s		$e_2$	$e_2$	85 s
$a''$	84 s				
$a'$	140 s		$e_2$	$e_2$	152 s
$a''$	157 vs				
$a'$	(219)		$e_3$	$e_3$	243 w
$a''$	235 vw				
				$a'$	250 vw
				$a''$	261 w

can be expected to be of strong Raman intensity and should be located near 80  $cm^{-1}$ . We assign the strong Raman lines at 91 and 70  $cm^{-1}$  to these modes and consider all wavenumbers below 70  $cm^{-1}$  to be lattice modes. In contrast to the 91- $cm^{-1}$  line the 70- $cm^{-1}$  Raman line has not been observed for TDPO·2 $S_7NH$ <sup>26</sup> and  $(S_7N)_2SO$ .<sup>29</sup> However, in  $S_7NH$  and  $S_7ND$   $\tau(a')$  is strongly coupled with  $\delta_{NH(D)}$  which may remove the incidental degeneracy of  $\tau(a')$  and  $\tau(a'')$  which must be assumed for the two derivatives. The lattice vibrations of  $S_8$  have been found below 65  $cm^{-1}$  and some of them give rise to strong Raman lines.<sup>30,31</sup> In  $S_8O$  the lattice vibrations also occur below 65  $cm^{-1}$ .<sup>9</sup> Since  $S_7NH$  is of similar shape and mass as  $S_8$  and  $S_8O$  the wavenumbers of the lattice vibrations should be similar too. Since the unit cell of heptasulfur imide is centrosymmetrical ( $D_{2h}^6$ )<sup>11-13</sup> the lattice vibrations may be either Raman or infrared active.

For the assignment of the remaining fundamentals it must be taken into account that only frequencies occurring in all compounds containing the  $S_7N$  unit can be ring bending modes of  $S_7NH$ . Since this is not the case for the Raman lines at 171, 220, and 251  $cm^{-1}$  these frequencies must represent combination vibrations or overtones. The remaining wavenumbers are assigned according to their IR intensities and by analogy with  $S_8$  and  $S_8O$ . The strong Raman line at 160  $cm^{-1}$  slightly split in solid heptasulfur imide has been observed for  $S_8$  at 152  $cm^{-1}$  and for  $S_8O$  at 140/157  $cm^{-1}$  and must represent two modes  $\delta_{SSS}(a' + a'')$  since there is no second line of similar intensity nearby. The splitting in the solid state may arise from correlation field interaction since it is not observed for solid TDPO·2 $S_7NH$ .<sup>26</sup>

The strongest Raman line of  $S_7NH$  occurs at 215  $cm^{-1}$ . This wavenumber is characteristic for eight-membered sulfur rings since it has been observed with high Raman intensity for  $S_8$  (216) and  $S_8O$  (219) also but not for  $S_6$ ,  $S_7$ , and  $S_{12}$ .<sup>4</sup> In the IR spectrum of dissolved  $S_7NH$  two bands occur at 204 and 211  $cm^{-1}$  which correspond to the IR absorption of solid  $S_7NH$  at 212  $cm^{-1}$  and the Raman line at 215  $cm^{-1}$  and represent two SSS bending modes ( $a'' + a'$ ).

The three bending modes left are assigned to the IR absorptions at 276( $a'$ ), 260( $a''$ ), and 250( $a'$ )  $cm^{-1}$ . The 276- $cm^{-1}$  frequency must be the SNS bending mode because of its high IR intensity and its shift on isotopic substitution (in  $CS_2$ :  $S_7NH$  272,  $S_7ND$  270,  $S_7^*NH$  270,  $S_7^*ND$  268  $cm^{-1}$ ).

In Table V the ring bending and torsional modes of  $S_8$ ,  $S_8O$ , and  $S_7NH$  are compared. No differences in the spectra of  $S_7NH$ ,  $S_7ND$ ,  $S_7^*NH$ , and  $S_7^*ND$  were observed below 260  $cm^{-1}$ .

## Force Field

The force constant calculations were made using a modified Urey-Bradley force field since this field was shown to be suitable for  $S_8^2$  as well as for  $S_4N_4H_4$ <sup>32</sup> and should therefore be applicable to  $S_7NH$  too. The details have been discussed in earlier papers.<sup>1-4,9,32</sup>

The following 16 independent force constants were used:

$K_1$	SS stretching
$K_2$	SN stretching
$K_3$	ND stretching
$H_1$	bending at S
$H_2$	SNS bending
$H_3$	SNH bending
$H_4$	NH wagging
$F_1$	SS repulsion
$F_2$	SN repulsion
$F_3$	SH repulsion
$Y_1$	SS torsion
$Y_2$	SN torsion
$C$	long-range SS and SN repulsion
$P_1$	bond-bond interaction at S
$P_2$	bond-bond interaction at N
$U$	NH wagging-SN torsion interaction

With these constants the potential energy becomes

$$\begin{aligned}
 2V = & \sum^6 K_1(\Delta r)^2 + 2\sum^6 K_1'r(\Delta r) + \sum^2 K_2(\Delta R)^2 \\
 & + 2\sum^2 K_2'r(\Delta R) + K_3(\Delta R)^2 + 2K_3'R(\Delta R) \\
 & + \sum^7 H_1(r\Delta\alpha)^2 + 2\sum^7 H_1'r(r\Delta\alpha) + H_2(r\Delta\alpha)^2 \\
 & + 2H_2'r(r\Delta\alpha) + \sum^2 H_3(\bar{r}\Delta\beta)^2 + 2\sum^2 H_3'\bar{r}(\bar{r}\Delta\beta) \\
 & + H_4(R\Delta\gamma)^2 + 2H_4'R(R\Delta\gamma) + \sum^6 F_1(\Delta q_1)^2 \\
 & + 2\sum^6 F_1'q_1(\Delta q_1) + \sum^2 F_2(\Delta q_2)^2 + 2\sum^2 F_2'q_2(\Delta q_2) \\
 & + \sum^2 F_3(\Delta q_3)^2 + 2\sum^2 F_3'q_3(\Delta q_3) + \sum^6 Y_1(r\Delta\tau)^2 \\
 & + 2\sum^6 Y_1'r(r\Delta\tau) + \sum^2 Y_2(r\Delta\tau)^2 + 2\sum^2 Y_2'r(r\Delta\tau) \\
 & + \sum^8 C(\Delta q')^2 + 2\sum^8 C'q'(\Delta q') + 2\sum^7 P_1\Delta r\Delta r' \\
 & + 2P_2\Delta r\Delta r' + 2\sum^2 U\Delta\gamma\Delta\tau
 \end{aligned}$$

The coordinates  $q$  and  $q'$  are the distances between atoms  $i$  and, respectively,  $i + 2$  and  $i + 3$ , and  $r$  and  $r'$  are the distances of adjacent bonds within the ring. Since all the distances  $q'$  are very similar ( $4.15 < q' < 4.45$  Å) only one force constant  $C$  was used.<sup>33</sup> Any long-range repulsion involving the hydrogen atom was neglected. The constants  $F'$  and  $C'$  were constrained by the conventional assumptions  $F' = -0.1F$  and  $C' = -0.1C$ . All constants  $K'$ ,  $H'$ , and  $Y'$  are eliminated in the removal of the redundant coordinates  $q$  and  $q'$ .

## Calculations

The calculations were performed by a CD 6500 computer using the programs UBZM by Schachtschneider<sup>34</sup> to calculate the  $Z$  matrix elements for the force constant  $C$  and BGLZ and LSMA by Shimanouchi<sup>35</sup> to calculate all matrices, the frequencies, and potential energy distribution. The valence force constants were obtained from the  $F$  matrix.

The Cartesian coordinates were taken from the recent low temperature x-ray structure analysis.<sup>13</sup> However, the NH bond length was assumed to be 1.03 Å which is the average in a large number of NH compounds and the hydrogen was assumed to be in the plane of the neigh-

boring atoms ( $\beta_1 = \beta_2 = 118.1^\circ$ ).<sup>36</sup> The symmetry coordinates with exception of the NH wagging coordinate  $S = \Delta\gamma$  were taken from  $S_8O^9$  ( $\gamma$  is the angle between the NH bond and the plane of atoms 6-8).

## Force Constants

The first set of frequencies was calculated with assumed Urey-Bradley force constants whose values were chosen using the force constants of  $S_8^2$  and  $S_4N_4H_4$ .<sup>32</sup> To adjust the calculated to the observed frequencies by the least-squares method 38 observed values were used for  $S_7NH(\nu_2-\nu_4, \nu_7-\nu_{14}, \nu_{18}-\nu_{21})$ ,  $S_7ND(\nu_1-\nu_{21})$ ,  $S_7^{15}NH(\nu_{14})$ , and  $S_7^{15}ND(\nu_{14})$ .  $\nu_{NH}$  was neglected because of its anharmonicity. Solution frequencies were taken above  $750\text{ cm}^{-1}$ , otherwise solid state values were used.

First groups of force constants were varied but in the last run all 16 force constants were allowed to vary simultaneously until the corrections became zero. The frequencies obtained as well as the potential energy distribution are given in Table VI. The force constants are listed in Tables VII and VIII.

The maximum difference between observed and calculated wavenumbers amounts to  $9\text{ cm}^{-1}$ .

## Discussion

The Urey-Bradley and valence force constants of  $S_7NH$  can be compared with those of  $S_8^2$  and  $S_4N_4H_4$ .<sup>32</sup> This comparison shows that all corresponding values are very similar indicating that the frequency assignment of  $S_7NH$  is correct and that the force field is appropriate. It should be pointed out, however, that the force constants connected with the wagging mode of  $S_7NH$  cannot be considered as reliable as those of  $S_4N_4H_4$  which exhibits three wagging modes from which the force constants can be determined more accurately. The normal-coordinate treatment of  $S_4N_4H_4$  has shown that in addition to the wagging-torsion interaction also wagging-stretching and wagging-bending interaction force constants are necessary which, however, could not be used in the case of  $S_7NH$  because of the only one wagging frequency. Nevertheless, all constants connected with the NH group are very similar in  $S_7NH$  and  $S_4N_4H_4$ .

There exist relationships between bond distances and  $SN$ <sup>39</sup> and  $SS$ <sup>5</sup> stretching force constants. The mean values calculated for  $S_7NH$  (Table VIII) are in agreement with these equations (calcd  $f_r(SN) = 3.9$ ,  $f_r(SS) = 2.47\text{ mdyn/\AA}$ ). However, we have no explanation for the two different SS stretching force constants.

The average SS stretching frequency of  $S_7ND$  of  $453\text{ cm}^{-1}$  is in agreement with the value of  $458\text{ cm}^{-1}$  calculated from the bond distance-stretching frequency relationship.<sup>5</sup> The average SN stretching frequency of  $S_7NH$  ( $751\text{ cm}^{-1}$ ), however, does not fit the known bond distance-stretching frequency relationship<sup>40</sup> derived from only a few values some of which are not longer valid. Therefore, this relationship should be reinvestigated.

Nelson<sup>14</sup> observed a number of very weak Raman lines in the SN stretching region of  $S_7NH$  whose frequencies do not agree with the two infrared active  $\nu_{SN}$  modes. She explained these lines by factor group splitting of the  $\nu_{SN}$ . However, we did not observe these lines and the small frequency shift of the two  $\nu_{SN}$  modes on dissolution of  $S_7NH$  in  $CS_2$  does not support the idea of any measurable correlation field splitting. We therefore believe that the weak Raman lines are combination vibrations. We did also not observe the splitting of  $\delta_{SNH}(a'')$  reported by Nelson.

The most peculiar detail of the  $S_7NH$  spectrum is the NH wagging mode giving rise to three strong IR bands near

TABLE VI: Observed and Calculated Wavenumbers of S<sub>7</sub>NH and S<sub>7</sub>ND and Potential Energy Distribution to the Symmetry Coordinates<sup>a</sup>

		S <sub>7</sub> <sup>14</sup> NH			S <sub>7</sub> <sup>14</sup> ND		
		Wavenumber, cm <sup>-1</sup>		Potential energy, (%)	Wavenumber, cm <sup>-1</sup>		Potential energy, %
		Obsd	Calcd		Obsd	Calcd	
a'	$\nu_1$	(3334)	3393	100 $\nu_{\text{NH}}$	2475	2475	99 $\nu_{\text{ND}}$
	$\nu_2$	694	693	83 $\nu_{\text{SN}}$ , 13 $\delta_{\text{SNS}}$	680	681	84 $\nu_{\text{SN}}$ , 12 $\delta_{\text{SNS}}$
	$\nu_3$	498	498	45 $\gamma$ , 44 $\nu_{\text{SS}}$	474	477	88 $\nu_{\text{SS}}$
	$\nu_4$	472	465	88 $\nu_{\text{SS}}$	463	461	85 $\nu_{\text{SS}}$ , 12 $\delta_{\text{SSS}}$
	$\nu_5$	(456)	450	93 $\nu_{\text{SS}}$	439	448	97 $\nu_{\text{SS}}$
	$\nu_6$	(433)	436	52 $\nu_{\text{SS}}$ , 38 $\gamma$	367	369	37 $\delta_{\text{SSN}}$ , 36 $\gamma$ , 12 $\nu_{\text{SS}}$
	$\nu_7$	356	357	60 $\delta_{\text{SSN}}$ , 12 $\tau_{\text{SN}}$ , 12 $\nu_{\text{SS}}$	327	327	56 $\delta_{\text{SSN}}$ , 20 $\tau_{\text{SN}}$ , 15 $\gamma$
	$\nu_8$	279	281	39 $\delta_{\text{SNS}}$ , 22 $\gamma$ , 13 $\tau_{\text{SN}}$ , 13 $\delta$	276	274	37 $\delta_{\text{SNS}}$ , 33 $\gamma$
	$\nu_9$	249	245	75 $\delta_{\text{SSS}}$	247	244	69 $\delta_{\text{SSS}}$ , 14 $\gamma$
	$\nu_{10}$	215	214	63 $\delta_{\text{SSS}}$ , 18 $\tau_{\text{SS}}$	214	213	61 $\delta_{\text{SSS}}$ , 14 $\tau_{\text{SS}}$
	$\nu_{11}$	160	162	77 $\delta_{\text{SSS}}$	159	161	75 $\delta_{\text{SSS}}$ , 11 $\gamma$
	$\nu_{12}$	71	70	39 $\gamma$ , 33 $\tau_{\text{SN}}$ , 21 $\tau_{\text{SS}}$	70	70	39 $\gamma$ , 33 $\tau_{\text{SN}}$ , 21 $\tau_{\text{SS}}$
a''	$\nu_{13}$	1288	1290	98 $\delta_{\text{NH}}$	970	968	81 $\delta_{\text{ND}}$ , 19 $\nu_{\text{SN}}$
	$\nu_{14}$	805.8	808	98 $\nu_{\text{SN}}$	774.5	773	93 $\nu_{\text{SN}}$
	$\nu_{15}$	(472)	462	93 $\nu_{\text{SS}}$	463	462	93 $\nu_{\text{SS}}$
	$\nu_{16}$	(456)	459	87 $\nu_{\text{SS}}$	455	459	87 $\nu_{\text{SS}}$
	$\nu_{17}$	(427)	423	99 $\nu_{\text{SS}}$	428	423	99 $\nu_{\text{SS}}$
	$\nu_{18}$	261	256	59 $\delta_{\text{SSN}}$ , 28 $\delta_{\text{SSS}}$	262	255	58 $\delta_{\text{SSN}}$ , 29 $\delta_{\text{SSS}}$
	$\nu_{19}$	212	214	58 $\delta_{\text{SSS}}$ , 18 $\tau_{\text{SS}}$	211	213	57 $\delta_{\text{SSS}}$ , 22 $\tau_{\text{SS}}$
	$\nu_{20}$	160	168	70 $\delta_{\text{SSS}}$ , 23 $\delta_{\text{SSN}}$	159	168	70 $\delta_{\text{SSS}}$ , 23 $\delta_{\text{SSN}}$
	$\nu_{21}$	91	92	65 $\tau_{\text{SS}}$ , 26 $\tau_{\text{SN}}$	91	92	64 $\tau_{\text{SS}}$ , 25 $\tau_{\text{SN}}$

S<sub>7</sub><sup>15</sup>NH:  $\nu_{\text{SN}}(a'')$  obsd 787.0, calcd 788S<sub>7</sub><sup>15</sup>ND:  $\nu_{\text{SN}}(a'')$  obsd 762.0, calcd 760<sup>a</sup>  $\geq 10\%$ ; wavenumbers in brackets were not used in the force constant calculation.

TABLE VII: Urey-Bradley Force Constants of Heptasulfur Imide (mdyn/Å)

$K_1(\text{SS})$	1.751	$H_4(\text{NH})$	0.180	$Y(\text{SS})$	0.023
$K_2(\text{SN})$	2.805	$F_1(\text{SS})$	0.347	$Y(\text{SN})$	0.045
$K_3(\text{ND})$	5.749	$F_2(\text{SN})$	0.703	$C$	0.039
$H_1(\text{S})$	0.053	$F_3(\text{SH})$	0.552	$U(\gamma/\tau)$	0.142
$H_2(\text{SNS})$	0.199	$P_1(\text{S})$	0.236		
$H_3(\text{SNH})$	0.109	$P_2(\text{N})$	0.572		

TABLE VIII: Valence Force Constants of Heptasulfur Imide (mdyn/Å)<sup>2</sup>

$f_{\text{r}}(\text{SS})$	2.23 ( $r_1 - r_4$ )	$f_{\text{a}}$	0.23 ( $a_1 - a_5$ )
$f_{\text{r}}(\text{SN})$	2.53 ( $r_5, r_6$ )	$f_{\text{a}}$	0.36 ( $a_6, a_7$ )
$f_{\text{r}}(\text{ND})$	3.98	$f_{\text{a}}$	0.33 ( $a_8$ )
$f_{\text{rr}}(\text{SS/SS})$	6.37	$f_{\beta}$	0.28
$f_{\text{rr}}(\text{SS/SN})$	0.52	$f_{\gamma}$	0.18
$f_{\text{rr}}(\text{SN/SN})$	0.80	$f_{\tau}$	0.03 (SSSS)
$f_{\text{rR}}(\text{SN/NH})$	0.90	$f_{\tau}$	0.04 (SSSN)
$f_{\text{ra}}$	0.41	$f_{\tau}$	0.05 (SSNS)
$f_{\text{r}\beta}(\text{SN/NH})$	0.15-0.31	$f_{\gamma\tau}$	0.14
	0.31		

<sup>a</sup>  $f_i$ , diagonal constants;  $f_{ij}$ , interaction constants between the nearest coordinates indicated.

450 cm<sup>-1</sup>. The potential energy distribution shows  $\gamma_{\text{NH}}$  to be mixed with many other a' vibrations but this result may be partly unreal since the PED with respect to  $\gamma_{\text{NH}}$  was quite sensitive to the kind and the values of certain force constants (94 different sets of force constants were examined). We, therefore, doubt that the three IR bands at 427, 456, and 500 cm<sup>-1</sup> arise all from coupling of  $\gamma_{\text{NH}}$  with two or three SS stretching vibrations. Only the highest band at 500 cm<sup>-1</sup> is believed to be a mixture of  $\gamma_{\text{NH}}$  and  $\nu_{\text{SS}}$ . The remaining "doublet" at 427/456 cm<sup>-1</sup> must be caused by a double minimum potential as discussed above or by Fermi resonance of  $\gamma_{\text{NH}} \approx 450$  cm<sup>-1</sup> with a combination vibration. There are indeed several suitable binary combinations belonging to the a' species (for example, 2·214, 2·212, 356 + 71, 279 + 160). However, there are also combinations close to  $\gamma_{\text{ND}} = 367$  cm<sup>-1</sup> but no Fermi resonance is observed. We therefore favor the explanation

by a double minimum potential.

*Acknowledgment.* The author is grateful to Miss B. Pawlaczyk for her assistance in preparing heptasulfur imide and to Dipl.-Chem. F. Rose for running the low temperature spectra. The financial support by the Bundesminister für Wirtschaft (ERP-Sondervermögen) and the Verband der Chemischen Industrie is also gratefully acknowledged.

## References and Notes

- (1) L. A. Nimon and V. D. Neff, *J. Mol. Spectrosc.*, **26**, 175 (1968).
- (2) D. W. Scott, J. P. McCullough, and F. H. Kruse, *J. Mol. Spectrosc.*, **13**, 313 (1964).
- (3) R. Steudel and D. F. Eggers, *Spectrochim. Acta, Part A*, **31**, 879 (1975).
- (4) R. Steudel, *Spectrochim. Acta, Part A*, **31**, 1065 (1975).
- (5) R. Steudel, *Z. Naturforsch. B*, **30**, 281 (1975).
- (6) R. Steudel and J. Latte, *Angew. Chem.*, **86**, 648 (1974).
- (7) P. Luger, H. Bradaczek, R. Steudel, and M. Rebsch, *Chem. Ber.*, **109**, 180 (1976).
- (8) R. Steudel and M. Rebsch, *J. Mol. Spectrosc.*, **51**, 334 (1974).
- (9) R. Steudel and D. F. Eggers, *Spectrochim. Acta, Part A*, **31**, 871 (1975).
- (10) J. Bojes and T. Chivers, *J. Chem. Soc., Dalton Trans.*, 1715 (1975).
- (11) J. Weiss, *Z. Anorg. Allg. Chem.*, **305**, 191 (1960).
- (12) J. Weiss and H.-S. Neubert, *Acta Crystallogr.*, **18**, 815 (1965).
- (13) H. J. Hecht, R. Reinhardt, R. Steudel, and H. Bradaczek, *Z. Anorg. Allg. Chem.*, **426**, 43 (1976).
- (14) J. Nelson, *Spectrochim. Acta, Part A*, **27**, 1105 (1971).
- (15) E. R. Cole and R. F. Bayfield in A. Senning, "Sulfur in Organic and Inorganic Chemistry", Vol. 2, Marcel Dekker, New York, N.Y., 1972, p 223.
- (16) T. Chivers and I. Drummond, *Inorg. Chem.*, **13**, 1222 (1974).
- (17) R. Steudel, *Z. Anorg. Allg. Chem.*, **360**, 143 (1968).
- (18) D. J. Gardiner, *J. Mol. Spectrosc.*, **38**, 476 (1971).
- (19) C. D. Bass, L. Lynds, T. Wolfram, and E. E. DeWames, *J. Chem. Phys.*, **40**, 3611 (1964).
- (20) G. E. Moore and R. M. Badger, *J. Am. Chem. Soc.*, **74**, 6076 (1952).
- (21) R. Steudel and F. Rose, unpublished results.
- (22) E. M. Tingle and F. P. Olsen, *Inorg. Chem.*, **8**, 1741 (1969).
- (23) R. Clements, R. L. Dean, T. R. Singh, and J. L. Wood, *Chem. Commun.*, 1125, 1127 (1971).
- (24) R. L. Somorjai and D. F. Hornig, *J. Chem. Phys.*, **36**, 1980 (1962).
- (25) J. L. Wood, *J. Mol. Struct.*, **12**, 283 (1972).
- (26) R. Steudel, F. Rose, and J. Pickardt, *Z. Anorg. Allg. Chem.*, in press.
- (27) The bending mode of the triatomic molecule S<sub>2</sub>O occurs at 382 cm<sup>-1</sup>.<sup>28</sup>
- (28) A. G. Hopkins, F. P. Daly, and C. W. Brown, *J. Phys. Chem.*, **79**, 1849 (1975).
- (29) R. Steudel and F. Rose, *Z. Naturforsch. B*, **30**, 810 (1975).
- (30) A. T. Ward, *J. Phys. Chem.*, **72**, 744 (1968).

- (31) G. A. Ozin, *J. Chem. Soc. A*, 116 (1969).  
 (32) R. Steudel and F. Rose, *Spectrochim. Acta*, submitted for publication.  
 (33) The correlation of Urey-Bradley force constants with structural parameters of sulfur rings has been discussed in ref 4.  
 (34) J. H. Schachtschneider, "Vibrational Analysis of Polyatomic Molecules V", Reprint no. 231-64, Emeryville, Calif.  
 (35) T. Shimanouchi, Computer Programs for Normal Coordinate Treatment of Polyatomic Molecules, Tokyo, 1968.  
 (36) See the structures of  $S_2N_4H_4$ <sup>37</sup> and of  $(SNCH_3)_4$ <sup>38</sup> the geometry at the nitrogens of these molecules is planar or quasiplanar.  
 (37) T. M. Sabine and G. W. Cox, *Acta Crystallogr.*, **23**, 574 (1967).  
 (38) A. L. MacDonald and J. Trotter, *Can. J. Chem.*, **51**, 2504 (1973).  
 (39) O. Glemser, A. Muller, D. Bohler, and B. Krebs, *Z. Anorg. Allg. Chem.*, **357**, 184 (1968).  
 (40) A. J. Banister, L. F. Moore, and J. S. Padley, *Spectrochim. Acta, Part A*, **23**, 2705 (1967).

## A Detailed Study of *N,N,N',N'*-Tetramethyl-*p*-phenylenediamine Luminescence in Organic Glasses. Evidence for a Protonation Reaction

J. Blais and M. Gauthier\*

*E.R. CNRS 98, Laboratoire de Chimie Physique Bât. 350, Université Paris-Sud 91405, Orsay, France (Received February 22, 1976; Revised Manuscript Received November 8, 1976)*

Publication costs assisted by CNRS

The solvent and temperature dependence of an anomalous long-lived luminescence ( $\lambda_{\max}$  430 nm), observed simultaneously with the ordinary fluorescence and phosphorescence of tetramethyl-*p*-phenylenediamine (TMPD) in ethanol and in some other organic solvents at 77 K, has been studied. These results together with some complementary observations on absorption spectra have been interpreted as indicative of a protonation by ethanol of the TMPD molecule in its ground state. It is also shown that when excited to the first singlet,  $TMPDH^+$  is partially decomposed to  $TMPD^S$ , the spectral properties of which are different from that of the directly excited TMPD. The mechanism of protonation and the importance of the environment on spin-orbit coupling of TMPD are discussed.

### Introduction

Aromatic amines in organic glasses have been the subject of several luminescence studies in the last decade.<sup>1-3</sup> Among them, *N,N,N',N'*-tetramethyl-*p*-phenylenediamine (TMPD) is of particular interest. Due to its low ionization potential, it is the most commonly used solute for photoionization studies in liquid or glassy solutions. Its UV excited luminescence<sup>4</sup> as well as the neutralization luminescence following photoionization<sup>5</sup> have been extensively studied. In a previous paper,<sup>6</sup> we reported the existence of a new type of long-lived luminescence characterized by excitation and emission spectra which appear quite distinct from the TMPD absorption and emission. The species responsible for this emission was tentatively identified with a solute-solvent charge transfer state, the existence of which had been repeatedly postulated in glasses<sup>7</sup> as well as in liquids<sup>8</sup> to account for some anomalies noted in photoionization studies.

Further experimental results do not support this early interpretation and the experimental evidence given below shows that the luminescence is associated with the protonated form  $TMPDH^+$ . Moreover, it has been observed that upon excitation  $TMPDH^+$  is partly decomposed to  $TMPD^*$  and that the luminescent properties of the latter are somewhat different from those of the directly excited TMPD molecule.

### Experimental Section

**Reagents.** TMPD was liberated from the hydrochloride salt with NaOH and purified by several sublimations just before use. Methylcyclohexane (Eastman Kodak spectrograde) and 3-methylpentane (Koch Light) were purified by chromatography on activated silica gel and alumina ("standard" MCH and 3MP). Ethanol (Merck) was distilled on acid 2,4-dinitrophenylhydrazine and dried over  $I_2$ -Mg in accord with the Lund and Bjerrum method

("standard" ethanol). Triethylamine (TEA, Fluka) was distilled over potassium hydroxide. The solvents were purified just before use and their purity was tested by absorption and emission spectroscopy. The classical methods of purification described above have been used in most experiments. However, for solvents denoted below as "dry" further dehydration was performed by keeping the solvent several hours on a sodium mirror (for MCH and TEA), on anhydrous  $CaSO_4$  (for ethanol), or on molecular sieves (for MCH, ethanol, 2,2,2-trifluoroethanol (Fluka), acetonitrile (uvasol Merck)). In all cases, the treatment was done under vacuum and the solutions were prepared by dilution in the same vacuum system after distillation of the solvent. The samples were finally sealed in a nonfluorescent silica tube (3 mm i.d.) for low temperature measurements or in a 10-mm square silica cell for room temperature experiments.

**Apparatus and Measurements.** The absorption spectra were obtained with a Zeiss PMQ II spectrophotometer equipped to make low temperature measurements.<sup>9</sup> The luminescence spectra were recorded with a Jobin-Yvon "Bearn" spectrofluorimeter equipped with a phosphoroscope. The spectral bandwidth was 3-6 nm for excitation and 6-12 nm for analysis. The relative emission intensities were obtained from areas measured on intensity vs. wavenumber curves. It has been determined that the intensity vs. wavelength dependence of the analyzing monochromator and photomultiplier system is constant to within 10% in the 350-510-nm spectral range. An abrupt decrease of sensitivity only occurs for wavelengths longer than 550 nm. Thus the intensity data were determined from the observed uncorrected emission spectra. The observed excitation spectra were corrected to a constant number of photons in the exciting beam. The spectral composition of the exciting light was itself obtained by the use of rhodamine B as a quantum counter.

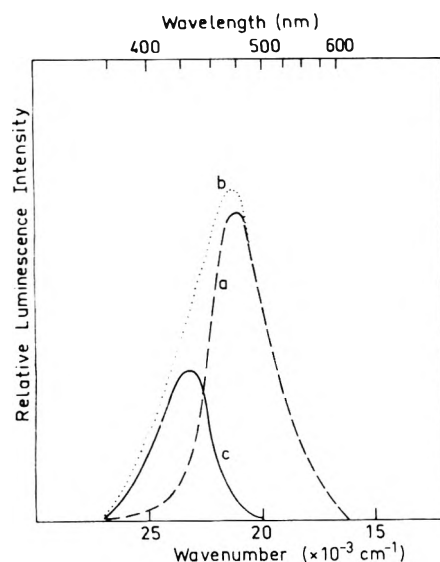


**Figure 1.** Long-lived emission of TMPD in glassy ethanol: (curve a)  $\lambda_{\text{exc}}$  350 nm; (curve b)  $\lambda_{\text{exc}}$  310 nm; (curve c) obtained by subtraction of (a) from (b).  $[\text{TMPD}] = 2 \times 10^{-4}$  M.

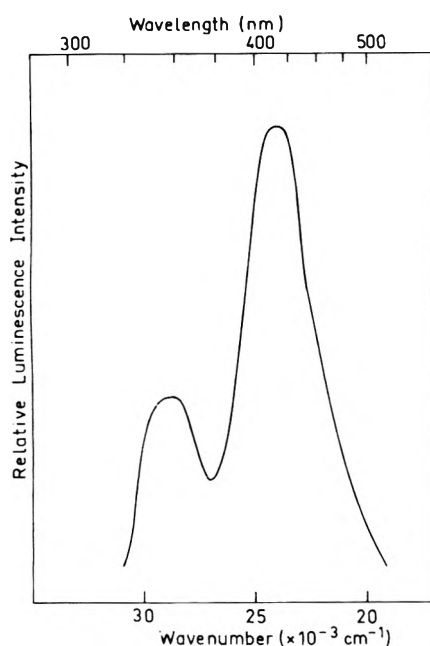


**Figure 2.** Total luminescence spectrum of TMPD in acidic ethanol at 77 K.  $[\text{TMPD}] = 2 \times 10^{-4}$  M.

The relative fluorescence quantum yields were determined at room temperature, using right angle geometry, by comparing the emission intensity of dilute TMPD solutions ( $10^{-5}$  M) with that of quinine sulfate in aqueous 1 N sulfuric acid. The concentration of the latter was adjusted so that each determination, at a given excitation wavelength, gave the same optical density as the TMPD solution at this particular wavelength.

## Results

As previously reported,<sup>6</sup> the luminescence spectrum of TMPD in glassy solutions at 77 K is strongly dependent on the excitation wavelength. This dependence is particularly striking for the long-lived luminescence (recorded with a phosphoroscope) as shown in Figure 1 for TMPD in ethanol. Curve a shows the phosphorescence, denoted by  $P$  ( $\lambda_{\text{max}}$  470 nm) and produced by excitation at 350 nm, near the solute absorption threshold. Curve b shows the spectrum obtained by excitation at shorter wavelengths. It is the superposition of  $P$  and another emission, denoted

**TABLE I**

	TMPD concn, M	$X_P/P^a$	Absorption max (77 K)
TMPD/ethanol	$10^{-3}$	0.35	320
+ KOH	$1.5 \times 10^{-4}$	0.5	312
+ Na ethanolate	$2 \times 10^{-4}$	0.1	315
+ HCl	$2 \times 10^{-4}$	$\approx 7$	304
TMPD/ethanol <sup>b</sup>	$3 \times 10^{-4}$	0.27	315
TMPD/ethanol <sup>b</sup>	$10^{-4}$	0.4	315
TMPD/ethanol <sup>c</sup>	$10^{-4}$	0.28	
TMPD/MCH	$10^{-4}$	0.15	320
+ HCl	$10^{-4}$	0.7	315
TMPD/MCH <sup>d</sup>	$10^{-4}$	$< 0.1$	323
TMPD/MCH <sup>d</sup>	$10^{-4}$	$\approx 0$	
TMPD/TEA	$10^{-4}$	$< 0.1$	325

<sup>a</sup>  $X_P/P$  have been measured for an excitation wavelength of 310 nm from emission spectra areas. <sup>b</sup> Ethanol dried on anhydrous  $\text{CaSO}_4$ . <sup>c</sup> Ethanol dried on molecular sieves. <sup>d</sup> MCH dried on sodium mirror. <sup>e</sup> MCH dried on molecular sieves.

by  $X_P$ . The maximum of  $X_P$  is at 430 nm, as shown by curve c which was obtained by subtracting curve a from b. It is shown that the corrected excitation spectrum for  $X_P$  (which is to be identified with  $\text{ITL}_1$  in ref 6) is maximum at 310 nm.

1. *Identification of the Species Responsible for the  $X_P$  Emission.* In order to elucidate the nature of the species responsible for the  $X_P$  emission, the effect of the nature of the solvent on the luminescence and the absorption spectra of TMPD has been examined in detail. Quantitative results are summarized in Table I. The  $X_P/P$  intensity ratio, measured from the emission bands areas, and the absorption maxima are given in columns III and IV, respectively, for the different solutions examined below.

1.A. *Luminescence. Ethanol Glasses.* A very large effect of the acidity of the glass on the spectral distribution of the luminescence has been observed. In ethanol made basic by addition of potassium hydroxide (0.5 M), or sodium ethanolate, the  $X_P/P$  intensity ratio decreases. On the contrary, in the presence of hydrochloric acid (about  $10^{-4}$  M)  $X_P/P$  is greatly enhanced. Moreover, in the latter case, the TMPD fluorescence ( $\lambda_{\text{max}}$  385 nm) is no longer observed in the emission spectrum recorded without the phosphoroscope. In turn, a new fluorescence denoted by  $X_F$  appears. It has a maximum at 350 nm. As for  $X_P$ , the  $X_F$  excitation spectrum is maximum for 310 nm. It must be added that  $X_F$  has also been detected in neutral ethanol. The  $X_P/P$  intensity ratio is slightly reduced in "dry" ethanol but it always remains greater than 0.25 and it may be concluded that  $\text{H}_2\text{O}$  is not responsible for the  $X_P$  emission. The increase of  $X_P/P$  at low solute concentration already noted in the preceding paper and illustrated in Table I for standard ethanol or ethanol dehydrated on  $\text{CaSO}_4$  may show that in these cases traces of water are of some importance at low solute concentration.

*Methylcyclohexane (MCH) Glasses.* It was noted in the preceding paper<sup>6</sup> that  $X_P$  is much less intense in MCH than in ethanol. It has now been observed that with "dry" MCH, the  $X_P$  emission is greatly reduced and becomes negligible. As was observed with ethanol, the addition of anhydrous hydrochloric acid (about  $10^{-4}$  M) enhances the  $X_P$  emission. However, the TMPD phosphorescence always remains more intense than  $X_P$ .

*Mixed MCH-Ethanol Glasses.* The addition of ethanol in MCH solutions enhances the  $X_P/P$  ratio. This effect is noticeable at very low concentration of ethanol and a saturation value is reached for a concentration of about  $2 \times 10^{-4}$  M (Figure 3).

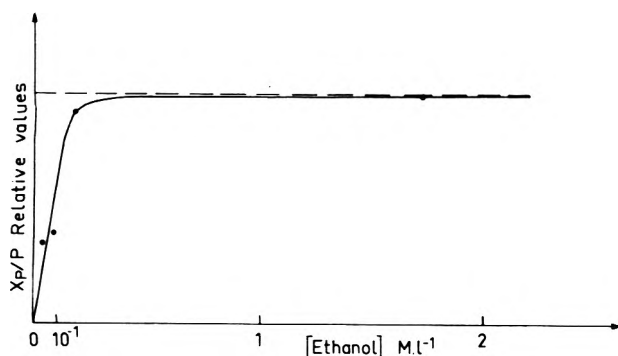


Figure 3. Dependence of  $X_p/P$  intensity ratio on ethanol concentration of TMPD-MCH glasses at 77 K:  $[TMPD] = 10^{-4}$  M;  $\lambda_{exc}$  310 nm. The  $X_p/P$  ratios have been determined from the corresponding areas in the emission spectrum.

**Other Solvents.** It has been noticed<sup>6</sup> that  $X_p$  is also observed in standard 3MP. The  $X_p$  intensity is of the same order as that obtained in standard MCH. In "dry" TEA the  $X_p/P$  intensity ratio is lower than 0.1 as is observed in "dry" MCH. The study of other solvents is limited by the fact that most are crystalline at low temperature. Nevertheless, it has been noticed that in crystalline "standard" MCH<sup>44</sup>  $X_p$  is still observed. However, the intensity is somewhat lower than in the glassy sample. In crystalline dry acetonitrile  $X_p$  is not detectable. In crystalline 2,2,2-trifluoroethanol the  $X_p$  emission is at least a factor of 2 more intense than the TMPD phosphorescence and its excitation spectrum is maximum at 300 nm.

**1.B. Absorption.** The different parameters which strikingly affect the luminescence of TMPD glassy solutions also modify the absorption, but to a lesser extent. The absorption maximum  $\lambda_{max}$  for the basic ethanol solution is at a longer wavelength than for the acid solution. In neutral ethanol, at the same TMPD concentration,  $\lambda_{max}$  lies at an intermediate wavelength (see Table I, column IV).

The effect of dilution is illustrated in Figure 4. When the molarity is changed from  $10^{-3}$  to  $10^{-4}$  M the absorption maximum is shifted toward the blue, but, due to a noticeable flattening of the band, it becomes more difficult to determine the maximum precisely. Unfortunately, due to experimental difficulties, it was not possible to examine more dilute solutions.

A comparison of columns II and IV of Table I clearly shows that the more intense the  $X_p$  emission, the larger the blue shift of the absorption maximum. In basic ethanol or in MCH  $X_p$  is quite low and  $\lambda_{max}$  lies at 315–320 nm. In acidified ethanol the  $X_p$  emission is predominant and  $\lambda_{max}$  lies at 305 nm.

The luminescence results presented above in glassy solvents show that the occurrence of the  $X_p$  emission is related to the proton-donating property of the solvent. Such a correlation is also substantiated by the results obtained with crystalline samples. The striking enhancement of  $X_p/P$  in trifluoroethanol compared to ethanol must be related to the higher acidity of the former (the  $pK_a$  values measured in aqueous solutions are 12.4 for fluoroethanol and 15.6 for ethanol<sup>43</sup>). Moreover, the absence of  $X_p$  in acetonitrile shows that the polarity of the solvent is not responsible for this emission.

The protonation of aromatic amines in acid solutions is well known. The  $pK_a$  values of TMPD have been determined in aqueous solution ( $pK_1 = 6.35$  and  $pK_2 = 2.29$ )<sup>10</sup> and the absorption spectra of the mono- (TMPDH<sup>+</sup>) and diprotonated (TMPDH<sub>2</sub><sup>2+</sup>) forms of TMPD have been

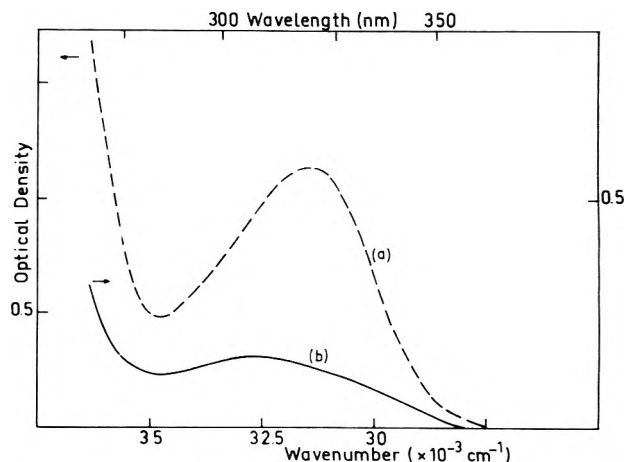


Figure 4. Effect of dilution on the absorption spectra of TMPD in ethanol at 77 K: (curve a)  $[TMPD] = 10^{-3}$  M; (curve b)  $[TMPD] = 10^{-4}$  M.

obtained in liquid benzene.<sup>11</sup> TMPDH<sup>+</sup> presents an absorption maximum at 310 nm while TMPDH<sub>2</sub><sup>2+</sup> absorbs only at wavelengths shorter than 280 nm. Thus, the presently observed  $X$  emission, which is more intense when excited in the 300–310-nm region and which is enhanced in acidic media, may be identified with the fluorescence and phosphorescence of TMPDH<sup>+</sup>. This implies that TMPDH<sup>+</sup> is present in its ground state in ethanol glasses, or in hydrocarbon glasses when they are not carefully dried.

In neutral ethanol the change in the shape of the absorption spectrum and the blue shift obtained upon dilution show that the observed spectrum must be considered as the superposition of the absorption spectra of TMPD ( $\lambda_{max}$  320–325 nm) and of TMPDH<sup>+</sup> ( $\lambda_{max}$  300–310 nm). Due to the strong overlapping of the two bands, it is impossible to decompose the spectrum and to obtain the true concentration of each species. However, from the results of Table I, it is clear that the TMPDH<sup>+</sup> concentration is of the same order as that of untransformed TMPD for a  $10^{-4}$  M initial concentration.

**2. The Luminescence of TMPD in the Presence of TMPDH<sup>+</sup>.** As mentioned above, the observed luminescence of TMPD in neutral ethanol glasses is always the superposition of the TMPD and the TMPDH<sup>+</sup> emission unless the excitation is performed near the absorption threshold of TMPD at about 350 nm. The results which are presented below concern some anomalies observed in the emission of TMPD.

The fluorescence excitation spectrum, recorded at an analyzing wavelength of 375 nm where the contribution of TMPDH<sup>+</sup> emission is negligible, presents, in addition to the maximum at 325 nm due to the absorption of TMPD, a shoulder at about 300 nm (Figure 5, curve a). This appears particularly clearly if the mirror image of the fluorescence is drawn (curve a'). Then it is obvious that the absorption by TMPDH<sup>+</sup> contributes to populate the first excited singlet of TMPD.

This result might be expected since it is well known<sup>12–15</sup> that the acid–base properties of a molecule depend on its electronic state. According to the Förster's cycle the blue shift of the absorption spectrum of TMPDH<sup>+</sup> relatively to that of TMPD indicates an enhancement of the acidity of the molecule in the  $S_1$  state. At room temperature the change in  $pK_a$  value measured in this way is  $\Delta pK_a = -4.4$ . At 77 K all reactions rates are greatly reduced and the acid–base equilibrium may not be reached during the lifetime of the  $S_1$  state. Nevertheless, the above result shows that the increase of the acidity leading to the deprotonation of TMPDH<sup>+</sup><sup>S<sub>1</sub></sup> state also occurs.

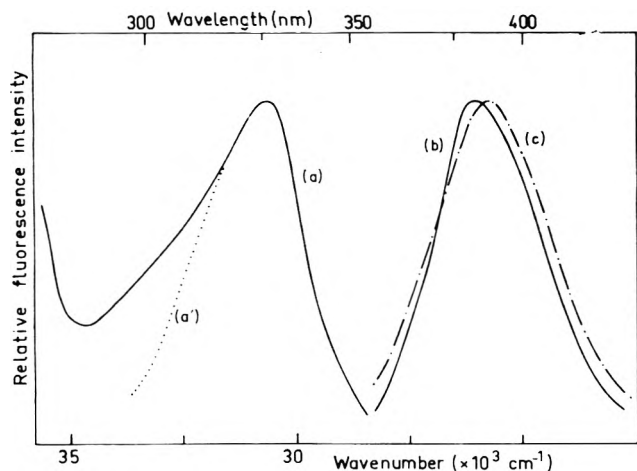


**Figure 5.** Corrected fluorescence excitation spectrum observed at 375 nm (curve a) and fluorescence spectra (curves b and c) of TMPD in ethanol at 77 K: (curve b)  $\lambda_{exc}$  350 nm; (curve c)  $\lambda_{exc}$  310 nm; (curve a') mirror image of fluorescence excited at 350 nm,  $[TMPD] = 10^{-4}$  M.

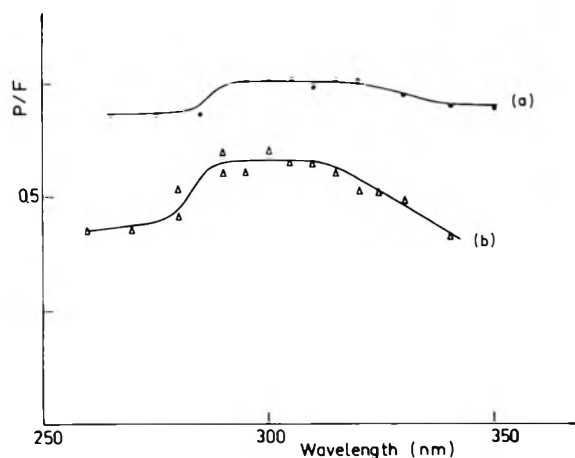


**Figure 6.** Dependence of  $P/F$  intensity ratios measured from the corresponding areas in the emission spectrum at 77 K: (curve a) in MCH, (curve b) in ethanol,  $[TMPD] = 10^{-4}$  M.

When  $TMPD^*$  is populated in such an indirect way, the emission characteristics are somewhat different from those observed when TMPD is directly excited at 350 nm: (1) The fluorescence maximum is shifted to the red by 5 nm as shown in Figure 4 (curves b and c). One may notice the  $X_F$  contribution on the high energy side of curve c. (2) The  $P/F$  intensity ratio is greatly enhanced (Figure 6, curve b). (3) The phosphorescence lifetime  $\tau_P$  is lowered from 2.7 s when excited at 350 nm to less than 2.3 s when excited at 290 nm (Figure 7, curve b). Moreover, in the latter case, the decay is exponential only at the beginning and a slower component appears after the intensity has decreased about 80%.

None of these spectral anomalies are observed in dry MCH. The fluorescence excitation spectrum is very similar to the absorption,  $P/F$  varies only slightly with excitation wavelength (Figure 6, curve a), the phosphorescence lifetime is constant within experimental errors ( $\delta\tau_P = \pm 0.05$  s) (Figure 7, curve a), and the decay is always strictly exponential.

3. *Effect of Temperature and Phase.* The relative quantum yields of fluorescence  $\phi_F$  have been measured for  $10^{-5}$  M solutions of TMPD in MCH and in ethanol at room temperature. Figure 8 clearly shows that  $\phi_F$  is constant (relative error  $\approx 13\%$ ) in dry MCH (Figure 8, curve a) while in dry ethanol (curve b) a minimum  $\phi_F$  is observed around 300 nm. In the latter case, the decrease is more

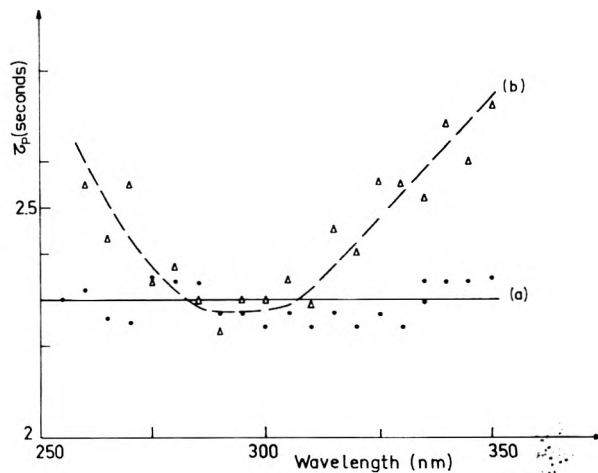


**Figure 7.** Dependence of the phosphorescence lifetime of TMPD on excitation wavelength at 77 K: (curve a) in MCH; (curve b) in ethanol,  $[TMPD] = 10^{-4}$  M. The analyzing wavelength has been fixed at 510 nm to prevent any contribution from the  $X_F$  emission.

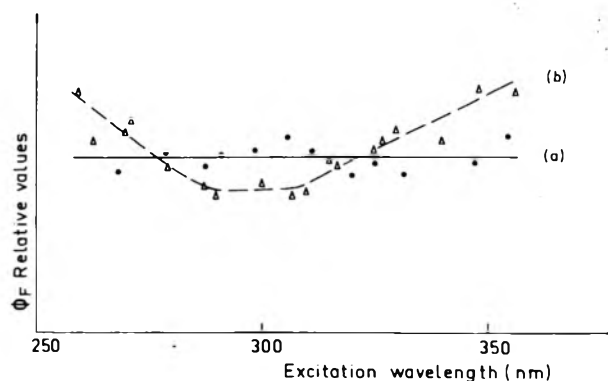


**Figure 8.** Dependence of the relative quantum yield of the fluorescence emission on excitation wavelength at room temperature for  $10^{-5}$  M TMPD in dry MCH (curve a) and in ethanol (curve b). The quantum counter used is a solution of quinine sulfate in 1 N  $H_2SO_4$ .

pronounced if water is added ( $[H_2O] = 3$  M). Similar results have previously been observed in ethanol<sup>16</sup> and it was also claimed that  $\phi_F$  decreased at low wavelength in liquid MCH<sup>16</sup> and in other nonpolar solvents.<sup>17</sup> It may also be noted that in 3MP glass, Albrecht did not observe any variation of  $\phi_F$ .<sup>7</sup> These results strongly suggest that  $TMPDH^+$  is present in those dilute liquid solutions and significantly contributes to the absorption around 300 nm, thus decreasing  $\phi_F$  but a direct proof could not be obtained. Indeed, it was not possible to detect any  $X_F$  fluorescence of  $TMPDH^+$  either in ethanol or MCH. However, this result may be somewhat ambiguous since deprotonation, which is certainly more rapid in the liquid than at 77 K, may efficiently compete with the  $X_F$  emission.

A more convincing result was obtained from the absorption spectra of TMPD solution in a mixed MCH ethanol solvent. At 77 K a blue shift is observed for ethanol concentrations lower than  $2 \times 10^{-1}$  M due to an increasing contribution of the  $TMPDH^+$  band. At room temperature the absorption maximum shift occurs over the whole concentration range. This is due to the trivial effect of the solvent dielectric constant; there is no evidence for  $TMPDH^+$  absorption. Moreover, there is no significant change in the absorption spectrum of TMPD in neutral ethanol upon addition of sodium ethanolate. From the above results it thus appears that *protonation is weak in the liquid but strongly favored at low temperatures.*

Finally it is worth noting that annealing a glassy sample at 110 K, which is above the glass transition temperature, leads to a significant decrease of the  $X_P/P$  ratio measured

at 77 K (about 30% for an annealing time of 60 min).

## Discussion

**Mechanism of TMPDH<sup>+</sup> Formation.** From the experimental results, it has been concluded above that TMPDH<sup>+</sup> is formed in ethanol glasses at 77 K. Similar protonation reactions have already been observed, by absorption or emission spectroscopy, in solutions of aminoacridines in liquid<sup>18</sup> or solid ethanol.<sup>19,20</sup> Two alternate interpretations have been proposed. Ferguson and Mau<sup>18</sup> and Bykovskaya et al.,<sup>21</sup> who used very dilute solutions, consider that the protonation is due to the free protons formed by the dissociation of ethanol or of traces of water. Such an interpretation might also be valid for TMPD. However, it cannot quantitatively account for our experimental results. In effect, the dissociation constant for ethanol is  $10^{-19}$  at room temperature,<sup>22</sup> and is expected to decrease with temperature. Therefore it would be negligible compared to the solute concentration. Furthermore,  $X_p$  is not completely absent in basic solutions, and it is inconceivable that free protons exist in the latter case.

The other interpretation, proposed by Shablya et al.,<sup>19,20</sup> stresses the role played by H-bonded solvent-solute complexes and attributes the reaction to H<sup>+</sup> migration along the H bond. In the present work, such an interpretation is substantiated by the results obtained in MCH solutions, namely, the appearance of the  $X_p$  emission in the presence of traces of water or of small amounts of ethanol. Let us also remark that the protonation of ammonia<sup>23</sup> or pyridine<sup>24</sup> by water has been suggested to account for NMR results.

Several studies have emphasized the close connection between the formation and strength of the H bond in solute-solute complexes and the ability to promote a proton transfer. Several factors increase the H bond strength and hence the proton transfer ability. These include an increase of the solvent polarity,<sup>25</sup> lowering of the temperature,<sup>26,27</sup> UV excitation of solutes (such as  $\beta$ -naphthol) which are more acidic in the excited state than in the ground state,<sup>28</sup> and an increase of the proton-donating power of series of solutes<sup>29</sup> or solvents.<sup>30</sup>

The description given by Sokolov<sup>31,32</sup> of the different possible potential curves for an AH...B complex provides an understanding of the proton transfer mechanism. In addition to the main minimum located near A, a second minimum appears near B which gradually deepens as the bond energy increases or alternatively as the A-B distance decreases. Simultaneously, the potential barrier between the two minima decreases and the proton transfer from one minimum to the other becomes feasible through tunneling. The A...H<sup>+</sup>B ion pair is then stabilized by solvent polarization. On going from room temperature to 77 K, the ethanol solutions undergo a 20% contraction. Consequently the correlative shortening of the intermolecular distance enhances proton transfer through the potential barrier. It should be noted that, after rapid cooling to 77 K, the A-B distance may be somewhat shorter than the equilibrium distance due to local strains in the surrounding molecules, as evidenced by the decrease in  $X_p/P$  observed after annealing the sample above the glass transition temperature.

In conclusion, if such a picture is correct the  $X$  emission would indeed be the emission of the TMPDH<sup>+</sup>...OC<sub>2</sub>H<sub>5</sub> complex which is expected to be very similar to that of TMPDH<sup>+</sup>.<sup>33,34</sup>

**Luminescence of TMPD and the Influence of Experimental Conditions on Spin-Orbit Coupling.** Figures 6 and 7 show that  $P/F$  ratios as well as the phosphorescence lifetime  $\tau_p$  largely depend on experimental conditions. To

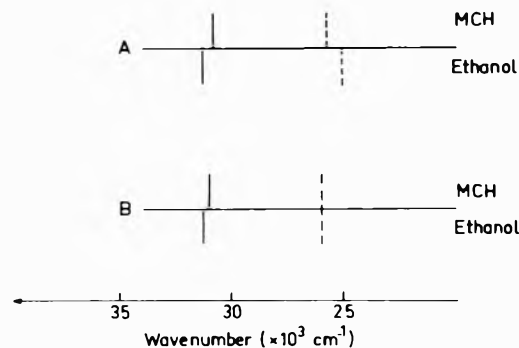


**Figure 9.** Wave number for the maxima of absorption (full lines) and fluorescence emission (dashed lines) for TMPD in MCH and in ethanol: (A) at room temperature and (B) at 77 K.

interpret those results, two factors have to be considered, namely, the geometry of the amino group and the relaxation of the molecule and its environment during the excited state lifetime.

The influence of the geometry of the amino group on the spin-orbit coupling have been examined by several authors.<sup>2,35,36</sup> The nonbonding electrons of the nitrogen atom play a major role. According to Kasha<sup>35,37</sup> they occupy an  $l$  orbital which form an angle  $\theta$  with the  $\pi$  orbitals of the ring. When  $\theta$  increases, that is when the amino group is inclined out of the plane of the ring, the charge transfer character of the singlet transition increases and the spin-orbit coupling becomes larger. As a consequence,  $P/F$  increases and  $\tau_p$  decreases.<sup>2,35,36</sup> Then, the influence of the H bond on TMPD luminescence, as demonstrated by the differences of  $P/F$  and  $\tau_p$  values in MCH and ethanol, becomes clear. In effect, as emphasized by Rowland<sup>38</sup> in amines the C-N-C angles are expected to open slightly on H bonding. Thus the TMPD molecule would be more planar in ethanol than in MCH. In ethanol a lower value of spin-orbit coupling would lead to the observed decrease of  $P/F$  and increase of  $\tau_p$  relatively to the values obtained in an aprotic solvent such as MCH. The influence of H bonding on the luminescence has been noted for glassy solutions of different amines<sup>1,3</sup> as well as in the liquid phase for TMPD.<sup>16,39</sup>

The second factor which deserves comment is the relaxation in the excited state. In the liquid, TMPD, as in other amines,<sup>41,42</sup> undergoes an important change in geometry on excitation. This is shown by the unusually large Stoke's shift shown in Figure 9. In ethanol the shift is still greater than in MCH which indicates an additional relaxation of the solvent as a consequence of the weakening of the H bond in the excited state. At 77 K the changes in geometry are largely hindered and the relaxation time is much longer than the fluorescence lifetime. Hence the observed Stoke's shift is smaller than in the liquid phase and is nearly identical in ethanol and in MCH.

These observations may be of importance to understand the behavior of TMPD\* formed through deprotonation. The fluorescence red shift (390 nm compared to 385 nm for the directly excited molecule) shows that the environment is different from that of the directly excited molecule. It may be assumed that the energy released upon deprotonation (about 0.25 eV as measured from the difference in fluorescence wavelength for TMPD and TMPDH<sup>+</sup>) is sufficient to relax the solute and solvent in the equilibrium configuration of the excited state. Since the H bond is weaker than in the ground state, the TMPD geometry would be intermediate between that obtained in MCH and in ethanol in the ground state configuration. As observed experimentally the resulting  $P/F$  ratio should also be intermediate between the two extreme values

obtained by a direct excitation.

As a general conclusion we would like to stress the implications of the above results in photoionization experiments. In effect many experimental results have proved that two intermediate states intervene in the biphotonic ionization of TMPD either in the liquid or in the solid state and the existence of a solute solvent charge transfer or semi-ionized state has been repeatedly postulated. In the present study, we have demonstrated the existence of a protonated form of the solute both in ethanol and in nonpolar solvents which have not been carefully dehydrated. This solute-solvent complex plays a major role when 310-nm excitation is used, which is almost always the case. It may contribute to photoconductivity by deprotonation or to photoionization by a biphotonic mechanism which involves an intermediate  $\text{TMPDH}^+$  triplet state. This may explain some previously described anomalies.<sup>7,8</sup>

### References and Notes

- (1) V. L. Ermolaev, *Opt. Spectrosc.* **11**, 266 (1961).
- (2) E. C. Lim and S. K. Chakrabarti, *J. Chem. Phys.*, **47**, 4726 (1967).
- (3) R. S. Davidson and M. Santhanam, *J. Chem. Soc. B*, 1151 (1971).
- (4) A. H. Kalantar and A. C. Albrecht, *Ber. Bunsenges. Phys. Chem.*, **68**, 361 (1964).
- (5) W. M. McClain and A. C. Albrecht, *J. Chem. Phys.*, **43**, 465 (1965).
- (6) J. Blais and M. Gauthier, *J. Lumin.*, **9**, 143 (1974).
- (7) G. E. Johnson and A. C. Albrecht, *J. Chem. Phys.*, **11**, 3179 (1966).
- (8) M. Ottolenghi, *Chem. Phys. Lett.*, **12**, 339 (1971).
- (9) A. Bernas and D. Grand, *J. Chim. Phys.*, **67**, 566 (1970).
- (10) Perrin, "IUPAC Dissociation Constants of Organic Bases in Aqueous Solution", Butterworths, London, 1965.
- (11) J. Steigmann and W. Cronkright, *J. Am. Chem. Soc.*, **92**, 6729 (1970).
- (12) T. H. Forster, *Naturwissenschaften*, **36**, 186 (1949); *Z. Elektrochem.*, **54**, 42 (1950); **54**, 531, (1950).
- (13) A. Weller, *Z. Elektrochem.*, **56**, 662 (1952); **61**, 956 (1957); see also A. Weller, *Prog. React. Kinet.*, **1**, 189 (1961).
- (14) G. Jackson and G. Porter, *Proc. R. Soc. London, Ser. A*, **260**, 13 (1961).
- (15) E. Van der Donckt, *Prog. React. Kinet.*, **5**, 273 (1966).
- (16) A. Aichalal and M. Ottolenghi, *Chem. Phys. Lett.*, **17**, 117 (1971).
- (17) S. S. Takeda, N. E. Houser, and R. C. Jarnagin, *J. Chem. Phys.*, **54**, 3195 (1971).
- (18) J. Ferguson and A. W. H. Mau, *Chem. Phys. Lett.*, **17**, 543 (1972).
- (19) A. V. Shablya, "Elementary Photoprocesses in Molecules", B. S. Neporent, Ed., 1968, p. 145.
- (20) A. N. Terenin, A. V. Shablya, G. J. Lashkov, and K. B. Demidov, *Proc. Int. Conf. Lumin.*, 137 (1968).
- (21) L. A. Bykovskaya, R. I. Personov, and B. M. Kharlamov, *Chem. Phys. Lett.*, **27**, 80 (1974).
- (22) G. Briere and F. Gaspard, *J. Chim. Phys.*, **64**, 1071 (1967).
- (23) R. A. Ogg, *J. Chem. Phys.*, **22**, 560 (1954).
- (24) J. Reuben, *J. Am. Chem. Soc.*, **91**, 5725 (1969).
- (25) A. Matsuzaki, S. Nagakura, and K. Yoshihara, *Bull. Chem. Soc. Jpn.*, **47**, 1152 (1974).
- (26) H. Baba, *J. Chem. Phys.*, **49**, 1763 (1968).
- (27) G. Favaro, *Chem. Phys. Lett.*, **31**, 87 (1975).
- (28) N. Mataga and Y. Kaifu, *J. Chem. Phys.*, **36**, 2804 (1962); *Mol. Phys.*, **7**, 137 (1964).
- (29) M. Nakamizo, *Spectrochim. Acta*, **22**, 2039 (1966).
- (30) N. Mataga, Y. Kaifu, and M. Koizumi, *Bull. Chem. Soc. Jpn.*, **29**, 373 (1956).
- (31) N. D. Sokolov, *Ann. Chim.*, **10**, 497 (1965).
- (32) E. A. Pshenichnov and N. D. Sokolov, *Int. J. Quantum Chem.*, **1**, 855 (1967).
- (33) R. Potashnik and M. Ottolenghi, *Chem. Phys. Lett.*, **6**, 525 (1970).
- (34) H. Masuhara, N. Tsujino, and N. Mataga, *Bull. Chem. Soc. Jpn.*, **46**, 1088 (1973).
- (35) M. Kasha and H. R. Rawls, *Photochem. Photobiol.*, **7**, 561 (1968).
- (36) J. E. Adams, W. W. Mantulin, and J. R. Huber, *J. Am. Chem. Soc.*, **95**, 5477 (1973).
- (37) M. Kasha, "Light and Life", McElroy and Glass, Ed., John Hopkins Press, Baltimore, Md., 1961, p. 31.
- (38) T. J. Rowland, *J. Chem. Phys.*, **63**, 608 (1975).
- (39) J. T. Richard and J. K. Thomas, *Trans. Faraday Soc.*, **66**, 621 (1970).
- (40) G. Perichet and B. Pouyet, *C. R. Acad. Sci.*, **276**, 37 (1973).
- (41) P. J. Krueger, *Spectrochim. Acta*, **19**, 705 (1963).
- (42) M. A. El Bayoumi, J. P. Dalle, and M. F. O'Dwyer, *J. Lumin.*, **1,2**, 716 (1970).
- (43) P. Ballinger and F. A. Long, *J. Am. Chem. Soc.*, **82**, 1 (1960).
- (44) The crystalline MCH sample was prepared by annealing a shock-cooled sample at least 1 h by several thermal cycles some degrees below the melting point of the crystal (147 K).

## Electron Spin Resonance of Radicals in $\gamma$ -Irradiated Mono- and Polycyclic Olefins. 4. Electronic Structure and Electron Spin Resonance Properties of a Norbornenyl Fused Cyclopentadienyl Radical

A. Faucitano,\* A. Buttafava, F. Faucitano Martinotti,

*Istituto di Chimica Generale dell'Università di Pavia, 27100 Pavia, Italy*

S. Cesca,

*SNAM Progetti S.p.A., Polymer Research Laboratories, San Donato Milanese, Italy*

and R. Fantechi

*C.C.R., Ispra, Italy (Received December 31, 1975)*

*Publication costs assisted by E.N.I., Roma*

The results of ESR single-crystal measurements on the radical formed by  $\gamma$  irradiation of tricyclo[5.2.1.0<sup>2,6</sup>]deca-2,5,8-triene are reported. This radical can be classified as a  $\pi$  cyclopentadienyl whose orbital degeneracy is removed by the electron repelling effect of the norbornenyl moiety. Another interesting feature is represented by an unusually large long-range interaction with the anti proton at C<sub>10</sub> in the norbornenyl section. The mechanism of magnetic interactions and the electronic structure of the radical are discussed on the basis of MO calculations to the INDO and HMO (McLachlan) levels of approximation.

### Introduction

As anticipated in a previous paper<sup>1</sup> the  $\gamma$  irradiation of polycrystalline tricyclo[5.2.1.0<sup>2,6</sup>]deca-2,5,8-triene (DDCP) yields an ESR spectrum consisting of a doublet of doublets with hyperfine splitting constants (hfsc) of approximately

13 and 7 G which were tentatively assigned to the fused cyclopentadienyl radical formed by loss of a bisallylic hydrogen atom from the parent olefin molecule (eq 1). This radical is of theoretical interest for the following reasons: (a) it belongs to a class of radicals, e.g., the cyclopentadienyls bearing nonaromatic substituents, which

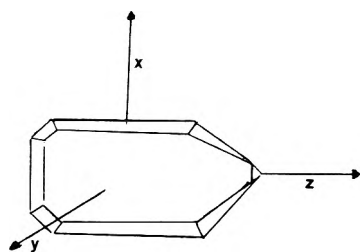


Figure 1. A single crystal of DDCP showing  $x$ ,  $y$ , and  $z$  reference axis system.

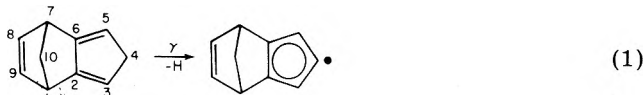


TABLE I: MO Calculations of Proton hfsc and  $\pi$  Spin Densities for the DDCP Radical

Position	INDO <sup>a</sup>				HMO (McLachlan)	
	UW		RW		p <sup>z</sup>	
	a <sup>H</sup> , G	p <sup>z</sup> orbital spin density	a <sup>H</sup> , G	p <sup>z</sup> orbital spin density	a <sup>H</sup> , G	p <sup>z</sup> orbital spin density
1,7	1.70		1.33		1.61 <sup>b</sup>	
2,6		0.369		0.256		0.379
3,5	2.78	-0.150	0.03	0.02	2.75	-0.095
4	-11.04	0.474	0.02	0.335	-12.56	0.433
8,9	0.58		0.4			
10(anti)	6.11		5.6			
10(syn)	-1.23		0.0			

<sup>a</sup> UW and RW represent unrestricted and restricted wave function, respectively. <sup>b</sup> Calculated from the equation  $a_{1,7}^H = (50 \cos^2 \vartheta) \rho^\pi$ . The dihedral angle  $\vartheta = 73^\circ$  was derived from geometrical parameters reported in Figure 2.

has not yet been studied by ESR spectroscopy; (b) it is suitable for studying the effect of alkyl type substituents on the orbital degeneracy of the cyclopentadienyl radical; (c) its polycrystalline spectrum is consistent with the existence of an unusually large, long-range coupling to a proton which, by symmetry, is expected to be located at C<sub>10</sub>. It was therefore decided to pursue this investigation with the purpose of confirming the nature of the radical and elucidating its electronic structure and ESR properties. This note reports on single-crystal ESR measurements and SCF molecular orbital calculations to the INDO and HMO (McLachlan) levels of approximation.

## Experimental Section

DDCP was prepared following the method described by Alder.<sup>2</sup> Single crystals of DDCP were grown by slow sublimation under vacuum of powdered samples which were kept in a mild temperature gradient at about 260 K. The irradiations were performed at 77 K with a <sup>60</sup>Co source with total doses of about 5 Mrads. The electron resonance spectrometer was a V 4500 X band equipped with a 100-kHz field modulator and a rectangular cavity. After warming to room temperature, the crystals were mounted on the shaft of a single goniometer head and the ESR spectra were taken at 10° intervals about each of the orthogonal axes. The shape of a typical crystal used for the measurements and the choice of the reference axes are illustrated in Figure 1.

Fortran IV programs have been employed for molecular orbital calculations to the INDO<sup>3</sup> and HMO (McLachlan)<sup>4</sup> levels of approximation as well as for the computer simulation of ESR spectra.<sup>5</sup> HMO calculations of  $\pi$  cyclopentadienyl orbitals, to be used in the McLachlan method, were performed according to the inductive model; Streitwieser parameters ( $h = -0.5$ ) were adopted in the Hückel matrix for Coulomb integrals pertaining to substituted carbon atoms C<sub>2</sub> and C<sub>6</sub>. This implies that the bicycloheptene section of the radical has been considered as two electron repelling substituents of strength comparable to that of the methyl group. The INDO proton hfsc were obtained by using the equation  $a = 539.86\rho_{1s1s}$ ,<sup>3</sup> where  $\rho_{1s1s}$  is the unpaired electron density of the valence 1s orbital of the hydrogen atom. This quantity was obtained either from the unpaired spin density matrix ( $P^\alpha - P^\beta$ ) or from the squares of hydrogen 1s orbital coefficients, depending on whether the spin restricted or the spin unrestricted wave function approximations were used. In connection with the HMO (McLachlan) method,  $\alpha$  and  $\beta$  proton hfsc have been obtained from the McConnell equations  $a_\alpha^H = Q_\alpha \rho^\pi$  ( $Q_\alpha = 29$  G),  $a_\beta^H = (B_0 + B \cos^2 \delta) \rho^\pi$

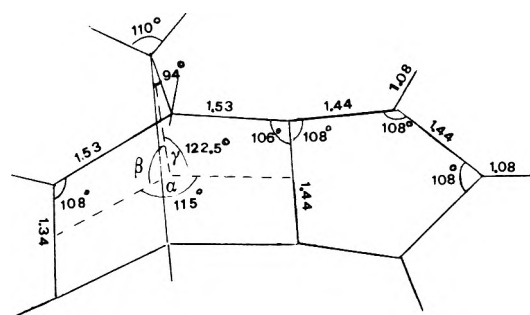


Figure 2. Geometrical parameters of the DDCP radical employed for INDO calculations.

( $B_0 \sim 0$ ,  $B \sim 50$  G), where  $\rho^\pi$  is the unpaired spin density in the conjugated section of the radical and  $\delta$  is the dihedral angle between the C-H <sub>$\beta$</sub>  bond direction and a perpendicular to the cyclopentadienyl plane. Because of the lack of reliable relationships, the application of the McLachlan method is limited to  $\alpha$  and  $\beta$  type protons. As a consequence, calculations pertaining to long-range interactions with  $\gamma$  and  $\delta$  type protons have been performed by using exclusively the INDO method.

## Results and Discussion

*Molecular Orbital Calculations of  $\pi$  Spin Densities and Proton hfsc.* Table I shows the proton hfsc and the  $\pi$  spin densities of the DDCP radical as obtained from INDO and HMO (McLachlan) molecular orbital calculations. The atomic coordinates necessary for the INDO method were derived from the geometry shown in Figure 2.

All carbon atoms in the C<sub>2</sub>, C<sub>3</sub>, C<sub>4</sub>, C<sub>5</sub>, C<sub>6</sub> ring section were assumed to be in a planar sp<sup>2</sup> hybridization state; the other parameters pertaining to the norbornenyl section were obtained from the structure of related molecules described in the literature.<sup>7</sup> Both MO methods indicate the existence of a nonuniform spin density distribution characterized by maxima at C<sub>2</sub>, C<sub>4</sub>, C<sub>6</sub> and small negative minima at C<sub>3</sub>, C<sub>5</sub>. The dominant magnetic interactions are those of the  $\alpha$  proton at C<sub>4</sub> and the  $\gamma$  proton at C<sub>10</sub> (anti position) which give rise to a doublet of about 11 and 6 G, respectively. All the other proton hfsc are predicted to be at least a factor of 3-4 smaller. Attempts at computer simulation based essentially on INDO proton hfsc's reported in Table I show that, with an experimental line width of 3 G, the ESR spectrum should appear as a barely resolved quartet of about 6 G average peak-to-peak sep-

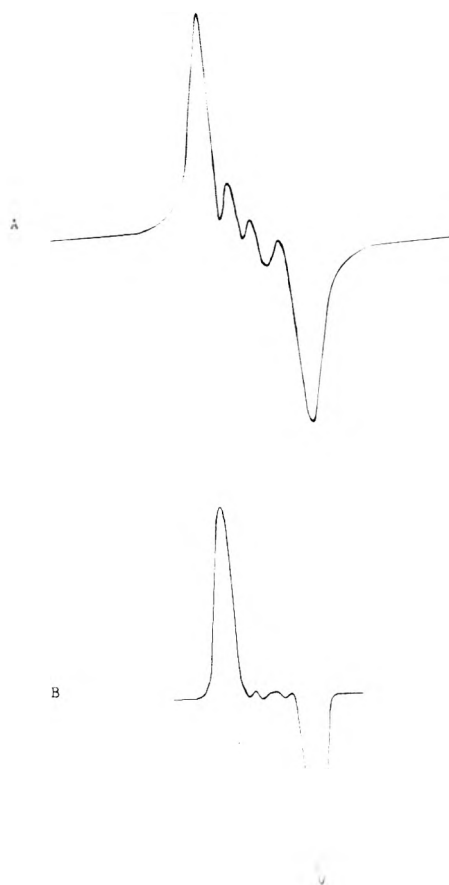


Figure 3. Experimental (A) and calculated (B) polycrystalline spectra of the DDCP radical. The computer simulation was performed by using the proton hfsc derived from INDO calculations (Table I) except that  $a_i^H$  was assumed to be 12 G instead of 11.04 G.

ation, which compares satisfactorily with the one experimentally obtained from polycrystalline DDCP (Figure 3).

**X Band Single-Crystal Spectra of the DDCP Radical.** Following the indications stemming from MO calculations and the polycrystalline spectrum, the anisotropy of the DDCP radical is discussed on the basis of the structure shown in Figure 2. The following assumptions are also made: (a) the only significant hyperfine interactions are those of the  $\alpha$  proton at  $C_4$  and the  $\gamma$  proton at  $C_{10}$ ; (b) the anisotropy of the  $g$  tensor and of the  $\gamma$  proton are negligibly small in comparison to that of the  $\alpha$  proton; the Hamiltonian representing the magnetic interactions experienced by the  $\alpha$  proton and the unpaired electron in the externally applied magnetic field is given by

$$\mathcal{H} = \beta g S \cdot H + S \cdot T \cdot I - g_{H\beta} \beta_H H \cdot I$$

where the first term is the Zeeman energy of the electron, the second term describes the magnetic hyperfine interactions between the unpaired electron and the  $\alpha$  proton, and the third term is the Zeeman energy of the  $\alpha$  proton. At the magnetic field used in these experiments ( $H = 3300$  G), the second and third terms of this equation are of the same order of magnitude; when this is the case, it can be shown that the usual selection rules  $\Delta m_l = 0$ , when  $\Delta m_s = \pm 1$ , are no longer applicable so that a four-line inner and outer pair can be observed. The relative intensity of the two pairs depends on the relative magnitudes of the second and third terms and is, of course, dependent on the angle of orientation of the crystal.

McConnell et al.<sup>8</sup> developed the following expressions for the electron resonance transition frequencies,  $\nu_{\pm i}$ ,  $\nu_{\pm 0}$ ,

TABLE II: Principal Values and Isotropic Component of  $a_i^H$  Hyperfine Tensor and Corresponding Direction Cosines for the DDCP Radical

Principal values	Direction cosines in $x, y, z$ axes system		
(-) 7.7	0.996 1	-0.086 99	0.014 50
(-) 13.0	0.080 99	0.837 18	-0.540 89
(-) 21.0	0.034 9	0.539 9	0.840 9
13.9	Isotropic component		

and the relative intensities,  $R_{\pm i}$ ,  $R_{\pm 0}$ , of the inner and outer doublets:

$$\nu_{\pm 0} = |\nu_e| \pm 1/2(\nu_+ + \nu_-)$$

$$\nu_{\pm i} = |\nu_e| \pm 1/2(\nu_+ - \nu_-)$$

$$(\nu_{\pm})^2 = (\nu_p \pm 1/2A)^2 \cos^2 \vartheta + (\nu_p \pm 1/2B)^2 \sin^2 \vartheta \cos^2 \varphi + (\nu_p \pm 1/2C)^2 \sin^2 \vartheta \sin^2 \varphi$$

$$R_0 - R_i = \frac{1}{\nu_+ \nu_-} \{ \langle (\Delta\nu)^2 \rangle_{av} - 2(\nu_p)^2 \}$$

$$R_0(\nu^+ + \nu^-)^2 + R_i(\nu^+ - \nu^-)^2 = \langle (\Delta\nu)^2 \rangle_{av}$$

$$\langle (\Delta\nu)^2 \rangle_{av} = A^2 \cos^2 \vartheta + B^2 \sin^2 \vartheta \cos^2 \varphi + C^2 \sin^2 \vartheta \sin^2 \varphi$$

where  $\delta$  and  $\varphi$  define, in the usual manner, the direction of the magnetic field relative to the principal axes;  $\langle (\Delta\nu)^2 \rangle_{av}$  is the second moment of the resonance quartet; and  $A$ ,  $B$ , and  $C$  are the principal values of the hyperfine tensor. These equations were used in a computer program for spectrum simulation in order to predict the X band spectrum of the DDCP radical at different orientations in the principal axes system. Theoretical values of  $A$ ,  $B$ , and  $C$  necessary for the calculations were derived from the INDO  $P^z$  orbital spin densities at  $C_4$  by using the equations<sup>8</sup>

$$A_{th} = A_M \frac{\rho_{C_4} \pi}{\rho_M} = 6.0 \text{ G}$$

$$B_{th} = B \frac{\rho_{C_4} \pi}{\rho_M} = 12.3 \text{ G}$$

$$C_{th} = C_M \frac{\rho_{C_4} \pi}{\rho_M} = 18.5 \text{ G}$$

where  $A_M = 10.7$  G,  $B_M = 21.8$  G, and  $C_M = 32.8$  G are the experimental principal values of the  $\alpha$  proton in the malonic acid radical  $\text{CH}(\text{COOH})_2$ ,<sup>8</sup>  $\rho_M$  is the  $C^*$  spin density of  $\text{CH}(\text{COOH})_2$ , assumed to be approximately equal to that of the free radical center in  $\dot{\text{C}}\text{H}(\text{CH}_3)_2$  ( $\rho_M \approx \rho_{\text{CH}(\text{CH}_3)_2} = 0.84^9$ ).

According to the results, the effect of forbidden transitions becomes significant (e.g.,  $R_{\pm 0} \approx R_{\pm i}$ ) only when  $\langle (\Delta\nu) \rangle_{av} (h/g\beta)$  is between about 9 and 12 G; outside this range, only two normal hyperfine components are observed for the  $\sigma$  proton. The latter situation is the most commonly encountered so that, when the isotropic doublet of about 7 G due to the  $\gamma$  proton is included and a line width of 2-3 G is assumed, the resulting spectra are seen to consist of triplets, 1:2:1, and quartets, 1:1:1:1, depending on whether  $\langle (\Delta\nu) \rangle_{av} (h/g\beta)$  is below 9 G or above 12 G, respectively. At angles where  $R_{\pm 0} \approx R_{\pm i}$ , the quantity  $(\nu_0 - \nu_i)(h/g\beta)$  is generally smaller than the experimental line width and, as a consequence, the forbidden transitions do

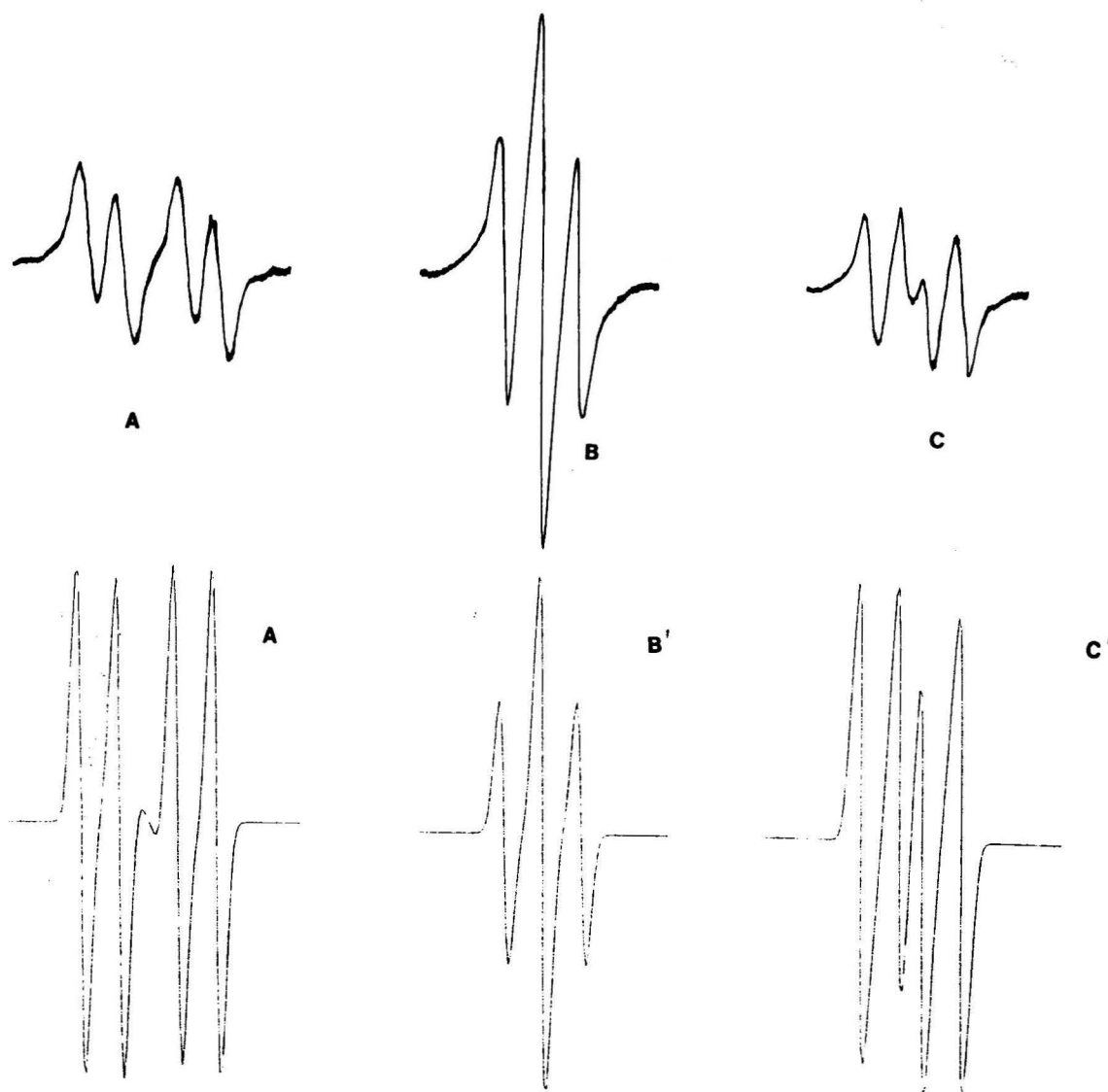


Figure 4. Experimental (A, B, C) and calculated (A', B', C') single-crystal spectra of the DDCP radical. A, B, and C were taken in the  $xz$ ,  $yz$ , and  $xy$  plane, respectively. At the magnetic field directions (with respect to the  $x, y, z$  system)  $[0.86, 0, 0.34]$ ,  $[0, 0, 1]$ ,  $[0.174, 0.98, 0]$ .

not give rise to new observable hyperfine features but rather only influence the shape and intensity ratios of the quartets and triplets (Figure 4). These expectations are fully consistent with the experimental results summarized in Table II and in Figures 4 and 5.

Most of the X band spectra of the DDCP radical in the X, Y; X, Z; and Y, Z quadrants do effectively consist of triplets, 1:2:1, and quartets, 1:1:1:1; furthermore analysis of the angular dependence of line positions, measured at angles where forbidden transitions are negligible, confirms the presence of two proton hfsc one of which, equal to 7.7 G, is nearly isotropic while the other one is strongly anisotropic. Finally the anisotropic splitting follows closely the theoretically calculated one for an  $\alpha$  proton having principal values  $A = 7.7$ ,  $B = 13.0$ ,  $C = 21.0$  G and isotropic component  $A = 13.9$  G (Table II, Figure 5).

On the basis of these results, we feel that it can confidently be stated that the basic assumptions pertaining to the nature and the structure of the DDCP radical are essentially correct.

**Mechanism of Long-Range Proton hfsc.** The INDO method, when used within the restricted wave function scheme (RW, single determinant wave functions with one unpaired electron and  $2n$  other electrons paired in  $n$  molecular orbitals), is suitable only for yielding information about the spin delocalization with electron transfer in the

isotropic proton hyperfine splitting mechanism. On the other hand, when used within the unrestricted wave function scheme (UW, single determinant wave functions with different orbitals for electrons of  $\alpha$  and  $\beta$  spins and retention of one center exchange integrals), the INDO method is capable of accounting for both spin delocalization and spin polarization. There exists, therefore, the possibility of analyzing the proton hyperfine splitting mechanism by simply comparing the results obtained from the two formalisms (Table I). This method seems to work properly at least on a qualitative basis; thus, the  $\alpha$  protons at  $C_3, C_4, C_5$  are correctly predicted to be 100% spin polarized. The couplings of the  $\beta$  protons at  $C_{7,1}$  are shown to arise from about 25% spin polarization ( $(a)_{1,7}^{\text{polzm}} = 0.37$  G) and 75% spin delocalization ( $(a)_{1,7}^{\text{delzm}} = 1.33$  G). The latter value substituted into the McConnell equation  $(a)_{1,7}^{\text{delzm}} = (B \cos^2 \vartheta) \rho_{6,2}^{\sigma}$ , with  $B = 50$  G and  $\rho_{6,2}^{\sigma} = 0.37$  (Table I), yields a dihedral angle  $\vartheta = 75^\circ$ , close to the expected one ( $\vartheta \approx 73^\circ$ ). The application of this method to the antiproton at  $C_{10}$  yields  $(a)_{10}^{\text{H(anti)delzm}} = 5.6$ , which accounts for more than 90% of the INDO (UW) value (70% of the experimental one); it follows that this unusually large, long-range interaction is based mainly on spin delocalization with electron transfer. In the valence-bond formalism, such a mechanism can be described in terms of participation of the homohyperconjugative

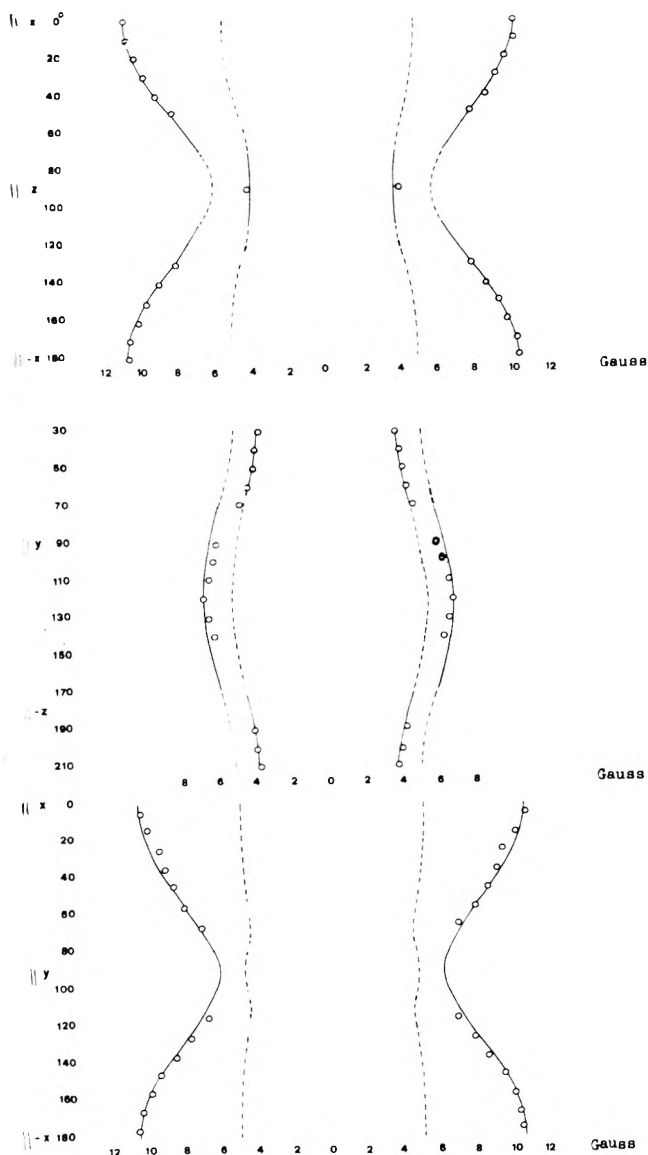
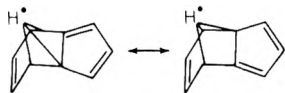


**Figure 5.** Splittings due to the  $a_4^H$  hyperfine coupling. The circles represent the experimental values; lines represent theory with the coupling tensor of Table I, full lines relate to lines with over 50% of intensity; dashed lines less than 50%.

#### structures



(2)

A 100% contribution would correspond to  $a_{10}^H(\text{anti}) \approx 507$  G, while a contribution of ca. 1.5% would account for the experimental value of 7.7 G. As the relative importance of these VB structures in the radical increases, the  $C_{10}-C_2$  and  $C_{10}-C_6$  bonds are expected to become stronger, while on the contrary, the strength of the  $C_{10}-H(\text{anti})$  bond should decrease; concomitantly, the magnitude of the  $a_{10}^H(\text{anti})$  coupling should increase. In an attempt to obtain evidence for this type of correlation, we have analyzed, within the INDO UW model, the changes of bond indices between  $C_{10}-C_2$ ,  $C_{10}-C_6$ , and  $C_{10}-H(\text{anti})$  as a function of the magnitude of  $a_{10}^H(\text{anti})$  coupling. Variable values of the  $a_{10}^H(\text{anti})$  coupling were obtained by allowing the angular parameter  $\alpha$  (Figure 6) to increase from 110 to 120°. The results, which are summarized in Figure 6, clearly show that the trend of variation of bond indices with respect to the  $a_{10}^H(\text{anti})$  coupling is consistent with the homohypercon-

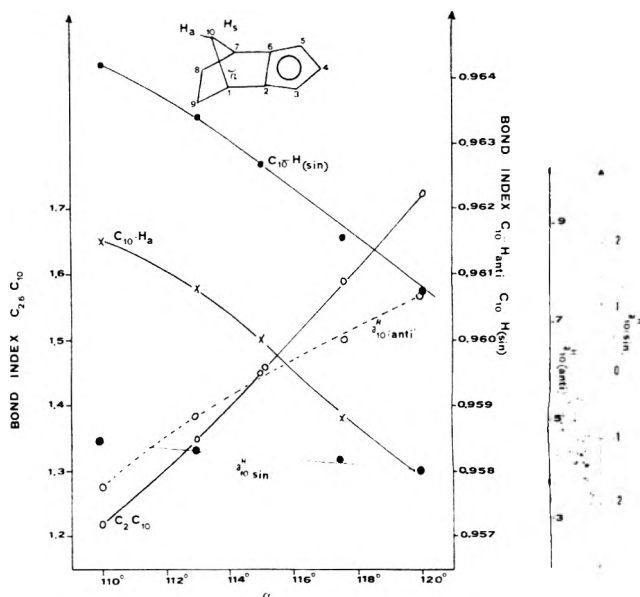
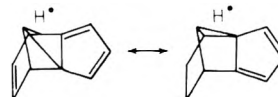


**Figure 6.** Diagrams showing the relationship between bond indexes at  $C_{10}-H(\text{anti})$  and the coupling constant of the anti proton at  $C_{10}$  ( $a_{10}^H(\text{anti})$ ). Bond indexes are the sum of the squares of bond orders between the atoms in question. This sum of the squares appear to be closely related to the bond character.<sup>13</sup> For the sake of comparison also the bond index at  $C_{10}-H(\text{syn})$  and the  $a_{10}^H(\text{syn})$  coupling are reported.

jugative model, thus lending further support to the hypothesis of spin delocalization by electron transfer. In Figure 6 also the  $C_{10}-H_{10}(\text{syn})$  bond index and the  $a_{10}^H(\text{syn})$  coupling are reported for the sake of comparison. It is readily seen that, in this case, the variations of bond indices and the  $a_{10}^H(\text{syn})$  coupling are not consistent with the homohyperconjugative structures:



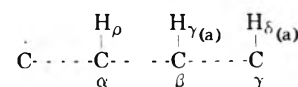
(3)

This suggests that a different mechanism may apply for the  $a_{10}^H(\text{syn})$  coupling (see below).

The prominence of the delocalization mechanism in the  $a_{10}^H(\text{anti})$  coupling results also from the application of the Luz valence bond treatment<sup>10</sup> for the evaluation of through bond spin polarization contributions in hydrocarbon radicals. Following the Luz analysis, the  $\gamma$  and  $\delta$  contributions to  $a_{10}^H(\text{anti})$  can be determined via the equations:

$$a_{10}^H(\text{anti}) = (-1.14 \cos^2 \vartheta_1 - 0.88 \cos^2 \vartheta_2) \rho_{2,6}^{\pi}$$

$$a_{10}^H(\text{anti}) = (1.35 \cos^2 \vartheta_2 \cos^2 \vartheta_3) \rho_{2,6}^{\pi}$$



where  $\vartheta_1$  is the angle between the  $P^z$  orbital carrying the unpaired spin density and the  $C_\alpha, C_\beta, C_\gamma$  plane;  $\vartheta_2$  is the angle between the  $C_\alpha, C_\beta, C_\gamma$  and  $C_\beta, C_\gamma, H_{\gamma\alpha}$  planes;  $\vartheta_3$  is the angle between the  $C_\beta, C_\gamma, C_\delta$  and  $C_\gamma, C_\delta, H_{\delta(\text{anti})}$  planes;  $\rho_{2,6}^{\pi}$  is the  $P^z$  orbital spin density at  $C_{2,6}$ , as obtained from the INDO (UW) method. In the DDCP radical,  $\vartheta_3 = 90^\circ$ , and as a consequence,  $\delta$  contributions vanish and only two of the four paths available for transmission of the spin information, namely,  $C_2, C_1, C_{10}, H_{\gamma(\text{anti})}$  and  $C_6, C_7, C_{10}, H_{\gamma(\text{anti})}$ , need to be considered. The results yield  $a_{10}^H(\text{anti})_{\text{polzn}} = -0.96$  G, which corresponds to a contribution of 10–15% to the overall coupling. On the contrary, spin polarization is expected to prevail in the case of the syn

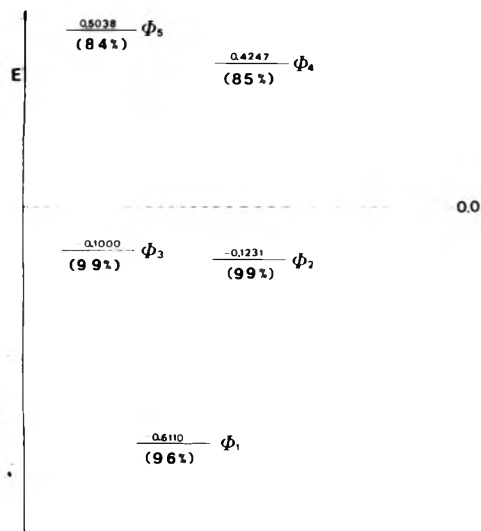


**Figure 7.** DDCP radical INDO (RW) molecular orbital energy level scheme having approximate symmetry with respect to the  $C_2 \div C_6$  plane. The percentages in brackets relate to the contribution of the  $p_z$  orbitals of the  $C_2 \div C_6$  carbon atoms.

proton at  $C_{10}$ ; this is inferred from the fact that the Luz analysis and INDO (UW) yield  $a_{10}^H(\text{syn}) = -0.56$  and  $-1.2$ , respectively, while the  $a_{10}^H(\text{syn})$  from INDO (RW) is negligible.

Finally the mechanism of the magnetic interaction of vinyl protons at  $C_{8,9}$  has been considered. The small positive values of 0.58 G predicted by INDO (UW) should be attributed mainly to delocalization with electron transfer, judging from the fact that  $a_{8,9}^H(\text{delzn})$  from INDO (RW) is 0.40. An alternative mechanism based on direct 1,3  $\pi$  overlap (eq 4), which is thought to be prevalent in



the bicyclo[2.2.1]hept-5-ene-2,3-semidione,<sup>11</sup> seems to be of minor importance in this case. This is inferred from the INDO (RW)  $P_z$  orbital coefficients of the unpaired electron wave function at  $C_{8,9}$ , which yields a small negative coupling of  $-0.12$  G for  $a_{8,9}^H$ .

**Electronic Structure of the DDCP Radical.** Figure 7 shows the INDO (RW) scheme of molecular orbitals having  $\pi$  symmetry with respect to the  $C_2, C_3, C_4, C_5, C_6$  plane. This scheme corresponds closely to the  $\pi$  system of cyclopentadienyl except in one important respect: the  $\Psi_2, \Psi_3$  orbitals, which in the planar cyclopentadienyl are degenerate, are now separated by an energy gap of 0.023 hartree (17 kcal/mol). This energy difference is large with respect to  $kT$  and, as a consequence, no possibility exists of thermal mixing. Further, the ESR properties of the

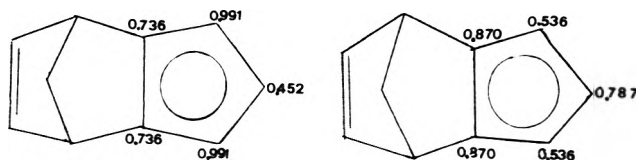
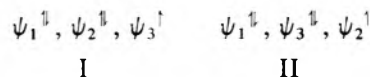


**Figure 8.** Diagrams showing INDO (RW) total  $\pi$  electron densities distributions in the DDCP radical relative to structures I and II (see text).

DDCP radical reflect the characteristics of the highest singly occupied molecular orbital ( $\Psi_3$ ). The latter is essentially a combination of  $C_{2-6} P_z$  orbitals ( $\Psi_3 = -0.5060P_2^z + 0.1489P_3^z + 0.5787P_4^z + 0.1489P_5^z - 0.5060P_6^z$ ) but it also contains an appreciable contribution from atomic orbitals in the bicyclo[2.2.1]heptene section: mainly the  $1s$  orbital of the anti proton at  $C_{10}$  (1%), the  $s, P^x,$  and  $P^z$  orbitals at  $C_{8,9}$  (4.7%), and the  $P^z$  orbitals at  $C_{1,7}$  (1.2%). The delocalization of the unpaired electron into the norbornenyl system accounts for about 10% of the overall unpaired spin density. The lifting of the orbital degeneracy in the DDCP radical can be treated in terms of a purely inductive effect of the norbornenyl substituent assumed to be electron repelling. This is illustrated in Figure 8 which shows the INDO (RW) total electron densities relative to structures



Structure I is favored by the norbornenyl moiety since it minimizes electron repelling effects. Similar reasoning was originally applied to explain the effects of substitutions on the ESR spectra of the benzene radical anion,<sup>12</sup> and more recently, the spectra of the pentaphenylcyclopentadienyl radical.<sup>13</sup>

**References and Notes**

- (1) A. Fautitano, F. Fautitano Martinotti, and S. Cesca, *J. Chem. Soc. Perkin Trans.*, 1694 (1974).
- (2) K. Alder, F. M. Flock, and P. Janssen, *Chem. Ber.*, **89**, 2689 (1956).
- (3) J. A. Pople and D. L. Beveridge, *J. Chem. Phys.*, **51**, 3327 (1969).
- (4) A. D. McLachlan, *Mol. Phys.*, **2**, 233 (1960).
- (5) ESR calculations (C.C.R., Ispra).
- (6) H. M. McConnell, *J. Chem. Phys.*, **24**, 632 (1956); C. Heller and H. M. McConnell, *ibid.*, **32**, 1535 (1960).
- (7) H. Konish, I. Kato, and T. Yonezawa, *Bull. Chem. Soc. Jpn.*, **43**, 1676 (1970); A. Yokozeki and K. Kuchitsu, *ibid.*, **44**, 2356 (1971); Y. Morino, K. Kuchitsu, and A. Yokozeki, *ibid.*, **40**, 1553 (1967); J. F. Chiang, C. F. Wilcox, and S. H. Bauer, *J. Am. Chem. Soc.*, **90**, 3154 (1968).
- (8) H. M. McConnell, C. Heller, T. Cole, and R. W. Fessenden, *J. Am. Chem. Soc.*, **82**, 766 (1960).
- (9) R. W. Fessenden and R. H. Schuler, *J. Chem. Phys.*, **39**, 2147 (1963).
- (10) Z. Luz, *J. Chem. Phys.*, **48**, 4186 (1968).
- (11) G. A. Russell, G. W. Holland, K.-Y. Chang, R. G. Keske, J. Mattox, C. S. C. Chung, K. Stanley, K. Schmitt, R. Blankespoor, and Y. Kosugi, *J. Am. Chem. Soc.*, **96**, 7237 (1974).
- (12) J. R. Bolton and A. Carrington, *Mol. Phys.*, **4**, 497 (1961).
- (13) K. Mobius, H. Van Willigen, and A. H. Maki, *Mol. Phys.*, **20**, 289 (1971).
- (14) K. B. Wiberg, *Tetrahedron*, **24**, 1083 (1967).

# An Electron Spin Resonance Study of the Benzene Anion Radical. A Model of Its Ion Pair with Alkali Metal Ions

M. T. Jones\* and T. C. Kuechler†

Department of Chemistry, University of Missouri—St. Louis, St. Louis, Missouri 63121 (Received June 23, 1976)

A detailed study of the ESR of potassium, rubidium, and cesium benzenide solutions is described. The  $g$  values, metal hyperfine splitting (hfs), and line widths have been measured as a function of solvent, temperature, and metal ion. The  $g$  values have been found to depend upon the alkali metal, the temperature, and the solvent. In the case of potassium benzenide, the metal hfs depends upon the temperature and may to a very small extent depend upon the solvent. Estimates of the rubidium and cesium metal hfs are presented. The ESR line width in the case of potassium benzenide is shown to be dependent upon the solvent and the temperature. These various phenomena are strongly suggestive of the existence of an alkali metal ion–benzene anion radical pair. A model for the ion pair is proposed in which the metal ion is placed on the sixfold axis of the benzene anion radical. However, for the temperature dependent effects upon the  $g$  values and metal hfs to be observed it is necessary for the metal ion to oscillate parallel to the plane of the benzene ring but with an average position centered on the benzene sixfold axis. MO calculations are presented to show that the expected experimental observations calculated on the basis of the model presented are consistent with the actual experimental observations.

## Introduction

The purpose of the study which is described here is to characterize the molecular and electronic structure of the benzene anion radical–alkali metal cation pair. Previous studies<sup>1–3</sup> of the ESR line shape and  $g$  values suggested that the benzene anion radical prepared in ether type solvents by reduction with potassium metal is ion paired. It was of interest to investigate the effects of other alkali metal counterions and the variation of solvent upon the benzene anion radical and to consider the results in terms of possible ion-pair structures. In particular, one would expect that if the previously observed line shape and  $g$  value variations were due to ion pairing, then changes in the counterion and/or solvent would produce variations in the observed line shapes and  $g$  values and additional information regarding the ion-pair structure.

## Experimental Section

A. *ESR Spectrometer.* The ESR measurements were performed on a Varian E-12 spectrometer equipped with a dual cavity. The dual cavity spectra were recorded on a dual channel L & N Speedomax XL recorder.

The magnetic field drift was minimized by careful control of the magnet and room temperature and by allowing the magnet to warm up overnight before recording any spectra. The temperature of the magnet cooling water was controlled within  $\pm 0.5$  °C with a Neslab refrigerated recirculating heat exchanger (HX-3000) so that the magnet operated at a temperature of approximately 3 °C above room temperature. The exterior of the dual cavity was thermally insulated with urethane foam rubber. The latter reduces the klystron frequency drift relative to the magnetic field.

The sample temperature was maintained to  $\pm 1$  °C with a Varian V-4540 temperature control. The actual sample temperature was measured with a copper–constantan thermocouple which was inserted into the variable temperature dewar along side the sample.

B.  *$g$  Value and Line Shape Measurements.* The  $g$  value and magnetic field scan rate reference standard was a dilute sample of lithium tetracyanoethylene in tetra-

hydrofuran. The  $g$  value of this reference sample relative to those reported for anthracene and pyrene anion radicals is  $2.002766(\pm 0.000002)$ .<sup>4</sup> This  $g$  value is corrected for the error reported by Allendoerfer<sup>5,6</sup> but is not corrected for second-order shifts. The hyperfine splitting is equal to 1.574 G.<sup>7</sup>

The reference sample was field modulated at 100 kHz and the unknown at 10 kHz. For the  $g$  value measurements a combination of magnetic field scan rate and recorder chart speed was selected so that (a) slower magnetic field scan rates did not result in changes in the observed magnetic field differences between the reference and unknown samples and (b) the precision of the measurement of the magnetic field difference between the reference and unknown sample was equivalent to  $\pm 1$  part in  $10^6$  (i.e.,  $\pm 3.4$  mG) in the  $g$  value. In general, two forward and two reverse field scans were averaged to give a single  $g$  value. Measurements were taken only after the sample had reached thermal equilibrium. This usually occurred within 10–15 min after changing temperature.

The following relationship between the  $g$  value of the reference and the unknown sample was used:

$$g_{\text{unk}} = g_{\text{ref}} - (g_{\text{ref}})^2 \Delta H \beta / (h\nu_0) \quad (1)$$

$g_{\text{unk}}$  and  $g_{\text{ref}}$  are the  $g$  values of the unknown and the reference samples, respectively;  $\Delta H$  is the magnetic field difference between the reference and unknown samples;  $\beta$ , the Bohr magneton;  $h$ , is Planck's constant, and  $\nu_0$  the spectrometer frequency. The spectrometer frequency was obtained by directly counting the frequency of the microwave radiation with a Hewlett-Packard 5245L frequency counter and a matched 5260A frequency divider.

The spectra for the line shape studies were recorded at 10 kHz field modulation using either the L & N recorder or the Varian E-12 recorder. An advantage associated with the use of the L & N recorder is that spectra could be recorded with field scans in either the forward or reverse direction. In the case of the Varian recorder, it is only feasible to scan in the upfield direction. The considerations with respect to faithful line shape reproduction discussed in ref 8 were observed.

C. *Materials and Sample Preparation.* The solvents used in this study were 1,2-dimethoxyethane (DME), tetrahydrofuran (THF), and hexamethylphosphoramide

† UMSL Undergraduate. Present address, Department of Chemistry, University of Illinois, Urbana, Ill. 61801.

TABLE I: Reaction of Benzene with Various Alkali Metals

Metal	Solvents	Remarks
Li	Mixed THF/DME	No reaction
Na	Mixed THF/DME	No reaction
K	Mixed THF/DME, THF, DME, DME + HMPA, and DME + 18-crown-6-ether	Forms benzene anion
Rb	THF and DME	Forms benzene anion
Cs	THF and DME	Forms benzene anion

(HMPA). They were purchased from Eastman. With the exception of the HMPA the solvents were prepared by previously described procedures.<sup>9,10</sup> We frequently hear reports that DME and THF cannot be prepared so that they are free of benzene. We have had no difficulty in this regard as long as the alkali metals used to dry the solvents have never been stored under oil. That is why we use alkali metal prepared and stored under an inert gas. The HMPA was successively dried over  $\text{CaH}_2$  for 24 h, refluxed over  $\text{CaH}_2$  for 24 h, and then distilled from  $\text{CaH}_2$  before use.

The samples were prepared using high vacuum techniques which have been described.<sup>10</sup> The sample tubes were constructed from 3-mm o.d. thin-wall pyrex tubing. HMPA and 18-crown-6-ether (obtained from PCR, Inc.) were introduced into the sample vessels via vacuum breakseals. All alkali metal mirrors with the exception of lithium were prepared by the thermal decomposition of the alkali metal azide.<sup>11</sup> The HMPA and 18-crown-6-ether concentrations were 5 vol % and 0.15 M, respectively.

## Results

**A. Reaction with Alkali Metals.** A brief summary of our attempts to prepare the benzene anion radical under various conditions is given in Table I. These results are consistent with the reported solubilities of the various alkali metals in DME and THF.<sup>12,13</sup> Just as the solubility of the alkali metals in these solvents decreases with increasing temperature, so does the observed benzene anion radical ESR intensity.

We have observed a tendency for the benzene to form biphenyl in the presence of alkali metals when there is a high concentration of cation present, e.g., as might occur when the solvents are impure or small quantities of water are introduced into the reaction vessel. There were no such complications when pure dry solvents were used. Under the latter conditions, the samples were stable at dry ice temperatures for periods of several months. The stability of the sample depends upon the alkali metal in order potassium > rubidium > cesium.

**Potassium.** In all the solvents noted in Table I, resolved, seven-line, benzene anion radical ESR spectra were observed. Both pure HMPA and DME (to which 18-crown-6-ether had been added) displayed narrow single-line ESR spectra in the absence of benzene. The addition of benzene to the pure HMPA sample did not change the observed ESR spectrum nor was the benzene anion radical spectra observed. However, in DME to which the crown ether had been added the narrow line ESR spectrum was replaced by that of the benzene anion radical at temperatures less than approximately  $-40^\circ\text{C}$ . Above that temperature, the two spectra were superimposed.

**Rubidium.** A broad line, but resolved benzene anion radical, ESR spectrum was observed in THF (see Figure 1). However, only a single broad line spectrum with a temperature dependent width was observed in DME. The line width increased from 12 G at  $-70^\circ\text{C}$  to 14 G at  $-35^\circ\text{C}$ .

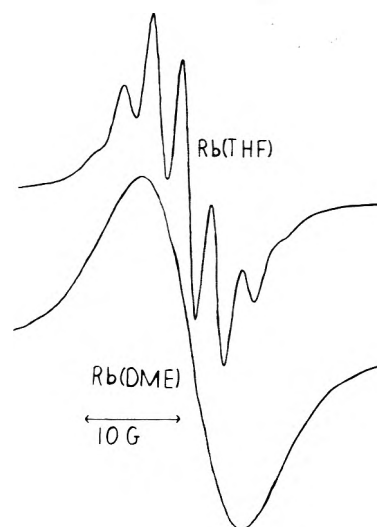


Figure 1. ESR spectra of rubidium benzenide in THF and DME at  $-65^\circ\text{C}$ .

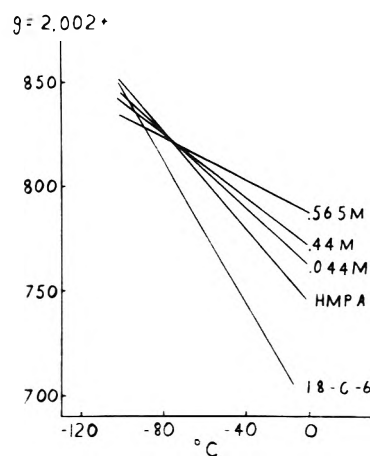


Figure 2. Loci of least-squares fits of  $g$  values to equations linear in temperature.

$^\circ\text{C}$ . There was no indication that the source of the broad lines was external, i.e., exchange broadening or electron transfer. Samples prepared in the absence of benzene displayed narrow line, low intensity ESR spectra which were not observed in the presence of the benzene.

**Cesium.** In both DME and THF, a single, broad line benzene anion radical spectrum was observed. Again there was no indication that the source of the broad lines was external. The line widths were temperature dependent. In THF they varied from 30 G at  $-107^\circ\text{C}$  to 65 G at  $+15^\circ\text{C}$ . In DME, the range is from 35 G at  $-68^\circ\text{C}$  to 66 G at  $+13^\circ\text{C}$ . Samples prepared in the absence of benzene displayed narrow line, low intensity ESR spectra. These spectra were not observed at all for THF upon addition of benzene. However, for DME such a signal was observed to be superimposed upon that of the benzene anion radical at temperatures above  $-50^\circ\text{C}$  and prevented the measurement of the  $g$  value for this particular solvent system.

**B.  $g$  Values.** Figure 2 shows the loci of least-squares fits to equations linear in the temperature of the  $g$  values of potassium benzenide in various solvent systems. Approximately 200 data points were included in the analyses. That is too many data points to present clearly in a single figure. For that reason they are not included in Figure 2. However, Table II presents a summary of the least-squares parameters from which the lines in Figure 2 were drawn. First, one notes the strong dependence of the  $g$  value upon temperature and upon solvent composition at higher

TABLE II: Summary of the Potassium Benzenide  $g$  Values<sup>a</sup>

Initial benzene concn, M	Solvent system	$A^c$	$10^6 B^c$	Data temp range, °C	No. of points
0.044	THF(Na-K)	2.002 760 ( $\pm 3$ )	-0.773 ( $\pm 0.04$ )	-44 to -103	16
0.044	DME(K)	2.002 763 ( $\pm 4$ )	-0.797 ( $\pm 0.015$ )	-21 to -91	36
0.044	2:1 (THF/DME) (Na-K)	2.002 772 ( $\pm 3$ )	-0.700 ( $\pm 0.011$ ) <sup>d</sup>	-43 to -122	12
0.44	DME(K)	2.002 771 ( $\pm 2$ )	-0.687 ( $\pm 0.009$ )	-19 to -89	19
0.565	DME(K)	2.002 787 ( $\pm 3$ )	-0.453 ( $\pm 0.010$ )	-24 to -93	38
0.044	DME + 5% HMPA (K)	2.002 745 ( $\pm 3$ )	-1.047 ( $\pm 0.014$ )	-34 to -91	33
0.044	DME + 18-C-6 (K)	2.002 690 ( $\pm 4$ )	-1.567 ( $\pm 0.016$ )	-47 to -88	22
0.044 (C <sub>6</sub> H <sub>5</sub> D)	2:1 (THF/DME) (Na-K)	2.002 776 ( $\pm 5$ )	-0.660 ( $\pm 0.020$ ) <sup>d</sup>	-59 to -109	14
0.044 (C <sub>6</sub> H <sub>5</sub> D)	DME(K)	2.002 774 ( $\pm 4$ )	-0.651 ( $\pm 0.016$ )	-34 to -88	18

<sup>a</sup> Corrected for second-order shifts. <sup>b</sup> Alkali metals in parentheses indicate the use of sodium-potassium alloy (Na-K) or pure potassium metal (K). <sup>c</sup>  $g(T) = A + BT$ , where  $T$  is in °C. The uncertainty in  $A$  represents the root mean square deviation in the last place between the calculated and experimental values of  $g$  and that in  $B$  is derived from a standard regression analysis. <sup>d</sup> Data taken from ref 3.

TABLE III: Summary of Rubidium and Cesium Benzenide  $g$  Values<sup>a</sup>

Initial benzene concn, M	Solvent <sup>b</sup>	$A^c$	$10^6 B^c$	Data temp range, °C	No. of points
0.044	DME(Rb)	2.002 34 ( $\pm 3$ )	-0.98 ( $\pm 0.10$ )	-35 to -73	11
0.044	THF(Rb)	2.002 46 ( $\pm 3$ )	-1.64 ( $\pm 0.11$ )	-83 to -112	36
0.044	THF(Cs)	2.001 9 ( $\pm 3$ )		-84 to -102	10

<sup>a</sup> No second-order shift corrections were made as these are less than the accuracy of the data. <sup>b</sup> Alkali metal used in parentheses. <sup>c</sup>  $g(T) = A + BT$ , where  $T$  is in °C. The uncertainty in  $A$  represents the root mean square deviation in the last place between the calculated and experimental  $g$  values and that in  $B$  is derived from a standard regression analysis.

TABLE IV:  $g$  Value Shifts in Comparison with Spin-Orbit Interaction Parameter

Cation	$10^5 \Delta g^a$	$10^5 \Delta g^b$	Spin-orbit interaction <sup>d</sup> parameter, cm <sup>-1</sup>
K <sup>+</sup> <sup>c</sup>	0-4	0-4	38.48
Rb <sup>+</sup> <sup>c</sup>	47	24	158.40
Cs <sup>+</sup> <sup>c</sup>		94	369.41

<sup>a</sup> Solvent, DME. <sup>b</sup> Solvent, THF. <sup>c</sup> Relative to potassium benzenide at -90 °C. <sup>d</sup> See ref 15.

temperatures. Another noteworthy feature is the fact that at lower temperatures ( $T < -80$  °C) the  $g$  values appear to be almost independent of the solvent system.

Table III summarizes the  $g$  values obtained for rubidium and cesium benzenides. The line widths are considerably larger than for potassium benzenide. Hence, the accuracy with which the  $g$  values can be measured is reduced. In the case of rubidium benzenide it is still possible to measure  $dg/dT$ , which is negative. However, it was not possible to make the same measurement for the cesium benzenide.

The change in  $g$  value as one moves through the alkali metal ion series from potassium to cesium is important. Table IV compares the maximum  $g$  value shifts for the various alkali benzenides relative to potassium benzenide at -90 °C. Also included in the table are the spin-orbit interaction parameters for the alkali metals. There is a rough proportionality between the  $g$  value shifts and the spin-orbit interaction parameters. Such a relationship has

been considered symptomatic of ion-pair formation.<sup>14-16</sup>

C. *Metal Hfs.* The line shapes of the ESR spectra of potassium benzenide in various solvents have been analyzed using techniques previously reported.<sup>12</sup> The analysis assumed the presence of unresolved metal hfs due to a single spin ( $I = 3/2$ ). Spectral envelopes were also simulated for interaction with two equivalent spins ( $I = 3/2$ ) but they did not give as good agreement with the spectral line shapes. It is on the basis of this result that the benzene anion is believed to interact with only one metal ion. The results are shown in Table V and are listed by individual solvent systems. With the exception of the sample in DME to which 18-crown-6-ether has been added the results are essentially equivalent within experimental error. It should be noted here that the accuracy of the line shape analysis is not as high as that associated with the  $g$  value measurements. So it is possible (indeed very likely) that rather modest differences are obscured. The changes in the data are so small from those reported in ref 1 and 2 that the reader is referred there for plots of the metal hfs against temperature.

The situation with respect to potassium benzenide in DME to which 18-crown-6-ether had been added needs more discussion. There is a strong possibility that in addition to unresolved metal hfs there is a contribution to the line width from unresolved proton hfs arising from interaction with some of the protons on the crown ether. The two pieces of evidence which support this view are the following. First, the line shape analysis assuming interaction with a single ( $I = 3/2$ ) spin does not give as good agreement with the experimental line shape as it does

TABLE V: Metal Hfs in the Potassium Benzenide Ion Pair

Solvent	Counterion	$A,^a$ mG	$B,^a$ mG/°C	Temp range, °C	No. of points
THF/DME	K <sup>+</sup> (Na-K)	220 <sup>b</sup> ( $\pm 18$ )	2.55 ( $\pm 0.15$ )	-10 to -119	67
THF	K <sup>+</sup>	208 ( $\pm 8$ )	2.57 ( $\pm 0.10$ )	-58 to -95	12
DME	K <sup>+</sup>	231 ( $\pm 22$ )	2.63 ( $\pm 0.19$ )	-24 to -93	40
DME + 5% HMPA	K <sup>+</sup>	240 ( $\pm 16$ )	2.95 ( $\pm 0.14$ )	-50 to -89	5
All the above		222 ( $\pm 19$ )	2.61 ( $\pm 0.16$ )		124
DME + 18-C-6-E	K <sup>+</sup>	206 ( $\pm 8$ ) <sup>c</sup>	0.72 <sup>c</sup> ( $\pm 0.09$ )	-32 to -92	9

<sup>a</sup>  $Hfs(T) = A + BT$ , where  $T$  is in °C. The uncertainty in  $A$  represents the root mean square deviation in the last two places between the calculated and the experimental data points and that in  $B$  is derived from standard regression analysis. <sup>b</sup> See ref 2. <sup>c</sup> See Discussion in the text.

TABLE VI: Summary of Metal Hfs in All Benzenides

Metal ion	Solvent	Metal hfs range, G	Max spin density value
K <sup>+</sup>	THF and DME	-0.08 to +0.150	$1.8 \times 10^{-3}$
Rb <sup>+</sup> <sup>a</sup>	THF	0.8 to 1.0	$0.8 \times 10^{-3}$
Rb <sup>+</sup> <sup>a</sup>	DME	1.3 to 1.8	$1.5 \times 10^{-3}$
Cs <sup>+</sup>	THF	1 to 1.5	$1.2 \text{ to } 1.8 \times 10^{-3}$

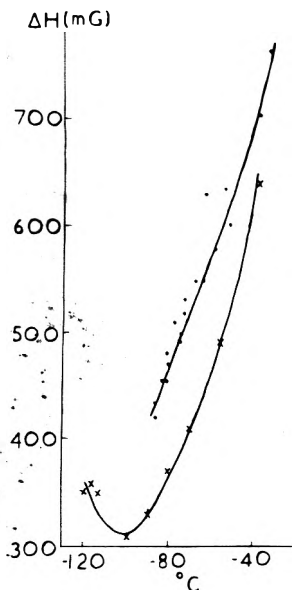
<sup>a</sup> <sup>87</sup>Rb.

Figure 3. Plot of potassium benzenide ESR line widths as a function of temperature. Dots represent data taken in DME and crosses data taken in 2:1 (THF/DME).

when the crown ether is not present. Second, it has recently been reported<sup>17</sup> that when potassium metal is used to reduce a neat sample of toluene to which 18-crown-6-ether has been added an ESR spectrum is observed in which there is partially resolved proton hfs due to interaction with the crown ether. The same authors report that when neat benzene is substituted for toluene their spectral simulations based on interactions with a single ( $I = 3/2$ ) spin and interaction with the same spin plus additional proton hfs arising from the crown ether give equally satisfactory fits to the experimental spectra. An attempt to resolve this question through the use of ENDOR spectroscopy was unsuccessful.<sup>18</sup> However, the data in Table V are reported as if the interaction were with a single ( $I = 3/2$ ) spin. It is hoped the reader will keep this uncertainty in mind.

The situation is also complex in the cases of rubidium and cesium benzenides. The line shapes are no longer uniquely determined by a single set of component line widths and metal hfs. However even so it is possible to estimate permissible ranges for the unresolved metal hfs. To do this we have assumed that the proton hfs and component line widths are equal to those observed in the potassium benzenide solutions. The estimates obtained from these crude analyses are shown in Table VI along with an estimate of the maximum spin density on the alkali metal ion which would give rise to such values of hfs.

D. *ESR Line Shapes and Line Widths.* The observed ESR line widths (and line shapes) as a function of temperature for potassium benzenide solutions in 2:1 (THF/DME) have been previously reported.<sup>1,2,10</sup> Additional data taken in DME show a decided dependence of the line width upon solvent.<sup>21</sup> Figure 3 shows a comparison of the line widths in these two solvents. Not shown are

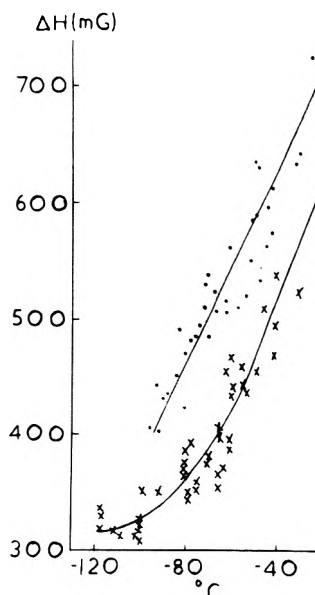


Figure 4. Plot of potassium benzenide ESR component line widths as a function of temperature. Dots represent data in DME and crosses data taken in 2:1 (THF/DME).

data taken in DME to which 5% HMPA has been added. At temperatures in the range  $-90$  to  $-60$  °C they fall somewhat above the DME data. At higher temperatures they appear to merge with the DME data. As noted in ref 1 and 2, the ESR line shapes of potassium benzenide solutions are inhomogeneously broadened due to the presence of unresolved metal hfs. The line shape analysis used to measure the metal hfs also yields the component line width (i.e., the true line width).<sup>1,2</sup> Figure 4 shows the component line widths in the two solvents 2:1 (THF/DME) and DME.

Careful studies of the line widths as a function of the amount of neutral benzene and benzene anion radical present have established that the increase in line width with increasing temperature is not due to either Heisenberg spin-spin exchange or to electron transfer between neutral benzene and its anion radical. The line widths are independent of neutral benzene concentration below 0.2 M.

We have not included data for solutions of DME to which 18-crown-6-ether have been added because of the uncertainty regarding the existence of unresolved proton hfs due to the crown ether. The line shape analysis yields values for the line widths which range from 620 to 670 mG at  $-90$  and  $-40$  °C, respectively.

It is possible to view the change in the component line width with increasing temperature as being due to some perturbation which increases with the temperature. That is

$$1/\tau = \sqrt{3} \gamma (\Delta H_c - \Delta H_0)/2 \quad (2)$$

and

$$1/\tau = A \exp(-\Delta E/kT) \quad (3)$$

Here  $\gamma$  is the electron gyromagnetic ratio,  $\Delta H_c$  is the observed component line width, and  $\Delta H_0$  is the component line width in the absence of the perturbation. A plot of  $\log(1/\tau)$  vs.  $1/T$  is shown in Figure 5 for the two solvent systems 2:1 (THF/DME). Table VII summarizes the values of the parameters in eq 3 which are the best fit to the data.

We were surprised to find the best fit for  $\Delta H_0 = 0$  since we expected that it might be of the order of  $1/2T_1$  in units of gauss.

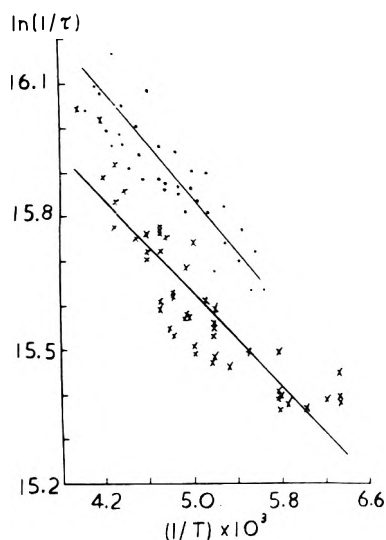


Figure 5. Plot of  $\log(1/\tau)$  against  $1/T$  for potassium benzenide solutions. Dots represent data taken in DME and crosses data taken in 2:1 (THF/DME).

TABLE VII: Parameters which Describe the Increase of Line Width with Temperature<sup>a</sup>

Solvent	2:1 (THF/DME)	DME
A, radians/s	$2.28 \times 10^7$	$3.34 \times 10^7$
Rms in A	$\pm 0.21 \times 10^7$	$\pm 0.22 \times 10^7$
$\Delta E$ , $\text{cm}^{-1}$	182	206
No. of data points	54	46
$\Delta H_0$	0	0

$$^a (1/\tau) = A \exp(-\Delta E/kT).$$

E. *Proton Hfs.* The strong temperature dependence of the proton hfs of the benzene anion radical has been known for sometime.<sup>9</sup> However, a recently reported detailed study has shown no dependence upon solvent composition.<sup>22</sup> The resolution obtained in the case of rubidium and cesium benzenides has prevented studies of the proton hfs in these salts.

## Discussion and Conclusions

A. *Model for the Ion Pair Structure.* The model for the structure of the alkali metal benzenide ion pair which we would like to consider here is one in which the metal ion is, on the average, located on the benzene anion radical sixfold rotation axis. The metal ion is placed on the benzene anion sixfold rotation axis because this is the position of strongest electrostatic attraction for a point, positive charge relative to a ring of negative charge uniformly distributed at the corners of a regular hexagon. There must be motion of the metal ion parallel to the plane of the benzene molecule because when the metal ion is exactly on the sixfold axis the overlap between the metal s and p orbitals and the degenerate set of  $\pi$ -molecular orbitals occupied by the unpaired electron is zero. Therefore, there could be no direct contribution to either metal hfs or to the  $g$  value. Whenever the metal ion moves off the sixfold axis these contributions become finite and we shall show by molecular orbital calculations that they are of the correct sign and magnitude.

The motion of the metal ion in a plane parallel to that of the benzene anion can be viewed as being caused by collisions between the benzenide ion pair and solvent molecules. However, it is also possible to view the motion of the metal ion as being harmonic where the metal ion moves in the potential field created by the charge distribution associated with the benzene anion radical.<sup>23</sup> Most likely the true situation involves both processes but attenuated by solvation effects.

B. *MO Calculations.* Two different types of MO calculations have been used to calculate the expected properties of the proposed ion-pair model.

The first set of MO calculations which we used were those described by Goldberg.<sup>27-29</sup> They were used to calculate (1) the amount of charge density transferred to the metal ion from the benzene anion radical (i.e., to estimate values of the metal hfs), (2) the effect of the electrostatic perturbation of the alkali metal ion upon the  $\pi$ -molecular orbital charge distribution, (3) the effect of the electrostatic perturbation of the alkali metal upon the individual  $\pi$ -molecular orbital energies, and (4) the effect of metal ion position relative to the benzene anion radical upon the energy of ion-pair association.

The second set of MO calculations which we used were those which have been described by Dalgard and Linderberg.<sup>30</sup> They were used to calculate the effect of ion-pair formation and the effect of ion-pair structure upon the benzenide  $g$  value. The particular program used was based on the energy weighted maximum overlap (EWMO) method and has been used to calculate the anisotropic  $g$  values for small radicals such as  $\text{ClO}_2$ ,  $\text{ClO}_4$ , etc.<sup>30</sup> This represents the first use of this type of program to calculate  $g$  values for organic free radicals.<sup>31</sup> The calculational procedure takes into account the values of the spin-orbit interaction parameters of all of the nuclei in the molecule and can be used to calculate directly the effect of position of the metal ion relative to the rest of the molecule upon  $g$  value.

A rather extensive amount of calculation has been performed based upon the Goldberg formulation and, of course, this resulted in a considerable quantity of quantitative detail. However, rather than present all this detail which has no quantitative predictive value, we have chosen to favor a more qualitative presentation. For our purposes here, we believe that the most important aspect of both sets of MO calculations is that they predict changes in experimentally observable parameters, based on the above model, which are in qualitative agreement with experiment.

Throughout the discussions which follow it should be borne in mind by the reader that there are two unique directions of metal ion motion away from the benzene sixfold rotational axis and parallel to the molecular plane. One is directed toward the carbon atoms and the other is directed toward the midpoint of the carbon-carbon bonds. For most of the calculations to be discussed, the results for motion along other directions are linear combinations of the results for motion along these two directions.

C. *Calculation of the Metal Hfs.* Calculations of the amount of unpaired charge density transferred to the metal ion for potassium, rubidium, and cesium benzenides have been performed. The calculations have been made as a function of the metal ion distance from the sixfold axis and its distance above the benzene molecular plane. The results can be summarized as follows. As the distance between the metal ion and the plane of the ring increases, the amount of charge density transferred to the metal ion decreases (see Figure 6). For a fixed distance between the metal ion and the plane of the ring, the amount of charge density transferred increases as one moves through the series from potassium to cesium (see Figure 7). For a fixed distance between the metal ion and the plane of the ring, the charge density transferred to the metal ion increases from zero, reaches a maximum, and then decreases as the metal ion is moved from the sixfold axis (see Figures 6 and 7).

Compare the results of the charge density calculations with the experimental observations of the potassium hfs.

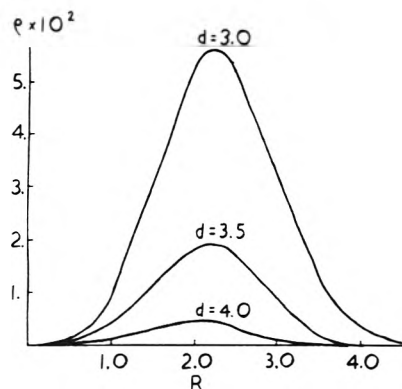


**Figure 6.** Plot of calculated unpaired charge density transferred to the rubidium cation as a function of distance ( $R$ , Å) from the sixfold axis. Three different distances ( $d$ , Å) from the plane of the molecule are shown.

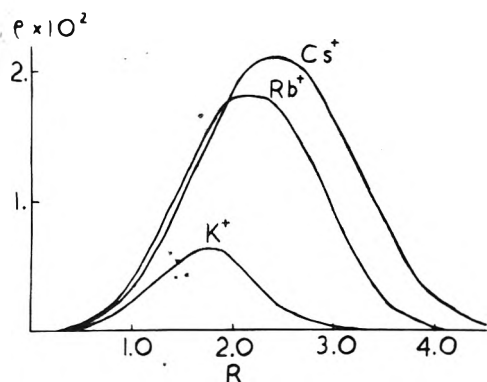


**Figure 7.** Plot of calculated unpaired charge density transferred to potassium, rubidium, and cesium cations as a function of the distance ( $R$ , Å) from the sixfold axis. All three calculations have been done at the same distance from the plane of the benzene ring (3.5 Å).

Experimentally, the hfs ranges from a value of  $-89$  mG at  $-119$  °C to a value of  $+285$  mG at  $-24$  °C.<sup>1,2</sup> This corresponds to a spin density on the potassium ion of  $-1.0 \times 10^{-3}$  and  $+3.5 \times 10^{-3}$ , respectively.<sup>32</sup> That the spin density is negative at low temperature suggests that the corresponding charge density is small or perhaps even equal to zero. Under these conditions one would expect the predominate mechanism for creating unpaired spin density at the metal ion to be through spin-polarization effects.<sup>33</sup> This is what one would expect at low temperatures for the proposed ion-pair model, i.e., localization of the metal ion on the sixfold rotation axis of the benzene anion, little or no charge density on the metal ion, and any metal hfs would arise from spin polarization effects.<sup>33</sup> As the temperature is increased the mean amplitude of motion of the metal ion relative to the sixfold axis remains zero but the mean amplitude squared increases in value. As the latter quantity increases so does the direct contribution to the charge density upon the metal ion via overlap of the metal  $s$  orbitals and the carbon  $2p$  orbitals perpendicular to the benzene ring. An increase in the charge density on the metal ion would yield an increase in the amount of positive spin density at the metal ion. Thus, if one started with a negative spin density it would gradually decrease in absolute magnitude, go through zero, and ultimately begin to increase in value. This exactly parallels the experimental situation.

**D. The Effect of the Metal Ion Position Upon Charge Distribution and  $\pi$ -Molecular Orbital Energies of the Benzene Anion.** When the metal ion is centered on the sixfold axis, the unpaired electron resides in a pair of molecular orbitals which are degenerate and for which the individual charge densities are those normally calculated

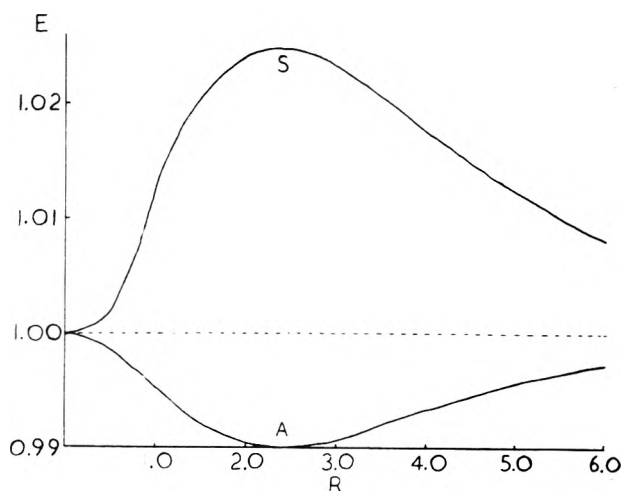


**Figure 8.** Plot of the molecular orbital energies (in units of  $\beta$ ) for the symmetric and antisymmetric (originally degenerate) antibonding molecular orbitals of the benzene anion as a function of metal ion distance from the sixfold axis. The metal ion is potassium and it is 3 Å above the benzene plane. The metal ion motion is toward the carbon-carbon bond and the lowest energy orbital is that labeled antisymmetric.

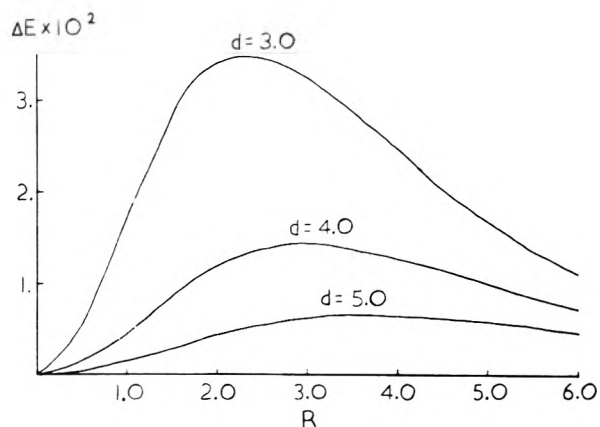


**Figure 9.** Plot of the difference between the symmetric and antisymmetric molecular orbital energies (in units of  $\beta$ ) as a function of metal ion distance from the sixfold axis for various distances above the molecular plane. The ion motion is toward the carbon-carbon bond. It is the potassium ion.

for the benzene anion radical. As the metal ion is moved away from the sixfold axis, the two degenerate orbitals interact with it differently and are split in energy. There is a corresponding redistribution of charge within each molecular orbital. Motion toward one of the carbon atoms stabilizes the symmetric orbital (both absolutely and relative to the antisymmetric orbital) whereas motion toward the center of a carbon-carbon bond stabilizes the antisymmetric orbital. The changes in symmetric and antisymmetric orbital energies for a fixed metal ion distance from the plane of benzene anion are shown in Figure 8. The changes are independent of the particular metal ion. Figure 9 shows the difference in energy between the originally degenerate symmetric and antisymmetric molecular orbitals for several different values of the distance between the metal ion and the benzene molecular plane. For random directions such as might occur because of ion pair-solvent collisions the average energy difference between the two orbitals would be zero, i.e., neither of the two orbitals is favored relative to the other. However, we believe that an interaction such as this can have an important effect upon the ESR spectrum because it modulates the energy of the electronic state associated with the ESR transition.

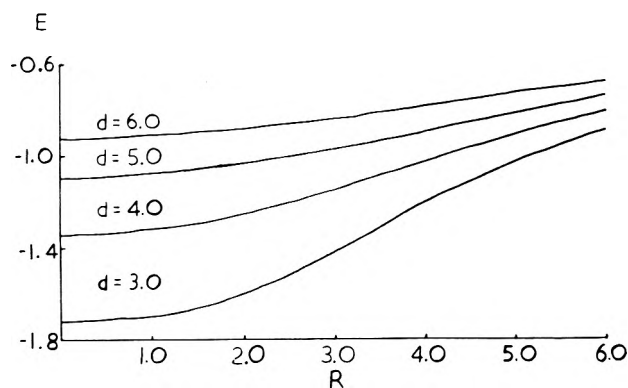


**Figure 10.** Plot of the ion-pair association energy (in units of  $\beta$ ) as a function of metal ion distance from the sixfold axis. The metal ion is potassium and its motion is directed toward the carbon-carbon bond.

Let us consider the hypothesis that the increase in the benzene anion radical component line width which is observed as the temperature is increased is due to this random modulation of the energy of the electronic state associated with the ESR transition. That is, as the metal ion moves relative to the benzene anion molecular plane, it modulates the energy splitting between the originally degenerate levels, which in turn causes an increased uncertainty in the energy of the electronic state in which the ESR transition takes place. This increased uncertainty in the electronic state energy then manifests itself as an increased line width. The effect we have in mind here is similar to the lifetime broadening one might observe in ESR studies of a photoexcited triplet whose lifetime is of the order of the ESR line width.

Experimentally the frequency of the perturbation increases with temperature. The motion we are considering here would be expected to increase in frequency and amplitude with increasing temperature. One might ask why there is no evidence of alternating line width effects if the frequency is as slow as it appears to be. Experimentally, the relative intensities of the proton hfs are those expected from six equivalent protons over the whole of the temperature range studied. Very likely, vibronic motions are sufficiently large to average out any asymmetric spin density distributions caused by the asymmetry of the metal ion position. However, whatever the uncertainty that such a motion creates in the energy of the associated electronic state it would not be averaged to zero.

**E. The Energy of Ion-Pair Association.** The energy of ion-pair association behaves as one would expect. As the metal ion is moved on a line which is parallel to the molecular plane and passes through the sixfold axis, the electrostatic energy of attraction is parabolic shaped (near the sixfold axis). Its minimum value is centered on the sixfold axis. As the distance between the metal ion and the molecular plane increases the depth of the curve decreases. Clearly, solvation of the cation will reduce the magnitude of the electrostatic interaction but it will not change the major features outlined above. Figure 10 shows a typical plot of the energy of ion pair association as a function of metal ion distance from the sixfold axis.

**F.  $g$  Value Calculations.** The  $g$  value calculations using the EWMO method have been carried out for potassium and rubidium benzenides for selected metal ion positions relative to the benzene ring. The results of these calculations can be summarized as follows. When the metal ion is on the sixfold axis the two degenerate  $\pi$  molecular states give identical isotropic  $g$  values and there is essentially no difference between the isotopic  $g$  values calculated for the free benzene anion radical and potassium benzenide. This

is not true for the rubidium benzenide, its isotopic  $g$  value is shifted to smaller values than that calculated for the free ion. The extent of the negative shift is inversely proportional to the distance between the metal ion and the plane of the benzene ring.

As the metal ions are moved off the sixfold axis and parallel to the benzene ring, the  $g$  value associated with the antisymmetric state is shifted to smaller values and that of the symmetric to larger values. However, the  $g$  values are not shifted in equal amounts relative to those calculated for the metal ion positioned on the sixfold axis. The negative shift is the larger. Thus, the average  $g$  value over the two states (assuming equal weighting) is smaller relative to that for which the metal ion is on the sixfold axis. The above description is independent of the direction in which the metal ion moves in the plane parallel to the benzene ring with the minor exception that the individual  $g$  values differ slightly.

We believe the results of these calculations are quite consistent with the proposed model for the benzenide ion pair. First, there is the negative shift in  $g$  value in going from potassium to rubidium. Second, there is the reproduction of the negative shift with temperature. That is, as the temperature is increased the amplitude of the metal ion motion is increased and hence the  $g$  value decreases.<sup>34</sup>

**G. Other Ion Pair Models.** The experimental evidence is strongly indicative of the existence of a benzenide ion pair in all the solvent systems studied. A model for the benzenide ion pair has been proposed and calculations based on that model are presented and shown to be consistent with experiment. It was not our intention to consider all possible ion-pair models but just that one which we felt was most consistent with the experimental observations. However, a reviewer has raised the question of whether the existence of a rapid equilibrium between two different types of ion pairs ( $B^-M^+ \rightleftharpoons B||M^+$ ) could be ruled out. Therefore we present the following discussion. Presumably the solvent separated species would be the more stable species at lower temperatures. Under these conditions one would not expect to observe negative spin density on the metal ion which is the case experimentally. It is true that, as the relative amount of the contact ion pair increases with temperature, one would expect the value of the metal hfs to increase (assuming the contact ion pair has a fixed value of metal hfs). However even here one has to explain how the metal hfs arises in the contact ion pair. If one were to try to argue that the contact ion pair were the more stable species at the lower temperature, it would clearly predict a temperature dependence of the metal hfs which is opposite to that of experiment. It would appear that the temperature dependence of the  $g$  value might be consistent with the existence of a solvent separated ion pair in equilibrium with a contact ion pair if one assumes that the  $g$  value of the solvent separated ion pair is that of the "free ion". However, as our  $g$  value calculations show the negative  $g$  value shift is significantly enhanced by the motion of the metal ion in a plane parallel to that of the benzene ring. We certainly believe solvation effects are important here but we do not believe that an equilibrium between a contact and a solvent separated ion pair can adequately explain the observed phenomena.

**Acknowledgment.** The partial support of this research by the National Science Foundation through Grant No. GP-28436 is gratefully acknowledged. One of us (M.T.J.) acknowledges the support of the Netherlands Foundation for Chemical Research (SON) and the Netherlands Or-

ganization for the Advancement of Pure Research (ZWO) as well as the hospitality of the University of Groningen (The Netherlands) and the University of Sheffield (Great Britain) during which time this work was prepared for publication. Professor J. Linderberg's (Aarhus University) hospitality to M.T.J. is also acknowledged during which time the details of the EWMO program were learned. The ENDOR experiment was performed at the University of Sheffield.

### References and Notes

- (1) M. T. Jones, M. Komarynsky, and R. D. Rataiczak, *J. Phys. Chem.*, **75**, 2769 (1971).
- (2) M. T. Jones and M. Komarynsky, *J. Chem. Phys.*, **56**, 4404 (1972).
- (3) M. T. Jones, T. C. Kuechler, and S. Metz, *J. Magn. Reson.*, **10**, 149 (1973).
- (4) B. G. Segal, M. Kaplan, and G. K. Fraenkel, *J. Chem. Phys.*, **43**, 4191 (1965).
- (5) The value reported in ref 3 for TCNE was not corrected for the error reported by Allendoerfer (ref 6).
- (6) R. D. Allendoerfer, *J. Chem. Phys.*, **55**, 3615 (1971).
- (7) M. T. Jones and W. R. Hertler, *J. Am. Chem. Soc.*, **86**, 1881 (1964).
- (8) M. T. Jones, *J. Magn. Reson.*, **11**, 207 (1973).
- (9) M. T. Jones, *J. Am. Chem. Soc.*, **88**, 174 (1966).
- (10) R. D. Rataiczak and M. T. Jones, *J. Chem. Phys.*, **56**, 3898 (1972).
- (11) M. J. Feighan and M. T. Jones, *J. Am. Chem. Soc.*, **92**, 6756 (1970).
- (12) F. Cafasso and B. R. Sundheim, *J. Chem. Phys.*, **31**, 809 (1959).
- (13) S. H. Glarum and J. H. Marshall, *J. Chem. Phys.*, **52**, 555 (1970).
- (14) C. L. Dodson and A. H. Reddoch, *J. Chem. Phys.*, **48**, 3226 (1968).
- (15) W. G. Williams, R. J. Pritchett, and G. K. Fraenkel, *J. Chem. Phys.*, **52**, 5584 (1970).
- (16) J. L. Sommerdijk and E. de Boer, "Ions and Ion Pairs in Organic Reactions", Vol. 1, M. Szwarc, Ed., Wiley, New York, N.Y., 1972, Chapter 8.
- (17) G. V. Nelson and A. V. Zelewsky, *J. Am. Chem. Soc.*, **97**, 6279 (1975).
- (18) ENDOR experiments have been performed on solutions of potassium benzenide in pure DME, pure THF, and the 2:1 (THF/DME) solvent mixture to which 18-crown-6-ether had been added. The purpose of the experiments was to resolve any hfs arising from the protons attached to the crown ether and which was not resolvable through the use of ESR techniques. Although, the ENDOR experiments were run under conditions of concentration, temperature, and solvent which have proven successful for other anion radical systems including the *p*-xylene anion radical,<sup>19</sup> no ENDOR absorption was detected for either the benzene ring protons or protons attached to the crown ether. Similar results have been reported for the benzene anion radical in 2:1 (THF/DME) solution.<sup>20</sup>
- (19) M. T. Jones, *J. Phys. Chem.*, submitted for publication.
- (20) M. R. Das, S. B. Wagner, and J. H. Freed, *J. Chem. Phys.*, **52**, 5404 (1970).
- (21) The first report of such a dependence was made by Das et al.<sup>20</sup> However, they were unaware of the inhomogeneous nature of the benzene anion radical line shape and no corrections for unresolved metal hfs were performed.
- (22) M. T. Jones, S. Metz, and T. C. Kuechler, *Mol. Phys.*, in press.
- (23) We are indebted to Professor Shigeyuki Aono of Kanazawa University for pointing out that a calculation of the metal hfs<sup>24-26</sup> can be set up along such lines and for working out the details of its application to the benzenide ion pair. The details follow the outline previously published for the study of the metal hfs in the naphthalene and biphenyl anion radical ion pairs.<sup>24-26</sup> The results with respect to the metal hfs are in agreement with those obtained from the procedure outlined by Goldberg.<sup>28,29</sup> However, with the latter calculations we are able to calculate other features of interest, i.e., the energy of ion pair formation and the effect of electrostatic perturbation by the metal ion upon the  $\pi$ -molecular orbitals which contain the unpaired electron and how both are affected by changes in the position of the metal ion relative to the benzene ring.
- (24) S. Aono and K. Oohashi, *Prog. Theor. Phys.*, **30**, 162 (1963).
- (25) S. Aono and K. Oohashi, *Prog. Theor. Phys.*, **32**, 1 (1964).
- (26) S. Aono and K. Oohashi, *Kogyo Kagaku Zasshi*, **68**, 1507 (1965).
- (27) These calculations have been very well described and documented by Goldberg.<sup>28,29</sup> Therefore, we give no description here but refer the reader to the original sources.
- (28) I. B. Goldberg and J. R. Bolton, *J. Phys. Chem.*, **74**, 1965 (1970).
- (29) I. B. Goldberg, Thesis, University of Minnesota, 1969.
- (30) E. Dalgård and J. Linderberg, *Int. J. Quantum Chem.*, **S9**, 269 (1975).
- (31) The preliminary results of our calculations of *g* values for approximately 30 hydrocarbon (including some heterocyclic) radicals are as follows. As one moves from ring system to ring system (i.e., benzene, naphthalene, anthracene, cycloheptatrienyl, etc.) the experimental changes in the *g* values are not reproduced. However, if one asks what happens as various substituent groups are interchanged on a given ring system, the EWMO method does reproduce experimentally observed trends. A few preliminary calculations on the effect of ion-pair formation upon the *g* value using the EWMO method are also quite encouraging. The results of these calculations will be reported at length later.
- (32) J. H. Sharpe and M. C. R. Symons, ref 16, Chapter 7.
- (33) See, for example, J. E. Wertz and J. R. Bolton, "Electron Spin Resonance", McGraw-Hill, New York, N.Y., 1972, pp 118-121.
- (34) The *g* value calculations reported here do not take into account possible effects of electron orbital angular momentum which may result from the orbital degeneracy of the benzene anion radical (see ref 35). If the *g* value shifts due to the existence of such orbital angular momentum were positive, then the metal ion motion of the type proposed would partially destroy the orbital angular momentum and lead to negative shifts, thence to decreased *g* values as the temperature is increased. Such an effect may be contributing to the total change of the *g* value with temperature. However, it is difficult to rationalize the increasing negative shifts in the *g* values as one moves through the series potassium to cesium on such a basis.
- (35) R. E. Moss and A. J. Perry, *Mol. Phys.*, **22**, 798 (1971).

## Substituted Benzylidenemalononitrile Anion Radicals

Arthur McB. Block,

Division of Physical Sciences and Terrestrial Ecology Program, Puerto Rico Nuclear Center, Rio Piedras, Puerto Rico

Rosario Concepción, and Gerald R. Stevenson\*

University of Puerto Rico, Department of Chemistry, Rio Piedras, Puerto Rico 00931 (Received August 24, 1976)

Publication costs assisted by the University of Puerto Rico

The anion radicals of several substituted benzylidenemalononitriles have been generated by alkali metal reduction in etheral solvents. The observed ability of these para-substituted anion radicals to resist anionic polymerization and the previously reported ability of these compounds to deactivate the growth of transplanted cancerous tumors in mice varies identically with the para substituent ( $\text{NO}_2 > \text{CN} > \text{H} > \text{OCH}_3 > \text{CH}_3$ ). This is just the opposite order found for the increasing spin density in the vinyl moiety. While the ESR coupling constants correlate well with the corresponding substituted benzaldehyde anion radicals, there is only poor correlation with the INDO calculated coupling constants. However, the INDO calculations do suggest the same trends. Further, they suggest that the C-N and/or C-CN bond distances are different for the cis and trans cyano groups.

Corson and Stoughton<sup>1</sup> first isolated a number of substituted benzylidenemalononitriles from a base condensation between the corresponding aldehyde and

malononitrile. Although these workers were primarily interested in the isolation and chemistry of these new compounds, they noted sternutatory and irritant properties

TABLE I: Coupling Constants in Gauss for Some Anion Radicals of Para-Substituted Benzylidenemalononitriles and the Corresponding Benzaldehydes

Compound	$A_{\text{subst}}$	$A_{\text{vinyl}}$	$A_{\text{o}}$	$A_{\text{N(cis)}}$	$A_{\text{N(trans)}}$	$A_{\text{M}}$	Ref
I	5.05 (H)	5.30	0.73, 0.46 <sup>a</sup>	0.73	5.30	0	This work
Benzaldehyde	1.5 (H)	5.50	1.13			0.45	10
II	2.80 (N)	3.88	0.68, 0.48 <sup>a</sup>	0	0.80	1.28	This work
<i>p</i> -Nitrobenzaldehyde	5.1 (N)	1.37	0.38, 0.23 <sup>a</sup>			2.95, 2.26 <sup>a</sup>	10
III	1.18 (N)	3.30	1.65, 1.40 <sup>a</sup>	0.50	1.40	1.65, 1.40 <sup>a</sup>	This work
<i>p</i> -Cyanobenzaldehyde	1.4 (N)	5.56	3.14, 2.73 <sup>a</sup>			0.75, 0.19 <sup>a</sup>	10

<sup>a</sup> The two ortho or meta protons are not equivalent.

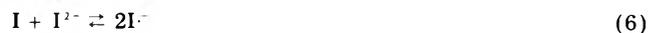
for several of the benzylidenemalononitriles. Indeed, 2-chlorobenzylidenemalononitrile has been used as the active ingredient in a wide range of devices that are employed in civil disturbances and warfare.<sup>2</sup>

It is most likely that the mechanism leading to this physiological activity involves an electron transfer from a nerve ending to the benzylidenemalononitrile to produce the anion radical of benzylidenemalononitrile. It is expected that these benzylidenemalononitriles are good electron acceptors when the structural resemblance to tetracyanoethylene (TCNE), one of the most powerful electron acceptors known,<sup>3</sup> is noted.

Israel and Jones<sup>4</sup> have reported that the physiological effects of this series of compounds is dependent upon the position and nature of the substituent on the aromatic ring. The intensity of the physiological reaction caused by a particular substituted benzylidenemalononitrile is then dependent upon several factors other than electron accepting ability (i.e., lipid solubility and steric considerations).

Since free radicals are often connected to the growth of cancerous tissue, any strong electron acceptor (radical trap) may have some anticancer activity.<sup>5</sup> This possibility has been recognized for benzylidenemalononitriles.<sup>6</sup> In fact, injections of *p*-nitrobenzylidenemalononitrile in mice with cancerous tumors did lead to a reduction in tumor size.<sup>6</sup> However, such activity could not be confirmed in humans.<sup>7</sup>

The anion radical of benzylidenemalononitrile ( $I^{\cdot-}$ ) has been generated by alkali metal reduction in dimethoxyethane (DME), and it has been shown that the concentration of monomeric anion radical is controlled by a series of equilibria (eq 1-6), in which many diamagnetic species



are formed.<sup>8</sup> In order to observe the presence of the monomer anion radical it is necessary to add large amounts of alkali metal ( $\text{NaK}_2$ ). This promotes the formation of the dimer dianion ( $I-I^{\cdot-}$ ), which cleaves to form the monomer anion radical due to the electron-electron repulsion. The  $\alpha$ -phenylbenzylidenemalononitrile anion radical does not undergo the formation of dimers and polymer, but for this system the anion radical concentration is controlled by the disproportionation to form the dianion (eq 6).

Even though the chemistry of the benzylidenemalononitrile anion radical has been well studied, this previous report<sup>8</sup> contains some errors in the assigned ESR coupling constants.<sup>9</sup> Prompted by the possible biological importance of the benzylidenemalononitrile anion radicals, we thought it of value to correct the erroneous spin densities and report on the spin densities and tendency

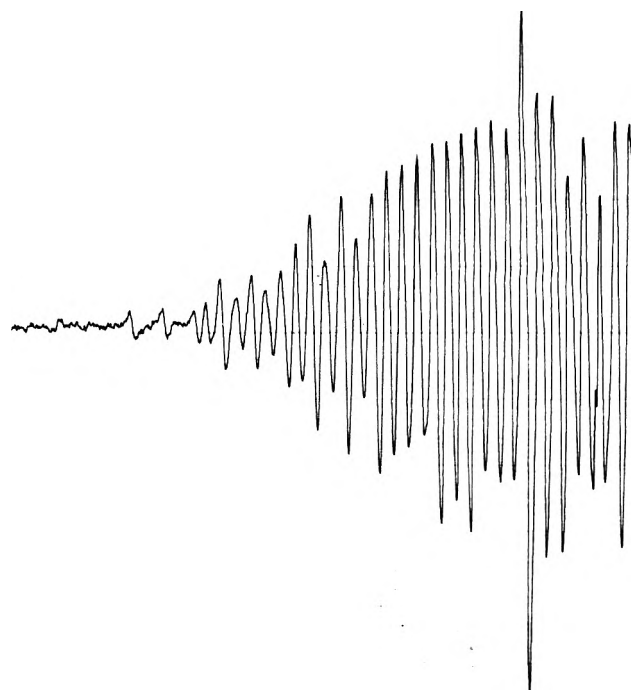


Figure 1. ESR spectrum of the anion radical of *p*-cyanobenzylidenemalononitrile in HMPA at room temperature. Only the low field half of the spectrum is shown.

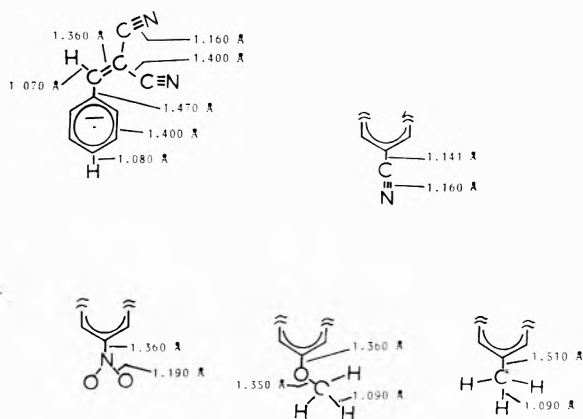
to form polymer for some para-substituted benzylidenemalononitriles.

## Results

Vigorous shaking of a 0.1 M solution of I in DME at  $-80^\circ\text{C}$  with  $\text{NaK}_2$  leads to a blue solution, which yields the same ESR pattern that has been previously reported. If the sample is allowed to warm to above about  $-10^\circ\text{C}$  a rapid irreversible polymerization takes place with consequent loss of the ESR signal. At this point polymeric material can be seen precipitating from the solution. A computer simulation shows that the ESR pattern for  $I^{\cdot-}$  can be described in terms of the coupling constants given in Table I. Less vigorous shaking of the neutral molecule solution with  $\text{NaK}_2$  at  $-80^\circ\text{C}$  leads to the formation of a red solution that yields a single broad line upon ESR analysis. This red solution probably consists of dimer and higher analogue anions, eq 1-5. The 45-line pattern previously reported to be due to the dimer anion radical<sup>8</sup> could not be reproduced and was probably due to a biphenyl impurity.

The monomer anion radical of *p*-nitrobenzylidenemalononitrile (II) could be formed by gentle shaking of the DME solution with  $\text{NaK}_2$ , and the anion radical proved to be stable even at room temperature. Essentially the same results were obtained for the *p*-cyano system (III). However, a well-resolved ESR pattern could not be obtained for  $III^{\cdot-}$  in DME as it could for  $II^{\cdot-}$ . When the reduction of *p*-cyanobenzylidenemalononitrile is carried

## Scheme I

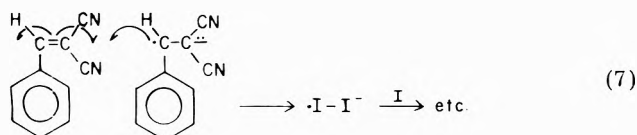


out in hexamethylphosphoramide (HMPA) a well-resolved ESR pattern can be obtained, Figure 1.

Repeated attempts to obtain an ESR signal for the anion radical of *p*-methylbenzylidenemalononitrile (IV) proved to be unsuccessful, and only the formation of polymer could be obtained. The results were similar for *p*-methoxybenzylidenemalononitrile (V), although a fleeting ESR signal could be obtained for V<sup>-</sup> at -100 °C, and only a weak poorly resolved signal could be obtained.

## Discussion

The presence of an electron-withdrawing group in the para position greatly stabilizes the system toward anionic polymerization and at the same time decreases the spin density in the dicyanoethylene moiety (see Table I). This correlation between the coupling constant for the vinyl proton and the tendency to undergo anionic polymerization is expected, since the polymerization proceeds via the joining of the ethylenic groups as shown in eq 7. Our



experiments indicate that the tendency toward anionic polymerization is  $\text{CH}_3 > \text{OCH}_3 > \text{H} > \text{CN} > \text{NO}_2$  for the para substituents used in this study.

It is interesting to correlate the observed spin densities and tendency toward anionic polymerization with the anticancer properties of these compounds. It has been observed that the deactivation of the growth of transplanted cancerous tumors in mice is dependent upon the para substituent on the injected benzylidenemalononitrile.<sup>6</sup> This order of deactivation is  $\text{NO}_2 > \text{CN} > \text{H} > \text{OCH}_3 > \text{CH}_3$ .<sup>6</sup> This is the same order found for the ability of the anion radical to resist anionic polymerization, which is essentially opposite to the order found for the spin density in the vinyl moiety.

Calculations of coupling constants for homologous series of substituted anion radicals using self-consistent-field (SCF) molecular orbital approaches with intermediate neglect of differential overlap (INDO)<sup>11</sup> have proved useful in interpreting ESR spectra these radicals.<sup>12,13</sup> In the case of benzylidenemalononitriles, however, the unusual steric requirements all but prohibit consistent assignment of coupling constants for both the hydrogen and nitrogen atoms of the molecule. The situation is considerably worse in the latter case with INDO apparently incapable of reproducing the experimentally determined difference in coupling constants between the two cyano nitrogens unless different C-N bond lengths are assumed for each.

TABLE II: INDO Calculated Coupling Constants (*G*) for the Vinyl H and the Cis and Trans Cyano Nitrogens in Para-Substituted Benzylidenemalononitrile Anion Radicals

Substituent	$A_{\text{H(vinyl)}}$	$A_{\text{N(cis)}}$	$A_{\text{N(trans)}}$
-OCH <sub>3</sub>	-7.964	1.581	1.533
-CH <sub>3</sub>	-7.129	1.579	1.546
-H	-7.496	1.590	1.556
-CN	-5.053	1.559	1.535
-NO <sub>2</sub>	-0.024	1.358	1.364

The initial calculations were performed using the bond lengths shown in scheme I. The bond angles were considered to be 109.46° for sp<sup>3</sup> and 120 for sp<sup>2</sup> hybridized atoms. All assignments were based upon X-ray crystallographic data for analogously structured molecules.<sup>14</sup>

The steric requirements of the molecule are responsible for the somewhat unreasonably long ring-C distance associated with the ethylenic moiety. If a shorter distance is used and the ethylenic moiety left in the plane of the ring, there is less than a bond length left between the ortho hydrogen and the N atom. The interatomic distances were generated by a double precision version of the computer program COORD.<sup>15</sup>

If the ethylenic moiety is rotated out of the plane of the ring around the axis formed by the ring-C bond, the shortest this bond can be is 1.47 Å, since shorter distances lead to nonconvergent INDO single electron energies. For the bond length of 1.47 Å, rotations of 20, 25, and 30° resulted in ortho H-cyano C interaction distances of 1.808, 1.901, and 2.007 Å, respectively, while the ortho H-cyano N distances were found to be 1.870, 1.996, and 2.138 Å respectively. Recognizing that the van der Waal radii of H and N are 1.2 and 1.5 Å, respectively, and that the given van der Waals radius can be approximated by adding 0.80 Å to the normal covalent bond,<sup>16</sup> the larger dihedral angles are considered most reasonable. However, severe rotations by as much as 90° would be precluded, since considerable spin density is observed in the ethylenic moiety even with the strongly electron-withdrawing NO<sub>2</sub> group in the para position. On this basis, the intermediate angle (ca. 30°) was the angle employed in the calculations.

Using these assumptions, the INDO calculated coupling constants for the vinyl H followed the same trend as the experimental tendency toward polymerization, if the CH<sub>3</sub> substituted derivative is excluded (reactivity: NO<sub>2</sub>, CN, H, OCH<sub>3</sub>, CH<sub>3</sub>; calculated  $A_{\text{H}}$ : NO<sub>2</sub>, CN, CH<sub>3</sub>, H, OCH<sub>3</sub>). Nevertheless, no substantial difference in the cis and trans cyano nitrogen coupling constants were derived from the INDO calculations for any of the para-substituted compounds, Table II.

The small difference between the INDO-derived cis and trans cyano N coupling constants suggests that perhaps the C-N and/or the C-cyano carbon bond distances are different. Indeed lengthening either of these bonds for the trans cyano group resulted in larger calculated cyano N coupling constants and larger differences in the coupling constants between the cis and trans nitrogens, but no reasonable structural adjustments used with the INDO calculation produced any N coupling constants close to those observed experimentally, Table II.

## Experimental Section

X-band ESR spectra were recorded on a Varian E-9 spectrometer. The temperature was controlled within ±3 °C with a Varian V-4557 variable temperature controller, which was calibrated with an iron-constantan thermocouple.

The benzylidenemalononitriles were synthesized by condensing the appropriate aldehyde with malononitrile in

95% ethanol as described by Patai and Rappaport.<sup>17</sup> The compounds were then repeatedly recrystallized from propanol to give a constant melting point.

The INDO program was obtained from the Quantum Chemical Program Exchange (QCPE).

**Acknowledgment.** We are grateful to the National Institute of Health for support of this work. The NIH support was from Grant No. RR-8102 of the Division of Research Resources. We also wish to thank Dr. Ira Goldberg for pointing out to us that the coupling constants reported in ref 8 are in error. G.R.S. is grateful to the sabbatical leave host (Stanford University) where part of this report was prepared.

### References and Notes

- (1) B. B. Corson and R. W. Stoughton, *J. Am. Chem. Soc.*, **50**, 2835 (1928).
- (2) D. H. Finn, M. A. Hogg, and D. Richton, British Patent, 967 600 (1964); G. T. White and L. R. Rothstein, U.S. Patent, 3 314 835 (1967); P. J. R. Bryant, A. R. Owen, and F. S. Scanes, U.S. Patent 3 391 036 (1968).
- (3) For example, see F. E. Stewart and M. Eisner, *Mol. Phys.*, **12**, 173 (1967).
- (4) G. N. R. Jones and M. J. Israel, *Nature (London)*, **228**, 1315 (1970).
- (5) W. A. Pryor, *Chem. Eng. News*, **34** (June 7, 1971).
- (6) N. L. Petrakis, H. R. Bierman, and M. B. Shimkin, *Cancer Res.*, **12**, 573 (1952).
- (7) E. M. Gal, F. H. Fung, and D. M. Greengerg, *Cancer Res.*, **12**, 565 (1962).
- (8) F. J. Smentowski and G. R. Stevenson, *J. Phys. Chem.*, **74**, 2525 (1970).
- (9) R. Chang and R. D. Allendoerfer, *J. Phys. Chem.*, **76**, 3384 (1972).
- (10) P. H. Rieger and G. K. Fraenkel, *J. Chem. Phys.*, **37**, 2811 (1967).
- (11) J. A. Pople and D. Beveridge, "Approximate Molecular Orbital Theory", McGraw-Hill, New York, N.Y., 1971.
- (12) G. R. Stevenson, A. E. Alegria, and A. M. Block, *J. Am. Chem. Soc.*, **97**, 4859 (1975).
- (13) G. R. Stevenson, M. Colon, I. Ocasio, J. G. Concepcion, and A. M. Block, *J. Phys. Chem.*, **79**, 1685 (1975).
- (14) L. E. Sutton, Ed., "Tables of Interatomic Distances and Configuration in Molecules and Ions", The Chemical Society, London, Burlington House, W. 1., 1958.
- (15) M. J. S. Dewar and N. C. Baird, Quantum Chemical Program Exchange, Department of Chemistry, Indiana University, Bloomington, Ind.
- (16) L. Pauling, "The Nature of the Chemical Bond", Cornell University Press, Ithica, N.Y., 1960.
- (17) S. Patai and Z. Rappaport, *J. Chem. Soc.*, 383 (1962).

## Effects of Solvent and Concentration on the Diffusion of Triplet Anthracene

R. D. Burkhart

Department of Chemistry, University of Nevada, Reno, Nevada 89557 (Received October 28, 1976)

Publication costs assisted by the U.S. Energy Research and Development Administration

The delayed fluorescence spectrometer used to measure triplet diffusion by the space intermittency method has been modified to augment the intensity of emission signals and to facilitate data handling by computer methods. As a result a significant improvement in precision has been achieved. Measurements of triplet anthracene diffusion have been carried out in methylcyclohexane and cyclooctane at 25 °C. A decrease in measured diffusion coefficient with increasing concentration has been observed, the effect being greater in the less viscous solvent. At the lowest concentrations used  $D$  (in methylcyclohexane) =  $2.67(\pm 0.18) \times 10^{-5}$  cm<sup>2</sup>/s and  $D$  (in cyclooctane) is  $1.42(\pm 0.14) \times 10^{-5}$  cm<sup>2</sup>/s.

### Introduction

During the past few years several published studies have appeared on the solution-phase or liquid-phase mobility of aromatic triplets.<sup>1-5</sup> Most of these studies utilize annihilation or, P-type, delayed fluorescence to monitor the spatial distribution of triplets following an irradiation pulse which produces triplets in a spatially intermittent array. Noyes and co-workers applied a somewhat similar method to the measurement of free-radical diffusion coefficients.<sup>6</sup> Triplet exciton migration in anthracene crystals also was studied using this technique.<sup>7</sup>

Part of our motivation for studying triplet migration is to try to characterize the physical state in which these species exist in solution. It is hoped that this can be accomplished by comparing observed mobilities with those which would be expected either from Stokes-Einstein behavior or from measured mobilities of the corresponding ground state species. An additional motivation is provided by the realization that accurate diffusion data for molecules in fluid media which mimic the characteristics of biological cells can provide very useful information about the hydrodynamics of the cell environment.<sup>8,9</sup> It is difficult to apply conventional diffusion techniques in such studies.

None of these hoped-for objectives will be realized unless the execution of the experiments can be reduced to a fairly

simple procedure which is known to give reliable results with good precision. The purpose of this paper is to describe some modifications of the earlier experimental setup, including methods of data handling, which have led to a significant improvement in the precision of diffusion results. In addition, some new data have been obtained on the solvent dependence and concentration dependence of triplet anthracene diffusion which will be useful in characterizing the general properties of the translational motion of triplets in solution.

### Experimental Section

Both methylcyclohexane and cyclooctane were treated with concentrated H<sub>2</sub>SO<sub>4</sub>, neutralizing base, and several water washes before being dried and then doubly distilled. The anthracene sample is 99.999% pure material purchased from James Hinton of Columbia, S.C.

The optical system is very similar to that previously described<sup>10</sup> with the following modifications. The light source is a Hg-Xe lamp which has a variable power output from about 250 to 1000 W. Patterns consisting of opaque and translucent strips of equal width are inserted in the light beam and, using the optical system described earlier, the sample is irradiated with a reduced image of these patterns. Since the optical path through the sample is only

1 mm, the pattern image stays in focus during its passage through the solution. A major modification of the optical system is that the photomultiplier has been moved into a position which is in-line with the excitation beam rather than at 90°. This has made a considerable improvement in the signal level obtained with very little sacrifice in the stray light level. The excitation light is filtered using a Corning CS 7-60 filter which has a fairly sharp cutoff at 400 nm transmitting only at wavelengths shorter than this.

The emission signal is chopped at 30 Hz and is picked up by the photomultiplier after passing through a cutoff filter transmitting above 400 nm. Each delayed fluorescence decay pulse is sent to a Nicolet 1072 multichannel analyzer and, after a signal level sufficient for analysis has been accumulated, the data are punched out on tape and then stored on the computer. Curve fitting procedures are then applied (*vide infra*) to extract the desired information.

All solutions are degassed on a high vacuum system. Enough freeze-pump-thaw cycles are used so that residual gas causes a pressure jump of less than  $3 \times 10^{-6}$  Torr, as measured on a Penning gauge at the beginning of a pumping stage. The solutions are sealed off under vacuum with the frozen solution open to the vacuum pump during seal off. Solutions prepared in this way gave constant delayed fluorescence lifetimes over periods of many weeks.

### Experimental Results

In the limit of sufficiently small triplet concentrations such that second-order processes for their removal have a negligible rate compared with first order processes, one may write

$$\partial T/\partial t = \phi q(x, t) + D\nabla^2 T - T/\tau \quad (1)$$

In this equation  $\phi q(x, t)$  is the time-dependent and spatially-dependent rate of triplet formation;  $\phi$  being the triplet quantum yield and  $q(x, t)$  being the rate of light absorption. The triplet diffusion coefficient is symbolized by  $D$ ,  $\tau$  is the triplet lifetime, and  $T$  is meant to represent the concentration of triplets. The diffusion term is important because the spatially intermittent formation of triplets leads to delayed fluorescence intensities which are dependent upon diffusion rates.

The solutions are irradiated through a pattern consisting of parallel light and dark strips and we symbolize the width of a light plus dark strip, or repeat distance as  $X_0$ . In these particular patterns the light and dark strips have equal width so the window-to-period ratio,  $r$ , is 0.5.

The solution to eq 1 for delayed fluorescence decay is<sup>11</sup>

$$\phi_N(t) = \{ \exp(-2\beta t) + \sum_i A_i \exp[-2(1 + a^2 l^2) \beta t] \} / N(a) \quad (2)$$

where

$$a = 2\tau(D\tau)^{1/2}/X_0 \quad (3)$$

$$A_i = 2 \sin^2(l\pi r)/r^2 \pi^2 l^2 (1 + l^2 a^2)^2 \quad (4)$$

and

$$N(a) = 1 + \sum_i A_i \quad (5)$$

In these equations  $\beta = 1/\tau$  and  $\phi_N(t)$  is the delayed fluorescence intensity normalized to unity at  $t = 0$ .

To measure a diffusion coefficient it is necessary, first of all, to determine the triplet lifetime under conditions of homogeneous illumination. The delayed fluorescence decay is collected by storing several thousand decay events on the multichannel analyzer. The data are transferred to the computer and a weighted least-squares program is

TABLE I: Lifetimes and Diffusion Coefficients of Triplet Anthracene in Two Different Solvents and Different Concentrations at 25 °C

[Anthracene], M $\times 10^5$	Solvent	$\tau$ , <sup>a</sup> ms	$D$ , <sup>b</sup> cm <sup>2</sup> /s $\times 10^5$
0.99	Methylcyclohexane	8.19	2.67
2.0	Methylcyclohexane	3.22	1.52
4.9	Methylcyclohexane	5.75	1.24
12.4	Methylcyclohexane	3.15	<1.0
0.94	Cyclooctane	4.81	1.42
1.89	Cyclooctane	3.76	1.33
4.72	Cyclooctane	1.82	0.9

<sup>a</sup> Average deviations in  $\tau$  values were about 2%. <sup>b</sup> Average deviations in  $D$  values were about 10%.

used to calculate delayed fluorescence lifetimes,  $\tau_{df}$ , from the equation

$$I_{df} = A + B \exp(-t/\tau_{df}) \quad (6)$$

An indication that the scattered light intensity is quite low is provided by the fact that  $A$  is found to be less than 1% of  $B$ . Good fits to an exponential decay were found in these experiments and the  $\tau_{df}$  values were independent of incident light intensity over the range used for diffusion measurements. Thus, the assumption that steady state triplet concentrations are independent of second-order processes is valid so that  $\tau = 2\tau_{df}$ .

The delayed fluorescence decay observed when the sample was irradiated using an appropriately sized strip pattern was found to have a shorter lifetime than with homogeneous irradiation. This is because a certain fraction of the triplets diffuse into nonilluminated regions where the average triplet concentration is significantly reduced. Only a very small fraction of these triplets will ever become involved in triplet-triplet annihilation and most are lost, therefore, as far as delayed fluorescence emission is concerned. This effect is most pronounced for a values (eq 3) equal to 1.0.

In these experiments the smallest  $X_0$  value used was 0.00312 cm. Thus, to achieve  $a = 1$  for a diffusion coefficient of, for example,  $2 \times 10^{-5}$  cm<sup>2</sup>/s requires  $\tau$  equal to about 12 ms. At the temperature used in these experiments (25 °C) the  $\tau$  values varied from about 2 to 8 ms so we never really achieved the best conditions for diffusion measurements. It is noteworthy, however, that the best precision was found with the sample for which  $\tau$  was largest.

When the samples were irradiated using a strip pattern, the delayed fluorescence decay signals were again accumulated on the multichannel analyzer for several thousand decay events after which the data were transferred to the computer. The best fit to the equation

$$I_{df} = P + Q\phi_N(t)$$

was then determined by successive adjustment of the parameter  $a$ , again using a weighted least-squares program. From the best  $a$  value,  $D$  could be calculated using eq 3.

Table I summarizes some measurements made on triplet anthracene at different concentrations in two different solvents, methylcyclohexane and cyclooctane.

### Discussion

The results of Table I show that one of the primary goals of this work has been accomplished, that is, the achievement of a significant improvement in precision. The best precision was found for the  $D$  value of  $2.67 \times 10^{-5}$  cm<sup>2</sup>/s in methylcyclohexane for which the average deviation was  $\pm 7\%$ . The best precision found in earlier efforts<sup>1</sup>

was  $\pm 25\%$  so there has been almost a fourfold improvement in the degree of reproducibility of these measurements.

Two modifications in the operation of the experiment have been primarily responsible for this. First of all, the use of collection optics located at  $180^\circ$  from the excitation source has resulted in much more intense delayed fluorescence signals. Secondly, by means of the multi-channel analyzer it has been possible, not only to build up a signal of reasonable size, but also this final signal is in digital form, suitable for computer processing. In earlier work it was necessary to use delayed fluorescence ratios obtained with and without patterns in place as the raw data,<sup>1</sup> but these ratios of absolute intensities were very dependent on exact placement of the patterns in the excitation beam. It was also necessary to be able to account for variable transmittance of the excitation light through the translucent strips of the different patterns. The mode of data analysis used in the present work does not depend on absolute delayed fluorescence intensities, only on the time dependence of these intensities which can be measured with better precision.

In order to compare the data of Table I with diffusion results found by other workers, it is useful to consider the diffusion coefficient of  $2.8 \times 10^{-5} \text{ cm}^2/\text{s}$  found for anthracene in paraffin solvents at  $20^\circ\text{C}$ . The viscosity of the solvent was such that  $T/\eta = 5.8 \times 10^{-4}$ . Thus, the Stokes-Einstein equation yields an effective hydrodynamic radius of  $1.5 \text{ \AA}$  for anthracene. If this same radius is then used to calculate a diffusion coefficient for anthracene in methylcyclohexane, for which  $\eta$  is  $0.00687^{13} \text{ P}$  at  $25^\circ\text{C}$  one finds  $D_{\text{calcd}} = 2.1 \times 10^{-5} \text{ cm}^2/\text{s}$ . The largest value measured here is  $2.67 \times 10^{-5} \text{ cm}^2/\text{s}$  which, in view of the approximations inherent in the Stokes-Einstein equation, is not bad agreement. For cyclooctane the agreement is not so good. For this solvent  $\eta$  is  $0.0203^{14} \text{ P}$  and  $D_{\text{calcd}}$  is  $0.72 \times 10^{-5} \text{ cm}^2/\text{s}$ , only slightly greater than one-half the measured value for the most dilute solution.

These observations are consistent with earlier findings that triplet diffusion coefficients are somewhat larger than would be predicted from the behavior of ground state species. As a possible rationale for this behavior the suggestion was made that energy transfer may be contributing to the net translational motion. From the results of the concentration studies it is clear that such is not the case. That is, the triplet mobility is seen to decline with growing anthracene concentration rather than to increase, as would be required for energy transfer. It is, perhaps, noteworthy that the concentration effect is much less marked in the solvent of higher viscosity.

It appears that a molecular association process is occurring between triplet anthracene and ground state molecules, which results in a smaller effective mobility with increasing concentration. Such a process might, for ex-

ample, be a dipole-induced dipole interaction. Although the attractive potential associated with such a process depends on the dipolar character of the triplet and might be rather small, the activation energy for diffusive displacements is likewise very small. Furthermore, a bimolecular association process would occur at a slower rate as the viscosity of the medium increases, hence the effect of concentration ought to be less marked in more viscous solvents as is observed.

The fact that triplet anthracene diffusion is larger than predicted by the Stokes-Einstein equation is more likely associated with problems in utilizing this particular equation rather than due to special properties of the diffusing triplets. In terms of molecular size, the two solvents used here are not greatly different but there is a factor of 3 difference in their viscosities. The larger viscosity of cyclooctane is not due to any polar effects either, so apparently the viscosity difference is due primarily to molecular shape.

Whatever the source of the viscosity difference, it is reasonable to believe that the rapidity with which local solvent structure rearranges is greater for the less viscous solvent. Thus, as a solute molecule probes a given microscopic region of space by a net translational motion, the greater the solvent mobility the more closely will this probed region approach the character of a macroscopic region with the same number density of solvent molecules and the same mean velocity.<sup>15</sup> Since the Stokes-Einstein equation is based on a macroscopic model it is not surprising that it gives better agreement with experiment in more fluid solvents.

*Acknowledgment.* The author is grateful to Mr. Robert Rechtsteiner who helped in the construction of the equipment and to ERDA for financial support under contract no. AT (26-1)-535.

## References and Notes

- (1) R. D. Burkhart, *J. Am. Chem. Soc.*, **96**, 6276 (1974).
- (2) R. B. Kellogg and A. Prock, *J. Chem. Phys.*, **63**, 3161 (1975).
- (3) B. Nickel and E. G. Meyer, "Luminescence of Crystals, Molecules and Solutions", F. Williams, Ed., Plenum Press, New York, N.Y., 1975, pp 297-303.
- (4) B. Nickel and U. Nickel, *Ber. Bunsenges. Phys. Chem.*, **76**, 584 (1972).
- (5) B. Nickel, *Ber. Bunsenges. Phys. Chem.*, **76**, 582 (1972).
- (6) S. A. Levison and R. M. Noyes, *J. Am. Chem. Soc.*, **86**, 4525 (1964).
- (7) R. E. Merrifield, *Acc. Chem. Res.*, **1**, 129 (1968).
- (8) K. R. Naqvi, J.-P. Behr, and D. Chapman, *Chem. Phys. Lett.*, **26**, 440 (1974).
- (9) L. A. Sklar, B. S. Hudson, and R. D. Simoni, *Proc. Natl. Acad. Sci. U.S.A.*, **72**, 1649 (1975).
- (10) R. D. Burkhart and J. W. Kenney, III, *J. Chem. Instrum.*, **6**, 37 (1975).
- (11) V. Ern, P. Avakian, and R. E. Merrifield, *Phys. Rev.*, **148**, 862 (1966).
- (12) E. J. Bowen and W. S. Metcalfe, *Proc. R. Soc. London, Ser. A*, **206**, 437 (1951).
- (13) Landolt-Bornstein, II. Band, Transport-Phänomene I, Springer-Verlag, New York, N.Y., 1969, p 159.
- (14) Reference 13, p 161.
- (15) R. D. Burkhart and J. C. Merrill, *J. Chem. Phys.*, **46**, 4985 (1967).

# Tape Cassettes From The American Chemical Society Famous Scientists

## ENERGY

- Energy & Industry**  
A. Waterland  
**Energy & Environment**  
Dr. S. Manahan
- Energy on the Shelf**  
H<sub>2</sub> and You  
Dr. D. Gregory
- Green-Thumb Energy**  
Dr. D. Kless  
**Methane from Coalbeds**  
Dr. R. Stefanko
- The Promise of Hydrogen**  
Jack Russell
- Optical Communications**  
J. Cook, B. DeLoach, A. D. Pearson
- Energy in the Future**  
Dr. Paul Donovan
- Solar Homes for the Future**  
Dr. I. Kugelmann
- Coal's New Face**  
Dr. Bernard Lee  
**More Power, Less Pollution**  
Dr. Daniel Blenstock
- Cleaning A Dirty Fuel**  
H. Feldman  
**From Wastes to Energy**  
H. Feldman
- Energy: A Critique**  
Dr. Dean Abrahamson  
**Puzzles of Air Pollution**  
Arthur Levy
- Fusion: Prospects & Pitfalls—I**  
Dr. H. Furth & Dr. H. Forsen  
**Fusion: Prospects & Pitfalls—II**  
Dr. H. Furth & Dr. H. Forsen
- Antidote to the Energy Crisis**  
George Long  
**Chemicals In the Environment**  
Dr. Samuel Epstein
- Fusion and Fission: An Appraisal**  
Dr. James L. Tuck  
**The Prospects for Energy**  
Dr. M. King Hubert

## ENVIRONMENT

- The Spray Can Threat**  
Dr. F. S. Rowland
- The Invisible Enemy**  
Dr. R. Stewart
- Cities & Weather—I**  
Dr. R. Graham
- Cities & Weather—II**  
Dr. R. Graham
- Putting Potatoes in Plastics**  
Lead Poisoning in Children  
Dan Darrow
- New Look in Phosphorus Removal**  
Dr. Gilbert Levin  
**A Solution for Metals**  
Thomas Chapman
- Turning Insects Against Themselves**  
Daniel Lazare  
**Updating Aluminum**  
Dr. Allen Russell
- Energy and Environmental Thrift**  
Dr. S. Berry  
**Tracing the Skeleton's Image**  
Dr. T. Raby
- Seafood From Waste**  
J. Huguennin  
**Underwater World of Communications**  
Dr. J. Atema
- Water Supply of the Future**  
Dr. I. Kugelmann  
**The Secrets of Salmon**  
Dr. A. Hasler
- Cleaner Water Through Chemistry**  
D. Parker  
**Bromine Chloride: A Better Disinfectant**  
Dr. J. Mills
- The Damaged Air—I**  
**The Damaged Air—II**  
Dr. John Amodeo  
**How Smells Shape Up**  
Urban Auto Design
- Tough Filaments of Fragile Liquid Electricity from Rooftops**  
James Bacon  
Dr. Charles Backus
- The Struggle for Clean Water—I**  
**The Struggle for Clean Water—II**  
The Oil Mystery  
Harold Bernard  
**The Language of Odors**  
Dr. Stanley Freeman
- The Lonely Atom**  
Dr. Philip Skellern  
**How Green The Revolution**  
Lester Brown
- Mercury: Another Look—Part I**  
Dr. John Wood  
**Mercury: Another Look—Part II**  
Dr. John Wood & D. G. Langley
- The Troubles with Water**  
Dr. Daniel Okun  
**Pure Oxygen for Polluted Water**  
Dr. Jack McWhirter

- Monitoring High Risk Pregnancies**  
Dr. K. Stiles & J. Hobbins  
**Progress in Enzyme Replacement Therapy**  
Dr. Roscoe Brady
- Safety for Premature Infants**  
Dr. John Morrison  
**Help for the Critically Ill**  
Dr. Joseph Meylan
- Pinpointing Hepatitis Viruses**  
Dr. Robert Purcell  
**New Key to Heart Disease**  
Dr. Antonio Gotto
- Nature's Own Toxicants in Foods Added, Not Imported**  
Dr. J. M. Coon  
Dr. H. Kraybill
- Seventy-Two Per Minute—I**  
Dr. L. Harmonson  
**Seventy-Two Per Minute—II**  
Dr. N. Razor
- Two Drugs, More or Less**  
Dr. K. Hussar  
**Filling the Molar Gap**  
Dr. J. Cassel
- A Tilt at Genetic Ills**  
V. Aposthian  
Dr. H. Garfinkel
- Early Prenatal Diagnosis of Genetic Disease**  
Dr. M. L. Moss  
**From Mother to Child**  
Dr. M. Horning & Dr. R. Hill
- Insulin & Diabetes—I**  
Dr. George Cahill  
**Insulin & Diabetes—II**  
Dr. George Cahill
- Stalking the Molecules of Memory**  
Dr. Leslie Iverson  
**Immunotherapy**  
Dr. Kenneth Bagshawe
- Engineering Enzymes**  
Dr. Victor Edwards  
**Drugs, Plasticizers, & Mass Spec**  
Dr. G. W. A. Milne
- Birth Control: Problems & Prospects**  
Dr. Carl Dierassi  
**Hormones, Terpenes, & the German Air Force**  
Dr. A. J. Birch
- Prospects for Implants**  
Dr. Donald Lyman  
**New Dimensions for Polymers**  
Dr. Alan Michaels
- Fabricating Life**  
An Essay Report  
Dr. R. W. F. Hardy
- Chemistry of the Mind: Schizophrenia**  
Dr. Larry Stein  
**Chemistry of the Mind: Depression**  
Dr. Joel Elkes
- The Molecules of Memory**  
Dr. W. L. Byrnie & Dr. A. M. Golub  
**The Matter with Memory**  
Dr. J. McGeugh

- Dissonant Harmony**  
Dr. Denham Harman  
**Why We Grow Old**  
Dr. Howard Curtis
- New Materials for Spare Parts**  
Dr. V. Gott & Dr. A. Rignall  
**Against Individuality**  
Dr. R. Reisfeld & Dr. B. Kahan
- A Richness of Lipids**  
Dr. Roscoe O. Brady  
**Life: Origins to Quality**  
Dr. Stanley Miller
- The Nitrogen Fixer**  
Dr. Eugene van Tamsel  
**Prostaglandins: A Potent Future**  
Dr. E. J. Corey & Dr. S. Bergstrom
- Chemical Evolution**  
Dr. Russell Doolittle  
**An Evolving Engine**  
Dr. R. E. Dickerson

## CANCER RESEARCH

- Cancer & the Cell Membrane**  
Dr. R. Barnett  
**Interferon: From Colds to Cancer**  
Dr. S. Baron
- Cancer & Chemicals—I**  
Dr. Charles Heidelberger  
**Cancer & Chemicals II**  
Dr. Charles Heidelberger
- Screening for Cancer Agents**  
Dr. Bruce Ames  
**Narcotics & the Brain**  
Dr. Avram Goldstein
- Chemicals Combating Cancer**  
Dr. David Grassetti  
**Chemical Essence of Beer & Ale**  
Dr. Rao Palamand
- Cancer Research I—Perspective & Progress**  
Dr. Frank Rauscher  
**Cancer Research II—Viruses**  
Dr. R. Gallo & Dr. G. Todaro
- Cancer Research III—Chemotherapy**  
Dr. C. Gordon Zubrod  
**Cancer Research IV—Immunology**  
Dr. Paul Levine
- Cancer Research V—Environmental Agents**  
Dr. Umberto Saffroni  
**Cancer Research VI—NCI Roundtable**

## BIO-MEDICAL

- Fighting Fat**  
Dr. J. J. Marshall  
**Tackling Tooth Decay**  
Dr. J. Cassel
- Progress Against Diabetes**  
Dr. D. Steiner  
**The Sickle Cell Problem**  
Dr. R. Jackson
- A New Look at Stroke**  
Dr. R. Wurtman  
**Chemical Look at Mental Illness**  
Dr. S. Key
- Nutrition & the Brain**  
Dr. J. Fernstrom  
**The Forgotten Nutrient**  
Dr. J. Scala
- Remodeling the Body**  
Dr. S. Carr  
**Nuclear Medicine**  
Dr. W. Wolf

- The View from Space**  
Dr. R. Maddole & R. Anderson  
**The Attraction of Magnets**  
David Kelland
- Cosmic Ray Astronomy**  
Dr. P. Meyer  
**The Reactor Never Lies**  
T. Raby
- Wine From Native American Grapes—I**  
Dr. A. Rice  
**Wine From Native American Grapes—II**  
Dr. A. Rice
- Community Needs: New Emphasis in Research**  
Dr. H. Guyford Stever  
**Aspirin vs. Prostaglandins**  
Dr. John Vane
- A Breakdown in Plastics—I**  
Drs. J. Guillet & G. Scott  
**A Breakdown in Plastics—II**  
Drs. J. Guillet & G. Scott
- Protein: The Next Big Production?**  
Dr. Steven Tannenbaum  
**Clean Energy: A One-Way Dream**  
Dr. J. R. Eaton
- Nitrosamines: A Reappraisal**  
Dr. Phillip Issenberg  
**The Emperor of Ice Cream**  
Dr. Wendell Attkettle
- Ethics and Genetics**  
Dr. Robert F. Murray  
**The American Diet: A Critique**  
Dr. Arnold Schaefer
- Probing Creation**  
Dr. Myron A. Coler  
**New Directions in U.S. Science**  
Dr. William McElroy
- Aspirins, Enzymes, & Fragrant Redheads**  
An Essay Report  
**Vitamin D: A New Dimension**  
Dr. Hector DeLuca
- Engineering Microbes**  
Dr. Elmer Gaden  
**Liquid Crystals: A Bright Promise**  
Dr. George Helmeier
- Lively Xenon**  
Dr. Neil Bartlett  
**The Repressor Hunt**  
Dr. Mark Ptashine

## NOBEL PRIZE WINNERS

- Dr. Linus Pauling**  
The Committed Scientist  
**Dr. Jacob Bronowski**  
Science and Man
- Dr. Glenn Seaborg**  
The Atomic World of Glenn Seaborg  
**Dr. George Wald**  
Vision, Night Blindness, & Professor Wald
- Dr. Melvin Calvin**  
The Search for Significance—Parts I & II

## SCIENCE

- Tapping the Oceans**  
Dr. O. Roels  
**Davy Jones' Treasure**  
Dr. S. Gerard
- The Need for Nitrogen**  
Dr. R. Hardy  
**Modifying Milk for Millions**  
A. Rand & J. Hourigan
- The Seas in Motion**  
Dr. Wallace Broecker  
**Rumbles in the Earth**  
Dr. Christopher Scholz

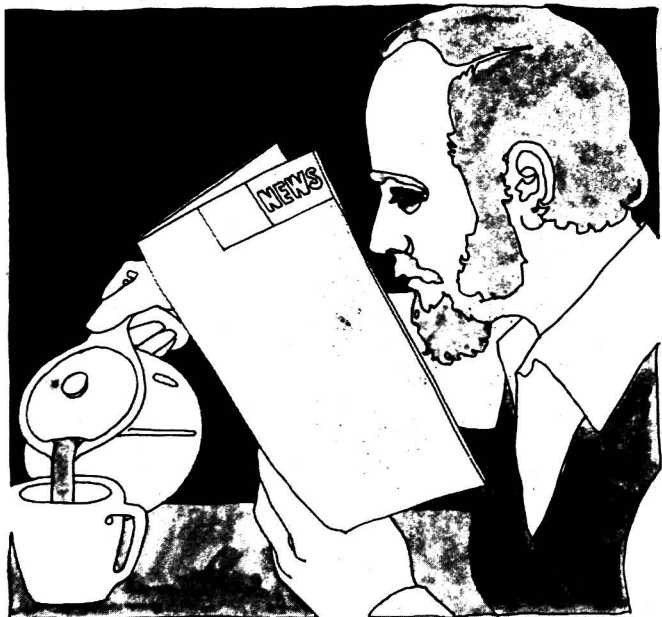
**ACS Members** \$5.95  
**Nonmembers** \$6.95  
**Single cassette** \$4.95/cassette  
**Any Eight cassettes** \$4.95/cassette  
**Any 20 or more cassettes to one address** \$4.00/cassette  
**10% Discount if payment accompanies order**

Name \_\_\_\_\_

Address \_\_\_\_\_

City \_\_\_\_\_ State \_\_\_\_\_ Zip \_\_\_\_\_

Order from: American Chemical Society, Dept. 9H  
1155 16th St., N.W., Wash., D.C. 20036  
Allow 4 to 6 weeks for delivery



**WARNING! Chemical & Engineering News may become habit forming!**

Over 120,000 chemists and chemical engineers have the C&EN habit *now* and more of them are becoming addicted every week.

They've discovered it's the most valuable way to start the week . . . with up-to-the-minute news of the chemical world.

Join their number and you'll know about every major new development in industry, government, research organizations, and educational institutions around the world. You'll read about the latest controversy and current discussions going on in science. Environmental problems . . . chemical welfare . . . crucial shortages . . . latest legislation . . . all are probed and explored.

For pennies a week you can find C&EN on your desk each week. Just complete and mail in

the order form on this page. We'll do the rest!

**Chemical & Engineering News 1977**

Please enter my 1977 introductory subscription to CHEMICAL & ENGINEERING NEWS at the rate checked.

Nonmember offer only.

Allow 45 days for your first copy to be mailed.

**AMERICAN CHEMICAL SOCIETY**  
1155 Sixteenth Street, N.W.  
Washington, D.C. 20036

	U.S.	PUAS	Canada and Foreign
One Year	<input type="checkbox"/> \$17.50	<input type="checkbox"/> \$25.50	<input type="checkbox"/> \$27.00
Three Years	<input type="checkbox"/> \$37.50	<input type="checkbox"/> \$61.50	<input type="checkbox"/> \$66.00

Payment Enclosed  Bill Company  Bill Me

Name \_\_\_\_\_ Title or Position \_\_\_\_\_  
 Mailing  Home \_\_\_\_\_  
 Address:  Business \_\_\_\_\_  
 City \_\_\_\_\_ State \_\_\_\_\_ Zip \_\_\_\_\_  
 Billing Address (If other than the above) \_\_\_\_\_  
 City \_\_\_\_\_ State \_\_\_\_\_ Zip \_\_\_\_\_  
 Company \_\_\_\_\_